SYNTHESIS, CHARACTERISATION AND OPTOELECTRONIC PROPERTIES OF PHOSPHORESCENT IRIDIUM COMPLEXES: FROM FIVE TO SIX-MEMBERED RING CHELATES

Claus Hierlinger

A Thesis Submitted for the Degree of PhD
at the
University of St Andrews

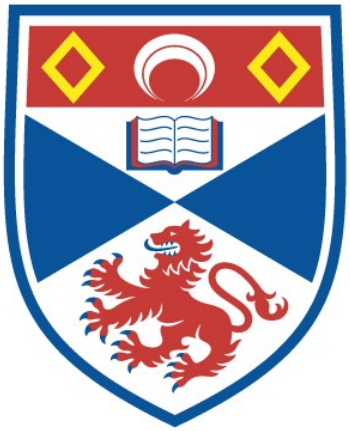

2018

Synthesis, Characterisation and Optoelectronic Properties of Phosphorescent Iridium Complexes: from five to six-membered ring chelates.

Claus Hierlinger

Candidate's declaration

I, Claus Hierlinger, do hereby certify that this thesis, submitted for the degree of PhD, which is approximately 50,000 words in length, has been written by me, and that it is the record of work carried out by me, or principally by myself in collaboration with others as acknowledged, and that it has not been submitted in any previous application for any degree.

I was admitted as a research student at the University of St Andrews in September 2015.

I confirm that no funding was received for this work.

02/07/2018

Date Signature of candidate

Supervisors' declaration

We hereby certify that the candidate has fulfilled the conditions of the Resolution and Regulations appropriate for the degree of PhD in the University of St Andrews and that the candidate is qualified to submit this thesis in application for that degree.

02/07/2018

Date Signatures of supervisors

Permission for publication

In submitting this thesis to the University of St Andrews we understand that we are giving permission for it to be made available for use in accordance with the regulations of the University Library for the time being in force, subject to any copyright vested in the work not being affected thereby. We also understand, unless exempt by an award of an embargo as requested below, that the title and the abstract will be published, and that a copy of the work may be made and supplied to any bona fide library or research worker, that this thesis will be electronically accessible for personal or research use and that the library has the right to migrate this thesis into new electronic forms as required to ensure continued access to the thesis.

I, Claus Hierlinger, have obtained, or am in the process of obtaining, third-party copyright permissions that are required or have requested the appropriate embargo below.

The following is an agreed request by candidate and supervisor regarding the publication of this thesis:

Printed copy

Embargo on all of print copy for a period of 1 year on the following ground(s):

- Publication would preclude future publication

Supporting statement for printed embargo request

Some of the work presented is unpublished at present.

Electronic copy

Embargo on all of electronic copy for a period of 1 year on the following ground(s):

- Publication would preclude future publication

Supporting statement for electronic embargo request

Some of the work is unpublished at present.

Title and Abstract

- I agree to the title and abstract being published.

02/072018

Date Signature of candidate

02/07/2018

Date Signatures of supervisors

Underpinning Research Data or Digital Outputs

Candidate's declaration

I, Claus Hierlinger, understand that by declaring that I have original research data or digital outputs, I should make every effort in meeting the University's and research funders' requirements on the deposit and sharing of research data or research digital outputs.

02/07/2018

Date Signature of candidate

Permission for publication of underpinning research data or digital outputs

We understand that for any original research data or digital outputs which are deposited, we are giving permission for them to be made available for use in accordance with the requirements of the University and research funders, for the time being in force.

We also understand that the title and the description will be published, and that the underpinning research data or digital outputs will be electronically accessible for use in accordance with the license specified at the point of deposit, unless exempt by award of an embargo as requested below.

The following is an agreed request by candidate and supervisor regarding the publication of underpinning research data or digital outputs:

Embargo on all of electronic files for a period of 1 year on the following ground(s):

- Publication would preclude future publication

Supporting statement for embargo request

Some work is unpublished at present.

02/072018

Date Signature of candidate

02/07/2018

Date Signatures of supervisors

Abstract

Here, the design, synthesis and characterisation and the optoelectronic properties of Ir(III) complexes for application in nonlinear optical and electroluminescent devices are described. The type of complexes varies from those of the form $[Ir(C\hat{}N)_2(N\hat{}N)]^+$ with conjugated and nonconjugated ligands (where C^N = cyclometalating ligand and N^N = neutral ligand) to those of the form [Ir(C^N^C)(N^N)Cl] (where C^N^C = tridentate tripod ligand).

Chapter 1 gives an introduction into photophysics occurring in transition metal complexes and possible applications in visual displays. The background of nonlinear optical (NLO) properties and the use of transition metal complexes as NLO chromophores is described.

In Chapter 2, the impact of the use of sterically congested cyclometalating ligands on the photoluminescence properties of cationic iridium(III) complexes and their performance in light-emitting electrochemical cells is investigated.

Chapter 3 explores the use of electron donors on the cyclometalating ligand towards modulating the NLO properties of the complexes. Combining strongly electron-donating substituents on the C^N ligand and electron-accepting substituents on the N^N ligand results in strong NLO activity.

Chapter 4 summarises a new series of cationic iridium(III) complexes bearing benzylpyridinato as cyclometalating ligands. The methylene spacer in the C^N ligands provides flexibility, resulting in two conformers. NMR studies combined with density functional theory (DFT) studies show how the fluxional behaviour is influenced by the choice of the ancillary ligand.

In Chapter 5, Ir(III) complexes bearing an unusual nonconjugated bis(six-membered) tridentate tripod ligand of the form [Ir(C^N^C)(N^N)Cl] are introduced. Depending on the

substitutions of the C^N^C ligand phosphorescence ranging from yellow to red was obtained. Substitution of the N^N results in a panchromatic NIR dye, suitable for DSSC applications.

In Chapter 6, the concept of a nonconjugated ligand was expanded to the N^N ligand. Blue-green and sky-blue emission was obtained, demonstrating a strategy to successfully tune the emission to the blue.

Declaration

I fully acknowledge that the work presented herein is my own. The research carried out during my PhD studies in the groups of Dr Véronique Guerchais (University of Rennes 1) and Dr Eli Zysman-Colman (University of St Andrews), however is highly interdisciplinary with contributions from collaborators and co-authors, that are listed below:

Chapter 1: I am the primary author of the text.

Chapter 2: The synthesis of the organic compounds was carried out by me. The synthesis of the iridium dimer of complex **1** was carried out by Muriel Escadeillas. All other dimers and all complexes were synthesised by me. The UV-vis and fluorescence spectroscopy described in this chapter was carried out by me. Single crystal data collection and structure solving was performed by Dr Loïc Toupet and Dr Elzbieta Trzop. Light-Emitting Electrochemical Cells (LEECs) were fabricated by Jorge Ávilla and Dr Antonio Petergás in the group of Dr Henk Bolink (University of Valencia). I am the primary author of the text. The work in this chapter has been published.

1) C. Hierlinger, E. Trzop, L. Toupet, J. Ávila, M. La-Placa, H. J. Bolink, V. Guerchais, E. Zysman-Colman. *J. Mater. Chem. C*, **2018**, 6, 6385–6397.DOI: 10.1039/C8TC01130C

Chapter 3: The syntheses of the organic ligands, the iridium(III) dimers and complexes **29a-31a** were carried out by me. The syntheses of the complexes **29b-31b** were performed by Dr Alessia Colombo in the group of Dr Dominique Roberto (University of Milan). I performed the UV-vis and fluorescence spectroscopy of complexes **29a-31a**. Dr Alessia Colombo performed the UV-vis spectroscopy of complexes **29b-31b**. The NLO studies (EFISH technique) were carried out by Dr Stefania Righetto and Dr Claudia Dragonetti. Single crystal data collection and structure solving was performed by Dr David B. Cordes. Density Functional

Theory (DFT) calculations were carried out by Dr Denis Jacquemin. Dr Dominique Roberto and I are the primary authors of the text. The work in this chapter has been published.

2) C. Hierlinger, D. B. Cordes, A. M. Z. Slawin, A. Colombo, C. Dragonetti, S. Righetto, D. Roberto, D. Jacquemin, V. Guerchais, E. Zysman-Colman. *Dalton Trans.*, **2018**, 47, 8292–8300. DOI: 10.1039/C8DT00754C

Chapter 4: The synthesis of iridium(III) dimers were carried out by Dr Amlan K. Pal (for **38**) and by me. The synthesis of complexes **33-36** was carried out by me. The synthesis of complex **38** and ancillary ligands for complexes **35** and **36** was carried out by Dr Amlan K. Pal. UV-vis and fluorescence spectroscopies for complexes **33-36** described in this chapter was performed by me. Dr Amlan K Pal carried out the UV-vis and fluorescence spectroscopies for complex **38**. The NMR studies were carried out by Dr Filippo Stella, Dr Tomas Lebl and me. Single crystal data collection and structure solving was performed by Dr David B. Cordes. Density Functional Theory (DFT) calculations were carried out by Dr Denis Jacquemin. I am the primary author of the text. The work in this chapter has been published.

3) C. Hierlinger, A. K. Pal, F. Stella, T. Lebl, D. B. Cordes, A. M. Z. Slawin, D. Jacquemin, V. Guerchais, E. Zysman-Colman. *Inorg. Chem.*, **2018**, 57, 2023–2034. DOI: 10.1021/acs.inorgchem.7b02940

Chapter 5: The synthesis was carried out by me. The UV-vis and fluorescence spectroscopies described in this chapter was performed by me. Single crystal data collection and structure solving was performed by Dr Thierry Roisnel (complex **39**), Prof Alexandra M. Z. Slawin (complex **40**) and David B. Cordes (complexes **41** and **42**). Density Functional Theory (DFT) calculations were carried out by Dr Denis Jacquemin. Heather V. Flint fabricated the dye-sensitized solar cells (DSSCs) in the group of Dr Elizabeth A. Gibson (University of Newcastle). I am the primary author of the text. Part of the work described in this chapter has been published:

4) C. Hierlinger, T. Roisnel, D. B. Cordes, A. M. Z. Slawin, D. Jacquemin, V. Guerchais, E. Zysman-Colman. *Inorg. Chem.*, **2017**, *56*, 5182–5188. DOI: 10.1021/acs.inorgchem.7b00328

5) C. Hierlinger, H. V. Flint, D. B. Cordes, A. M. Z. Slawin, E. A. Gibson, D. Jacquemin, V. Guerchais, E. Zysman-Colman. *Polyhedron*, **2018**, 140, 109–115. DOI: 10.1016/j.poly.2017.12.003

Chapter 6: The synthesis of the organic ligands and iridium(III) dimers for complex **61** was performed by Dr Adam F. Henwood. The synthesis of the organic ligands and iridium(III) dimers for complex **62** was performed by me. The synthesis of the complexes was carried out by me. The UV-vis and fluorescence spectroscopy described in this chapter was performed by me. Single crystal data collection and structure solving was performed by Dr David B. Cordes. Density Functional Theory (DFT) calculations were carried out by Dr Denis Jacquemin. I am the primary author of the text. This work has been published.

6) C. Hierlinger, D. B. Cordes, A. M. Z. Slawin, D. Jacquemin, V. Guerchais, E. Zysman-Colman. *Dalton Trans.*, **2018**, *Advance Article*. DOI: 10.1039/C8DT00467F

General Acknowledgements

So many people need to be thanked for making this thesis happen. I would like to start with my two supervisors, Dr Véronique Guerchais (Université de Rennes 1, France) and Dr Eli Zysman-Colman (University of St Andrews, UK), for giving me the opportunity to carry out a joint PhD with them. They have consistently helped to spur on my academic progress with their suggestions and helpfulness and made me the scientist I have become. It was a great journey in Rennes and in St Andrews. Thank you very much.

I would like to thank the members of the jury for agreeing to review my work, Dr Valery Kozhevnikov from the Northumbria University, Dr Paul Elliott from the University of Huddersfield, Dr Claude Lapinte from the Université de Rennes 1 and Dr Andreas Stasch from the University of St Andrews.

I would also like to thank all the Chemistry Department technical staff of both Universities who contributed to the efforts of making this work a possibility. In particular, the NMR as well as the X-ray crystallography section from both universities.

Special about this PhD were the great well-established collaborations. So, I truly thank the many partners from various institutions: Dr Tomas Lebl for the detailed NMR study; Dr Loïc Toupet, Dr Elzbieta Trzop, Dr Thierry Roisnel, Dr David Cordes and Prof Alexandra Slawin for solving crystal structures; Dr Denis Jacquemin for the theoretical calculations; Jorge Ávilla, Dr Antonio Petergás and Dr Henk Bolink for the LEECs; Heather V. Flint and Dr Elizabeth A. Gibson for the DSSCs; Prof Ifor Samuel for the facilities in the School of Physics and Astronomy and Prof Dominique Roberto for the NLO project and especially for sending students to both of my research groups.

A big thank you and hug goes to the members of the VG group and the EZ-C group. People come and go. I have done this more than usual during a PhD. In April 2016, I left Rennes

without forgetting what a great time I had in France. Merci! Joining the School of Chemistry was easy thanks to the great people I have met in St Andrews. During my PhD in these two research institutions I have met so many new people. I was lucky enough to be able to spend time with many of them and to make friends. Living and working in two different countries with colleagues coming from all over the world made this joint PhD so special. Thank you for the experience and teaching me the real language (both French and English). I will benefit from the experiences all my life.

At the end I would like to direct my biggest expressions of gratitude to my family. Thank you for supporting me every day! Thank you for coming to visit me wherever I am.

And to everyone really reading this I can say: Go abroad, learn new languages. Meet local people and try as many new things as possible. You are going to have a good time.

Thanks for all the Fish (& Chips).

Merci pour toutes les galettes (saucisses).

Funding

This work was supported by *Région Bretagne* and EPSRC (EP/M02105X/1).

Research Data

Research data underpinning this thesis are available at:

http://dx.doi.org/10.17630/b641a08a-a98c-4bbc-a1f6-5cadcbb69cc8

Table of Content

Table of Figures

Table of Tables

List of Abbreviations

°C	Degree Celsius
%	Percent
2-MeTHF	2-methyltetrahydrofuran
8-pq	8-phenylquinolinate
α	Linear polarizability tensor
A	Ampère
Å	Ångström
Ab	Absorption
Abs	Absorbance
acac	Acetylacetonate
Alq_3	Tris(8-hydroxyquinolinato)aluminium
a.u.	Arbitrary units
β	Nonlinear quadratic hyperpolarizability tensor
β_0	Dispersion-free hyperpolarizability
β_{EFISH}	Projection along the dipole moment axis
β_{vec}	Vectoral component of the tensor of the quadratic hyperpolarizability
bbthz	2,2'-bibenzo[*d*]thiazole
$bhpyH_2$	2-benzhydrylpyridine
biim	1*H*-1'*H*-2,2'-biimidazole
Bn	Benzyl
Bnpy	2-benzylpyridinato
bpm	Bis(pyrazol-1-yl)methane
bppy	2-([1,1'-biphenyl]-3-yl)pyridine
bpy	2,2'-bipyridine
br	Broad
bthz	2,2'-bithiazole
b-trz	Di(1H-tetrazol-5-yl)methane
$\chi^{(1)}$	First order electrical susceptibility

$\chi^{(2)}$	Second order electrical susceptibility
$\chi^{(3)}$	Third order electrical susceptibility
$\chi^{(n)}$	*n*th electrical susceptibility
c	Speed of light (2.998 x 10^8 m/s)
C_3	Symmetry element
cpy	Bis[2-(*N*-carbazolyl)pyridinato-N,C3’
C^N	Bidentate ligand coordinating with C and N
C^N^C	Tridentate ligand coordinating with C and N and C
CT	Charge transfer
CV	Cyclic voltammetry
Δ	Energy difference
ΔE_{redox}	Difference (V) between first oxidation and first reduction potentials
ΔG^o	Gibbs energy
Δμ	Difference of the dipole moment in the excited and ground state
D_{2d}	Symmetry Element
D_3	Symmetry Element
D_{3h}	Symmetry Element
deeb	Diethyl [2,2'-bipyridine]-4,4'-dicarboxylate
dFbpzH	1-(2,4-difluorobenzyl)-1*H*-pyrazole
dFmesppy	2-(2,4-difluorophenyl)-4-mesitylpyridiato
dFppy	2-(2’,4’-diflourophenyl)pyridinato
dfppzH	1-(2,4-difluorophenyl)-1H-pyrazole
DFT	Density functional theory
dmabpy	4,4’-*N*,*N*-dimethylamino-2,2’-bipyridine
dmbpy	4,4'-dimethyl-2,2'-bipyridine
dmdiim	1,1’-dimethyl-3,3’-methylenediimidazolium diiodide
dmppz	3,5-dimethyl-1-phenylpyrazolato
dpa	Di(pyridin-2-yl)amine
dpbpy	5,5’-diphenyl-2,2’-bipyridine

dpbpy	6,6’-diphenyl-2,2’-bipyridine
dPhPy	2,4-diphenylpyridine
dpm	Di(pyridin-2-yl)methane
dpmt	2-methyl-4,5-diphenylthiazolate
dpy-O	Di-2-pyridylketone
dpyOH-H	Di(pyridin-2-yl)methanol
dpyOH-CH_2CN	3-hydroxy-3,3-di(pyridine-2-yl)propanenitrile
dpy-N-NH_2	2,2’-(hydrazonomethylene)dipyridine
Dppe	1,2-bis(diphenylphosphino)ethane
DPV	Differential pulse voltammetry
DSSC	Dye-sensitized solar cell
d*t*Bubpy	4,4′-di*tert*butyl-2,2′-bipyridine
d*t*BubhpyH$_2$	2-(bis(4-(*tert*-butyl)phenyl)methyl)pyridine
d*t*Buphen	3,5-di-*tert*-butylphenyl
ε	Molar extinction coefficient
E	Energy in J
$\vec{E}$	Electric field strength
EFISH	Electronic field induced second harmonic generation
e.g.	For example
e_g^*	Metal based molecular orbital
EL	Electroluminescence
E_{ox}	Oxidation potential in V
EQE	External quantum efficiency
E_{red}	Reduction potential in V
Et	Ethyl
EU	European Union
Φ_{PL}	Photoluminescence quantum yield
F	Fluorescence
fac	Facial

Fc/Fc^+	Ferrocene/Ferrocenium
FF	Device fill factor
FIrpic	Bis[2-(4,6-difluorophenyl)pyridinato-C^2,*N*]-(picolinate)iridium(III)
FWHM	Full width at half maximum
γ	Cubic hyperpolarizability tensor
γ(−2ω; ω, ω, 0)	Second order polarizability
η	Power conversion efficiency
h	Plank's constant (6.625×10^{-34} J·s)
HLS	Harmonic Light Scattering
HOMO	Highest occupied molecular orbital
HRS	Hyper-Raleigh Scattering
HR-ESI	High-resolution electrospray ionisation
I_0	Intensity of incident light in $W \cdot m^{-2}$
I_1	Intensity of transmitted light in $W \cdot m^{-2}$
IC	Internal conversion
IL	Ionic liquid
ILCT	Intraligand charge-transfer transition
IPCE	Incident photon-to current conversion efficiency
IQE	Internal quantum efficiency
ISC	Intersystem crossing
ITO	Indium tin oxide
J	Joules
J_{sc}	Short-circuit current density at the $V = 0$ intercept
k_r	Radiative rate constant
k_{nr}	Nonradiative rate constant
λ	Wavelength in nm
λ_{em}	Emission maximum
λ_{abs}	Absorption maximum
l	Length

L	Litre
LC	Ligand-centred
LED	Light-emitting diode
LEEC	Light-emitting electrochemical cell
LLCT	Ligand-to-ligand charge-transfer
LMCT	Ligand-to-metal charge-transfer
LUMO	Lowest unoccupied molecular orbital
L^X	Bidentate ligand coordinating through L and X
μ	Electric dipole moment
μ_0	Molecular ground state electric dipole moment
m	Metre
M	Metal
man	Manisyl – 2,6-dimethyl,4-methoxyphenyl
MC	Metal-centred
Me	Methyl
Mebib	Bis(*N*-methyl-2-benzimidazolyl)benzene
Meppbpy	4-(3,5-dimethoxyphenyl)-6-phenyl-2,2'-bipyridine
mer	Meridional
mes	Mesityl
Mesppy	2-phenyl-4-mesityl-pyridinato
MLCT	Metal-to-ligand charge transfer
MO	Molecular orbital
Mol	Mole
N719	Di-tetrabutylammonium cis-bis(isothiocyanato)bis(2,2′-bipyridyl-4,4′-dicarboxylato)ruthenium(II)
***n*-BuLi**	*n*-Butyllithium
Nd:YAG	Neodymium-doped yttrium aluminium garnet; Nd:$Y_3Al_5O_{12}$
NHE	Normal Hydrogen Electrode
NIR	Near-infrared
NLO	Nonlinear optics

NMR	Nuclear magnetic resonance
N^N	Bidentate ligand coordinating with N and N
N^N^N^N	Tetradentate ligand coordinating with four N
N^O	Bidentate ligand coordinating with N and O
NOE	Nuclear Overhauser effect
NO_2-phen	5-nitro-phenthroline
NR	Nonradiative
OLED	Organic light-emitting diode
O^O	Bidentate ligand coordinating with two O
π	Bonding molecular orbital
π*	Antibonding molecular orbital
$\vec{P}$	Polarisation
$\overrightarrow{P_0}$	Intrinsic polarity
$P\bar{1}$	Space group
$P2_1$	Space group
pbpy	6-phenyl-2,2′-bipyridine
PCE	Power conversion efficiencies
PE	Power efficiencies
PEDOT:PSS	poly(3,4-ethylenedioxy-thiophene):poly(styrenesulfonate)
Ph	Phenyl
phen	Phenanthroline
PhOLED	Phosphorescent OLED
pic	Picolinate
$\overrightarrow{P_{ind}}$	Induced polarization
pmdp	2,2′-(phenylmethylene)dipyridine
PMMA	Poly(methyl methacrylate)
PL	Photoluminescence
ppy	2-phenylpyridinato
pq	2-phenylquinolinate

PS	Polystyrol
pymbi	3-methyl-1-(2-pyridyl)-benzimidazolin-2-ylidene-*C*,C^2
pytpy	4,4''-di-*tert*-butyl-4'-(pyridin-4-yl)-2,2':6',2''-terpyridine
pz$_3$CH	η^2–tri(1*H*-pyrazol-3-yl)methane
ROESY	Rotating-frame Overhauser Spectroscopy
σ	Bonding molecular orbital
s	Seconds
S_0	Ground state
S_1	First singlet excited state
S_2	Second singlet excited state
SCE	Saturated Calomel Electrode
sh	Shoulder
SHG	Second-harmonic generation
S_n	*n*th singlet excited state
S_NAr	Nucleophilic aromatic substitution
SOC	Spin orbit coupling
SOS	Sum over state method
SSL	Solid state lighting
τ_{PL}	Emission lifetime
T_1	First triplet excited state
T_2	Second triplet excited state
t_{2g}	Metal based molecular orbital
$t_{1/2}$	Time to reach half of the maximum luminance
***t*Bu**	*tert*-butyl
T_d	Symmetry Element
TD-DFT	Time-dependant density functional theory
THF	Tetrahydrofuran
TLC	Thin layer chromatography
Tot	Total

topy	2-*para*-tolylpyridinato
TPA	Triphenylamine
tp-pyim	2-(1-(4-tritylphenyl)-1H-imidazol-2-yl)pyridine
tpy	2,2':6',2''-terpyridine
TTA	Triplet-triplet annihilation
ttpy	2-([2,2':5',2''-terthiophen]-3'-yl)pyridinato
V_{oc}	Open-circuit voltage at the $J = 0$ intercept
W	Watts
wt%	Weight per cent
ζ	Spin orbit coupling constant
Z	Atomic number

Chapter 1

Introduction

The photophysical and photochemical properties of transition metal complexes have been investigated in detail over the last decades and have lead them to play a key role when designing luminescent materials for a wide range of applications. One of the most investigated classes of transition metal complexes are those bearing polypyridyl ligands. The inter-disciplinary popularity of this class of transition complexes can be explained by their straightforward synthesis and chemical stability, combined with great redox properties as well as excited state reactivity and excited state lifetimes.[1] One of the first and possibly the most famous complexes of this class is tris-2,2'-bipyridinerutheniunim(II) chloride $[Ru(bpy)_3]Cl_2$ (where bpy is 2,2'-bipyridine), reported in 1959 by Paris and Brandt, with the characteristic metal-to-ligand charge transfer (MLCT) excited state.[2] Especially second and third row transition metal complexes typically having low energy metal-to-ligand charge transfer (MLCT) processes, show very interesting properties.[1–9] Their good light absorbing capabilities are exploited in a wide range of applications like in solar cells,[10–13] as excited-state electron-transfer agent[14] and photocatalyst[15,16] and in molecular switches,[17,18] wires[19,20] and motors.[20] These complexes are also characterised by strong emission and therefore they are popular candidates for light-emitting devices,[8,21–23] in bioimaging,[24–26] and in sensors.[27] Exploiting their nonlinear optical properties has also become of great interest for applications in optical communications, optical data processing and storage and in photonic devices such as frequency doublers and electrooptic modulators.[17,28–30]

Despite the price and scarcity of iridium, complexes based on this metal have been very popular when designing luminescent materials and are widely used in for example optoelectronic applications.[22,23,31–34] Cyclometalated Iridium complexes are a highly attractive class of luminescent materials thanks to their highly efficient emission, multiple charge transfer

transitions with easy colour tunability ranging from blue to red, covering the whole visible spectrum.[5,33] Next to their excellent photophysical properties, Ir(III) complexes also stand out due to their high electrochemical, chemical and thermal stability.

A profound understanding of how these excellent photophysical properties arise is necessary to be able to study them in detail. Therefore, in this first chapter, optical phenomena in which these photoactive complexes are involved are discussed, starting with the role of light, the absorption of light and then processes of light emission. Selected synthesis routes of Ir(III) complexes and possible phosphorescence tuning by ligand design will be introduced, followed by a discussion of the popularity of Ir(III) complexes as a phosphor in light-emitting devices. The first part will be completed by an outline of different kind of lighting devices and a brief presentation of strategies to improve device performances through ligand design.

This chapter finishes with an introduction to nonlinear optical (NLO) properties explaining first the background and applications. A brief review of NLO chromophores based on transition metal complexes will be presented and the impact of the metal and the geometry of the complex will be discussed. Having established the importance of the choice of the metal, the excellent NLO properties of cyclometalated Ir(III) complexes will be outlined followed by strategies for designing new NLO chromophores.

Optical Phenomena

Light

The dual nature of light is essential to photochemistry.[35,36] For instance, light can be described as a wave moving through space or can behave like a particle, known as a photon, with a specific energy, E. The colour of light can be described by its wavelength, λ. The relation between the two aspects that are of great importance in photochemistry can be expressed by:

$$E = \frac{h \cdot c}{\lambda} \tag{1}$$

where λ is the wavelength in m, E is the energy in Joules per photon, h is Plank's constant (6.625×10^{-34} J·s) and c is the speed of light (2.998×10^{8} m/s). The range of visible light for the human eye is from about 400 – 700 nm.

Absorption of Light

When an atom or a molecule absorbs light of particular energy, it will be excited from its ground state S_0 to an excited state S_n with a characteristic energy. Atoms show sharp lines in their absorption spectra, related to the distinct transitions between ground and excited states. The absorption spectra of polyatomic molecules show however broad bands, which is due to different vibrational and rotational states with different energy levels. The intensity of bands is described by the Franck-Condon-principle.[35] This principle is based on the approximation that the electronic motion is much faster compared to the nuclear motion, due to the large mass difference. The transition of an electron to a different energy state takes place on an almost negligible short time scale compared to the motion of the nuclei. This results in different geometries of the molecule depending on the electronic states.

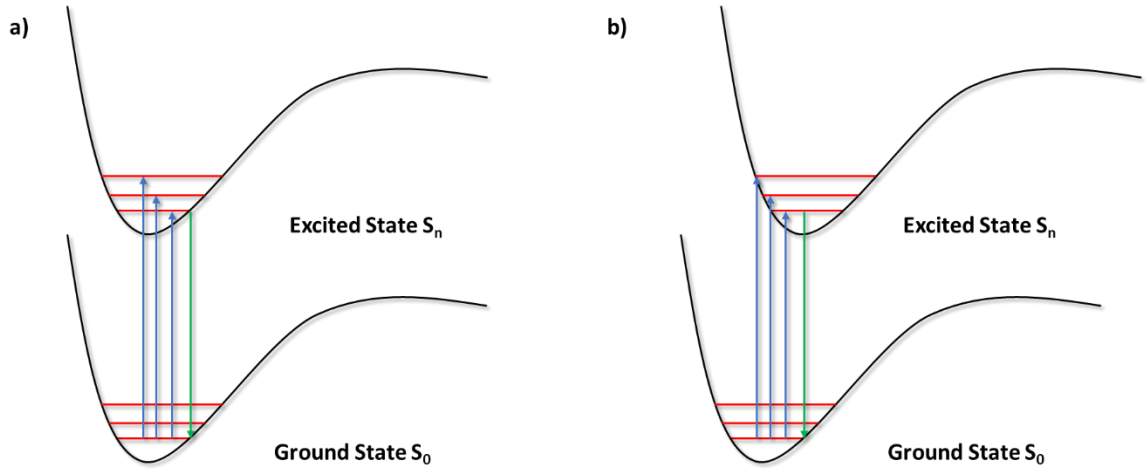

Figure **1**: Franck-Condon effect for absorption (blue arrows) and emission (green arrows) transitions between ground state S_0 and Excited State S_n. (a) for excited state and ground state of the same internuclear distance and/or bond angles (b) for a molecule with different geometry in excited and ground state.

Absorption can be described by the Beer-Lambert law, which is expressed in the equation (2):

$$Abs = log\frac{I_0}{I_1} = c \cdot l \cdot \varepsilon \tag{2}$$

where Abs is absorbance, I_0 and I_1 in $W \cdot m^{-2}$ are the intensities of incident and transmitted light, respectively, c is the concentration of the absorbant in M and l is the length of the light path in cm. The molar extinction coefficient ε in M^{-1} cm^{-1} describes how strong a substance absorbs light at a given wavelength.

Possible transitions can be described as spin-allowed or parity allowed transitions. Spin-allowed transitions obey the general electron spin selection rule of $\Delta S = 0$. Absorption takes place without a change in electron spin, meaning that a transition between a singlet and a triplet state is spin-forbidden. Secondly, the Laporte-rule (or parity rule) also needs to be considered. This selection rule states that transitions from an orbital with a centre of inversion to another orbital with a centre of inversion is "forbidden", when the molecule also has an inversion centre.

Thus, d-d transitions in octahedral transition metal complexes are Laporte-forbidden in centrosymmetric systems. This means these transitions can only take place in systems that are not always centrosymmetric. For example, in transition metal complexes in which the ligands may induce fluxional distortions these transitions can be observed but typically appear with low intensities in the absorption spectrum. For allowed transitions however higher intensities are characteristic.

For transitions in transition metal complexes that are forbidden by the spin-selection rule, ε is usually small (10^{-5} – 10^{-3} M^{-1} cm^{-1}) but can also be higher (10^{-2} – 10^{-1} M^{-1} cm^{-1}). For spin-allowed but parity forbidden transitions like a d-d transition in octahedral transition metal complexes ε is of the order of 10^{0} – 10^{3} M^{-1} cm^{-1}. The coefficient ε is large (in the range of 10^{3} – 10^{5} M^{-1} cm^{-1}) for transitions that are spin- and Laporte-allowed (e.g. ligand centred π-π^* transitions in octahedral transition metal complexes).

Charge transfer processes

In octahedral transition metal complexes like Ir(III) complexes of the form $[Ir(C\hat{}N)_2(N\hat{}N)]^+$ (where C^N is a mono-anionic bidentate chelated ligand such as 2-phenylpyridinato, ppy, and N^N is a neutral bidentate diimine ligand such as 2,2′-bipyridine (bpy)), electronic transitions can be classified into three categories: (1) transitions between the energy levels mainly located on the metal such as d-d transitions, (2) transitions mostly located on the ligands such as π–π* transitions of aromatic ligands or from one ligand to another ligand and (3) transitions where an electron is transferred from the ligand to the metal or vice versa.[37] It is important to state that the electron is not being transferred from one atom to another, but is moved from one molecular orbital (MO) to another. Multiple electronic states are generated in a complex multi-atomic structure like mixed-ligand Ir(III) complexes containing a heavy metal, anionic σ-donating ligands (such as a C^N ligand) and a π-accepting ligand (such as a neutral N^N ligand), resulting in a complex range of occurring electronic transition processes. Often it

is a challenging task to identify clearly all the bands in the absorption spectra reflecting the complexity of the occurring electronic states. Figure **2** shows schematically the characteristic transitions in octahedral transition metal complexes and are described in more detail in the following.

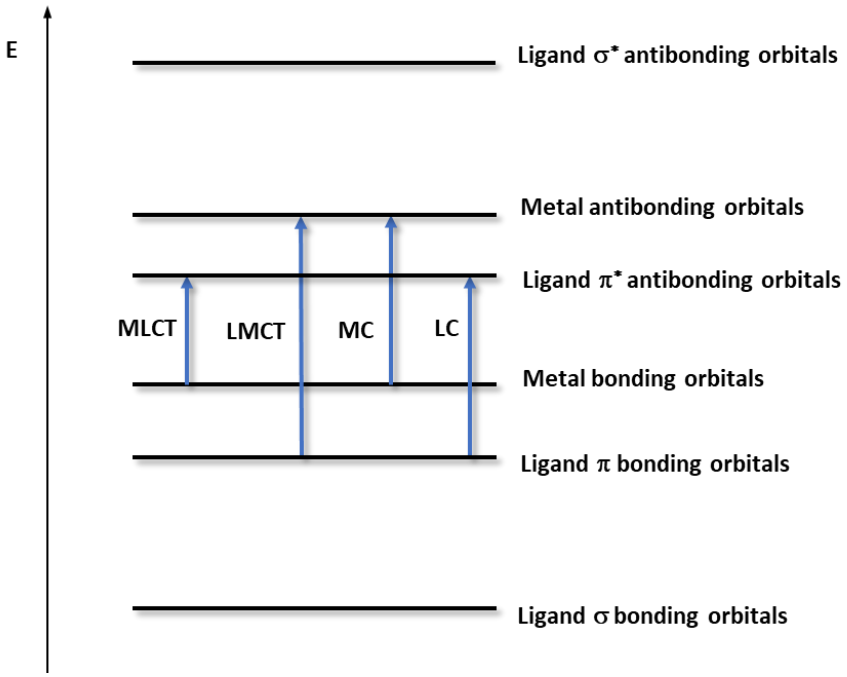

Figure **2**: Molecular orbital diagram for an octahedral transition metal complex. The blue arrows indicate four types of transitions based on localised MO configurations.[38]

One possible scenario is that an electron is promoted from a molecular orbital primarily located on metal orbitals to a molecular orbital primarily located on ligand orbitals and is termed metal-to-ligand charger transfer (MLCT).[37,39] If an oxidisable ligand, e.g. anionic, is bound to a metal which is electron-poor, ligand-to-metal charge transfer (LMCT) can be observed.[37] The more the ligand is electron-rich the more the ligand-to-metal transfer may occur at lower energies. A third metal centred electron transition (MC) may be observed involving only orbitals that are based on the metal. In a similar way, an electron can be promoted between molecular orbitals that are both ligand based such as intraligand charge transfer (ILCT) or ligand-to-ligand charge transfer (LLCT). For instance, ligand-centred π-π* transitions are

typically highly absorptive. Metal-centred transitions at low energies are typical for first row transition metal complexes.

In Figure **3**, the experimentally obtained absorption spectrum for $[Ir(ppy)_2(d\textit{t}Bubpy)]PF_6$ **1** (where ppy is 2-phenylpyridinato and d*t*Bubpy is 4,4′-di*tert*butyl-2,2′-bipyridine) is shown.

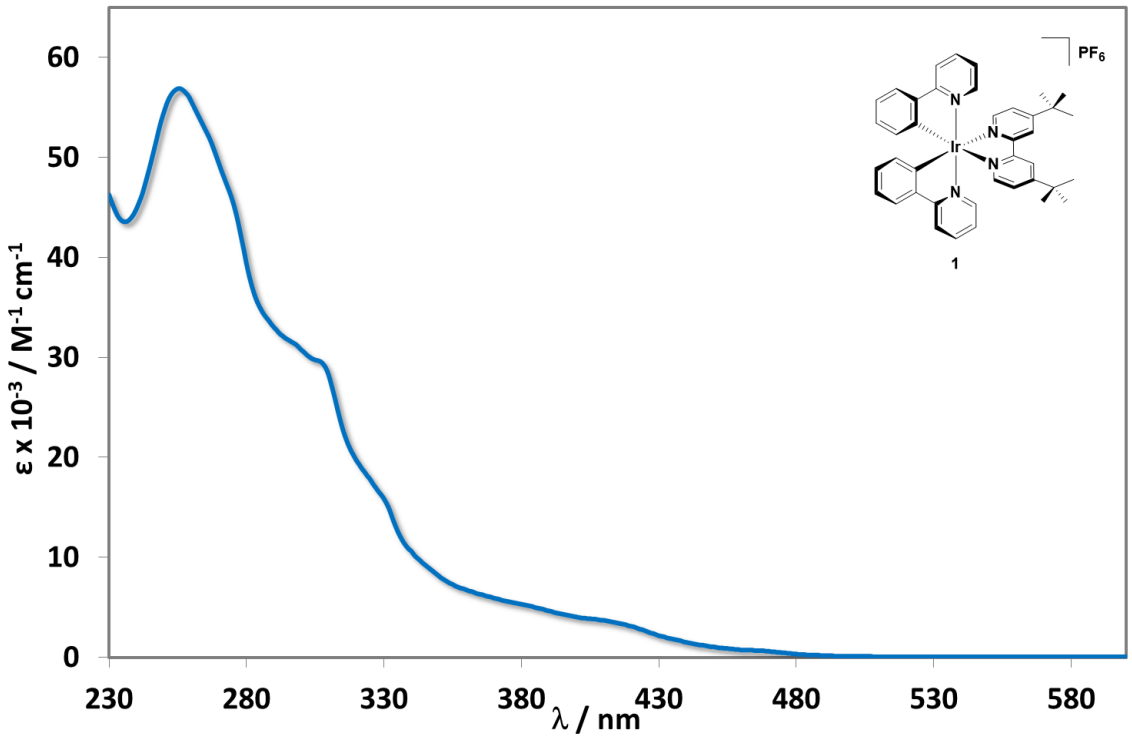

Figure **3**: Room-temperature UV-vis Absorption spectrum of **1** in acetonitrile (c = 1.8 x 10^{-5} M)

With the help of time-dependent density functional theory (TD-DFT) calculations, the bands can be assigned to their respective electronic transitions. The band of high intensity in the range of ε = 5-6 x 10^4 M^{-1} cm^{-1} at 255 nm are assigned to spin-allowed $^1\pi$–π^* ligand-centred (^{1}LC) transitions on both the ppy and d*t*Bubpy ligands. The intensity of the absorption spectrum drops off with other bands lower in intensity (1-3 x 10^4 M^{-1} cm^{-1}) in the ultraviolet, which can be attributed to an admixture of spin-allowed charge-transfer (^{1}CT) transitions consisting of dπ-$\pi^*_{d\textit{t}Bubpy}$ metal-to-ligand (^{1}MLCT) and π_{ppy}-$\pi^*_{d\textit{t}Bubpy}$ ligand-to-ligand (^{1}LLCT) transitions. Low intensity bands are observed in the visible at 408 nm (ε = 3 x 10^3 M^{-1} cm^{-1}) and the spectrum

tails out with other low intense transitions to the red of 466 nm ($\varepsilon = 4 \times 10^2$ M^{-1} cm^{-1}). These poorly absorptive bands can be best described as spin-forbidden ^{3}MLCT and ^{3}LLCT transitions that can be accessed due to the large spin-orbital coupling in Ir(III) complexes. This absorption profile is very characteristic for many Ir(III) complexes of the form $[Ir(C\hat{}N)_2(N\hat{}N)]^+$.[40,41]

Luminescence

Excitation

Historically, in traditional lighting, light is generated through the process of incandescence, which comes along with a rise of temperature. Luminescence, however, is a phenomenon of light production, which is not necessarily linked to a rise of temperature. Possible origins of luminescence can be electroluminescence, which occurs after an electric field is applied[42] and photoluminescence, where light is the source of energy.[43]

The process of photoluminescence is initiated when a molecule in the ground state S_0 absorbs light (or a photon) of particular energy. The absorbed photon excites an electron from the ground state to a higher energy level generating an excited state S_n; in other words, the excited state needs to be populated. Now, a variety of deexcitation pathways are possible (see Figure **4**). In principle, transitions between energy states of the same spin multiplicity are allowed and those between states with different multiplicity are forbidden.

Relaxation pathways

Firstly, according to Kasha's rule,[44] which states that emission only occurs from the lowest excited state of a given multiplicity, the excited electron undergoes a rapid 100% efficient deactivation via non-radiative pathways resulting in a metastable species in the lowest spin-allowed singlet excited state S_1. This process, called internal conversion (IC), occurs on a femtosecond timescale. From this populated state S_1, the electron can undergo different relaxation pathways to return to the ground state.

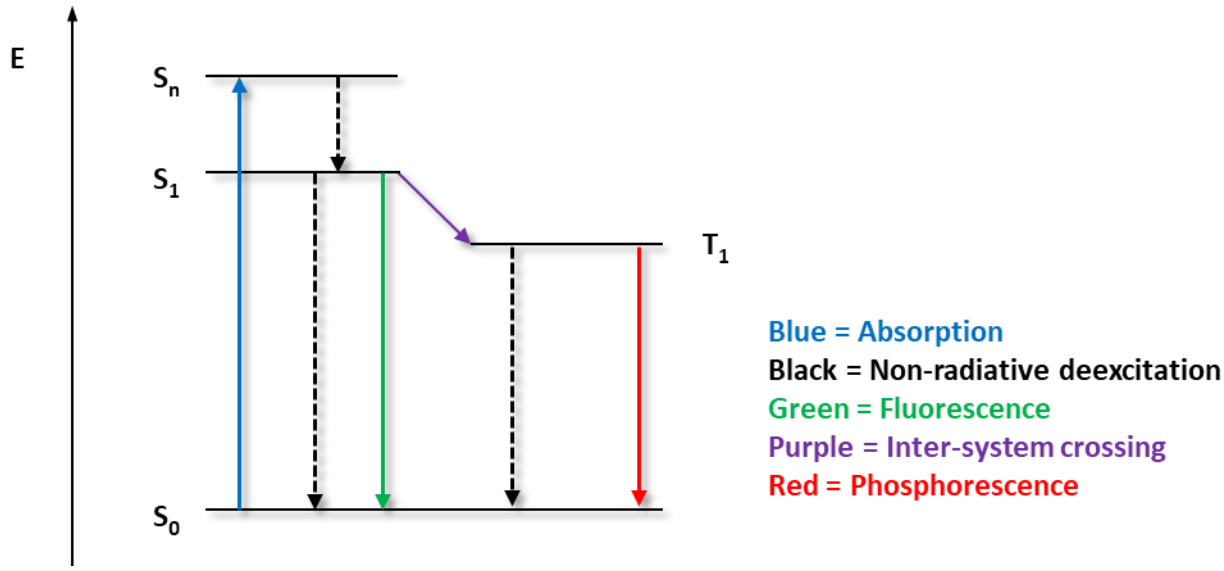

Figure **4**: Simplified Jablonski[45] diagram showing distinct energy levels. The colour coded arrows show the possible transitions between the electronic states (blue = Absorption, black = internal conversion (IC, non-radiative deexcitation), green = fluorescence, purple = inter-system crossing (ISC), red = phosphorescence).

In case the energy is transferred into vibrational, translational or rotational energy, the electron undergoes a non-radiative decay to return to S_n, releasing heat to the environment. When a photon with the energy corresponding to the difference between the energy levels of the excited state and the ground state is emitted, the decay is radiative. If the spin multiplicity is conserved, the spin selection rule is adhered. According to George Gabriel Stokes this transition can be termed fluorescence[46] and is a fast process that is on the order of nanoseconds.

A competing non-radiative pathway, intersystem crossing (ISC), can occur in systems where the electron moves fast enough to interact with its own spin to change the spin multiplicity. This process is termed spin orbit coupling (SOC) and another excited state, a triplet state T_n, is generated. Similar to the processes of the S_n states, deactivation to the lowest excited state T_1 occurs. Again, the energy can be transformed into vibrational, translational or rotational energy to generate non-radiative deexcitation. In the case of a radiative decay a change of spin

is necessary. This emission process is called phosphorescence.[38] In case of organic molecules, the lifetime of this spin-forbidden radiative transition is typically much longer compared to other competing relaxation pathways and so phosphorescence is typically not observed.

When a heavy metal is incorporated in the system, like in the case of metal complexes, the electron is accelerated by the metal leading to strong spin-orbit coupling and mixing of the singlet and triplet excited states removing the spin-forbidden nature of the triplet state. Efficient intersystem crossing is now possible, which is much faster than other competing deexcitation pathways from the singlet states. The lifetime of the triplet state is significantly shortened and therefore high phosphorescent efficiencies can be obtained.[23,47–49] For both radiative pathways the emitted photon is lower in energy than the absorbed photon and emission occurs at longer wavelengths compared to the incident light absorbed.

Quantum yield and lifetime

The quantum yield of a process, Φ, is defined as the ratio of photon absorption and of any deactivation processes and states the efficiency of an emitter.[50] For instance, the photoluminescence quantum yield is the ratio of emitted photons to absorbed photons by the system and can be expressed by:

$$\Phi = \frac{photons\ emitted}{photons\ absorbed} = \frac{k_r}{k_r + k_{nr}} \tag{3}$$

where k_r is the radiative rate constant and k_{nr} is the non-radiative rate constant. This equation refers to a first-order decay, assuming no nonradiative decay is occurring that is caused by external processes, like self-quenching or quenching through impurities or oxygen. In very dilute concentration (10^{-5} M) and a vigorously degassed and sealed environment both self-quenching and quenching through oxygen can be minimised. To obtain very high quantum yields two strategies are possible. Either increase efficiency of radiative transitions and therefore k_r. Or decrease the non-radiative relaxation pathways.

The lifetime of highly efficient fluorescence can range up to a few ns. In systems where spin orbital coupling does not occur phosphorescence lifetimes can be as longs hours. For systems with a heavy metal and strong SOC the phosphorescence lifetime may be in the microsecond (μs) to millisecond (ms) regime.[51] In other words, SOC influences k_r for phosphorescence. Efficient SOC can lead to efficient phosphorescence. SOC is stronger for heavier metals and in fact the SOC constant, ζ, is proportional to Z^4 (where Z is the atomic number). The SOC constant increases rapidly with atomic number and therefore heavier elements generally have higher SOC.[51] In fact, transition metals with one of the highest SOC constants are iridium (ζ = 3909 cm^{-1}), platinum (ζ = 4480 cm^{-1}) and gold (ζ = 5104 cm^{-1}), which is a reason why complexes based on these metals are typically highly luminescent and has made them popular in a wide range of applications.[52]

Ir(III) complexes

Photoactive Ir(III) complexes have found application in a wide range of techniques such as emitters in electroluminescent devices,[22,23,53,54] as chromophores in nonlinear optics,[55–57] as dyes in solar cells,[58,59] as solar fuels,[60] as photoredox catalysts[61,62] and in bioimaging.[25,26] Ir(III) complexes generally have high photoluminescence quantum efficiency, easy access colour tunability and highly efficient emission. The availability of strongly luminescent triplet emitters has made complexes based on Iridium(III) highly popular candidates for solid-state lighting (SSL).[23,52,63,64] The following focusses on the design, synthesis of Ir(III) complexes and their optoelectronic properties for further application.

Synthesis strategies for cyclometalated Ir(III) complexes

Cyclometalated Ir(III) complexes bearing three bidentate ligands form a very popular class of Ir(III) complexes. There are many synthetic routes for Ir(III) complexes; a selection of utilised strategies to synthesise cyclometalated Ir(III) complexes is depicted in Figure **5**.

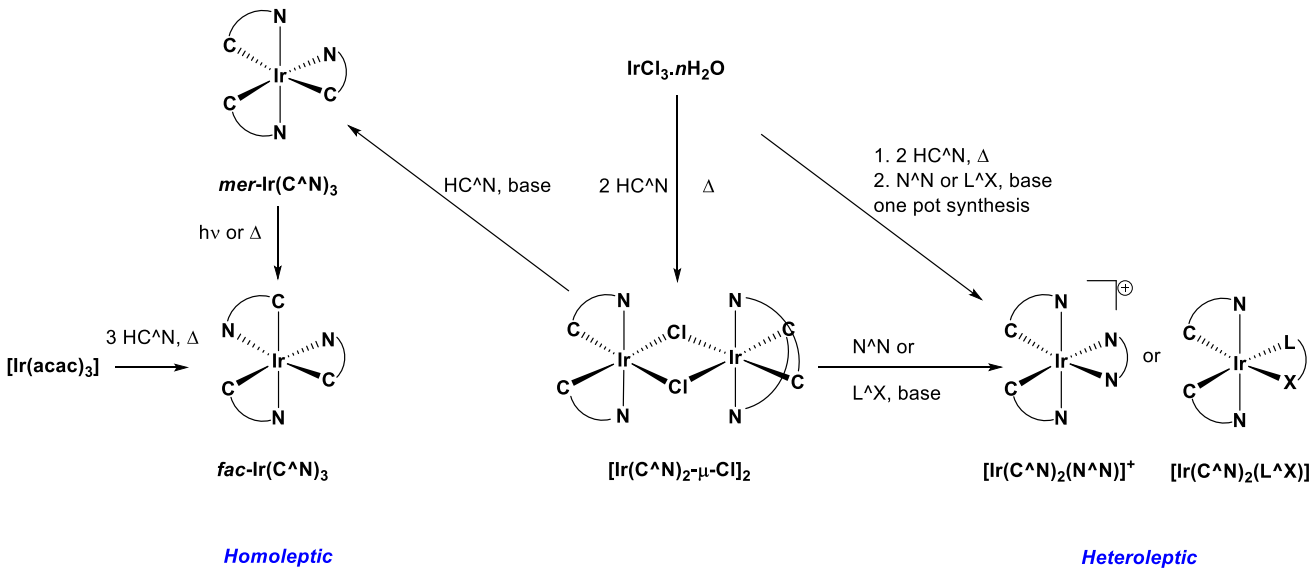

Figure **5**: Scheme of selected synthetic routes used for cyclometalated Ir(III) complexes

By far the most followed synthesis procedure is to form a μ-dichloro-bridged cyclometalated iridium dimer in a first step, refluxing a mixture of $IrCl_3.nH_2O$ and the

cyclometalating ligand (C^N) in a high boiling alcoholic solvent such as 2-ethoxyethanol, as first reported by Nonoyama using $Na_3[IrCl_6]$ as the Iridium source.[65] In this case, the ligands are identical and are coordinating to Ir(III) in a 5-membered metallacycle forming very strong quasi-covalent bonds between the Ir(III) and the carbon atom of the C^N ligand.[66] Typical C^N examples are 2-phenylpyridine (ppyH) and its derivatives. In the second step, the dimer can then be cleaved in the presence of a bidentate ligand to form the desired complex.[5,21–23,67,68]

Homoleptic complexes are obtained when using the identical cyclometalating C^N ligand. The thermodynamically favoured facial-configuration (*fac*) is obtained at high temperatures from the dimer in the presence of 1 equivalent of the C^N ligand and a base in glycerol at 200 °C.[69] Another strategy to obtain the *fac*-isomer is to react $Ir(acac)_3$ (where acac is acetylacetonate) with 3 equivalents of the C^N ligand in glycerol at 200 °C. To obtain the kinetically favoured meridional-complex (*mer*) from the dimer, a careful control of the synthetic conditions and the reaction temperature is needed. The *mer*-isomer can be thermally or photochemically converted into the *fac*-isomer.[70,71]

Upon reaction of the dimer with an ancillary ligand, heteroleptic complexes (see Figure **5**) are obtained where the C^N ligands are in *trans*-N,N configuration.[57,72–75] The ancillary ligand can be negatively-charged or charge-neutral, directly influencing the charge of the heteroleptic complex. Neutral complexes are obtained upon reaction of the dimer at higher temperatures (e.g. in refluxing 2-ethoxyethanol) in the presence of a base with ancillary ligands such as picolinates N^O[76–78] or acetylacetonates O^O.[57,77,79–82] The reaction of the dimer in mild conditions (e.g. in a refluxing mixture of 1:1 MeOH and CH_2Cl_2) with diimine N^N ligands (such as 2,2-bipyridines[5,23,56,83–85] and 1,10-phenanthrolines[34,58,86,87]) leads to cationic complexes. The many possibilities of ligands and conformations result in a large variety of electronic properties, that can be tuned by ligand design and influence the dominating pathways for excitation and deactivation.[5,22,23,66,88]

Tuning the phosphorescence wavelength of Ir(III) complexes

The nature of the excited states of Ir(III) complexes is generally a mixture of mixed ligand-centred (LC) and metal-to-ligand charge transfer (MLCT). Thus, changing the ligand environment can have drastic impact on the energy of the excited states. Density Functional Theory (DFT) calculations of a typical cationic Ir(III) complex of the form $[Ir(C\hat{}N)_2(N\hat{}N)]^+$ state that the highest occupied molecular orbital (HOMO) is a combination of the metal and the phenyl rings of the C^N ligands.[5,21,23,33,66,86] Generally, the lowest unoccupied molecular orbital (LUMO) is based only on the N^N ligand. Thus, by appropriate substitution, the energies can be altered and emission ranging from deep red to the blue can be obtained. However, the photoluminescence quantum yield (Φ_{PL}) of these complexes can decrease drastically when the energy is tuned towards the extremities of the visible spectrum. For example, according to the energy gap law by decreasing emission energy the rate of non-radiative decay increases as the vibrational modes of ground state and excited state match more closely.[89]

A strategy to tune the emission energy of Ir(III) complexes is the selective stabilisation and/or destabilisation of the frontier orbitals of the complex. Mixed-ligand Ir(III) complexes (e.g. of the form $[Ir(C\hat{}N)_2(N\hat{}N)]^+$) are particularly suitable in this context since the two different ligands can independently be introduced. With a careful design and the right choice of substitution the desired colour tuning can be obtained.[90,91] For instance, electron-withdrawing substituents decrease the donation of electron-density onto the orbitals leading to stabilisation of the frontier orbitals. On the other hand, when adding electron-donating groups destabilisation of the frontier orbitals through an increase of electron-density onto the orbitals is obtained.

The principles of colour tuning will be explained with the following three complexes shown in Figure **6**: $[Ir(dFppy)_2(dmabpy)]PF_6$ (**2**)[91] (where dFppy = 2-(2',4'-difluorophenyl)pyridinato and dmabpy = 4,4'-*N*,*N*-dimethylamino-2,2'-bipyridine),

$[Ir(ppy)_2(dtBubpy)]PF_6$ (**1**)[84] and $[Ir(topy)_2(debpy)]PF_6$ (where topy = 2-*para*-tolylpyridinato and deeb = diethyl [2,2'-bipyridine]-4,4'-dicarboxylate) (**3**).[91]

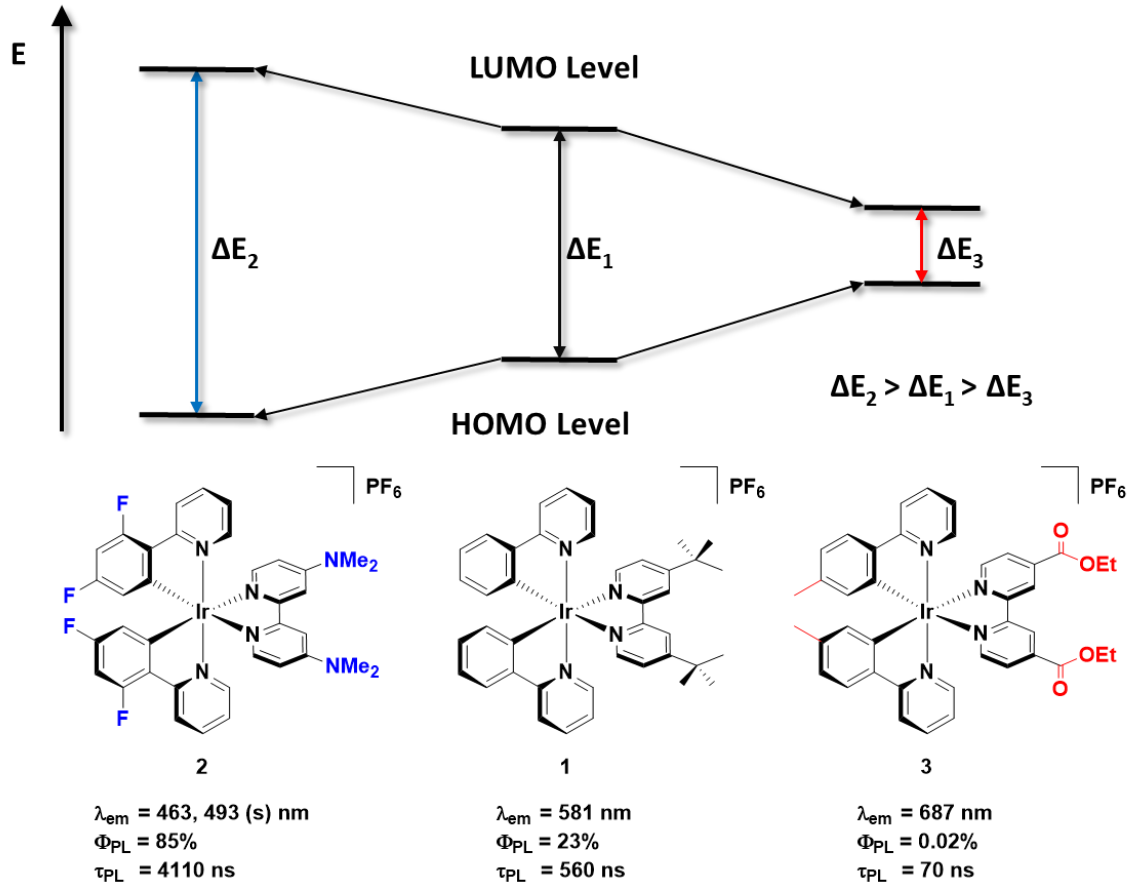

Figure **6**: Schematic representation of the effect of electron-withdrawing and donating groups on HOMO and LUMO levels of **1**-**3**.Complex **2** exhibits a λ_{em} = 581 nm (Φ_{PL} = 23%, τ_{PL} = 560 ns) in acetonitrile solution. A blue shift of 118 nm (5721 cm^{-1}) for complex **2** is achieved by adding electron-withdrawing fluorine atoms onto the phenyl of the C^N ligands, which stabilise the HOMO, and by substituting the di-*tert*-butyl groups with electron-rich di-methyl-diamine groups, which leads to a destabilisation of the LUMO. To obtain a bathochromic shift of 106 nm (5721 cm^{-1}) compared to **1** electron-donating methyl groups were added to the phenyl unit of the C^N ligands of **3** and the N^N ligand has been substituted with electron-accepting diethyl-ester groups.

The above examples of Ir(III) complexes all display ligands (C^N as well as N^N) forming five-membered rings around the Ir centre. Investigating the impact of going from a five-membered ring to a six-membered ring is much less explored. Cyclometalating ligands forming a six-membered ring are rare and belong to two categories depending on the presence of conjugated[92–94] or nonconjugated bidentate chelating ligands.[95–97]

The impact of a conjugated C^N ligand forming a six-membered chelate can be demonstrated when comparing complex $[Ir(pq)_2(acac)]$[98] **4** (where pq is 2-phenylquinolinate) and $[Ir(8\text{-}pq)_2(acac)]$[92] **5** (where pq is 8-phenylquinolinate, see Figure **7**).

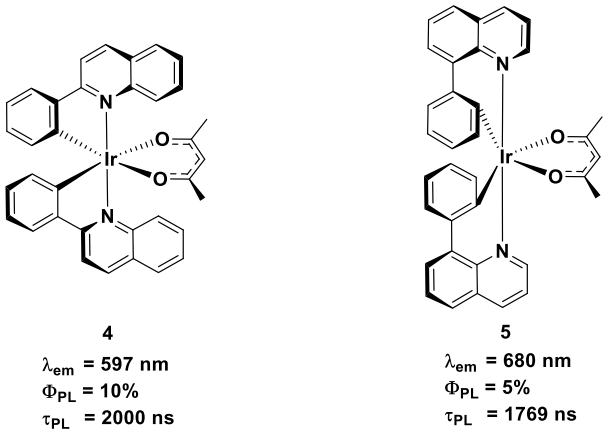

Figure **7**: Schematic representation of five-membered and six-membered chelated Ir(III) complexes

Complex **4**, bearing a five-membered ring, exhibits a λ_{em} of 597 nm in 2-MeTHF solution with a Φ_{PL} of 10% (τ_{PL} = 2000 ns).[98] The cyclometalating ligand of **5** is an isomer of the C^N ligand of **4** and forms a six-membered chelating ring. The effect on the photophysical properties is that a drastic red-shift is observed (λ_{em} = 680 nm, τ_{PL} = 1769 ns in MeCN solution),[92] reflecting the extension of the π-conjugation of the C^N ligand. The Φ_{PL} of 5% is notably lower compared to **4**, which can be explained by the emission in the red where nonradiative processes are more pronounced and by the nonrigid nature of the six-membered C^N ligand leading to flexibility.[92]

The other category of six-membered chelated Ir(III) complexes comprises nonconjugated cyclometalating ligands that bear a spacer between the two coordination moieties. The impact on the photophysical properties of disruption the electronic crosstalk can be illustrated with complexes $[Ir(dFppy)_2(fptz)]$[99] **6** (where fptzH is 3-trifluoromethyl-5-(2-pyridyl)-1,2,4-triazole] and $[Ir(dfbpz)_2(fptz)]$[96] **7** (where dfbpz is 1-(2,4-difluorobenzyl)-1H-pyrazolato, see Figure **8**).

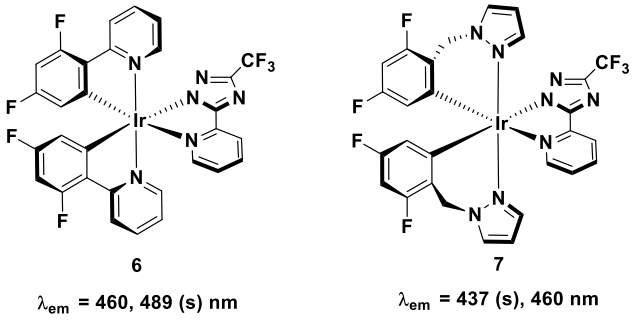

Figure **8**: Schematic representation of five-membered and six-membered chelated Ir(III) complexes

The cyclometalating ligand of complex **6** forms a five-membered ring around the Ir centre. In CH_2Cl_2 solution, **6** exhibits a λ_{em} = 460, 489 (s) nm.[99] Complex **7** however is bearing a six-membered chelating C^N ligand. Compared to **6** a small blueshift is observed with **7** (λ_{em} = 437 (s), 460 nm in CH_2Cl_2).[96] The introduction of the CH_2 spacer into the C^N ligand is successfully breaking the π-conjugation of the chelating ligand. As a consequence, the π orbital energies are lowered and the respective π* orbitals are destabilised.[96]

These findings demonstrate clearly how emission colour tuning of Ir(III) complexes is not only limited on modifying the substituents on the ligands but can also easily be achieved through expanding from a five-membered ring to a six-membered ring chelating ring.

Applications of luminescent material

Solid-state lighting

One of today's most pressing challenge is the increasing demand of energy. Energy production is mostly based on limited fossil fuels and nuclear power, but renewable energies have been widely introduced. Innovative concepts to cut energy consumption have been introduced on regional and global level. However, with a growing world population the demand will keep increasing. In the medium term (by 2020), the European Union (EU) declared in 2007 the aim (1) to decrease the energy consumption in the EU by 20%, (2) to reduce greenhouse gas emission by 20%, (3) to ensure a transition to low-carbon, renewable energy-based energy sources supplying 20% of the consumed energy and (4) to improve energy efficiency by 20%.[100–102] This is an ambitious undertaking giving how much energy is currently being used in transport, industry and households.

One major energy consumption section is the lighting. In 2014, 19% of the worldwide consumed electricity was consumed by lighting with a slightly smaller fraction used in the EU (14%).[103] Most of the lighting technologies that are used nowadays can be tremendously improved, presenting a huge potential for energy savings. One of the most energy-efficient and environmentally friendly state-of-the-art technology is solid state lighting (SSL). SSL technology is quickly evolving and has reached high efficiency levels of more than 276 lm/W (compared to 40-100 lm/W for fluorescent lamps).[103]

Compared to traditional lighting technologies, SSL reduces heat production and other unused emission in the non-visible spectrum.[104,105] SSL technologies are, for example, light-emitting diodes (LED) and organic light-emitting diodes (OLEDs). A LED is a device based on a semiconductor and generates light from electricity. The device architecture corresponds to a p-n junction diode, where the "p" side contains an excess of holes and "n" contains an excess of electrons. When electricity is applied, electrons can recombine with the electron holes

releasing energy in form of photons. The wavelength of the emitted light, and therefore its colour, is determined by the band gap of the semiconductor. LEDs are typically based on inorganic semiconductor materials. For example, blue LEDs that are used utilise the semiconductors GaN (gallium nitride) and InGaN (indium gallium nitride).[106] Thanks to their simple architecture, easy colour tunability and high efficiency, LEDs have shown to be a promising candidate replacing traditional lighting devices.[107,108] However, there are still challenges for this lighting technique. A trade-off between surface area and power density exists for this technology that yet has limited its potential for industrial scale lighting.[109] One of the major disadvantages is the materials used not being environment friendly. Hence, there is a motivation towards the use of greener materials.[107]

Replacing the inorganic semiconductors in LEDs through organic semiconductors adding an organic component to obtain organic light-emitting diodes (OLEDs) is of great academic and commercial interest. OLEDs have many advantages with respect to traditional lighting technologies. OLEDs are light and thin and can therefore find application in lightweight panels and curved or foldable screens. Other advantages are durability, fast switching times, higher colour quality and higher contrast ratios.[110]

Efficiency and in general the performance of light-emitting devices is evaluated by their external quantum efficiencies (EQE, the ratio of emitted photons per injected electron), current efficiency (emitted light per electric flux in candela per ampere) and power efficiency (emitted flux per electric input in lumens per electrical watt).[111] The lifetime $t_{1/2}$ (in h, time to reach half of the maximum luminance) and the total emitted energy E_{tot} (in J, the integration of the radiant flux vs. time from t = 0 (application of bias) to t = $t_{1/5}$)[112] indicate the device stability. In the following OLEDs are discussed in more detail, highlighting their architecture and utilised emitters.

Organic light-emitting diodes (OLEDs)

Organic light-emitting diodes (OLEDs) are a display technology typically based on photoactive organic molecules. The luminescent material is sandwiched in a multilayer stacking between two conductors (see Figure **9**).

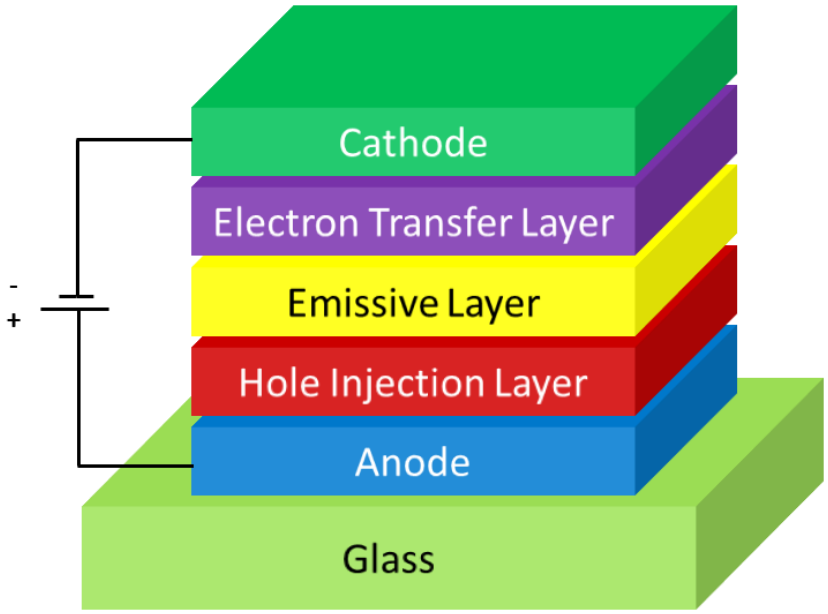

Figure **9**: Schematic representation of a typical architecture of an OLED.

The typical thickness of an OLED is of few hundred nm. Generally, two types of materials are used as emitters: polymers and small organic or organometallic molecules. When a potential is applied (between 3 and 12 V), electrons are injected from the cathode into the electron transfer layer. At the same time holes, positive charges, are injected from a transparent anode. In the applied electric field, the holes and the electrons migrate through the layers and generate excited states, known as excitons, upon recombination in the emissive layer. Ideally the excited states relax to the ground state by emitting photons, generating light. This process is called electroluminescence (EL). In PL, as described above, the S_1 is always populated first. The EL mechanism, however generates through the recombination of holes and electrons the excited state in a bimolecular fashion, meaning that even in systems possessing only atoms with low SOC (e.g. conjugated organic molecules) triplet excitons are generated. In fact, 75% of the

excitons generated in OLED are in the triplet spin state. When using an emitter that is purely fluorescent a statistical limit of 25% on their internal quantum efficiencies (IQE, the internal ratio of photons generated from electrons input into the device) is imposed, which generally does not make them a desirable candidate for OLEDs.

An efficient solution to the problem is the use of phosphorescent emitters in which the triplet states can be harvested.[113] Systems consisting of for example heavy transition metal complexes with strong SOC are suitable candidates with a theoretic internal quantum efficiency of 100%. This concept was first applied with the bright red emitting metal complex octaethylporphyrin platinum(II)[113] **8** (λ_{em} = 641 nm, Φ_{PL} = 60%, τ_{PL} = 6500 ns; see Figure **10**).

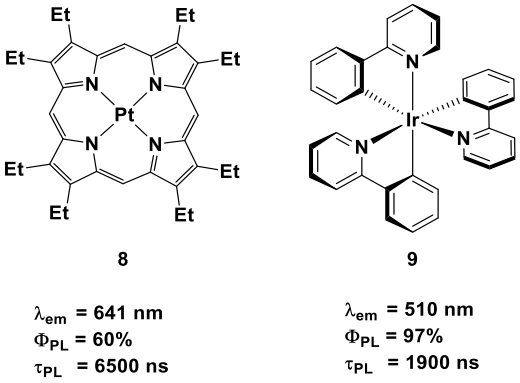

Figure **10**: Structure of the phosphorescent metal complex Platinum(II) octaethylporphyrin **8** and Iridium(III) complex used **9** used as dopant in OLEDs.

This complex was doped into Alq3 (tris(8-hydroxyquinolinato)aluminium(III)) and the device exhibited an internal quantum efficiency (IQE) of 23%, whilst the Alq3 transferred 90% of its energy to the complex. With a different host the device was further optimised resulting in an IQE of 32%.[114] However, the efficiency was found to drop drastically at higher currents, which is needed for higher brightness. This can be explained by triplet-triplet annihilation (TTA).[115] The lifetime of the triplet excited state of this platinum(II) complex is so long (τ_{PL} = 6500 ns) that as concentration of the excited molecules increases they have time to get close to one another to undergo a process that competes with phosphorescence.[116]

Shortly after this work, Ir(III) complexes were introduced as dopants in OLEDs. One of the most well-known is *fac*-Ir(ppy)$_3$ (complex **9**, see Figure **10**) bearing three phenylpyridinato ligands coordinated to the Ir(III) centre orientated in a facial arrangement. This neutral complex exhibits green phosphorescence (λ_{em} = 510 nm) in toluene solution with a very high photoluminescence quantum yield, Φ_{PL}, of 97%.[50] The lifetime of 1.9 μs is short enough to ensure there is no significant triplet-triplet annihilation (TTA) when doped into a host in an OLED, as was shown previously for complex **8**. The device performance of **9** gave an external quantum efficiency of 8.0%, proving the great potential Ir(III) complexes employed in solid state lighting application.

A sky-blue emitter widely used for vacuum sublimed OLEDs is FIrpic[54,76,99,117,118] (**10**) (bis[2-(4,6-difluorophenyl)pyridinato-C^2,*N*]-(picolinato)iridium(III), Figure **11**).

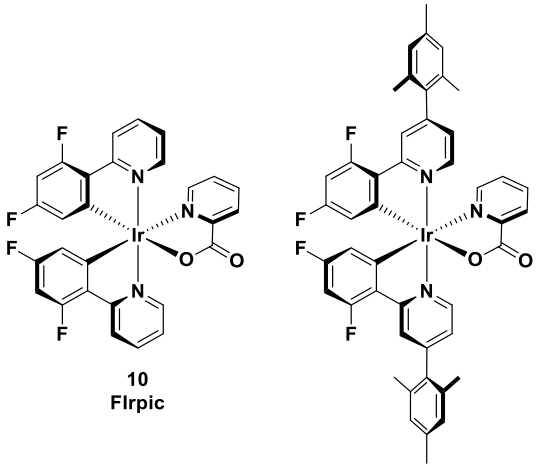

Figure **11**: Structure of FIrpic (**10**) and mesitylated analogue (**11**).

However, it is not a highly suitable candidate for solution-processed OLEDs due to its poor solubility.[76] A strategy to improve the performance of emitters based on **10** is to decorate the ligand with bulky hydrophobic substituents. This concept was investigated with the charge neutral complex [Ir(dFmesppy)$_2$(pic)][76] (**11**, where dFmesppy is 2-(2,4-difluorophenyl)-4-mesitylpyridine and pic is picolinate, Figure **11**) carrying a mesityl-substituent on the 4-position

of the pyridine of the C^N ligand, it was used as emitter in solution processed phosphorescent OLEDs (PhOLEDs).[76]

The bulky mesityl groups lead to (1) higher solubility of the complex in organic solvents having a positive impact on film morphology, (2) an increase of the steric bulk around the Ir(III) hindering intermolecular quenching processes, leading to higher photoluminescence quantum yields in solution and frequently in the device, (3) a mutual orthogonality of the mesityl groups compared to the pyridine of the C^N preventing an extension of the π-conjugation-system of the C^N ligand, impeding unwanted red-shifting in emission.

As a consequence, in toluene complexes **10** and **11** emit in the same region (λ_{em} = 469 nm and 473 nm, respectively) but with a drastic improvement in photoluminescence quantum yield (Φ_{PL} = 54% and 92%, respectively).[76]

Since the first report of **8** in an OLED, the device architecture of OLEDs has been improved enormously reaching EQEs of 40%.[21,119] Sophisticated encapsulated air-free multilayer systems are necessary to ensure a balanced injection of the charges across the device. State-of-the-art OLEDs may sometimes be comprised of up to 15 layers.[120] This multilayer architecture is typically prepared by vacuum sublimation, where only sublimable compounds can be used narrowing down the choice of luminescent materials significantly.[23] Another architecture that has been attracting considerable interest in the area of solid-state lighting is the light-emitting electrochemical cell (LEEC),[64,84,120] which has a potential in SSL technology.

Light-emitting electrochemical cells (LEECs)

Due to the above-mentioned limitations of OLEDs, new concepts have been emerging to minimise the complex multilayer systems. A device architecture that has shown to exhibit promising results is the light-emitting electrochemical cell (LEEC).[64,84,120] Simply speaking, only one main layer is needed for LEECs (Figure **12**).

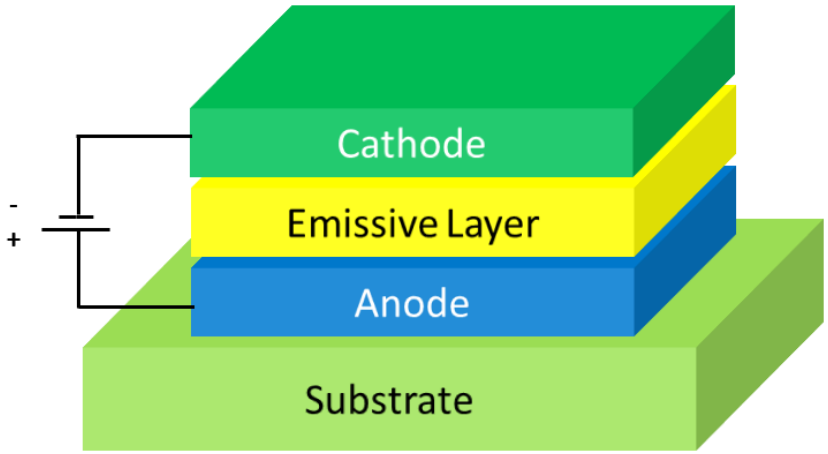

Figure **12**: Schematic representation of a typical architecture of a LEEC containing only one optoelectronically active layer. The ionic luminescent material enables the injected charge to migrate across the device.

The emissive layer, typically a neat film or highly concentrated film, is sandwiched between a cathode and an anode, which is deposited on a glass substrate. In contrast to OLEDs generally using a charge neutral emitter, LEECs are based on intrinsically charged emitters. The charged nature of the emitter permits more facile charge injection and transport and permits the device to work under lower working voltage. These devices can operate with air-stable electrodes allowing them to be solution processed giving rise to a complete different type of emitters compared to OLEDs. This simpler architecture and much milder working conditions leads to much lower production costs and makes LEECs a potential candidate for commercialisation.[64] One family of LEECs is based on charged ionic transition metal complexes.[64] A second family of LEECs is based on semiconducting polymers as emitting material and additional ion conduction polymers and inorganic salts.[121–123]

Efficiency & Stability

The emissive layer is generally a neat film of the emissive material and the molecules tend to aggregate. In such a closely packed system, excited state quenching is likely to occur, which has a direct effect on lowering the EQE values of the devices.[124] Therefore, it is not only

important to tune the emission colours, but incorporate features that may suppress self-quenching to successfully improve device performance.[125] To circumvent the issue of self-quenching in LEECs the emitting complexes can be decorated with bulky, hydrophobic substituents, which act to increase the intermolecular distance.[111] The hydrophobic substituents not only increase the solubility in organic solvents leading to a better dispersion in solution-processed devices, but also hinder the disadvantageous attack from small molecules leading to quenching.[42,76,84,126–128]

LEECs based on Ir(III) complexes

A simple design

As discussed above, the heavy metal containing Ir(III) complexes exhibit excellent photophysical properties making them suitable candidates as emitter in light-emitting devices. One of the simplest examples of Ir(III) complexes is the unsubstituted analogue $[Ir(ppy)_2(bpy)]PF_6$ (complex **12**, Figure **13**) and is investigated intensively in LEECs.[21,23,86]

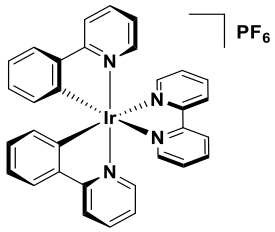

12

Figure **13**: Structures of $[Ir(ppy)_2(bpy)]PF_6$; a widely used Ir(III) complexes in LEECs.

Complex **12** is in acetonitrile solution an orange-yellow phosphorescent emitter (with λ_{em} = 585, Φ_{PL} = 14%, τ_{PL} = 430 ns, Table **1**).[86] The emission origins from a CT triplet state comprising ^{3}MLCT and ^{3}LLCT transitions.[40] In LEECs, complex **12** reaches $t_{1/2}$ = 70 h and E_{tot} = 2 J with and EQE of 2.1%.[86] Evidently, these results are not satisfactory and cannot compete with state-of-the-art lighting applications.

Table **1**: Summary of complexes **1,12-20**

Complex	Photophysics[a]					Device data		Ref.
	λ_{em} / nm	Φ_{PL} / %	τ_{PL} / ns	$t_{1/2}$ / h	E_{tot} / J	EQE / %	PE / lm · W^{-1}	
1	581	24	557			5	10	84
12	585	14	430	70	2	2.1	6.1	86
13	512	70	1400	9		14.9	39.8	129
14	605	23	330	54	-	7.1	22.6	125
15	472 (sh), 494	54	3990			7.6	18.0	130
16	623	17	575	110		0.3	0.46	72
17		2		0.5				87
18	595	3	500	1290	13.6	4.0	10.1	131
19	574	2	600	2000	18.7			132
20	579		98	1300	6.9	1.0	3.3	133

[a] The reported photophysical data were obtained in deaerated acetonitrile solution at 298 K.

However, given its simple design, it is a promising result, showing the great potential of emitters based on iridium. Generally, Ir(III) complexes of the form $[Ir(C\hat{}N)_2(N\hat{}N)]^+$ with a spatial distribution of the frontier orbitals allow an almost independent tuning of the ground level and excited state levels. Therefore, two approaches are possible: incorporating substituents on the C^N or the N^N ligand. Strategies to especially increase the efficiency are of particular interest to improve the overall device performance.[23,42,63,64,66,84,111,134–136]

The use of sterically congested substituents

It has been demonstrated that by adding sterically congested substituents onto Ir(III) complexes, the performance of LEECs could significantly be improved[42,83,138,84,111,124–126,130,131,137] (see Figure **14** for selected examples and Table **1** for the summary of data).

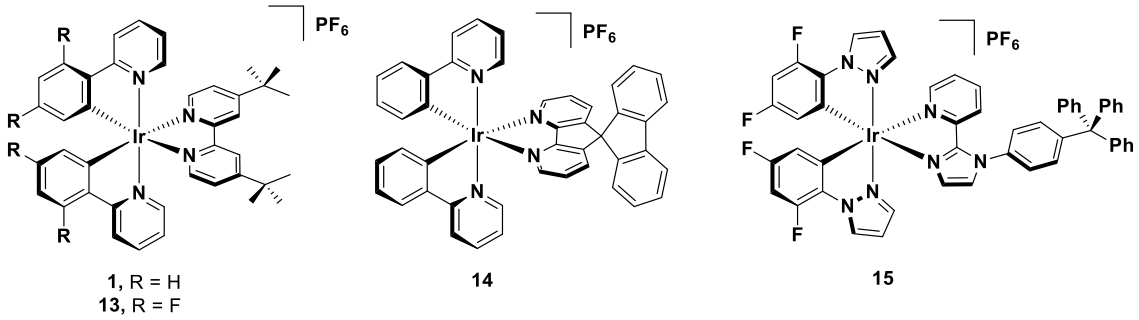

Figure **14**: Structures of cationic Ir(III) complexes (**1** and **13-15**) of the form $[Ir(C\hat{}N)_2(N\hat{}N)]PF_6$ bearing sterically congested substituents on the ancillary ligand

For instance, the cationic Ir(III) complex **14**[125] ($[Ir(ppy)_2$(4,5-diaza-9,9'-spirobifluorene)$](PF_6)$ bearing a sterically demanding ancillary ligand exhibits orange-yellow emission (with λ_{em} = 605) and excited state lifetimes of τ_{PL} = 330 ns with a Φ_{PL} = 23% in acetonitrile solution, which increases to 32% in neat film. LEECs based on complex **14** revealed high maximum external quantum efficiencies of 7.1% and power efficiencies of 26.2 lm W^{-1}. With the choice of this ancillary ligand the properties could be improved in solution as well as in device compared to the unsubstituted analogue complex **12** (Figure **13**). A higher performance could be obtained with the complex $[Ir(dFppy)_2(dtBubpy)]PF_6$ **13**[129] with electron-withdrawing fluorine atoms on the C^N ligand and large electron-donating *tert*-butyl groups on the N^N ancillary ligand. The emission colour is blue-shifted (λ_{em} = 512 nm) compared to **12** and **14**, due to both stabilisation of the HOMO with the fluorine atoms and destabilisation of the energy level of the LUMO thanks to the presence of the *tert*-butyl groups. The photoluminescence quantum yield in acetonitrile solution is significantly increased (Φ_{PL} = 70%) as well as the lifetime (τ_{PL} = 1400 ns) compared to both complexes **12** and **14**. In neat films complex **13** exhibits an impressive Φ_{PL} of almost unity (Φ_{PL} = 96%). High peak external quantum efficiencies of 14.9% and power efficiencies of 39.8 lm W^{-1} with half of the maximum luminance ($t_{1/2}$) of 9h at 3 V can be obtained for LEECs using complex **13** as emitter.

An approach to tune the electronic states of Ir(III) complexes is to modify the nature of the heterocycle in the ligand systems. Complex **15**[130] bears pyrazoles instead of pyridines on the C^N ligand and an imidazole bearing a sterically demanding substituent replacing one of the pyridines of the N^N ligand to produce the structure $[Ir(dfppz)_2(tp\text{-}pyim)]PF_6$ (where dfppzH is 1-(2,4-difluorophenyl)-1H-pyrazole and tp-pyim 2-(1-(4-tritylphenyl)-1H-imidazol-2-yl)pyridine). The emission energy in acetonitrile with λ_{em} = 472 (sh), 494 is notably blue shifted (18 nm) compared to **13**, the Φ_{PL} however is lower (Φ_{PL} = 54%), which may be explained by fluxional motion coming from the sterically demanding substituent, leading to non-radiative decay. However, **15** is still significantly brighter than the reference complex **12**. The lifetime is significantly higher (τ_{PL} = 3990 ns) than that of **13**. In LEECs complex **15** afforded a peak EQE of 7.6% and power efficiencies of 18.0 lm W^{-1}, which is a good result, but notably lower than the results for **13**.

Another strategy is obtained with the functionalised 5,5'-diphenyl-2,2'-bipyridine (dpbpy) as ancillary ligand. The emission of complex $[Ir(ppy)_2(dpbpy)]PF_6$, **16**[72] (Figure **15** and Table **1**) is red-shifted in MeCN solution (λ_{em} = 623 nm) by 18 nm compared to **12**. The quantum yield is slightly lower Φ_{PL} = 17% with lifetime (τ_{PL} = 575 ns) higher than **1**. The performance in LEECs are, very impressive with a superior figure of $t_{1/2}$ = 110 h (with a peak of EQE = 0.3% and power efficiencies of 0.46 lm W^{-1}).[65] The substituents on the ancillary ligand shield efficiently the excited state centre leading to long device lifetimes. At first sight, more and more steric bulk might sound an attractive strategy to follow. One example is the sterically demanding complex **17**[87] bearing bulky 9,9-dihexylfluorene side groups on the N^N ligand.

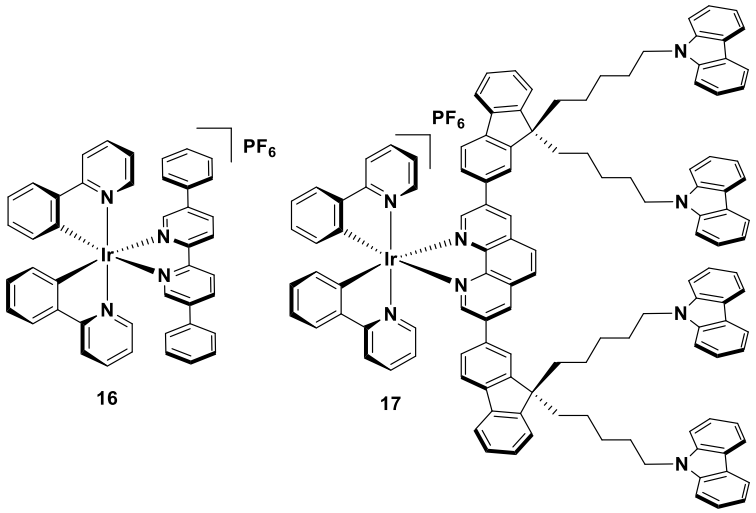

Figure **15**: Second set of structures of cationic Ir(III) complexes (**16** and **17**) of the form $[Ir(C\hat{}N)_2(N\hat{}N)]PF_6$ bearing sterically congested substituents on the ancillary ligand

In acetonitrile solution this complex exhibits a low Φ_{PL} of 2%, which is significantly increased in neat film (38%). The LEECs based on **17** showed device lifetimes of not even 30 min, which is a disappointing result. Consequently, the steric bulk cannot be just increased infinitely.

To conclude, one strategy to increase device performance is indeed adding sterically demanding hydrophobic substituents. It will increase the solubility of the complex leading to a better dispersion, the inter-nuclear distance will be increased suppressing excited state quenching when agglomerated and the excited state centre is slightly protected. On the other hand, too much steric bulk like in **17** can lower the ion mobility, especially of the emissive Ir(III) complex, resulting in a tremendous reduction of device performance.

Shielding through cage effect

One big issue during device operation is the degradation of the emitter through the attack of small nucleophiles.[126] It has been demonstrated that with complex $[Ir(ppy)_2(pbpy)](PF_6)$ (with 6-phenyl-2,2'-bipyridine as pbpy) **18**[131] (Figure **16**) this issues can be suppressed through shielding the centre of the complex. The substituted N^N ligand forms a face-to-face π-stacking

with the phenyl group of the ppy C^N ligand resulting in a cage effect, which shields the excited state centre of the complex efficiently. This orientation is kept in the ground state as well as in the excited triplet state.[131] In acetonitrile solution, the emission energy of **18** (λ_{em} = 595 nm) is minimally red-shifted (5 nm) compared to **12**.

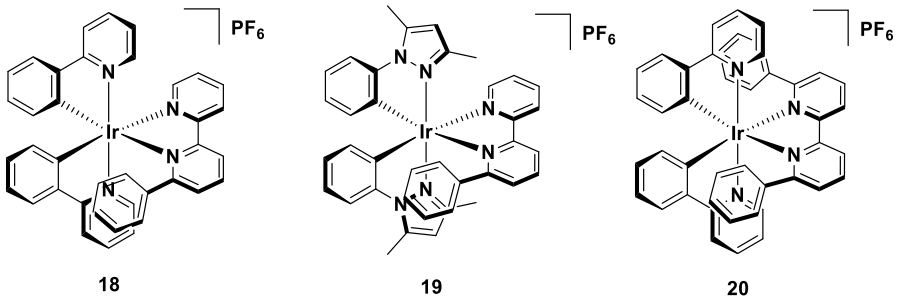

18 **19** **20**

Figure **16**: Structures of shielded cationic Ir(III) complexes (**18-20**) of the form $[Ir(C^N)_2(N^N)]PF_6$ bearing phenyl groups on the ancillary ligand to generate cage effect through intra-molecular π-stacking

The photoluminescence quantum yield in solution of Φ_{PL} = 3% is low in general and lower than the value for complex **1** (Φ_{PL} = 9%). In 5 wt% PMMA film, however there is an enhancement of the quantum yield (Φ_{PL} = 34%). The lifetime (τ_{PL} = 500 ns) is slightly increased with respect to **12**. Another example is the complex $[Ir(dmppz)_2(pbpy)](PF_6)$ **19**[132] (where dmppz is 3,5-dimethyl-1-phenylpyrazole, Figure **16**). Complex **19** exhibits a blue shift in acetonitrile of 21 nm (λ_{em} = 574 nm) with respect to **18**. Similar to **18**, the quantum yield in solution (Φ_{PL} = 2%) is low. The lifetime (τ_{PL} = 600 ns) is in the similar range, too.

When employing complex **18**[131] and **19**[132] in LEECs improved device stability can be obtained. The device based on **18** showed power efficiencies of 10 lm W^{-1} and more impressive high stability with $t_{1/2}$ = >1290 h and E_{tot} = 13.6 J, which was an enormous improvement compared to the performance of LEECs based on complex **1** and **12**. Even more as with complex **19**, LEECs with $t_{1/2}$ = 2000 h and E_{tot} = 18.7 J can be obtained surpassing the performances of **18**, which can be explained by the sterically more congested C^N ligand with

the methyl groups acting as an additional shield resulting in increased shield effect. Comparing these results with complex **12** ($t_{1/2}$ = 70 h and E_{tot} = 2 J), the cage effect on device performance is clearly distinct. A logical step appears to add a second phenyl unit on the ancillary ligand to obtain a symmetrical molecule and shield two sides leading to the complex $[Ir(ppy)_2(dpbpy)](PF_6)$ **20**[133] (where dpbpy is 6,6'-diphenyl-2,2'-bipyridine, Figure **16**). However, it turns out the cage effect is not improved in complex **20**. The opposite is the case as the second π-stacking interaction distorts the planarity of the N^N ligand causing sterically stress. The shielding of the complex centre is less efficient than in **18**. Still, LEECs employing complex **20** as emitter show excellent results ($t_{1/2}$ = 1300 h and E_{tot} = 6.9 J).

The above discussed examples show the impact of sterically congested substituents on the device performance. However, the trend in the studies focusses on substitution on the ancillary ligand. The impact of sterically congested substituents on the cyclometalated ligand of cationic Ir(III) complexes has not been investigated in as much detail as for the ancillary ligand.[23,111] Especially with the cationic complexes **13** and **14** and the neutral complex **11** it has been demonstrated how increasing the steric congestion is improving photophysical properties and solution processed device performances.[76]

Objectives

This part of the introduction has explored different approaches of improving the properties of cationic Ir(III) complexes through incorporation of bulky sterically congested substituents. These findings are the basis of the aim of part of this present work. One objective of this work is to design new cationic Ir(III) complexes with increasing steric bulk incorporated onto the cyclometalated ligands to investigate their impact on the optoelectronic properties. Expanding the chelating ring from a five-membered ring to a six-membered ring appears to be a largely unexplored strategy to modifying the electronics of Ir(III) complexes. This work aims to study the effects of six-membered ring chelates on C^N ligands as well as N^N ligands in more detail. Especially in the motivation of achieving blue emission, the use of nonconjugated chelates is investigated.

Chromophores in Nonlinear Optics (NLO)

Background

The field of "nonlinear optics" is the study of optical phenomena caused by the interactions of an applied electromagnetic field on a material and the generation of emission of new electromagnetic fields with altered photophysical properties (e.g. frequency, phase).[139–143] Typically lasers are used as light sources, since the applied field must be very strong to successfully modify the optical properties of the material. NLO is a process of transmitting and processing signals through photons instead of electrons. Simply speaking, it is a tool to manipulate photons.[144]

When an electric field, produced by incident radiation, is exposed to a material, an effect of polarisation can be observed, expressed by:

$$\vec{P} = \overrightarrow{P_0} + \overrightarrow{P_{ind}} = \overrightarrow{P_0} + \chi^{(1)}\vec{E} \tag{4}$$

where $\overrightarrow{P_0}$ is the intrinsic polarity, $\overrightarrow{P_{ind}}$ the induced polarisation, and $\chi^{(1)}$ the electrical susceptibility. In the case of very high electric field strengths, $\vec{E}$, as it happens when laser pulses are used, the perturbation is not linear, and the induced polarisation is expressed by:

$$\vec{P} = \overrightarrow{P_0} + \chi^{(1)}\vec{E} + \chi^{(2)}\overrightarrow{E^2} + \chi^{(3)}\overrightarrow{E^3} + \cdots + \chi^{(n)}\overrightarrow{E^n} \tag{5}$$

where $\chi^{(2)}$, $\chi^{(3)}$ and $\chi^{(n)}$ are, the second-, third-, and n^{th}-order electrical susceptibilities, respectively, describing the nonlinear response of the material.

If the electric field interacts with a molecule then the polarisation can be expressed by:

$$\vec{P} = \mu_0 + \alpha\vec{E} + \beta\overrightarrow{E^2} + \gamma\overrightarrow{E^3} + \cdots \tag{6}$$

where μ_0 is the molecular ground state electric dipole moment, α is the linear polarizability tensor, β and γ are the nonlinear quadratic and cubic hyperpolarizability tensors,

respectively, and describe the second- and third-order NLO effects. In a centrosymmetric environment both $\chi^{(2)}$ and β vanish. Thus, to obtain a second-order NLO response the medium must be non-centrosymmetric.[28]

One important second-order NLO phenomenon is the process of second-harmonic generation (SHG), where an input wave with frequency ω, is converted into an output wave with twice the input frequency 2ω (Figure **17**).[145]

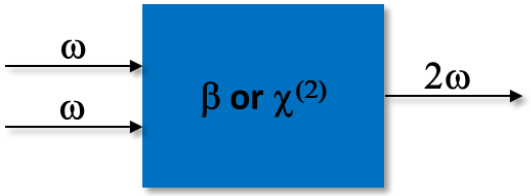

Figure **17**: Schematic representation of Second Harmonic Generation (SHG) , with frequency, ω, second-order electrical susceptibilities, $\chi^{(2)}$ and nonlinear quadratic hyperpolarizability, β.

One of the most famous examples for this process is the conversion of the fundamental infrared radiation of a Nd:YAG (neodymium-doped yttrium aluminium garnet; Nd:$Y_3Al_5O_{12}$) laser by a NLO material (e.g. Beta Barium Borate, BaB_2O_3)[146] to green light. To obtain a bulk material or a molecule with a significant NLO effect the tensors $\chi^{(2)}$ and β, must both be high. Theoretical methods can be used to calculate the molecular quadratic hyperpolarizability, β. One experimental determination of β of an NLO chromophore in solution uses the electric field induced second harmonic generation (EFISH) method, where the centrosymmetry of the liquid by a dipolar orientation of the molecules can be broken by a high-voltage electromagnetic field.[147,148] Through the EFISH technique $\gamma + \mu \cdot \beta / 5kT$ can be determined, where γ is the cubic hyperpolarizability of the molecule, μ is the dipole moment, and β the molecular quadratic hyperpolarizability along the dipole moment axis. For many molecules the third order contribution is very low and can be neglected. It is necessary to determine the ground state

dipole moment μ, which can be independently measured using the Guggenheim model; a procedure to compute electric dipole moments.[149]

Extrapolation to zero frequency (ω_L = 0.0 eV; $\lambda = \infty$) allows an estimation of the static quadratic hyperpolarizability β_0, a useful figure of merit to evaluate the basic second-order NLO properties of a molecule, which can be expressed by:

$$\beta_0 = \beta_\lambda \left[1 - \left(\frac{2\lambda_{max}}{\lambda}\right)^2\right]\left[1 - \left(\frac{\lambda_{max}}{\lambda}\right)^2\right] \quad (7)$$

where β_λ is the quadratic hyperpolarizability value at the incident wavelength λ (typically 1.907 μm) and λ_{max} is the absorption wavelength of the charge-transfer transition considered.[143] This is a simple way to estimate the frequency-dependant quadratic hyperpolarizability spectroscopic data, in cases when only one single charge-transfer dominates the NLO response.[143]

Requirements for large hyperpolarizabilities are non-centrosymmetry of the molecule and highly polarisable electrons, which means the ability to respond to an applied electric field. Through conjugation, where π electrons can be delocalised and easily move, large polarizability can be achieved. Push-pull molecules, in which electron-donating and accepting groups are incorporated at each end of the molecule, are non-centrosymmetric and therefore display a strong permanent dipole moment, as a result of induced moments. Consequently, the hyperpolarizabilities of dipolar compounds are controlled by the strength of the donor and acceptor groups and the nature of the π-conjugated bridge of the system.[140,150]

Important factors for NLO-phores

Compounds with second-order nonlinear optical (NLO) properties have attracted great interest as materials for optical communications, optical data storage, or electrooptical devices. In the last 25 years, coordination and organometallic complexes showing second-order NLO activity have become more and more popular as NLO-phores.[28,29,41,140,151,152] Coordination

compounds containing polypyridyl ligands are of special interest as they possess low-lying charged transfer transitions, such as metal-to-ligand charge-transfer (MLCT) or intraligand charge-transfer (ILCT) transitions, that can be exploited for NLO.

The metal centre can for example act as a "donor push system" to the π* orbitals of the ligand,[153] that acts as an acceptor "pull system", which is typical of complexes with MLCT absorption bands. On the other hand, LMCT transitions and ILCT can be exploited where the metal acts as the acceptor and the ligands as the donor. Finally, the metal can act as a bridge between two independent ligands, one acting as the donor and the other as the acceptor.[34] The metal in this final case is used as a template to control the geometry of the complex. The nature, coordination sphere and oxidation state of the metal and the ligand influences the electron density of the complex and by extension the nature of the CT transitions.[153]

There are two main approaches for NLO-active compounds. One concept comprises one-dimensional dipolar structures. Dipoles, however, have certain limitations e.g. the difficulty to achieve noncentrosymmetry to reach maximum bulk effect in the solid state due to head-to-tail arrangements.[154] The other approach is widened to encompass a more diversified range of molecules employing three dimensional octupolar molecules, a concept introduced by J. Zyss in 1994.[142] Octupolar molecules can offer advantages of better nonlinearity/transparency trade-off and are typically characterised by multidirectional charge transfer excitations.[155] Especially for potential second-order applications octupolar compounds are suitable candidates.[28,30,156]

Many systems have been investigated. In the case of octupolar molecules the Hyper-Raleigh Scattering (HRS), also termed Harmonic Light Scattering (HLS), method is employed to determine β experimentally.[28,157] Those based on octupolar tris[4,4′-bis[(dialkylamino)styryl]- 2,2′-bipyridine]metal(II) complexes with Fe, Zn, Ru, Ni and Cu have all shown large molecular first hyperpolarizability coefficients β.[29,153,158]

An archetype of an octupolar system is a cube with alternating donor and acceptor groups on the edges. From this general form pure octupolar symmetries can be derived (Figure **18**). For example, projection along a C_3 axis gives rise to D_3 or D_{3h} symmetry, or by fusion of one type of charge in the barycentre D_{3h}, D_3, T_d, or D_{2d} symmetry can be obtained (Figure **18**). The superiority of octupoles with respect to dipoles can be demonstrated by the three Zn(II) complexes **Zn1**-**Zn3** controlled by the number of 4,4′-bis(dialkylaminostyryl)-[2,2′]-bipyridine ligands coordinated to the metal centre (Figure **18** and Table **2**).[159]

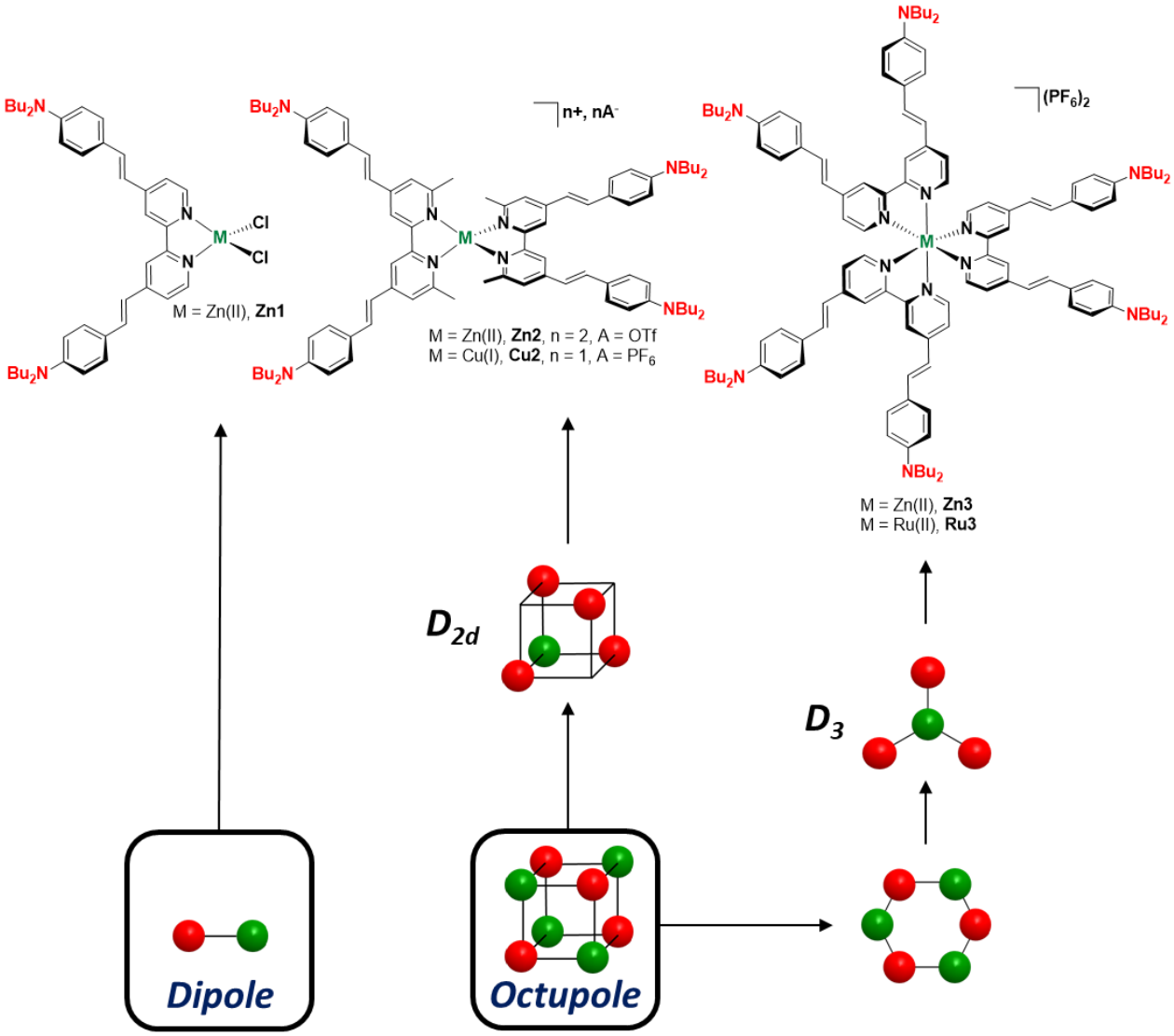

Figure **18**: Dipolar and octupolar (D_{2d} and D_3 symmetry) architectures based on metal complexes bearing 4,4′-bis(dialkylaminostyryl)-[2,2′]-bipyridine ligands

Table **2**: Linear and nonlinear optical properties of dipolar and octupolar metal complexes

Complex	**Solvent**	λ_{abs} / nm	ε / M^{-1} cm^{-1}	β x 10^{-30} / esu	β_0 [a] x 10^{-30} / esu
Zn1	$CHCl_3$	459	6 2000	172[b]	62
Zn2	CH_2Cl_2	529	125 000	245[c]	157
Zn3	CH_2Cl_2	466	17 5000	340[c]	241
Cu2	CH_2Cl_2	436	106 000	113[c]	86
		484	45 000		
Ru3	CH_2Cl_2	446	142 000	340[c]	-[d]
		520	150 000		

[a] Corrected at $\lambda \rightarrow \infty$ using the extrapolation model see equation (7).[160] [b] By working at 10^{-3} M; the error of EFISH measurements is ±10%, with incident wavelength of 1.34 μm. $\mu \cdot \beta$ = 1830 x 10^{-30} esu with μ = 10.65 D. [c] Measured by HLS (precision ±15%) in a (1-5)x10^{-2} M with incident wavelength of 1.91 μm. [d] β_0 value not determined because of the presence of two different ILCT and MLCT transitions

The dipolar complex [Zn(4,4′-bis(dibutylaminostyryl)-[2,2′]-bipyridine)Cl_2] **Zn1** bears one substituted bipyridyl ligand. The cationic zinc(II) complex **Zn3** ([Zn(4,4′-bis(dibutylaminostyryl)-[2,2′]-bipyridine)$_3$]$^{2+}$) is octupolar with a D_3 symmetry thanks to the three bipyridyl ligands coordinated around the metal centre. To ensure pseudotetrahedral D_{2d} symmetry i.e. an octupolar structure, the α,α'methyl substituted bipyridyl ligand was used to obtain the cationic complex **Zn2** [Zn(4,4'-bis(dibutylaminostyryl)-6,6'-dimethyl-2,2'-bipyridine)$_2$]$^{2+}$ bearing two bipyridyl ligands. All three complexes exhibit strong absorption bands (ε = 6-18 x 10^4 M^{-1} cm^{-1}, see Table **2**) in the visible spectrum assigned to intraligand charge transfer transitions (ILCT) from the NBu_2 groups to the bipyridine.[159] Metal-to-ligand charge transfer (MLCT) processes are not observed, which can be explained by the high third ionisation potential of Zn(II).[29,159]

On going from the dipolar **Zn1** to the octupolar **Zn3** the absorption maximum does not change notably (Δ = 7 nm) but the absorption intensity is largely increased for **Zn3** (ε = 17.5 x

10^4 M^{-1} cm^{-1}) compared to **Zn1** (ε = 6.2 x 10^4 M^{-1} cm^{-1}), thanks to the two extra bipyridyl ligands. Complex **Zn2** is significantly red shifted with respect to **Zn1** (Δ = 70 nm) and the intensity is doubled (ε = 12.5 x 10^4 M^{-1} cm^{-1}), but not as high as for **Zn3**.

The tetrahedral complex **Cu2**[161] [Cu(4,4'-bis(dibutylaminostyryl)-6,6'-dimethyl-2,2'-bipyridine)$_2$]$^{2+}$ and the octupolar complex **Ru3** ([Zn(4,4′-bis(dibutylaminostyryl)-[2,2′]-bipyridine)$_3$]$^{2+}$) (Figure **18**) are selected to investigate the role of the metal ion.[29,153] **Cu2** exhibits an ILCT band with λ_{abs} at 436 nm (ε = 10.6 x 10^4 M^{-1} cm^{-1}), that is slightly weaker in intensity with respect to **Zn2**. The absorption band is characterised by a shoulder at 480 nm which is attributed to metal-to-ligand charge transfer (MLCT) bands [Cu(I) → $\pi^*_{N\wedge N}$].[29] The absorption spectrum of complex **Ru3** is dominated by a broad band in the visible, attributed to the overlap of ILCT (λ_{abs} at 424 nm; ε = 14.2 x 10^4 M^{-1} cm^{-1}) and higher intense MLCT [Ru(II) → $\pi^*_{N\wedge N}$] (λ_{abs} at 520 nm; ε = 15.0 x 10^4 M^{-1} cm^{-1}) bands.[29] The λ_{ILCT} of **Zn3** and **Ru3** are roughly similar.[29,153]

The molecular hyperpolarizability coefficient β and the corresponding dispersion-free hyperpolarizability β_0 for compounds **Zn1**-**Zn3** are summarised in Table **2**. The $\mu\beta$ value of **Zn1** was measured by the EFISH method and β was then deduced by measuring the dipole moment μ according to the Guggenheim model.[149] The EFISH technique requires dipolar orientation in solution and hence is not suitable for purely octupolar molecules. The β values for the octupolar molecules were measured by the harmonic light scattering (HLS) method.[133] The β_0 values increase from **Zn1** to **Zn3** with respect to the number of N^N ligands coordinated to the metal centre (β_0 = 62, 157 and 241 x 10^{-30} esu, respectively). The transparency/nonlinearity trade-off for the octahedral **Zn3** is improved with respect to the tetrahedral **Zn2**. These results demonstrate the superiority of octupolar systems, since the β_0 value of **Zn3** is approximately four times larger compared to the dipolar complex **Zn1**, without and significant bathochromic shift of the ILCT transition.

As described above, the central metal ion has a significant impact on the linear optical properties. For instance, the red-shift of the ILCT transition using the same ligand system but different metal ions, can be attributed to the Lewis acidity of the central metal. The nonlinear optical properties also strongly depend on the nature of the metal, since **Zn2** exhibits a β_0 value (β_0 = 157 x 10^{-30} esu), that is approximately 2-fold larger than that of the related tetrahedral **Cu2** bearing the same ligands (β_0 = 86 x 10^{-30} esu), reflecting the better acceptor strength of Zn(II) compared to Cu(I). The complex **Ru3** exhibits a strong ILCT and a strong MLCT, this latter however has no significant influence on the nonlinear optical response. **Ru3** and **Zn3** both show the same value of β (340 x 10^{-30} esu with incident wavelength of 1.91 μm). The presence of the MLCT transition, however, does not permit the determination of β_0 following the extrapolation model described by equation (7).[160]

In summary, these results demonstrate that coordination chemistry is a powerful tool to elaborate octupolar (tetrahedral or octahedral) nonlinear optically active chromophores. The molecular quadratic hyperpolarizability (β) values are strongly affected by the symmetry of the complex. Increasing the coordination number, hence increasing the ligand-to-metal ratio, results in a significant enhancement of β. The nature of the central metal also has an important role controlling the symmetry of the complex. Additionally, the NLO activity is significantly enhanced by increasing the Lewis acidity of the metal.

This concept is not only limited to transition metal complexes, the nonlinear optical behaviour of chromophores featuring lanthanide metals has been investigated, too. These metals have been of particular interest because of their high coordination number and strong Lewis acidity, which induce strong intra-ligand charge transfer (ILCT) transitions and their ability to form a variety of coordination geometries.[41,162,163] Then studies extended to cyclometalating metal complexes and the following section is focussing on NLO activities of bis- and tris-cyclometalated Ir(III) complexes, neutral and cationic species.

Cyclometalated iridium(III) complexes as NLO chromophores

As discussed above, organometallic compounds have attracted great interest as they display strong NLO activities.[143] The use of iridium(III) as the metal centre has been far less explored and only in the last ten years, Ir(III) complexes bearing cyclometalated ligands have received increasing attention as chromophores for NLO.[143,152] In the following sections, the structure/property relationship is ascertained for cyclometalated Ir(III) complexes bearing substituted charge-neutral ancillary ligand of the form $[Ir(C\hat{}N)_2(N\hat{}N)]$ (where C^N is the cyclometalated ligand based on ppy and its derivatives and N^N is a diimine) or substituted with negatively charged ancillary ligands of the form $[Ir(C\hat{}N)_2(O\hat{}O)]$ (where O^O is an substituted acetylacetonate).

Neutral cyclometalated Ir(III) complexes as NLO chromophores

The neutral Ir(III) complex **Ir1a** $[Ir(ppy)_2(acac)]$[164] (where acac = acetylacetonate) (Figure **19**) has been shown to have promising linear photophysical properties,[165] which provided the motivation to investigate the second-order NLO activity of this complex. The absorption data of complex **Ir1a** are summarised in Table **3**.

Complex **Ir1a** exhibits a typical absorption spectrum for cyclometalated Ir(III) complexes with a characteristic high intense band ($\varepsilon = 4.5 \times 10^4\ M^{-1}\ cm^{-1}$) below 300 nm, which is attributed to ligand-centred (^{1}LC) ($^1\pi$–π^*) transitions based on ppy ligands. The low energy portion of the spectrum (until 300 nm) is dominated by metal-to-ligand charge transfer processes from the Ir(III) with contributions from the ppy to both π^*_{acac} and π^*_{ppy}.[164]

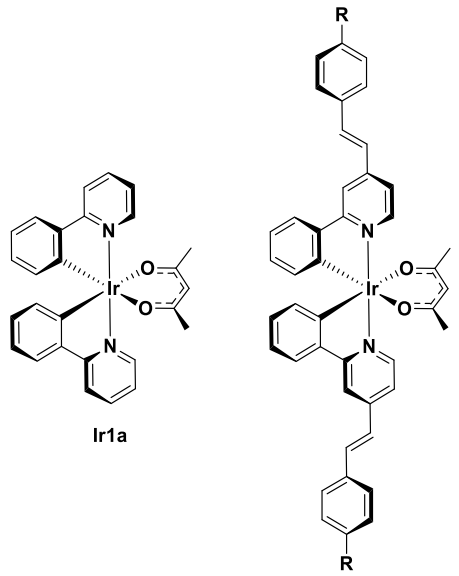

Figure **19**: Neutral Ir(III) complexes of the form $[Ir(C\hat{}N)_2(acac)]$

Table **3**: Absorption data and EFISH μβ of complexes **Ir1a** and **Ir1b-Ir1e** in dichloromethane

Complex	**Absorption maxima / nm, [ε / M^{-1} cm^{-1}]**	**$\mu\beta_{1.907EFISH}$[a] x 10^{-48} / esu**
Ir1a	260 [45000], 345 [38000], 412 [34000], 460 [33000], 497 [30000]	-910
Ir1b	265 [40000], 410 [23000], 433 [26000], 480 sh [5500]	-550
Ir1c	270 [62000], 330 [45000], 373 [39000], 415 sh [21000], 475 [5300]	-570
Ir1d	268 [44000], 306 [45000], 370 [25000], 410 sh [12000], 468 [4700]	-408
Ir1e	263 [38000], 282 [36000], 332 [48000], 400 [33000], 442 sh [18000], 518 [5200]	-895

[a] By working at 10^{-3} M; the error of EFISH measurements is ±10%, with incident wavelength of 1.907 μm.

The absorption data of **Ir1a**[164] and **Ir1b-Ir1e**[57,82] (Figure **19**) are summarised in Table **3**. The EFISH method was used to measure the second-order NLO response of **Ir1a** and **Ir1b-Ir1e** and the data are shown in Table **3**. Complex **Ir1a** exhibits a negative value of μβ, which is typical for MLCT and is in agreement with a negative value of Δμ (the difference of the dipole moment in the excited and ground state) upon excitation. The excited state dipole

moment is directed along the pseudo C_2 axis within the molecule. The computed dipole moment is generated by a charge transfer from the C^N ligands to the acac ligand originating from a charge asymmetry in which donation from the negatively charged C^N ligands to Ir(III) predominates the donation from the charged acac ligand.[164] The μβ value of **Ir1a** (-910 x 10^{-48} esu) is significantly higher compared to its Pt analogue ([Pt(ppy)(acac)] with μβ = -535 x 10^{-48} esu).[164]

The second-order NLO response in **Ir1a** is only partially dominated by metal-to-ligand charge transfer (MLCT) and ligand-to-ligand charge transfer (LLCT) processes with contributions of ppy and acac, since there is also significant contributions of the π–π* LC transitions based on the ligands (mainly C^N), with only a limited amount of metal character.[164] Therefore a careful choice of substituents on the C^N ligands can be a tool to control the nonlinear activity of this complex that is characterised by a good transparency. These results provided the motivation to design complexes **Ir1b-Ir1e** in which the substituents on the bpy ligand used in the octupolar systems (see above) are incorporated into the cyclometalating ligands of the Ir(III) complexes with the goal to investigate the effect of the ppy ligand containing an increase of the π-delocalisation decorated with electron-withdrawing or electron-donating substituents (Figure **19**) on the second-order nonlinear optical activity.

The absorption profiles of **Ir1b-Ir1e** show similar features with respect to **Ir1a**, displaying a high intense band (in the range of ε = 3.8 - 6.2 x 10^4 M^{-1} cm^{-1}) below 280 nm, attributed to ligand centred (^{1}LC) (^{1}π–π*) transitions based on C^N and ancillary ligands. These absorption profiles, however are dominated by characteristic intraligand charge transfer (ILCT) bands lower in energy compared to LC transitions with similar intensities (ε = 2.3 – 4.8 x 10^4 M^{-1} cm^{-1}). At lower energy (450 nm to 650 nm) moderately intense bands are observed for all complexes (ε = 2.5 - 3.9 x 10^4 M^{-1} cm^{-1}) and are assigned to mixed charged transfer transitions.

The absolute value of μβ, measured by the EFISH technique, for **Ir1b, Ir1c** and **Ir1d** are all in the similar range, whereas **Ir1e** exhibits a slightly higher value, which is comparable to the unsubstituted analogue **Ir1a**. As with the case of **Ir1a**, the second-order NLO response is a result of various charge-transfer transitions only partly dominated by MLCT processes, making it difficult to rationalise the trends.

Cationic 1,10-phenanthroline Ir(III) complexes

A second class of iridium complexes, namely cationic cyclometalated Ir(III) complexes bearing π-delocalised diimine ligands have shown intriguing properties for nonlinear optical activities. One of the earliest Ir(III) complexes investigated in NLO bore substituted phenanthrolines such as $[Ir(ppy)_2(5\text{-R-}1,10\text{-phen})]^+$ (R = H, Me, NMe_2, NO_2, with phen = phenanthroline) and $[Ir(ppy)_2(4\text{-R'},7\text{-R'-}1,10\text{-phen})]^+$ (R' = Me, Ph)[55] with the goal of investigating the role of the substituents on the 1,10-phenanthroline and of the nature of the cyclometalated moiety on the NLO properties of the complex. Density functional theory (DFT) calculations revealed that the HOMO of this class of Ir(III) complex are primarily comprised of a combination of metal-based orbitals and orbitals of the cyclometalated ligand and the LUMO is localised on the orbitals of the coordinated 1,10-phenanthroline.

Consequently, HOMO-LUMO transitions have a significant charge-transfer character. Figure **20** shows examples of cationic Ir(III) complexes bearing phenanthroline ancillary ligands. Relevant absorption bands and the values of EFISH μβ are reported in Table **4**. Generally, for these ionic NLO chromophores, ion pairing in solvents (e.g. dichloromethane or chloroform) may be relevant. The goal of the study is to demonstrate how the nonlinear response is affected by the concentration and the choice of the counterion, such as $C_{12}H_{25}SO_3^-$ or PF_6^-.

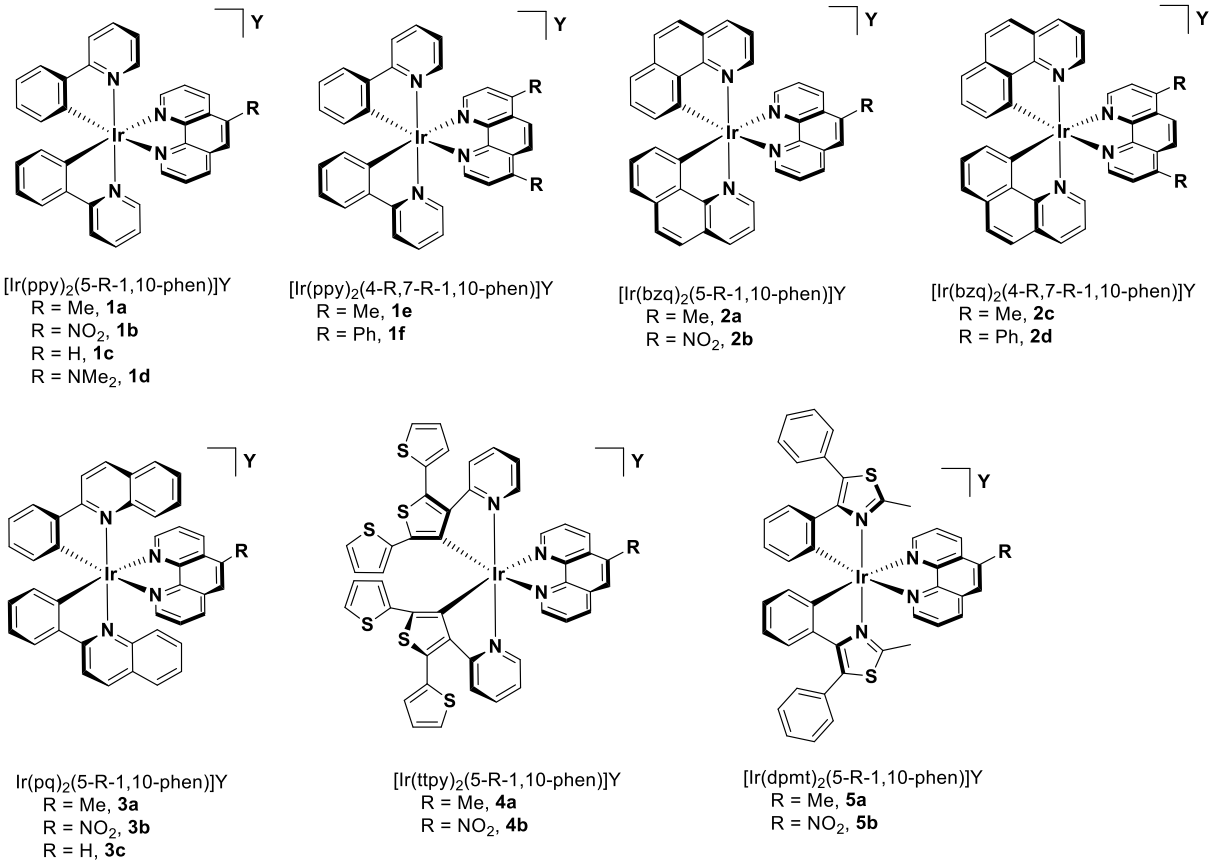

Figure **20**: Cationic Ir(III) complexes of the form [Ir(C^N)$_2$(substituted-1,10-phen)]Y (Y = PF_6^- or $C_{12}H_{25}SO_3^-$, Table **4**)

In this study the EFISH technique was used for the first time to measure the NLO response of cationic Ir(III) complexes.[34,55] All complexes show strong absorption bands in the ultraviolet before 290 nm, which is typical for cationic Ir(III) complexes of this form.[40,41] These bands can be assigned to π-π* ligand centred (LC) transition of the π-system of the substituted 1,10-phenanthrolines and the cyclometalated ligands. At longer wavelength between λ = 300 - 450 nm weaker bands are observed, that can be assigned to mixed charge transfer (CT). This band is sensitive to the substitution on the phen ligand. The iridium complexes in this study bearing ancillary ligands with a donor group show additional bands in the region of 350-450 nm originating from intraligand charge transfer (ILCT) based on the phen ligand.[55]

Table **4**: Absorption data and EFISH μβ in dichloromethane for Ir (III) complexes of the form [Ir(C^N)$_2$(substituted-1,10-phen)]Y

Complex	**Y$^-$**	**λ_{abs}[a] / nm, [ε / M^{-1} cm^{-1}]**	**$\mu\beta_{1.907EFISH}$[b] x 10^{-48} / esu**
1a	PF_6^-	255 (sh), 268 [60300], 333 (sh), 377 [8070]	-1565
1a	$C_{12}H_{25}SO_3^-$	251(sh), 270 [39400], 333(sh), 376 [8270]	-1350
1b	PF_6^-	254 (sh), 264 [86900], 378 [12400]	-2230
1b	$C_{12}H_{25}SO_3^-$	253(sh), 261 [52700], 378 [7200]	-1430
1c	PF_6^-	252 (sh), 264 [58500], 377 [9130]	-1270
1d	PF_6^-	252 (sh), 264 [81400], 334 (sh)	-1330
1e	PF_6^-	255 (sh), 265 [73000], 375 (sh)	-1454
1f	PF_6^-	269 [51300], 282 (sh) 385 [9020]	-1997
2a	PF_6^-	256 [55000], 325 [17000], 417 [6600]	-1680
2a	$C_{12}H_{25}SO_3^-$	256 [67000], 321 [20900], 415 [7940]	-1219
2b	PF_6^-	256 [107000], 313 [34800], 408 [12900]	-1905
2b	$C_{12}H_{25}SO_3^-$	255 [69500], 310 [16000], 408 [7400]	-1389
2c	PF_6^-	255 [77700], 325 [22100], 417 [7250]	-1588
2c	$C_{12}H_{25}SO_3^-$	255 [70300], 321 [21700], 420 [8980]	-1140
2d	PF_6^-	259 [68300], 283 (sh), 333 [28200], 418 [8580]	-1720
2d	$C_{12}H_{25}SO_3^-$	259 [117000], 280 [80500], 325 [42200]	-1298
3a	PF_6^-	273 [70400], 329 [20700], 347(sh), 431 [4750]	-2090
3b	PF_6^-	268 [81100], 324 [27600], 430 [6930]	-1720
3c	PF_6^-	269 [95000], 330 [41300], 433 [14700]	-1850
4a	PF_6^-	260 [44500], 319(sh), 396 [17378]	-1320
4b	PF_6^-	257 [62300], 315 [28100], 397(sh)	-1640
5a	PF_6^-	261 [48000], 272(sh), 358 [9400]	-1414
5a	$C_{12}H_{25}SO_3^-$	265 [59400], 356 [12800]	-1220
5b	PF_6^-	262 [67200], 357 [15200]	-1780

[a] All complexes possess a band tailing between λ = 400 nm and λ = 500–550 nm. [b] By working at 10^{-3} M; the error of EFISH measurements is ±10%, with incident wavelength of 1.907 μm.

Not all complexes show strong bands above 450 nm, meaning a second harmonic generation may be obtained without any significant cost in transparency, which is crucial when designing second-order NLO chromophores. The second-order nonlinear optical response of complexes **1a-5b** (Figure **20**, Table **4**) was determined to investigate the effect of the nature of the substituent of the 1,10-phenanthroline and the cyclometalating ligand on μβ values.

In the case of the series bearing the unsubstituted ppy ligand, the highest μβ value was for complex **1b.PF$_6$** in which a nitro group has been introduced at the 5-position of the ancillary ligand (μβ = -2230 x 10^{-48} esu). The influence of added methyl substituents is negligible on the absolute μβ values, since similar values can be obtained for complexes **1a.PF$_6$** (bearing one methyl group on the N^N ligand, μβ = -1565 x 10^{-48} esu) and **1e.PF$_6$** (bearing two methyl groups on the N^N ligand, μβ= -1454 x 10^{-48} esu). Replacing the methyl groups (**1e.PF$_6$**) with phenyl units (**1f.PF$_6$**), results in an increase of the absolute value μβ (-1997 x 10^{-48} esu), because of an increased π conjugation on the 1,10-phenanthroline. By contrast, adding a π-extended system on the cyclometalating ligand through using benzo[h]quinoline (μβ = -1680, -1905 and -1588 x 10^{-48} esu for **2a.PF$_6$, 2b.PF$_6$,** and **2c.PF$_6$, 2d.PF$_6$**, respectively) or 2-phenylquinoline (μβ = -2090, -1720 and -1850 x 10^{-48} esu, **3a.PF$_6$** – **3c.PF$_6$**, respectively) does not lead to a significant change in the absolute μβ value with respect to the ppy analogues bearing the same 1,10-phenanthroline. When using the C^N ligands 2-([2,2':5',2''-terthiophen]-3'-yl)pyridinato (ttpy) in complexes **4a,b.PF$_6$** (μβ = -1320 and -1640 x 10^{-48} esu, respectively) and 2-methyl-4,5-diphenylthiazolate (dpmt) in **5a,b.PF$_6$** (μβ = -1414 and -1780 x 10^{-48} esu, respectively) the absolute value of μβ was likewise not changing significantly. DFT and TD-DFT calculations provide insight into the electronic origins to explain the above trends.[34]

Throughout the series a common characteristic is observed. In all cases, the HOMO comprises a mixture of metal-based orbitals and π orbitals of the C^N ligand. Typically for

cationic Ir(III) complexes of this form, the LUMO is composed of π^* antibonding orbitals of the N^N ligand. For the complex **1b** bearing a nitro group on the 1,10-phenanthroline, the π^* antibonding orbitals of the N^N ligand intensely mix with the antibonding orbitals of NO_2. This leads to the lowering of the energy of 1,10-phenanthroline orbitals resulting in a significant reduction of the HOMO-LUMO gap compared to **1d** containing an electron-donating NMe_2 substituent on the ancillary ligand. Here, the NLO response is mainly controlled by metal-to-ligand charge transfer (MLCT) processes. The opposite trend can be observed for complexes **4a** and **4b**. The HOMO level in **4a** and **4b** is notably more stabilised compared to **1a** and **1b**. The metal character in the HOMO is significantly lower due to the extended π conjugation in the C^N ligand. The LUMO level is, however, not notably affected. This lowers the metal character in the HOMO. The contribution of MLCT will be reduced, which has detrimental effects on the absolute value of μβ.

The roles of the counterion and the concentration

Although, the cationic Ir(III) complex is the photoactive unit, the nature of the counterion plays an important role in ion-pairing, which can have a significant effect on the NLO response. Secondly, the concentration of the complex also affects the absolute value of μβ in dichloromethane. For example, the complexes **1a**, **1b**, **2a**, **2b**, **2c**, **2d**, and **5a** (see Table **4** and Figure **20**) exhibit notably higher absolute values for μβ in dichloromethane at lower concentrations and when the counterion is $C_{12}H_{25}SO_3^-$ instead of PF_6^-.[34] These results prompted a more detailed investigations on how the counterion and concentration may have an effect on the ion pairing. To probe this, complex **1b** that gave a high absolute μβ value in its PF_6^- salt was investigated in detail, with different counterions and at various concentrations (Table **5**). In dichloromethane solution, the absolute value for μβ of **1b**.$\mathbf{PF_6}$ almost doubles when decreasing the concentration from 10^{-3} M to 10^{-4} M reaching a value of ca. -5000 x 10^{-48} esu.

The response is not notably as sensitive to concentration with the counterion $C_{12}H_{25}SO_3^-$ as well as I^- but falls drastically off compared to the PF_6^- analogue.

Table **5**: EFISH μβ values x 10^{-48} esu of **1b** in CH_2Cl_2

Y^-	**C = 1 x 10^{-3} M**	**C = 5 x 10^{-4} M**	**C = 1 x 10^{-4} M**
PF_6^-[a]	-2230	-2390	-4990
$C_{12}H_{25}SO_3^-$	-1430	-1520	-1770
I^-	-1160	-1370	-1370

[a] at concentrations of 3 x 10^{-4} M and 5 x 10^{-5} M values of -3670 x 10^{-30} and -5012 x 10^{-48} esu were obtained, respectively.[34]

The results suggest that the absolute value of μβ is both counterion- and concentration-dependant. High absolute μβ can be obtained with a weakly interacting anion (e.g. PF_6^-) at low concentration (1 x 10^{-4} M in dichloromethane). With a counterion like $C_{12}H_{25}SO_3^-$ or I^- that form tight ion-pairs, μβ is, however, lower and does not vary significantly by concentration. This μβ trend is partially due to the perturbation of the LUMO π* levels of the N^N ligand by the counterion. The correlation between the μβ value and dilution shows that the effect of concentration is a factor that must be taken into careful consideration.[34]

Cationic 2,2-bipyridine Ir(III) complexes

This work on cationic Ir(III) complexes was extended to a series of complexes containing a substituted styryl bipyridine ligand. As mentioned above 4,4'-π-conjugated-[2,2']-bipyridines are suitable precursors for dipolar and octupolar metal complexes. It has been shown that modification of the π-linker and the donor groups generate tuneable chromophores and luminophores.[29,30,153,158] A series of Ir(III) complexes $[Ir(ppy\text{-}R')_2(bpy\text{-}CH{=}CH\text{-}Ar\text{-}R]Y$, **6**[56] (**a**, Ar-R = C_6H_4-NEt_2 and R' = Me; **b**, Ar-R = C_6H_4-O-Oct and R' = Me; **c**, Ar-R = C_6H_4-NO_2 and R' = C_6H_{13}; **d**, Ar-R = 2-methylthiophenyl-Me) and **6e** (with R' = Me and 4,4'-dimethyl-2,2-bipyridine as ancillary ligand), containing extended Ar-vinyl π-systems on the bipyridine ligand, have been studied (Figure **21**). The effect of the substituent R and the aryl-

substituent on the nonlinear optical (NLO) properties was investigated. The main absorption bands of complexes **6a-6e** are summarised in Table **6**.

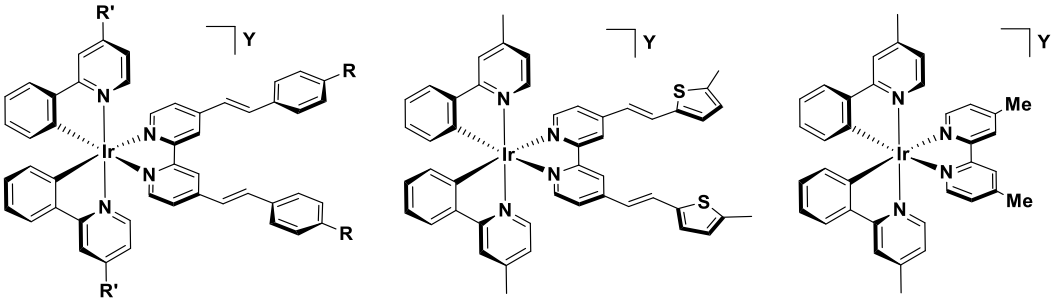

R = NEt_2, R' = Me, **6a**
R = OOct, R' = Me, **6b**
R = NO_2, R' = C_6H_{13} **6c**

6d **6e**

Figure **21**: Cationic Ir(III) complexes of the form [Ir(substituted-ppy)$_2$(substituted-bpy)]Y (Y = PF_6^- or $C_{12}H_{25}SO_3^-$, Table **6**)

Table **6**: Electronic Absorption Spectral Data (298 K) and EFISH μβ in dichloromethane

Complex	**Y$^-$**	**Absorption maxima / nm, [ε / M^{-1} cm^{-1}]**	**μβ$_{1.907EFISH}$[a] x 10^{-48} / esu**
6a	PF_6^-	390 [35 500], 473 [59 000]	-2770
6a	$C_{12}H_{25}SO_3^-$	-	-1015
6b	PF_6^-	360sh [47 600], 388 [51 400]	-2430
6c	PF_6^-	338 [52 500], 390 [32 200]	-2770
6c	$C_{12}H_{25}SO_3^-$	-	-1250
6d	PF_6^-	360 [39 200], 406 [48 400]	-2386
6e	PF_6^-	300sh [21 000], 345sh [12 000], 380 [6900], 420 [4100], 470 [1000]	-1420

[a] By working at 10^{-3} M; the error of EFISH measurements is ±10%, with incident wavelength of 1.907 μm

The assignments of the bands have been confirmed by time-dependent-DFT (TD-DFT) calculations.[56] The absorption spectra of **6a-6d** show high intense bands above 300 nm, decreasing in energy in the order **6c** > **6b** > **6d** > **6a**. Typically for cationic Ir(III) complexes, mixed CT transition bands that are very low in intensity (at least around one order of magnitude

with respect to the bands observed in this study) are found in this region of the spectrum.[40,41] These bands are assigned to ligand centred (LC) transitions within the styryl-substituted bipyridine ancillary ligand and are likely to obscure the low intensity bands like MLCT and LLCT transitions.[56] However, there is evidence in the spectra of **6b-6d** of weak bands tailing out at 420 – 650 nm, which is typically observed in cationic Ir(III) complexes and can be assigned to triplet metal-to-ligand CT (^{3}MLCT) states.[40,41] Complex **6a** bearing the diethylamino groups generates a low-energy band at 473 nm, that can be attributed to a mixture of IL transitions located on the bpy-styryl-NEt_2 ligand, with major contributions of ILCT character. The assignments of the bands have been confirmed by time-dependent-DFT (TD-DFT) calculations.[56]

To determine the second-order NLO response of the complexes **6a-6e** (with $Y^- = PF_6^-$) and **6a,6c** (with $Y^- = C_{12}H_{25}SO_3^-$) the EFISH technique was used, the values of which are reported in Table **6**. Complex **6e** bearing only methyl groups on the ancillary ligand was used in this study as a reference and exhibits an absolute μβ value of -1420 10^{-48} esu, which is almost unchanged compared to complex **1a** (Figure **20**, Table **4**) bearing a substituted 1,10-phenanthroline. This suggests that the use of either bpy or phen-based ancillary ligands and the methyl group on the ppy ligand in Ir(III) complexes of the form $[Ir(C\hat{}N)_2(N\hat{}N)]^+$ do not have significant changes in the second-order NLO responses. However, the increase of π delocalisation of the 2,2'-bipyridine with styryl substituents results in an increase of the absolute μβ value. The PF_6^- salts of complexes **6a-6d** all show higher values than **1b**. Similarly, to the previous studies (see above), the values increase as concentration decreases, and the response is weaker with $C_{12}H_{25}SO_3^-$ as the counterion.

In the case of a strong electron-withdrawing group (e.g. NO_2) the EFISH quadratic hyperpolarizability is the sum of negative contributions, originating mainly from LLCT/MLCT excitations where the phenanthroline acts as acceptor. When R is an electron-donating group

(e.g. NMe_2) there are counteracting positive (ILCT) and negative (LL'CT/MLCT) contributions to the EFISH quadratic hyperpolarizability, with the latter controlling the negative sign of the final value.[34,55] Thus, the second-order NLO response does not depend on the nature of the substituent on the styryl itself. These cationic complexes display large second-order (NLO) responses, which can be increased by extended Ar-vinyl π-systems and are controlled by the nature of the counterion as well as the concentration.

In summary, the above studies show that metal complexes are excellent NLO chromophores, including cyclometalated cationic and neutral Ir(III) complexes. The second order NLO response measured by the EFISH technique of cationic complexes has been fully investigated for the first time. These studies demonstrate that different features control the EFISH second-order NLO response: 1) design modification of the ligands (N^N as well as C^N ligands), 2) strength of the ion pairing mediated through the nature of the counterion, the solvent and the concentration. DFT and TD-DFT calculations indicate that μβ is mainly controlled by MLCT transitions involving the C^N ligand in the role as the donor and the π^* system of the ancillary ligand as the acceptor. It has been shown that the absolute μβ value can be increased by weak ion pairing and diluting in dichloromethane. This point is confirmed since the absolute μβ value strongly depends on the nature of the counterion. A loose ion pair increases the dipole moment μ and might also enhance the second-order NLO response.

This short overview illustrates the excellent nonlinear optical properties of transition metal complexes exhibiting large second-order NLO responses. Many organometallic compounds with various ligands (such as substituted bipyridines, phenanthrolines, acetylacetones or phenylpyridines) have been investigated as chromophores. It has been demonstrated that the metal centre of an organometallic complex is a flexible tool to tune the second-order NLO response. Through modulation of the electronic nature of the metal and the coordination sphere through the number and nature of the ligands the NLO response can be

enhanced significantly. The metal can also act as a bridge enabling electron-transfer processes between different coordination sites such as in cyclometalated chromophores. Theoretical approaches through TD-DFT calculations help to understand better the electronic origin of the NLO activity of transition metal complexes. The theoretical understanding may allow the design of new and efficient NLO chromophores based on metal complexes. The second-order NLO response increases by the extent of charge transfer, and therefore, the nature of the donor-acceptor pair becomes crucial. To optimise the push-pull system, strong acceptors and donors need to be introduced that are efficiently connected through a conjugation bridge. Among the various examples, neutral and cationic heteroleptic cyclometalated Iridium(III) complexes show excellent NLO properties.

In cationic Ir(III) complexes of the form $[Ir(C\text{^}N)_2(N\text{^}N)]^+$ the NLO response is controlled by charge transfer processes in which the cyclometalating ligand acts as the donor and the ancillary ligand as the acceptor and the metal centre as the conjugation bridge. This class of complexes is worthwhile to be further explored to understand better the involved electronic processes.

This overview of transition metal complexes demonstrates the high potential of Ir(III) complexes as NLO chromophores. Part of this present work deals with the nonlinear optical properties of cationic Ir(III) complexes of the form $[Ir(C\text{^}N)_2(N\text{^}N)]PF_6$ bearing π-delocalised triphenyl amino (TPA) substituents on the cyclometalating ligands. The effect of the position of the TPA moiety (meta or para to the Ir-$C_{C\text{^}N}$ bond or the Ir-$N_{C\text{^}N}$ bond) on the NLO properties has also been discussed within this study. The EFISH technique,[166,167] working with a non-resonant incident wavelength of 1907 nm, is used to determine the NLO response.

Chapter 2

Impact of the Use of Sterically Congested Cyclometalated Ligands on the Optoelectronic Properties and Device Performances in Light-Emitting Electrochemical Cells of Cationic Iridium(III) Complexes

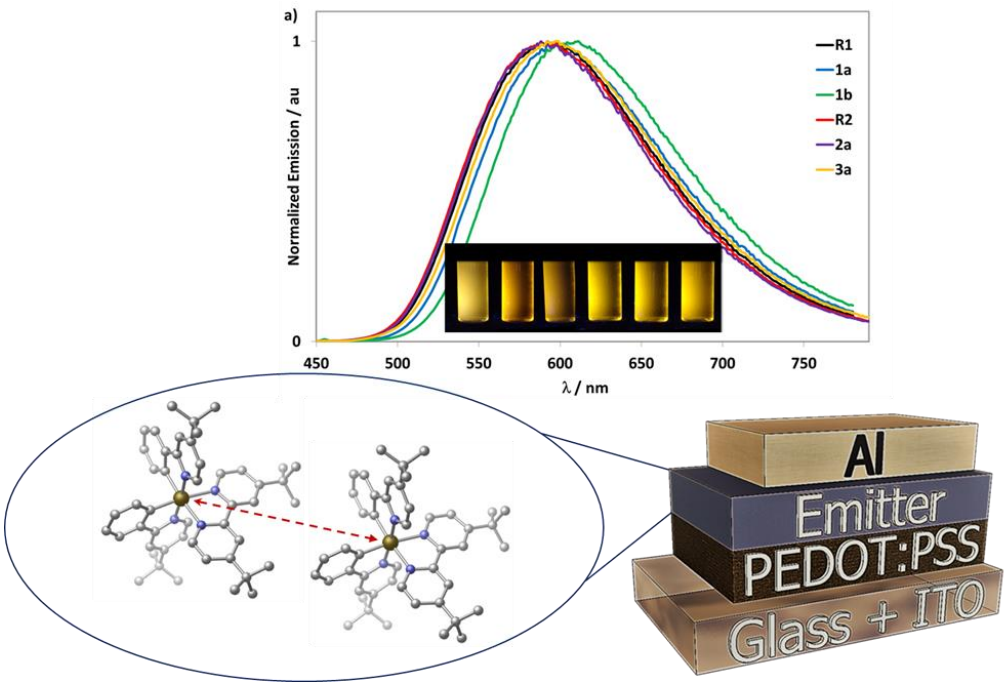

Cover picture: TOC graphic of publication arising from this chapter

Introduction

Chapter 1 gave an overview of the remarkable photophysical properties of Iridium(III) complexes,[88,168,169] that make them the go-to emitter class in solid-state electroluminescence (EL) devices, such as organic light-emitting diodes (OLEDs)[170] and in light-emitting electrochemical cells (LEECs).[21,171–173] LEECs possess a much simpler design, with fewer layers, compared to OLEDs, as they typically employ an ionic emissive material that is dually responsible for charge mobility and the emission of light within the device. The most popular and widely studied class of emitters for LEECs is the heteroleptic cationic Ir(III) complex of the form $[Ir(C\hat{}N)_2(N\hat{}N)]PF_6$ (C^N is a cyclometalating ligand, N^N is a diimine ancillary ligand).

Unlike in OLEDs where the emissive compound is present in only small concentrations as a dopant within a higher bandgap host, in LEECs the emissive layer is frequently composed either of a homogenous layer of emitter molecules or the emitter is the major component within the layer. As a consequence, one issue that can limit device performance is excited state self-quenching during device operation.[125] In Chapter 1 a strategy to circumvent this issue was discussed. Decorating the complexes with bulky, hydrophobic substituents that serve to increase the intermolecular distance while simultaneously hindering the disadvantageous attack of small molecules can hinder excited state self-quenching during device operation.[6] Figure **22** shows representative literature examples of iridium complexes bearing bulky substituents that have been used as emitters in light-emitting electrochemical cells.

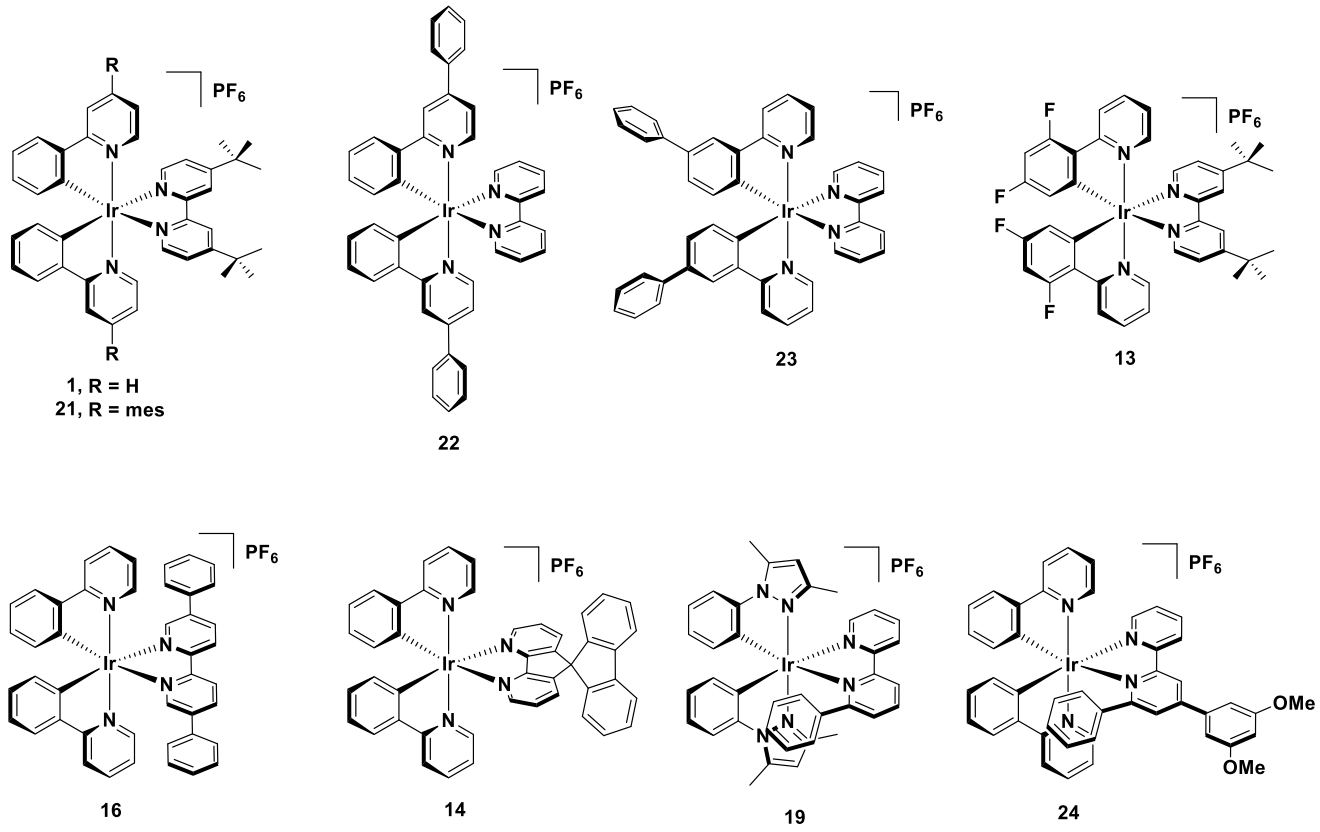

Figure **22**: Ir(III) complexes bearing bulky substituents.

In Chapter 1 the use of sterically congested N^N ancillary ligands in cationic iridium complexes was discussed. A successful molecular design that was applied to charge-neutral Ir(III) complexes for OLEDs was the incorporation of mesityl substituents at the C(4) position of the pyridyl ring of the ppy ligands in [Ir(dFmesppy)$_2$(pic)] (dFmesppyH = 2-(4,6-Difluorophenyl)-4-(mesityl)-pyridine and pic = picolinate). An increase in the photoluminescence quantum yield, Φ_{PL}, was observed, which also translated into enhanced external quantum efficiencies of the OLED devices compared to that employing the well-known [Ir(dFppy)$_2$(pic)], FIrpic (dFppyH = 2-(4,6-difluorophenyl)pyridine).[174] The enhancement in EQE compared to the FIrpic-based devices was attributed to reduced concentration quenching and increased solubility in organic solvents and therefore better dispersion during the fabrication of the solution-processed device. Notably, the mesityl group adopts an orthogonal conformation relative to the pyridine ring, resulting in a disruption of the

conjugation between these two aryl groups, minimizing the impact on the emission energy. Such an approach has been applied to cationic iridium complexes by us, where we have observed an enhancement of solution- and solid-state Φ_{PL} compared to the non-decorated analogue complex.[73,175,176]

A comparison of **1** and **21** of the form $[Ir(C\hat{}N)_2(dtBubpy)]PF_6$ (where C^N is ppy or mesppy for **1** and **21**, respectively and d*t*Bubpy is 4,4´-di-*tert*-butyl-2,2´-bipyridine) reveals the impact of the mesityl group on the photophysical properties in cationic complexes.[175] In CH_2Cl_2, the same emission maximum (λ_{PL} = 577 nm) is observed for both complexes while the Φ_{PL} is moderately enhanced for the mesitylated complex (Φ_{PL} = 35 and 40% for **1** and **21**, respectively). The LEECs fabricated with **1**,[175] showed a lifetime of $t_{1/2}$ = >1300 h and an EQE of 2.5%. Surprisingly and in contrast to the above-mentioned impact of the mesityl group, for LEECs based on **21** there was a reduction in the device lifetime ($t_{1/2}$ = 0.6 h) and EQE (1.4%) upon incorporation of the mesityl groups on the C^N ligands. However, with **21** faster response times could be achieved in devices compared to those based on **1**, as the mesityl groups induce a more efficient electronic communication and recombination within the device, which results in faster turn-on times. The related complex $[Ir(dPhPy)_2(bpy)]PF_6$, **22** (where dPhPy is 2,4-diphenylpyridine and bpy is 2,2´-bipyridine) bears a phenyl group on the 4-position of the pyridine of the C^N ligand in lieu of a mesityl group and contains a bpy N^N ligand in lieu of the d*t*Bubpy ligand.[27] In CH_2Cl_2, complex **22** exhibits yellow phosphorescence (λ_{em} = 598 nm) with a Φ_{PL} of 21% . A single-layer LEEC based on **22** containing a lithium salt additive showed improved device performance compared to the unsubstituted analogue. The device with **22** displayed a short response time (t_{on} = 5 min), favourable lifetime (extrapolated lifetime calculated at 100 cd m^{-2}, $t_{1/2}L_{100}$ of 3800 h), and a peak luminance of 5500 cd m^{-2} (with t_{on} = 191 min, $t_{1/2}L_{100}$ = 4752 h and a peak luminance of 2753 cd m^{-2} for the unsubstituted analogue).

The authors ascribed the improved LEEC performance to the bulky, hydrophobic nature of the phenyl substituent, which they asserted impeded self-quenching pathways of the the Ir(III) complex. Another analogous complex is $[Ir(Phppy)_2(bpy)]PF_6$, **23** (where Phppy is 2-([1,1'-biphenyl]-3-yl)pyridine), bearing a phenyl group *trans* to the Ir-$C_{C\wedge N}$ bond. Complex **23** exhibits a yellow-orange emission with a Φ_{PL} of 13% in CH_2Cl_2. LEECs based on **23** are likewise highly stable with $t_{1/2}$ = 2800 h and also are very bright with a maximum luminance of 1024 cd m^{-2}.[177]

The use of the sterically congested the d*t*Bubpy in 13[178,179] coupled with dFppy ligands contributed to a record maximum external quantum efficiency in the LEEC of 15%,[178] significantly higher than that reported for the LEECs with 13, with EQE values ranging from 0.6 - 5.0%.[83,175,180] LEECs fabricated with 16[83] incorporating a bulky ancillary ligand (5,5´-diphenyl-2,2´-bipyridine, dpbpy) showed long device lifetimes of 110 h (LEEC operating at 4 V), particularly compared to $[Ir(ppy)_2(dtBubpy)]PF_6$, 1 (1.3 h). Using 14,[125] which contained the 4,5-diaza-9,9´-spirobifluorene ancillary ligand, resulted in LEECs with a maximum external quantum efficiencies of 7.1% at a device lifetimes of 12 h and luminance value of 52 cd m^{-2}.

Very stable LEECs have been fabricated employing emissive complexes where there is a phenyl ring positioned adjacent to one of the coordinating nitrogen atoms of the ancillary ligand as exemplified in $[Ir(dmppz)_2(pbpy)]PF_6$, **19**, (where dmppz is 3,5-dimethyl-1-phenylpyrazole and pbpy is 6-phenyl-2,2´-bipyridine).[132] The phenyl ring of the pbpy forms a face-to-face π-stacking with the pyrazole unit of the C^N ligand, which insulates the complex from adventitious attack from small molecules.[181] High stability LEECs were fabricated with the complex $[Ir(ppy)_2(Meppbpy)]PF_6$, **24**,[182] (where Meppbpy is 4-(3,5-dimethoxyphenyl)-6-phenyl-2,2'-bipyridine) with a device lifetime of over 950 h and high luminance and current efficiency (183 cd m^{-2} and 8.2 cd A^{-1}, respectively). In the majority of cases, decorating the complex with bulky, hydrophobic substituents greatly improves the stability of LEECs.

These previous findings prompted us to design a family of cationic Ir(III) complexes of the form $[Ir(C\hat{}N)_2(dtBubpy)]PF_6$ in which the sterics about the C^N ligands are systematically modified via a combination of decoration at the 4-position of the pyridine ring and/or the 3-position of the phenyl ring in order to ascertain how the steric requirements the photophysics of the complexes and the corresponding LEEC device performance (Figure **23**). Complexes **1** and **21** were included into this study to serve as references.

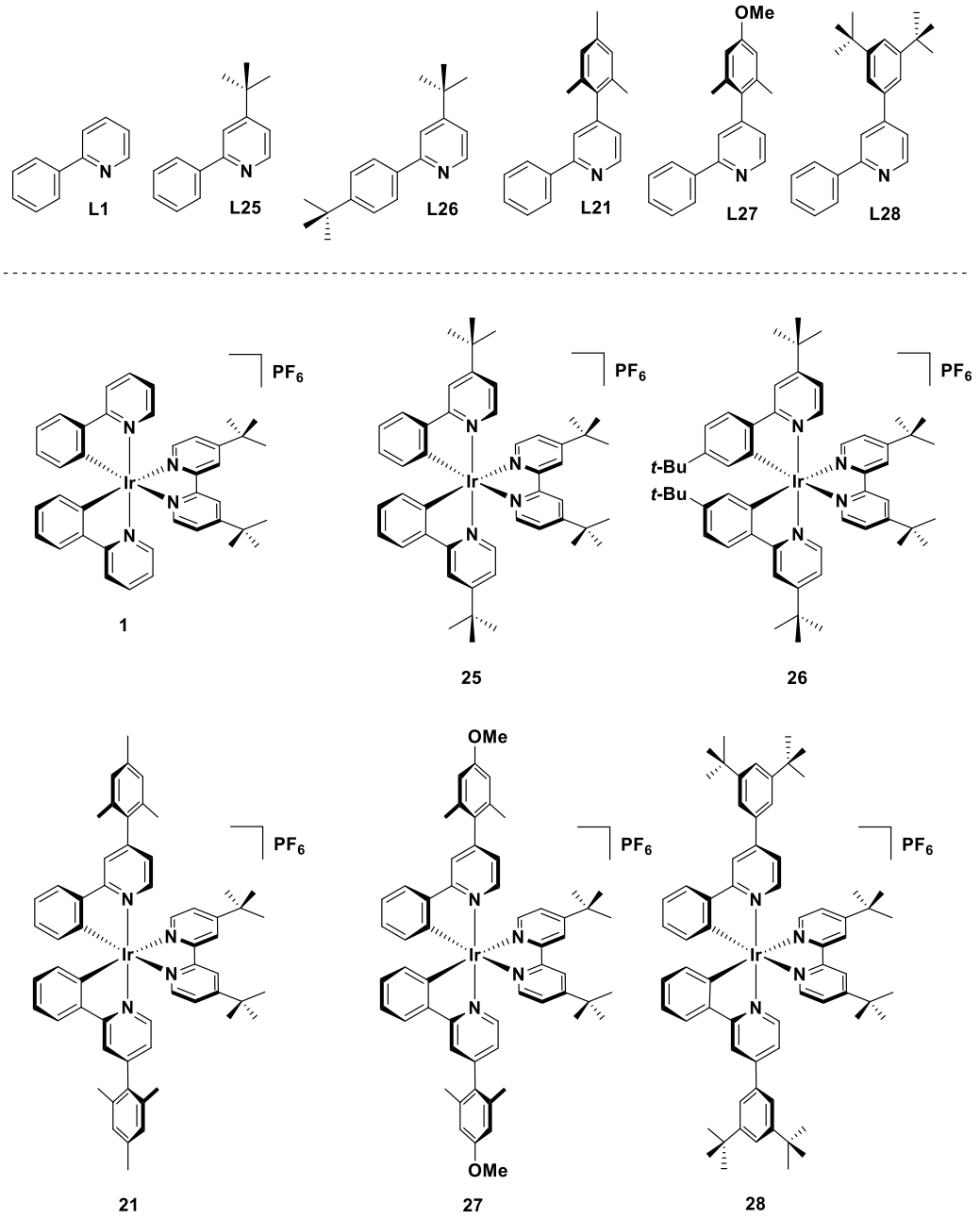

Figure **23**: Synthesised cationic Ir(III) complex bearing bulky substituents investigated in this chapter

Complexes **1**,[175,180] **26**[183] and **21**[175] have previously been reported and included into this study as a reference. **1**[175] and **21**[175] have previously been employed as emitter in LEECs.

Results and Discussion

Ligand Synthesis

The family of substituted 2-phenylpyridine (ppyH) cyclometalating C^N ligands bearing R_1 (at the 4-pyridine position) and R_2 (at the 4-phenyl position) can be divided into two classes: 4-substituted 2-phenylpyridine derivatives **L25**, **L21, L27** and **L28** [with R_1 = *tert*-butyl (*t*Bu), mesityl (mes), manisyl (man – 2,6-dimethyl,4-methoxyphenyl), and 3,5-di-*tert*-butylphenyl (d*t*Buphen), respectively, and R_2 = H)**,** and the substituted arylpyridine **L26** (where R_1 = R_2 = *tert*-butyl). The unsubstituted ppyH, **L21**, serves as a reference. (Figure **23**). Compounds **L25** and **L26** are accessible as colourless oils *via* direct C-H arylation of 4-*tert*-butylpyridine with arylboronic acid[184] in moderate yields (45 and 46%, respectively, Figure **23**), while **L1** was commercially available.

For **L21, L27** and **L28**, a two-step Suzuki-Miyaura cross-coupling strategy was adapted from 2-chloro-4-iodopyridine (Figure **24**).[11c] The mono-arylated 2-chloro-4-substituted compounds **Cl21, Cl27** and **Cl28** were isolated in excellent yields (94 – 96%) after purification by column chromatography. Key to the high yields is the use of excess $R_1B(OH)_2$, which led to easier purification of the intermediate 4-aryl-2-chloropyridines. A second Suzuki-Miyaura reaction with $PhB(OH)_2$ afforded **L21, L27** and **L28** in excellent yields (86 – 90%) (Figure **24**). The boronic acid bearing Ar_1 of **L28** [(3,5-di-*tert*-butylphenyl)boronic acid] was prepared following a modified method[185] in advance through subsequently reacting 1-bromo-3,5-di-*tert*-

butylbenzene with *n*-BuLi at -78 °C and triisopropyl borate followed by an acid treatment with 1M HCl. The obtained product was used without further purification.

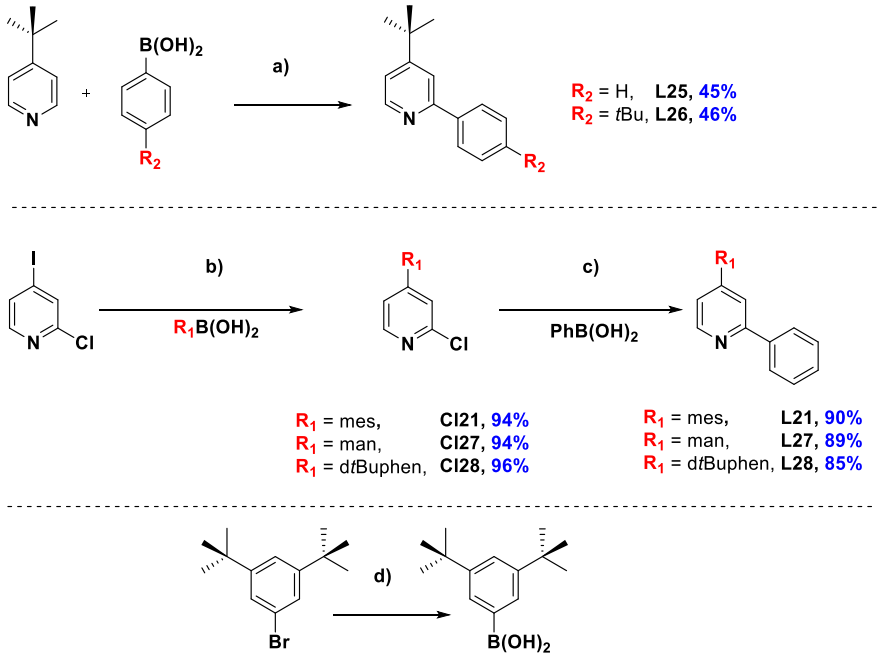

Figure **24**: Two step synthesis of the ligands. a) *tert*-butylpyridine, phenylboronic acid, trifluoroacetic acid, $AgNO_3$, $K_2S_2O_8$, CH_2Cl_2/H_2O (1/4), r.t., 6 h; b) $Ar_1B(OH)_2$, K_2CO_3 $Pd(PPh_3)_4$, dioxane/H_2O (4/1), 95 °C, 3 d; c) phenylboronic acid, K_2CO_3, $Pd(PPh_3)_4$, dioxane/H_2O (4/1), 95 °C, 18 h; d) i) 1-bromo-3,5-di-*tert*-butylbenzene, *n*-BuLi, THF, N_2, -80 °C, 45 min; ii) triisopropyl borate, -80 °C – r.t., 18 h; iii) aqueous HCl (1 M).

Complex Synthesis

Complexes **1, 21, 25 – 28** were obtained in a two-step synthesis following standard reaction conditions (Figure **25**).[65] In the first step, the $[Ir(C\text{^}N)_2Cl]_2$ dimer were quantitatively obtained as a yellow solid by treatment of the corresponding ligand (**L1, L21, L25 – L28**) with $IrCl_3.6H_2O$ in a 3:1 mixture of 2-ethoxyethanol/H_2O (125 °C, 24 h). This dimer was then cleaved with d*t*Bubpy.

The corresponding $[Ir(C^N)_2Cl]_2$ was reacted with d*t*Bubpy in a 1:1 mixture of CH_2Cl_2/MeOH (40 °C, 18 h) to afford the cationic Ir(III) complexes as their chloride salts. After column chromatography on silica (eluent: 5% MeOH in CH_2Cl_2) followed by an ion exchange with aqueous NH_4PF_6, complexes **1, 21, 25 – 28** were isolated in good yields (75% – 92%) as their hexafluorophosphate salts.

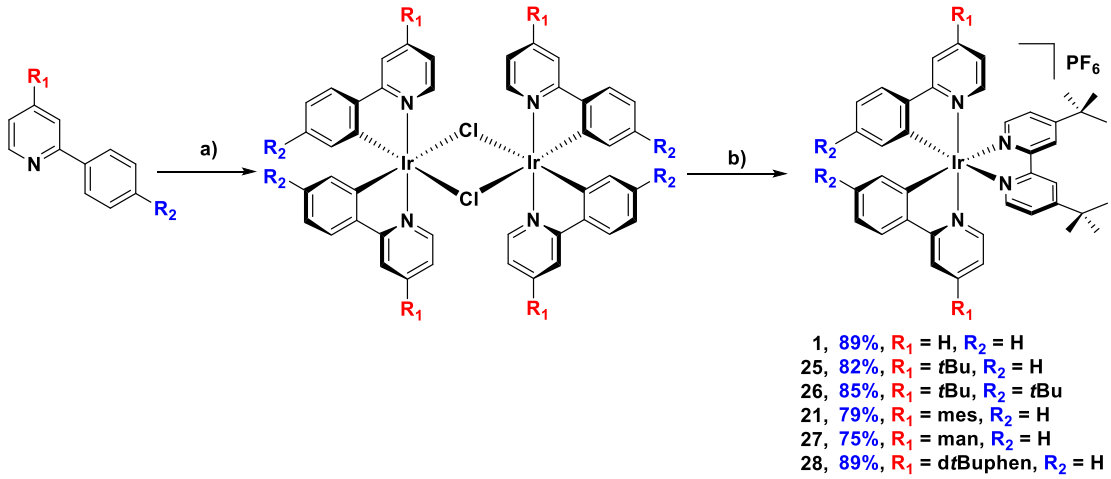

Figure **25**: Procedure for the synthesis of target complexes (**1, 21, 25 – 28**) in this study. a) $IrCl_3 \cdot 6H_2O$, corresponding C^N ligand, 2-ethoxyethanol/water (3:1), 125 °C, 24 h; b) 1. Corresponding Ir(III) dimer, d*t*Bubpy, MeOH/CH_2Cl_2 (1:1), 40 °C, 18 h. 2. aq. NH_4PF_6.

All complexes were characterized by ^1H, ^{13}C and ^{31}P NMR spectroscopy in $CDCl_3$, HR-ESI mass spectrometry and elemental analysis. The ^1H-NMR spectra show the expected number of resonances displaying symmetrical C^N ligands and characteristic singlets at around 8.38 ppm integrating as two hydrogens arising from the 3 position of the bpy based ancillary ligand and the singlet at around 1.43 ppm integrating as 18 hydrogens originating from the *tert*-butyl groups of the ancillary ligand. The Ir-C resonances in the ^{13}C NMR spectra appear typically at around 135 – 130 ppm. The ^{31}P-NMR spectra show the characteristic heptet at -144 ppm for the PF_6^- counterion. The characterised ion in HR-ESI mass spectrometry corresponds to the cationic species without a counterion. In elemental analysis, the characterising species includes the counterion.

Crystal Structures

Single crystals of sufficient quality of **25, 26, 21** and **27** were grown from CH_2Cl_2/Et_2O. The determined space groups are $P\bar{1}$ (for **25**) and $P2_1$ (for **26, 21** and **26**). The crystal structure of **21** has been previously reported.[175] The crystal structures are presented in Figure **26** selected crystallographic parameters are summarised in Table **7**.

In all complexes the pyridine rings of the C^N ligands are disposed in a mutually *trans* arrangement while the cyclometalating carbon atoms are *trans* to the nitrogen atoms of the N^N ligand, presenting an analogous binding mode to the majority of cationic Ir(III) complexes. Bond lengths and bond angles are as expected for this class of iridium complex.[85,86,175,176,186–188]

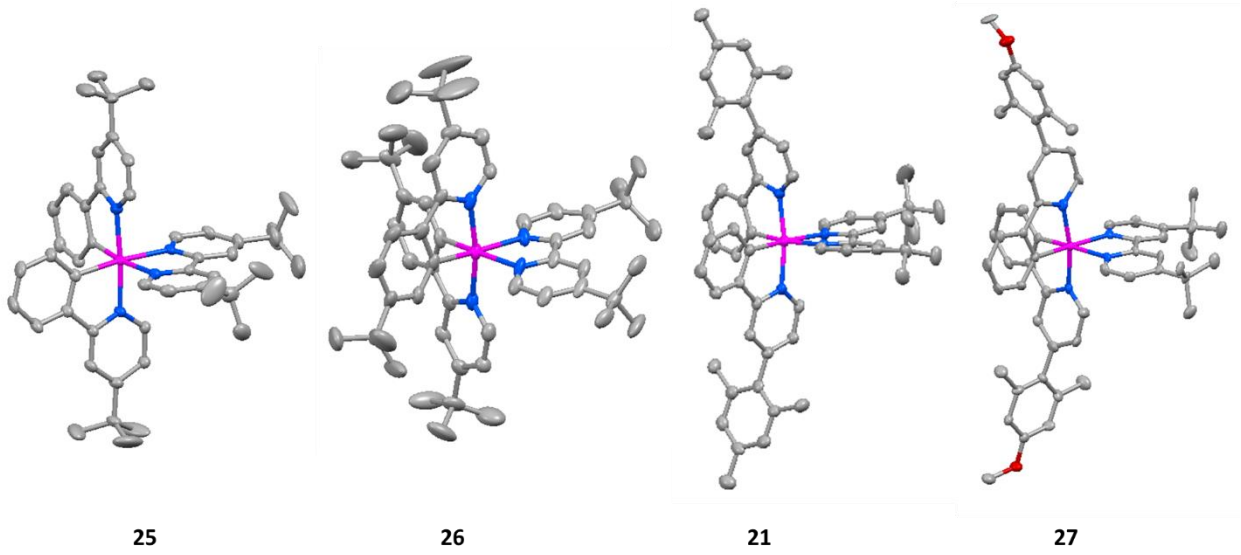

Figure **26**: Representation of the crystal structures **25**, **26**, **21** and **27**. The hydrogen atoms, solvent molecules, minor disorder as well as the counter ion PF_6^- are omitted for clarity. C = light grey, N = blue, O = red and Ir = magenta.

Table **7**: Selected crystallographic parameters for complexes **25, 26, 21** and **27**.

	Bond Length / Å			**Bond Angle / °**		**Torsion Angle / °[a]**
	Ir-C_{C^N}	Ir-N_{C^N}	Ir-N_{N^N}	C-Ir-N_{C^N}	N-Ir-N	
25	2.007(6)	2.051(3)	2.127(5)	80.0(2)	75.9(2)	-
	2.010(7)	2.049(4)	2.140(5)	79.7(2)		
26	2.036(7)	2.059(8)	2.143(8)	80.2(3)	76.3(3)	-
	2.034(8)	2.060(8)	2.141(5)	80.4(3)		
21	2.024(9)	2.051(6)	2.124(9)	80.6(3)	75.9(2)	78.32
	2.015(7)	2.044(6)	2.142(6)	80.5(3)		88.70
27	2.06(1)	2.05(1)	2.14(1)	80.9(5)	75.7(4)	81.58
	2.01(1)	2.05(4)	2.148(9)	80.2(5)		89.97

[a] Angle of torsion between plane of the pyridine of the C^N ligands and the phenyl bound to the pyridine.

The torsion angles between the R_1 and the pyridyl unit of the two C^N ligands in **21** and **27** range from 77(1)° to 81(2)°, respectively, similar to those previously reported for arylated C^N ligands in charged complexes,[73] but are notably larger to those found in **23** for which an average torsion angle of 26° between the phenyl and the pyridine rings of the C^N ligands is observed.[17]

The steric hindrance provided by the substituents on the C^N ligands modulates the inter-nuclear distance in the solid state. The shortest inter-iridium distance between adjacent complexes is approximately 7.24 Å in **25** and increases significantly in **21** and **27** (~10.55 and 10.97 Å, respectively). A similar Ir···Ir distance is observed when both R_1 and R_2 are *tert*-butyl groups in **26** (~10.86 Å). In **1** the distance 7.897 Å is notably higher The inter-iridium distance for **22**[27] is with 8.87 Å, which is significantly shorter compare to the distance in **21** and **25**.

Cyclic Voltammetry

The electrochemical behaviour of **1, 21, 25 – 28** was investigated by cyclic voltammetry (CV) in deaerated MeCN solution at 298 K with *n*-Bu_4NPF_6 as the supporting electrolyte at a scan rate of 100 mV s^{-1} and using ferrocene/ferrocenium (Fc/Fc^+) as the internal reference. All potentials are referenced with respect to SCE (Fc/Fc^+ = 0.38 V in MeCN).[189] The cyclic voltammograms are shown in Figure **27** and the electrochemistry data are given in Table **8**. Each complex displays a quasi-reversible oxidation wave attributed to an admixture of the Ir(III)/Ir(IV) redox couple and contributions from the aryl ring of C^N ligands.[187] The addition of *tert*-butyl groups in **25** and **26** renders the oxidation somewhat less reversible compared to the reference **1** though the oxidation potentials remain essentially unchanged, despite the inductively electron-donating character of this substituent.

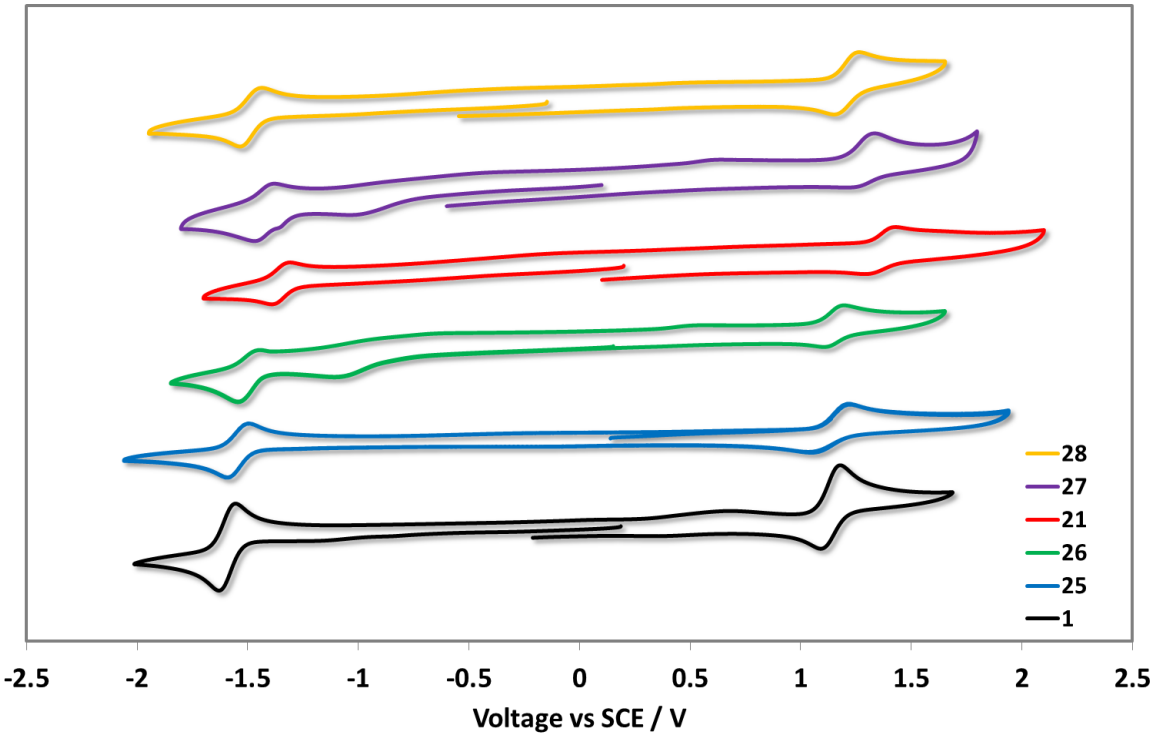

Figure **27**: Cyclic voltammograms of **1, 21, 25 – 28** measured in a deaerated MeCN with 0.1 M *n*Bu_4NPF_6 at a scan rate of 100 mV s^{-1} in the positive scan direction and Fc/Fc^+ as the internal standard and are referenced with respect to SCE (Fc/Fc^+ = 0.38 V in MeCN).

Upon addition of aryl groups to the 4-pyridyl position, the oxidation waves are anodically shifted, a reflection of the moderately strong electron-withdrawing character of these groups. This anodic shifting is somewhat mitigated by the conjugation present between the 3,5-di-*tert*-butylphenyl substituent and the coordinating pyridine in **28**, while in **21** and **27** the aryl groups are oriented perpendicular as a function of the *o*-methyl substituents on the arene; the magnitude of the inductively electron-withdrawing character of the aryl group is further modulated by the presence of the more strongly electron-donating methoxy substituent in **27** (E_{ox} = 1.29 V) compared to the mesityl substituent in **21** (E_{ox} = 1.35 V). In CH_2Cl_2, it has been previously shown that **21** possesses an oxidation wave at 1.14 V.[190]

Table **8**. Electrochemical data and orbital energies for complexes **1, 21, 25 – 28**.

	Electrochemistry[a]						
	$E_{1/2}^{ox}$ **/ V**	ΔE_p **/ mV**	$E_{1/2}^{red}$ **/ V**	ΔE_p **/ mV**	ΔE_{redox}[b] **/ V**	E_{HOMO}[c] **/ eV**	E_{LUMO}[c] **/ eV**
1	1.13	90	-1.61	70	-5.93	-3.20	2.74
25	1.13	180	-1.54	100	-5.93	-3.26	2.67
26	1.15	70	-1.52	90	-5.95	-3.29	2.67
21	1.35	90	-1.37	80	-6.16	-3.43	2.72
27	1.29	90	-1.43	70	-6.10	-3.38	2.72
28	1.21	100	-1.49	120	-6.01	-3.37	2.70

[a] in degassed MeCN at a scan rate of 100 mV s^{-1} with Fc/Fc^+ as internal reference, and referenced with respect to SCE (Fc/Fc^+ = 0.38 V in MeCN);[189] [b] ΔE_{redox} is the difference (V) between first oxidation and first reduction potentials; [c] $E_{HOMO/LUMO}$ = -[$E^{ox/red}$ vs Fc/Fc^+ + 4.8] eV;[191]

Thus, the solvent has an unusually large influence on the oxidation potential of this complex. All complexes display a single quasi-reversible reduction wave within the electrochemical window of MeCN. Despite the consistent assignment that the reduction is

localized on the ancillary d*t*Bubpy ligand, the reduction potential varies over a moderately large range from -1.37 V for **21** to -1.61 V for **1**. In CH_2Cl_2 **21** exhibits an irreversible reduction at -1.15 V.[190] The most inductively electron-withdrawing substituents on the C^N ligands induce the greatest shift to less negative potentials in **21** and **27**, this via modulation of the electron density on the iridium centre. Analogous to that observed for the oxidation potentials, this effect is counteracted by the increased conjugation present in **28**. Surprisingly, despite the electron-donating nature of the *tert*-butyl groups, the reduction potential is not further cathodically shifted, but instead is -1.54 V for **25** and -1.52 V for **26**.

Photophysical properties

The absorption spectra for **1, 21, 25 – 28** recorded in aerated MeCN at 298 K are shown in Figure **28** and the data summarized in Table **9**.

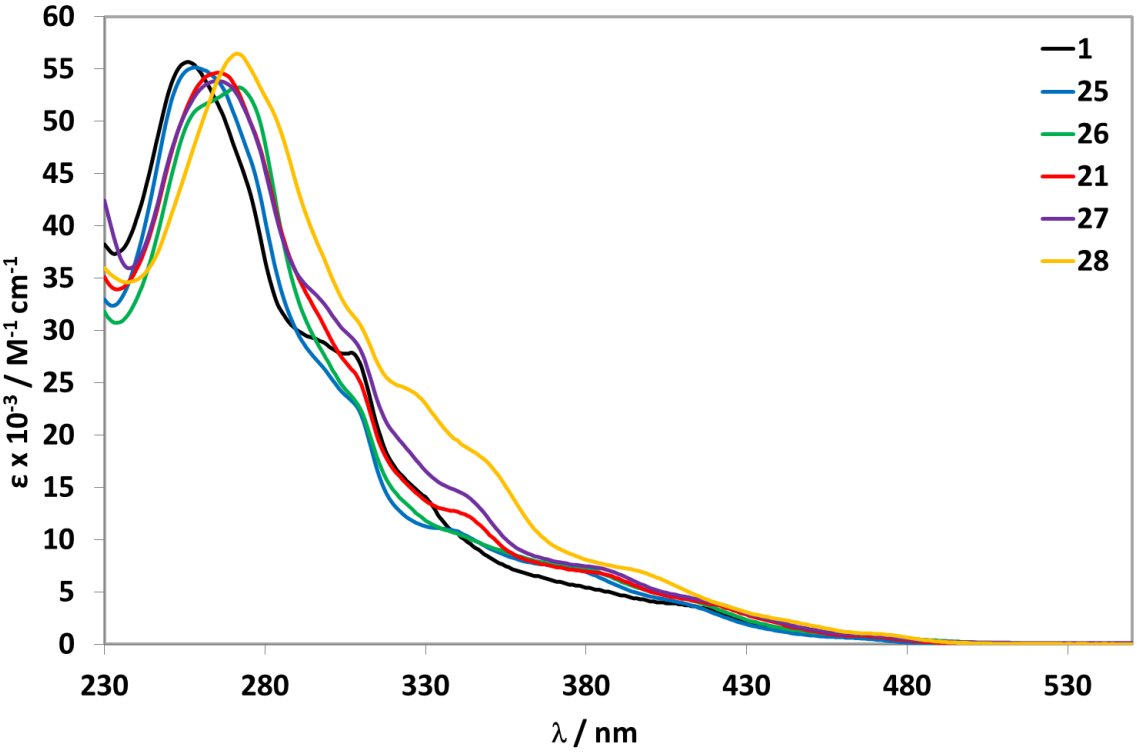

Figure **28**: UV-Vis absorption spectra of **1, 21, 25 – 28** recorded at 298 K in aerated acetonitrile.

The acquired absorption data for **1**,[187] **26**[183] and **21**[190] match those previously reported. For all complexes, the electronic absorption spectra show intense (ε on the order of 5.5×10^4

M^{-1} cm^{-1}) high-energy absorption bands between 255 – 272 nm that are assigned to $^1\pi$–π^* ligand-centred (^{1}LC) transitions on both the C^N and N^N ligands. Complex **28** shows a modest red-shift of the ^{1}LC band with respect to **1** that is due to capacity for the 3,5-di-*tert*-butylphenyl ring to conjugate with the pyridine ring while a similar red-shifting of this band is observed for **26**, also due to LUMO stabilization of the C^N ligands. The profiles of the low-energy bands are found to be insensitive to the nature of the substituents on the C^N ligands.

Table **9**. UV-vis absorption data of the investigated Ir(III) complexes

	λ_{abs} / nm [ε / $M^{-1}cm^{-1}$][a]
1	255 [56 853], 286 [34 421], 309 [28 841],
	329 [16 244], 408 [3 757], 466 [663]
25	258 [55 115], 309 [22 533], 323 [12 442],
	340 [10 817], 374 [7 397], 410 [3 976], 448 [941]
26	272 [53 237], 310 [22 321], 329 [12 109], 377 [7477],
	397 [5 357], 410 [4 408], 429 [2 455], 470 [837]
21	267 [54 540], 310 [24 832], 331 [13 504],
	344 [12 153], 385 [6 752], 419 [3 826], 471 [675]
27	265 [53 788], 296 [33 350], 310 [28 049],
	343 [14 195], 385 [7 269], 419 [4 019], 467 [855]
28	272 [56 407], 311 [29 765], 327 [23 945],
	350 [17 179], 402 [6 388], 439 [2 460], 472 [993]

[a] recorded in aerated MeCN at 298 K.

All complexes show moderately intense absorption bands in the range of 300 to 340 nm, which are assigned to spin-allowed mixed metal-to-ligand charge transfer transitions (^{1}MLCT) and ligand-to-ligand charge transfer transitions (^{1}LLCT). Weaker absorption bands are observed beyond 400 nm, tailing to 490 nm. These bands are assigned to spin-forbidden (^{3}MLCT/^{3}LLCT) transitions.[187]

The photoluminescence (PL) spectra of **1, 21, 25 – 28** in degassed MeCN are shown in Figure **29a** and the data are summarized in Table **10**. Upon excitation at 400 nm, all complexes show moderately intense yellow emission over a narrow range between 588 to 611 nm and show a broad and unstructured profile, indicative of an emission with mixed CT character. An increasing red-shifting of the emission spectra is observed upon addition of *tert*-butyl groups (5 nm, 140 cm^{-1} for **1** to **25** and 19 nm, 530 cm^{-1} for **25** to **26**). This trend is also observed for the LC band in the absorption spectra and correlates as well with a slightly smaller ΔE_{redox} gaps. The effect of the addition of electron-donating groups on the phenyl rings of the C^N ligands has been shown to induce a red-shift of the emission.[192]

A red-shift of 6 nm (169 cm^{-1}) in the emission spectrum is also observed for **28** compared to **1**, which is due to stabilization of the triplet state as a result of the increased conjugation within the C^N ligands. Given the orthogonal conformation of the aryl groups in **21** and **27** there is expectedly no significant change in the emission energy, consistent with previous studies.[175,176] This design approach permits a modulation of the bulkiness of the resulting complexes without substantially affecting the emission energy. The photoluminescence quantum yield (Φ_{PL}) values in deaerated MeCN solution at room temperature of all complexes are approximately in the same range (Φ_{PL} ~ 24 – 30%), except for **26**, which shows a lower Φ_{PL} of 11%. These values are comparable to those obtained for related cationic iridium complexes emitting in the same energy region.[128,175,176,180]

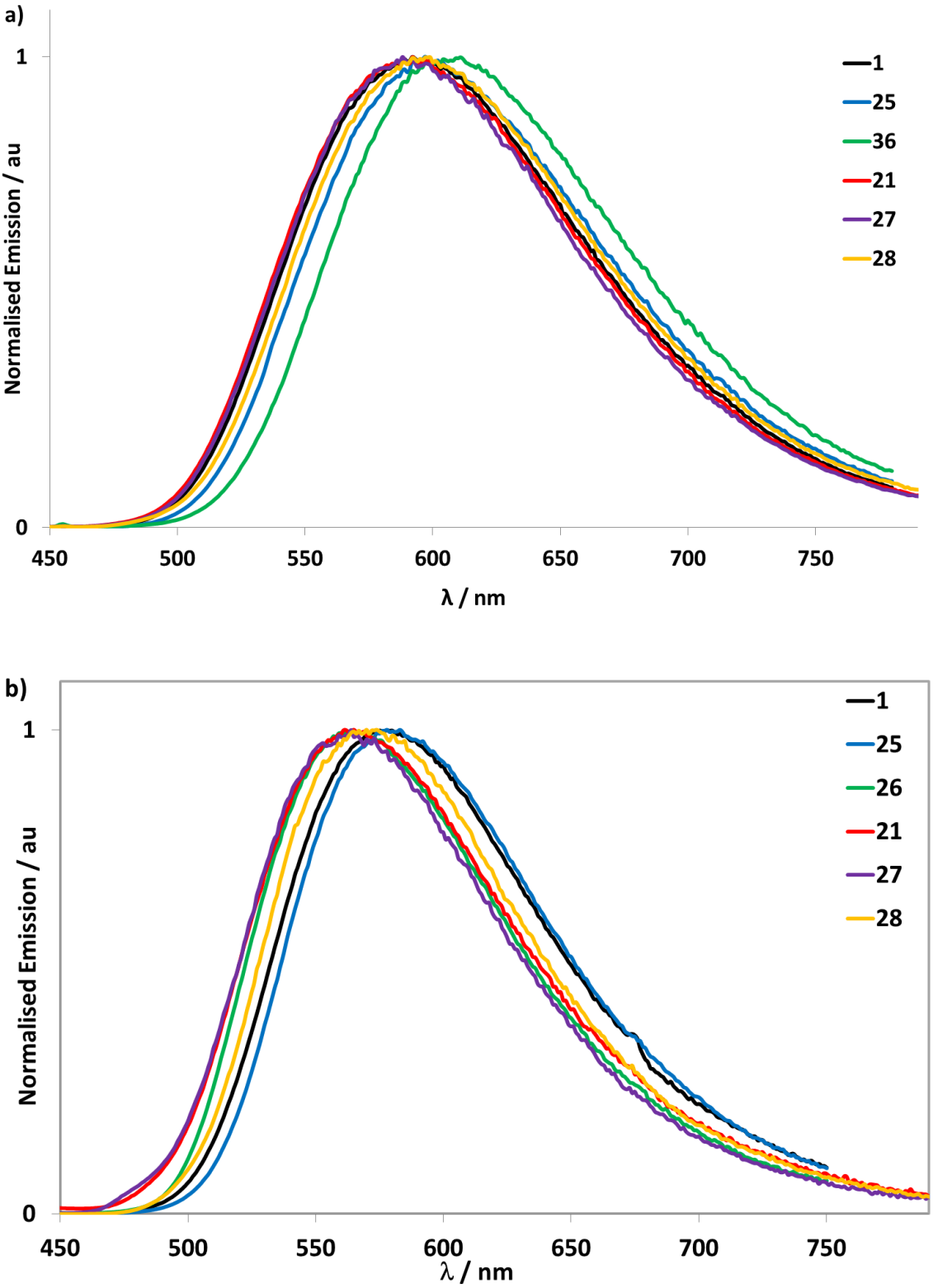

Figure **29**: Emission spectra of **1, 21, 25 – 28**. a) recorded at 298 K in deaerated MeCN, with λ_{exc} = 400 nm, b) dropcast thin films at 298 K, with λ_{exc} = 400 nm.

Table **10.** Photophysical data of **1, 21, 25 – 28**.

	MeCN					Neat film		
	λ_{PL}[a] / nm	τ_{PL}[a] / ns	Φ_{PL}[a,b] / %	k_r[c] × 10^{-5} / s^{-1}	k_{nr}[d] × 10^{-5} / s^{-1}	λ_{PL}[e] / nm	τ_{PL}[e,f] / ns	Φ_{PL}[g] / %
1	592	581	30	3.61	13.60	578	5 (11.7%) 29 (30.6%) 180 (57.7%)	23
25	597	497	24	3.42	16.70	579	9 (13.7%) 40 (33.2%) 200 (53.1%)	40
26	611	250	11	3.20	36.80	565	8 (7.7%) 43 (23.4%) 225 (68.9%)	27
21	592	643	27	2.95	12.60	565	10 (16.4%) 42 (37.5%) 171 (46.1%)	15
27	588	623	28	3.05	13.00	564	10 (14.4%) 42 (35.5%) 179 (50.1%)	16
28	598	501	24	3.39	16.57	570	8 (13.8%) 36 (34.3%) 183 (51.9%)	40

[a] recorded at 298 K in deaerated MeCN, with λ_{exc} = 400 nm; [b] $[Ru(bpy)_3]Cl_2 \cdot 6H_2O$ was used as reference (Φ_{PL} = 0.04 in 10^{-5} M aerated H_2O);[24] [c] $k_r = \tau_{PL} / \Phi_{PL}$. [d] $k_{nr} = 1/(\tau_{PL} - k_r) = [(1 - \Phi_{PL})/ \tau_{PL}]$; [e] values refer to dropcast thin films at 298 K, with λ_{exc} = 400 nm; [f] with contribution of component in parentheses; [g] values refer to dropcast thin films at 298 K using an integration sphere under an N_2 environment.

The emission decays are monoexponential and the lifetimes (τ_{PL}) are all in the sub-microsecond regime. The addition of increasing numbers of *tert*-butyl groups on the C^N ligands result in a decrease in the τ_{PL} values, a consequence of an increase in the non-radiative decay rate, k_{nr}. Over the series of substituted complexes, the radiative decay rate, k_r, remains similar, though lower than the reference complex **1**.

In order to emulate the emissive layer in the LEEC devices, neat films of **1, 21, 25 – 28** were prepared by drop-casting a dichloromethane solution onto a glass substrate, which was then dried under vacuum. The emission spectra of the neat films were recorded at 298 K open to air (Figure **29b** and Table **10**). All complexes display blue-shifted, broad and unstructured

emission spectra (~ 30 nm, 820 cm^{-1}) compared to the MeCN solution measurements. Multi-exponential emission decay kinetics are observed for all complexes, with the longest component in each being significantly shorter than the τ_{PL} found in MeCN solution. Photoluminescence quantum yields for **1**, **21** and **27**, remain essentially unchanged compared to solution measurements while those of **25**, **26** and **28** are enhanced, a function of reduced non-radiative decay in the neat film.

LEEC Devices

LEECs were prepared and the electroluminescence properties of complexes **1, 21, 25 – 26** are shown in Figure **30a-c** while Figure **30d** describes the device architecture. The LEEC data are summarized in Table **11**. The devices were built on ITO-patterned substrates, where a poly(3,4-ethylenedioxythiophene):poly(styrenesulfonate) (PEDOT:PSS) layer (80 nm) was deposited by spin-coating. The LEEC active layer (100 nm) was deposited from MeCN by spin-coating, which contained the emitting complex mixed with the ionic liquid (IL) 1-butyl-3-methylimidazolium hexafluorophosphate, [Bmim][PF_6], in a 4:1 molar ratio (complex:IL). Aluminium was evaporated as a top contact electrode.

For simplicity, the LEECs are referred as **D1**, **D21** and **D25** to **D26** containing complex **1, 21, 25 – 26**. LEECs were characterized by applying a bias and monitoring the emitted light over time. Unlike LEECs measured at constant voltage (DC), pulsed-current LEECs show faster response and improved device lifetime.[26] The devices were characterized under an inert atmosphere by applying an average pulsed current (1 kHz, 50% duty cycle) of 100 A m^{-2}.

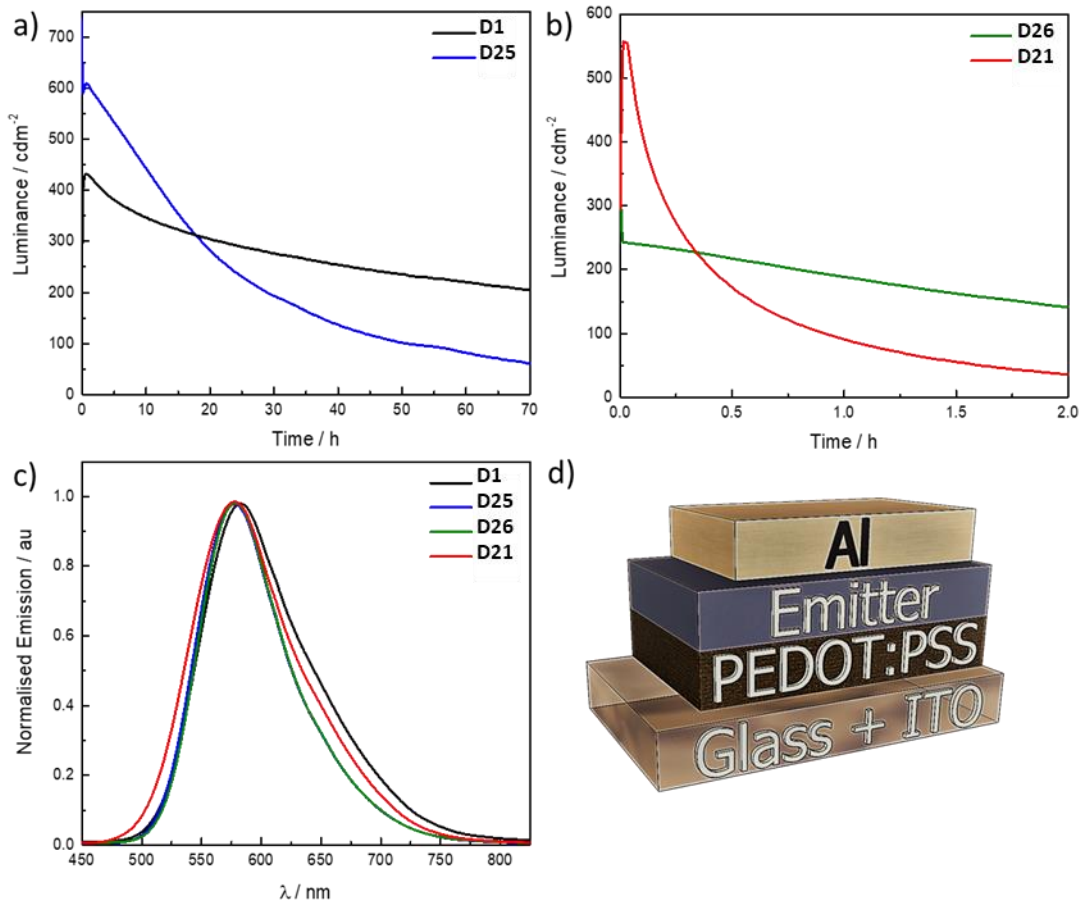

Figure **30**: Device performance of the LEEC. Luminance versus time (**D1** and **D25** in a) and **D26** and **D21** in b)) operated with a pulsed current of 100 A m^{-2} (1KHz, 50% duty cycle and block wave). c) Electroluminescence spectrum. d) LEEC architecture.

The yellow electroluminescence of the devices consists on one peaks centred at 582 nm for **D1** and 577 – 578nm for **D25**, **D26** and **D21** (see Figure **30c**). The electroluminescence spectra are narrower than the thin film photoluminescence spectra. The solubility of the **D27** and **D28** was poor (<15 mg mL^{-1}) in both MeCN and CH_2Cl_2, which led to poor morphology quality of the spin-coated films and devices with high leakage currents. Even if the solution is filtered (200 nm porous size), the saturated solutions form grains during the solvent evaporation by spin-coating, which was confirmed by optical microscopy.

Table **11**: Device performance of the LEEC: ITO/PEDOT:PSS/Complex:[Bmim][PF_6]/Al operated with a pulsed current of 100 A m^{-2} (1KHz, 50% duty cycle and block wave).

Device	**Lum_{max} / cd m^{-2}**	**t_{max} / s**	**$t_{1/2}$ / h**	**Efficacy / cd A^{-1}**	**PE / lm W^{-1}**	**EQE / %**	**λ_{EL} / nm**
D1	432	2400	62	4.3	2.3	1.8	582
D25	737	25	14	7.4	3.7	2.6	577
D26	353	<5	1.3	3.4	1.4	1.2	578
D21	557	54	0.3	5.6	2.1	2	578

[a] Maximum luminance; [b] Time to reach maximum luminance; [c] Time to reach one-half of the maximum luminance; [d] Maximum efficacy; [e] Maximum power efficiency; [f]Maximum external quantum efficiency; [g]Wavelength emission in electroluminescence.

The LEECs **D1, D21, D25 – D26** exhibit instantaneous luminance that increases rapidly leading to short turn-on time (t_{on}) of less than one minute, which is defined as the time to reach the maximum luminance, except **D1** where t_{on} is 2400 s. The devices are bright, with maximum luminance values in the same order of magnitude, between 350 and 750 cd m^{-2} across all devices. The devices are moderately efficient, with a maximum efficacy of 7.4 cd A^{-1} in the case of **D25**. Lower efficiencies are achieved for **D26**, **D1** and **D21**, following the trend in the photoluminescence quantum yield of the thin film. However, the LEECs differ in terms of their stability, defined as time to reach half of the maximum luminance. **D1** has a lifetime above 62 hours, which makes it the most stable device within this study, maintaining almost constant the luminance over the time about 300 cd m^{-2}. **D25** has a higher luminance (737 cd m^{-2}) although it is achieved only during few seconds and then proceeds to drop to ~600 cd m^{-2}, lasting for only 14 h. **D26** and **D21** present low stabilities. Initially **D26** displays luminance values around 350 cd m^{-2} but is stable for 1.3 h. **D21** shows higher turn-on luminance (~550 cd m^{-2}) however, the emission drops fast and the $t_{1/2}$ only 0.3 h.

Conclusions

In summary, we successfully synthesized and characterized a series of cationic Ir(III) complexes of the form $[Ir(C\hat{}N)_2(d\textit{t}Bubpy)]PF_6$ incorporating bulky substituents on the C^N ligand in order to develop new emissive materials for light-emitting electrochemical cells. The syntheses are straightforward allowing the introduction of *tert*-butyl, mesityl, manisyl, and 3,5-di-*tert*-butylphenyl groups into the C^N ligand. This systematic study revealed that the solubility of the complexes in standard organic solvents increased. At high concentrations (>15 mg mL^{-1}) complexes **27** and **28** however did not show good solubility in MeCN and CH_2Cl_2. All complexes have been structurally characterised and the single crystal structure determinations of complexes **25**, **26**, **21** and **27** confirm that by increasing the sterical congestion of the substituent the inter-nuclear distance between adjacent complexes increased in the solid state.

All complexes show bright yellow luminescence in MeCN, with moderate photoluminescence quantum yields. The yellow phosphorescence of the parent complex **1** is retained, due to a twisted conformation of the bulky aromatic substituents (in **21**, **27** and **28**) as they do not extend the π-conjugated system of the C^N ligand. Neat film photoluminescence quantum yields of up to 40% could be obtained. Complexes **1**, **25**, **26** and **21** were successfully employed in LEECs, showing yellow luminescence with moderate external quantum efficiencies.

Chapter 3

An investigation on the second-order nonlinear optical response of cationic bipyridine or phenanthroline iridium(III) complexes bearing two cyclometalated 2-phenylpyridines with a triphenylamine substituent.

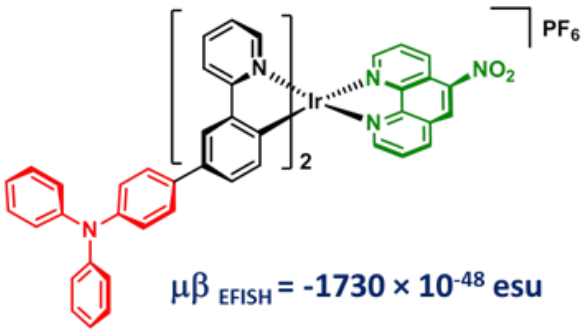

Cover picture: TOC graphic of publication arising from this chapter

Introduction

Chapter 1 gave an outline to second-order nonlinear optics (NLO), and how and why molecular structures with NLO properties are useful as materials acting as building blocks for application in optical communications, optical data processing and storage, or optoelectronic devices.[143,193] In particular, coordination compounds are of great interest because they provide additional flexibility, when compared to organic compounds, due to the presence of charge-transfer transitions between a combination of the metal and the ligands, typically at low energy and of high intensity. These conditions can induce large NLO responses and can be tuned by the nature, oxidation state and coordination sphere of the metal centre.[28,143,153,159,161,194]

As presented in Chapter 1, cationic cyclometalated iridium(III) complexes with π-delocalised ligands such as bipyridines[56,195] or phenanthrolines[34,55,194,196] can have a large second-order NLO response. Thus, $[Ir(C\hat{}N)_2(5\text{-R-1,10-phenanthroline})]PF_6$ (C^N is a cyclometalated ligand such as ppy and R = H, Me, NMe_2, NO_2) show a large negative second-order response ($\mu\beta_{EFISH}$ ranging from -1270 to -2230 x 10^{-48} esu).[55] The highest absolute $\mu\beta_{EFISH}$ value reported within this series is that of the complex carrying the phenanthroline with the strong electron-withdrawing NO_2 group, in accordance with the increased acceptor properties of the π* antibonding orbitals of the ancillary ligand (Figure **31**).

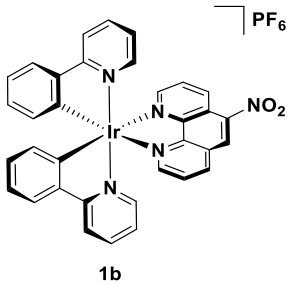

1b

Figure **31**: Cationic Ir(III) complex $[Ir(ppy)_2(5\text{-R-1,10-phenanthroline})]PF_6$ with a high absolute $\mu\beta_{EFISH}$ value reported to date ($\mu\beta_{EFISH}$ ranging -2230 x 10^{-48} esu).

An SOS-TDDFT investigation confirmed that the second-order NLO response of these Ir(III) complexes is mainly controlled by the MLCT/LLCT transitions from the HOMO located on the phenyl ring and Ir-based donor orbitals of the C^N ligands to the LUMO localised on the π* acceptor orbitals of the phenanthroline.[55] Similarly, the use of variously substituted 2,2'-bipyridines instead of 1,10-phenanthrolines leads to a high NLO response due to their analogously tuned LUMO π* acceptor orbitals.[195,197] In this kind of cationic iridium(III) complex, substitution of the ppy ligands with the more π–delocalised 2-phenylquinolinato (pq) ligands does not affect significantly the NLO properties, while a lower NLO response is observed for the related complexes with 3'-(2-pyridyl)-2,2':5',2''-terthiophene (ttpy) C^N ligands since the structure of ttpy induces a significant stabilisation of the HOMO energy, compared to the complexes bearing ppy and pq.[196] Cationic Ir(III) complexes bearing two π-delocalised cyclometalated 4-R-2-phenylpyridines (R = CH=CH-$C_6H_4NEt_2$) and a 4,4'-R',R'-2,2'-bipyridine ancillary ligand are characterised by a $\mu\beta_{EFISH}$ value (-960 x 10^{-48} esu),[195] almost twice that reported[198] for the related cyclometalated complex with acetylacetonate as the ancillary ligand, suggesting that substitution of acetylacetonate with a 2,2'-bipyridine is a valuable strategy to increase the second-order NLO properties of the Ir(III) complexes.[195]

These results prompted us to investigate the second-order NLO properties of a family of cationic Ir(III) complexes with cyclometalated 2-phenylpyridines bearing a π–delocalised triphenylamino (TPA) substituent, partnered with 4,4'-di*tert*butyl-2,2'-bipyridine (d*t*Bubpy) and 5-NO_2-1,10-phenanthroline (NO_2-phen) as the ancillary ligands. We were also curious to know the effect of the position of the TPA moiety (meta or para to Ir-C_{C^N} bond or Ir-N_{C^N} bond) on the NLO properties. The NLO responses of the prepared and characterised complexes **29 – 31** (a = d*t*Bubpy, b = NO_2-phen) (Figure **32**) were determined by the EFISH technique,[166,167] working with a non-resonant incident wavelength of 1907 nm, whose second harmonic (953 nm) is in a transparent region of the absorption spectra of the complexes.

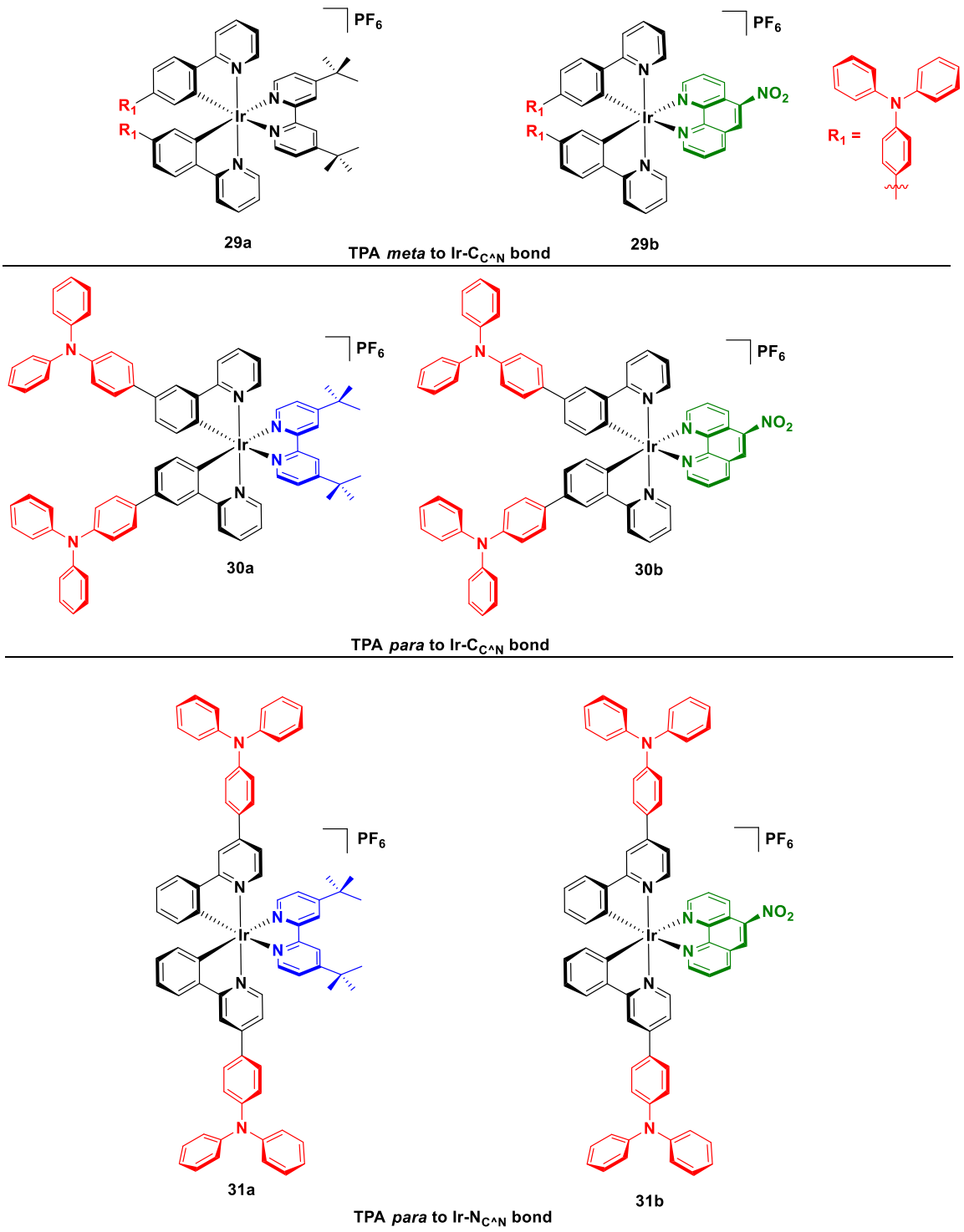

Figure **32**: Cationic Ir(III) complex investigated for their second-order nonlinear optical properties in this study

The nano-organisation of this kind of complex in a polymeric matrix was also investigated as well to obtain insight regarding the solid state response, used in technological applications.[143]

Results and Discussion

Ligand Synthesis

The ligands **L29 – L31** were obtained in a two-step synthesis (Figure **33**). In the first step the bromo-substituted phenylpyridines, 2-(4-Bromophenyl)pyridine, **29Br**,[185] 2-(3-bromophenyl)pyridine), **30Br**[185] and 4-bromo-2-phenylpyridine, **31Br**[199] were synthesised through a cross-coupling reaction following a modified previously reported method, wherein the substituted 2-bromo-pyridine was reacted with the aryl boronic acid. In the second step, the corresponding bromo-phenylpyridine (**29Br – 31Br**) was reacted with (4-(diphenylamino)phenyl)boronic acid to give the Ligands **L29 – L31**. (4-(diphenylamino)phenyl)boronic acid was prepared following a modified method[185] in advance through subsequently reacting 4-bromo-*N*,*N*-diphenylaniline with *n*-BuLi at -78 °C and triisopropyl borate followed by an acid treatment with 1M HCl. The obtained product was used without further purification.

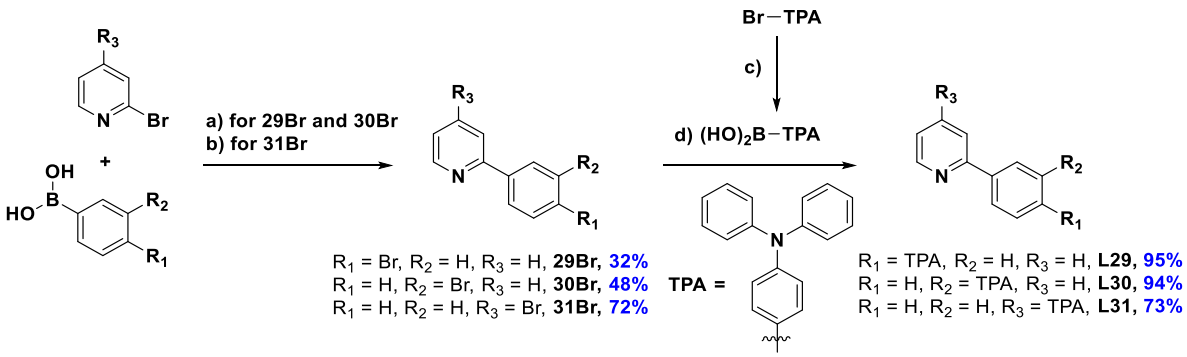

Figure **33**: Two step synthesis of the ligands **L29 – L31**. a) 2-bromo-pyridine, corresponding boronic acid, K_2CO_3, $Pd(PPh_3)_4$, 1,4-dioxane/water (4/1), N_2, 95 °C, 3 days; b) 2,4-dibromo-pyridine, phenylboronic acid, KOH, $Pd(PPh_3)_4$, 1,4-dioxane/water (4/1), N_2, 95 °C, 2 days; c) i) 4-bromo-*N*,*N*-diphenylaniline, *n*-BuLi, THF, N_2, -80 °C, 45 min; ii) triisopropyl borate, -80 °C – r.t., 18 h; iii) aqueous HCl (1 M). d) Corresponding substituted bromo-phenylpyridine, TPA-boronic acid, K_2CO_3, $Pd(PPh_3)_4$, 1,4-dioxane/water (4/1), N_2, 95 °C, 18 h.

Complex Synthesis

Complexes **29** – **31** were obtained in a two-step synthesis following standard reaction conditions (Figure **34**).[64,65] In the first step, the $[Ir(C^N)_2Cl]_2$ dimer (**Di29 – Di31**) were quantitatively obtained as a yellow solid by treatment of the corresponding ligand (**L29 – L31**) with $IrCl_3.6H_2O$ in a 3:1 mixture of 2-ethoxyethanol/H_2O (125 °C, 24 h). This dimer was then cleaved with 4,4'-di*tert*butyl-2,2'-bipyridine (d*t*Bubpy, Procedure A) or with 5-nitro-phenthroline (NO_2-phen, Procedure B).

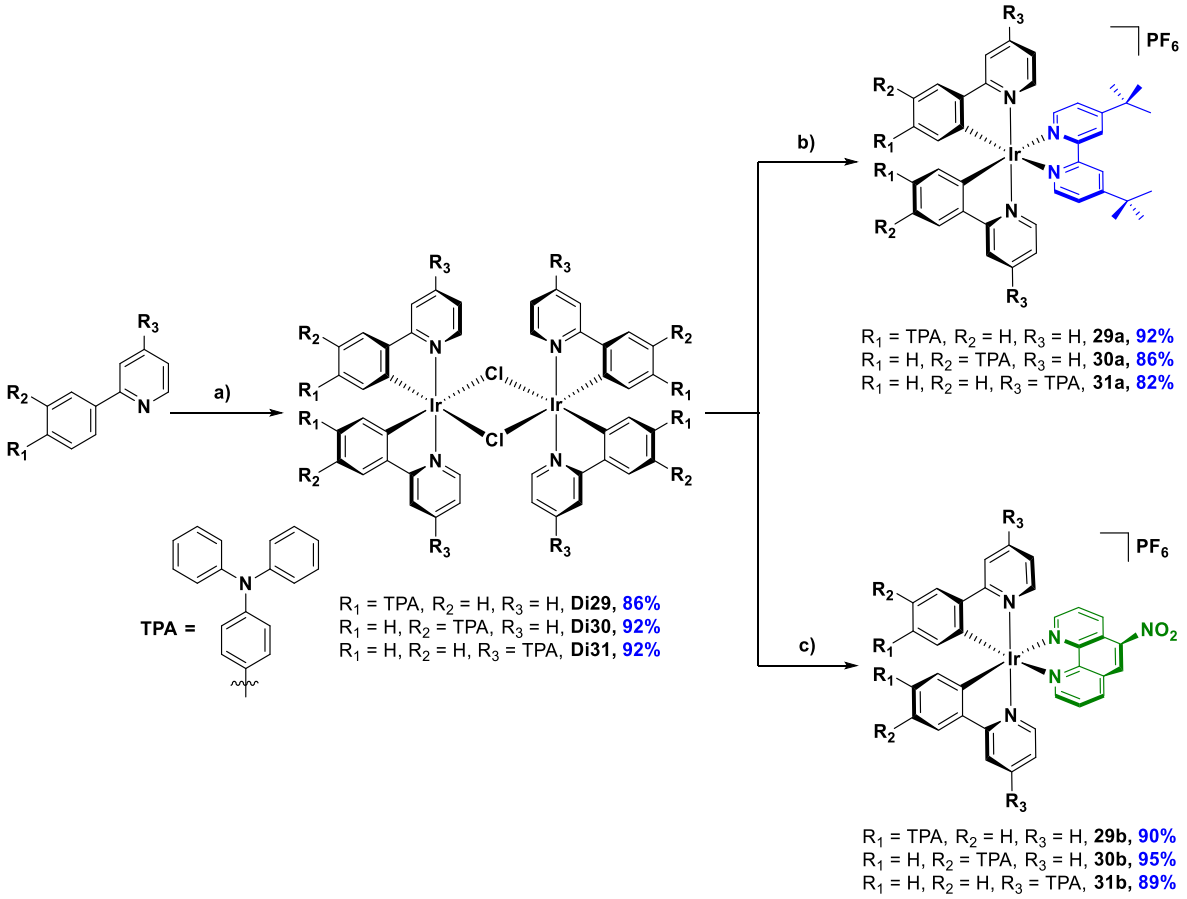

Figure **34**: Procedure for the synthesis of target complexes (**29** – **31**) in this study . a) $IrCl_3 \cdot 6H_2O$, corresponding C^N ligand, 2-ethoxyethanol/water (3:1), 125 °C, 24 h; b) 1. Corresponding Ir(III) dimer (**Di29 – Di31**), d*t*Bubpy, MeOH/CH_2Cl_2 (1:1), 40 °C, 18 h. 2. aq. NH_4PF_6; c) Corresponding Ir(III) dimer (**Di29 – Di31**), NO_2-phen, MeOH/CH_2Cl_2 (1:2), 40 °C, 6 h. 2. aq. NH_4PF_6.

In Procedure A, $[Ir(C\text{^}N)_2Cl]_2$ was reacted with d*t*Bubpy in a 1:1 mixture of CH_2Cl_2/MeOH (40 °C, 18 h) to afford the cationic Ir(III) complexes as their chloride salts. After column chromatography on silica (eluent: 5% MeOH in CH_2Cl_2) followed by an ion exchange with aqueous NH_4PF_6, complexes **29a – 31a** were isolated in excellent yield (82% – 92%) as their hexafluorophosphate salts. The General Procedure B was carried out to obtain **29b – 31b**, wherein a solution of $[Ir(C\text{^}N)_2Cl]_2$ and NO_2-phen in a 2:1 mixture of CH_2Cl_2/MeOH was heated under reflux. After 6 h, a 10-fold excess of NH_4PF_6 was added. After filtration and recrystallisation in CH_2Cl_2/Et_2O at 0 °C complexes **29b – 31b** were collected as precipitates. All complexes were characterised by ^{1}H, ^{13}C and ^{31}P NMR spectroscopy in $CDCl_3$, HR-ESI mass spectrometry and elemental analysis. The NMR spectra show the expected number of resonances characteristic for Ir(III) complexes based on ppy and bpy ligand systems. With respect to the complexes in Chapter 2 these complexes behave in a comparable way in HR-ESI mass spectrometry and elemental analysis. The structure of complexes **31a** was determined by single crystal X-ray diffraction.

Crystal Structures

Single crystals of sufficient quality were grown by slow vapor diffusion of hexane into a CH_2Cl_2 solution of complex **31a**. The structure of **31a** was determined by single-crystal X-ray diffraction (Figure **35**, Table **12**). Complex **31a** possess a distorted octahedral geometry. The pyridine rings of the C^N ligands are disposed in a mutually *trans* arrangement while the cyclometalating carbon atoms are *trans* to the nitrogen atoms of the N^N ligand, presenting an analogous binding mode to the majority of cationic Ir(III) complexes. Bond lengths and bond angles are as expected for this class of iridium complex.[85,86,175,176,186–188] The Ir-$C_{C\text{^}N}$ bonds are in average noticeably shorter [1.99(1) Å] than the Ir-$N_{N\text{^}N}$ bonds [2.035(4) Å]. These bond lengths are all similar to the bond lengths in analogous complexes. The bite angle of the N^N ligand in **31a** is 76.0(4). The bite angles of the C^N ligands are 80.0(5) and 81.3(5)°.

The torsion angles between the plane of the pyridine of the C^N ligands and the phenyl bound to the pyridine are 16.5(6)° and 41.4(3)°, respectively, which is notably different to $[Ir(dPhPy)_2(bpy)]PF_6$, **22** (where dPhPy is 2,4-diphenylpyridine and bpy is 2,2´-bipyridine)[128] with an average torsion angle of 26° between the phenyl and the pyridine of the C^N ligands.

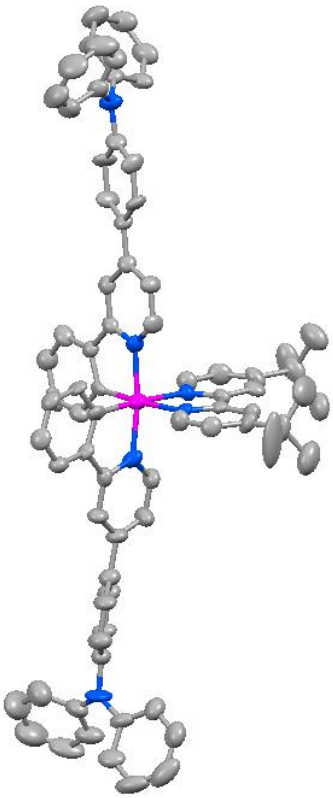

Figure **35**: Solid-state structures of complexes **31a**. Hydrogen atoms, PF_6^- counterions and solvent molecules are omitted for clarity. Colour codes for atoms are: C = light grey, N = blue and Ir = magenta.

Table **12**: Selected crystallographic parameters for complexes **31a**.

	Bond Length / Å			**Bond Angle / °**		**Torsion Angle / °[a]**
	$Ir\text{-}C_{C\wedge N}$	$Ir\text{-}N_{C\wedge N}$	$Ir\text{-}N_{N\wedge N}$	$C\text{-}Ir\text{-}N_{C\wedge N}$	N-Ir-N	
31a	1.99(1)	2.027(9)	2.13(1)	81.3(5)	76.0(4)	16.5(6)°
	1.99(1)	2.042(9)	2.13(1)	80.0(5)		41.4(3)°

[a] Angle of torsion between plane of the pyridine of the C^N ligands and the phenyl bound to the pyridine.

Photophysical properties

The UV-Vis absorption spectra of complexes **29 – 31** were recorded in $CHCl_3$ at 298 K are shown in Figure **36** and the data are summarised in Table **13**.

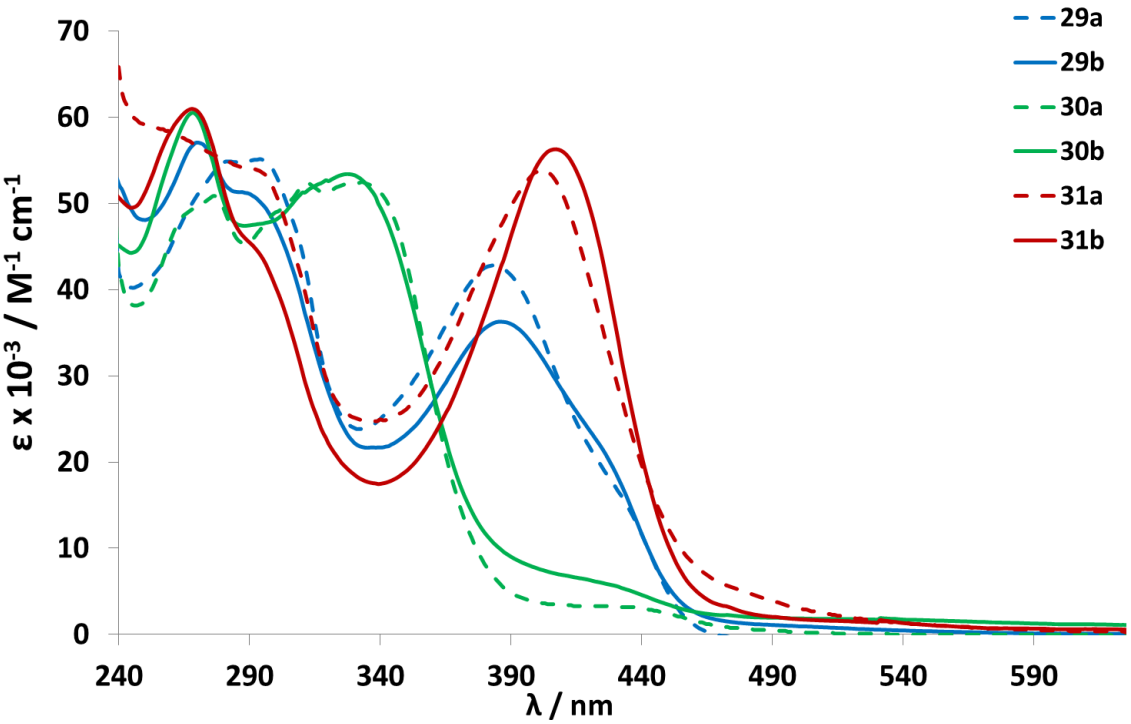

Figure **36**: UV−vis absorption spectra in $CHCl_3$ at 298 K of all complexes **29** – **31**.

All complexes show intense high-energy (ε on the order of 5.0 – 5.9 × 10^4 M^{-1} cm^{-1}) absorption bands below 300 nm, which are attributed to π–π* ligand-centred (^{1}LC) transitions localised on the N^N and C^N ligands. A distinguishing feature of each complex is the presence of an intense band at low energy, which is attributed, thanks to calculations, to an intraligand charge transfer (ILCT) from the TPA moiety to the phenyl and pyridyl rings of the C^N ligands bonded to the metal. For complexes **30a** and **30b**, this band is significantly less intense compared to the other complexes and appear as weak absorptions, the first intense absorption peaking at λ_{abs} of 333 and 327 nm (ε ~ 5.2 × 10^4 M^{-1} cm^{-1}), respectively. Complexes **29a** and **29b** show similar profiles, with the broad and intense ILCT band found at λ_{abs} at 384 and 381 nm (ε ~ 4.0 × 10^4 M^{-1} cm^{-1}), respectively.

Table **13**: Selected photophysical data for complexes **29** – **31**.

Complex	**Absorption[a] λ_{max} / nm [ε / M^{-1} cm^{-1}]**	**$\mu\beta_{EFISH}$[a,b] x 10^{-48} / esu**	**μ[c] / D**	**β_{EFISH}[d] x 10^{-30} / esu**
29a	280 [55 393], 294 [55 813], 384 [43 488], 426 [19 538]	-1260	19.8	-64
29b	270 [56 011], 293 [50 418], 381 [38 389], 426 [20 927]	-1370	14.2	-96
30a	279 [50 209], 333 [52 526], 435 [3 200]	-1560	23.6	-66
30b	271 [59 488], 327 [53 387], 435 [5 133]	-1730	19.6	-88
31a	295 [53 726], 403 [54 042]	-1880	12.0	-157
31b	273 [59 105], 413 [54 816]	-1890	6.4	-295

[a] In $CHCl_3$; [b] at 1.907 μm; estimated uncertainty in EFISH measurements is ±10%; [c] computed dipole moments of the cationic iridium complex using PCM-DFT. (d) β_{EFISH} was calculated using the computed μ value

The ILCT maxima are even further bathochromically shifted for complexes **31a** (λ_{abs} = 403 nm) and **31b** (λ_{abs} = 413 nm) and the intensity of the band enhanced with $\varepsilon \sim 5.4 \times 10^4$ M^{-1} cm^{-1}. As stated above, complexes **30a** and **30b** show much less intense ILCT bands at 435 nm (with intensities of ε = 3.2 and 5.13×10^4 M^{-1} cm^{-1}, respectively). For all complexes, weak absorption bands are observed beyond 450 nm, tailing to 590 nm. These bands are assigned to spin-forbidden transition to the triplet excited states (^{3}MLCT/^{3}LLCT).

We have used TD-DFT to provide insights into the nature of the low-lying excited-states of the different complexes. As can be seen in Figure **37**, the general shape provided by theory matches the experimental one, with in particular much less intense long-wavelength band for **30a** than for **29a** and **31a**. For **29a**, theory returns the two three significantly dipole-allowed (f>0.1) excited-states at 440, 433, and 411 nm. These three states correspond to the broad band in the visible domain experimentally.

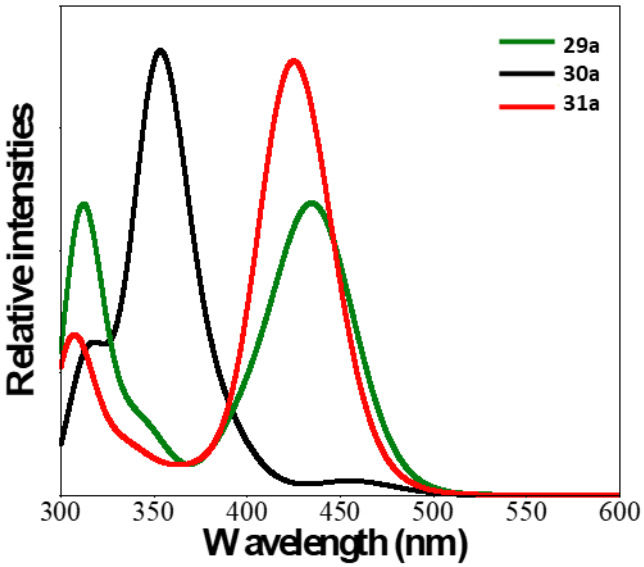

Figure **37**. Simulated UV spectra for complexes **29a**, **30a** and **31a.** Broadening Gaussian HWHM used: 0.15 eV.

In **29b**, theory returns excited-states at 449, 445, and 440 nm, slightly red shifted compared to **29a**, which is consistent with experiment. In **31a** and **31b**, TD-DFT returns a strong excited-state (f larger than 1) at 428 nm and 430 nm, other states presenting significantly smaller oscillator strength. This is rather consistent with experiment that shows slightly less broad bands in **31** than in **29**. In **30a** and **30b**, only one state significantly dipole-allowed appears above 400 nm, but the oscillator strength is much smaller than in the other dyes.

As can been seen from Table **14** and Figure **38**, the low-lying bands in **29a**, **30a** and **31a**, all correspond to HOMO to LUMO+1 transition, both being localised on the C^N ligand and displaying a very significant CT character. The LUMO, localised on the ancillary ligand is not involved in these (allowed) transitions, as HOMO to LUMO transitions present a vanishing oscillator strength due to the non-overlapping densities (Figure **38**).

Table **14**. TD-DFT data for complexes **29** – **31**: first three significantly allowed excited-states.

Compound	λ/nm	f	Dominant MO composition
29a	440	0.86	H to L+1 (0.63)
	433	0.35	H-1 to L+1 (0.61)
	411	0.25	H-1 to L+2 (0.49); H-2 to L+1 (0.48)
29b	449	0.39	H to L+2 (0.49); H to L+3 (0.37)
	445	0.57	H to L+3 (0.51); H to L+2 (0.34)
	440	0.28	H-1 to L+3 (0.59); H to L+4 (0.21)
30a	458	0.06	H to L+1 (0.61)
	386	0.35	H-4 to L (0.60); H-2 to L (0.30)
	366	0.31	H to L+5 (0.57); H-2 to L+1 (0.21)
30b	472	0.14	H-5 to L+2 (0.56); H-3 to L (0.21)
	361	0.21	H-2 to L+2 (0.33); H-16 to L (0.31)
	360	0.15	H-18 to L (0.63)
31a	428	1.52	H to L+1 (0.44); H-2 to L+1 (0.42); H-1 to L+2 (0.32)
	416	0.46	H-2 to L (0.54); H to L+1 (0.29); H-1 to L+2 (0.29)
	388	0.08	H-3 to L+1 (0.62); H-5 to L (0.22)
31b	433	0.12	H to L+3 (0.45); H-1 to L+4 (0.37); H-2 to L+3 (0.21)
	430	1.80	H to L+6 (0.56); H to L+7 (0.21)
	356	0.08	H-1 to L+3 (0.59); H to L+4 (0.21)

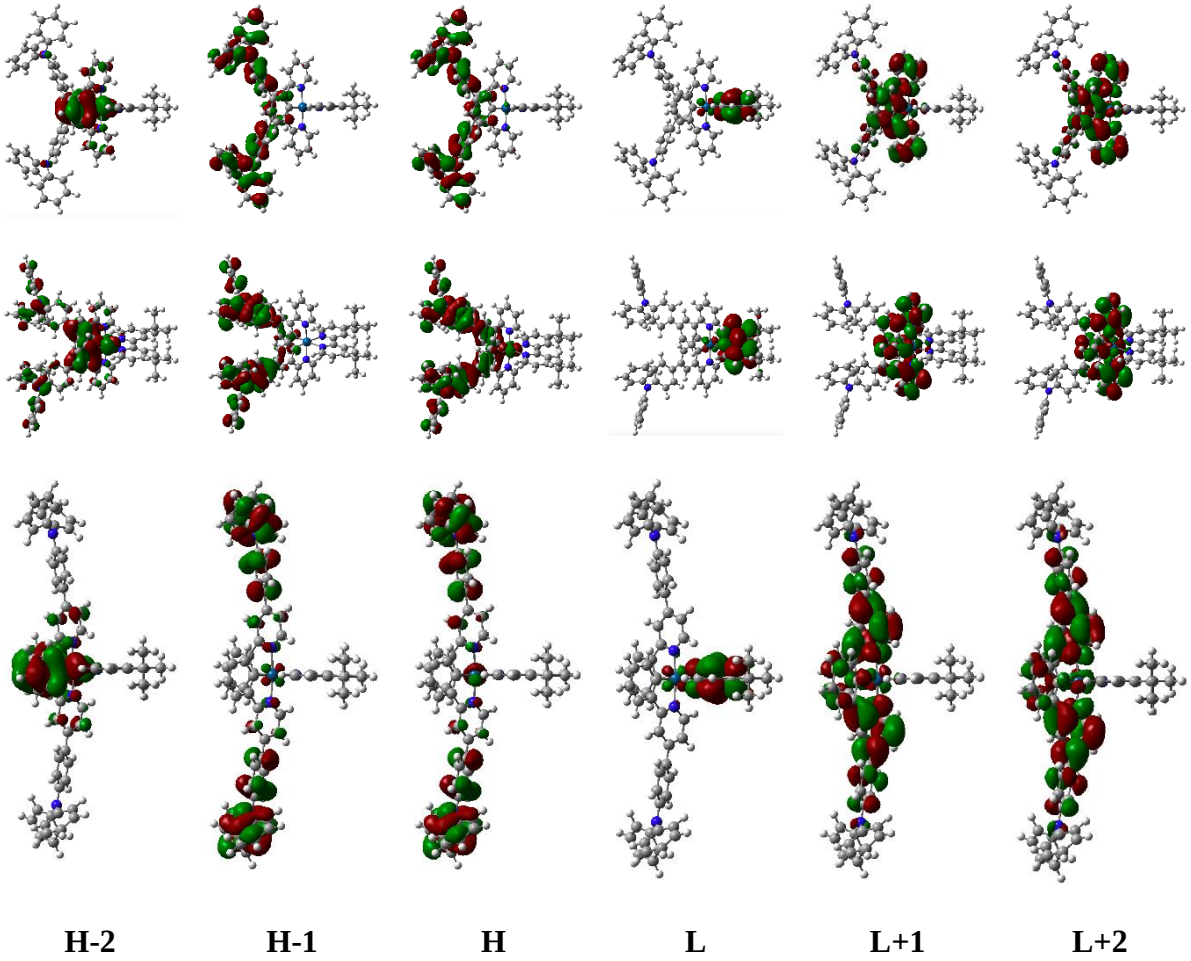

Figure **38**. Frontier orbitals of **29a** (top) **30a** (middle) and **31a** (bottom).

In solution ($CHCl_3$ and MeCN) the complexes show very weak emission, except for complex **31a**. For this reason, only the emission properties of **31a** are discussed. Figure **39** shows the normalised photoluminescence (PL) spectrum of **31a** in degassed MeCN and the data are summarised in Table **15**.

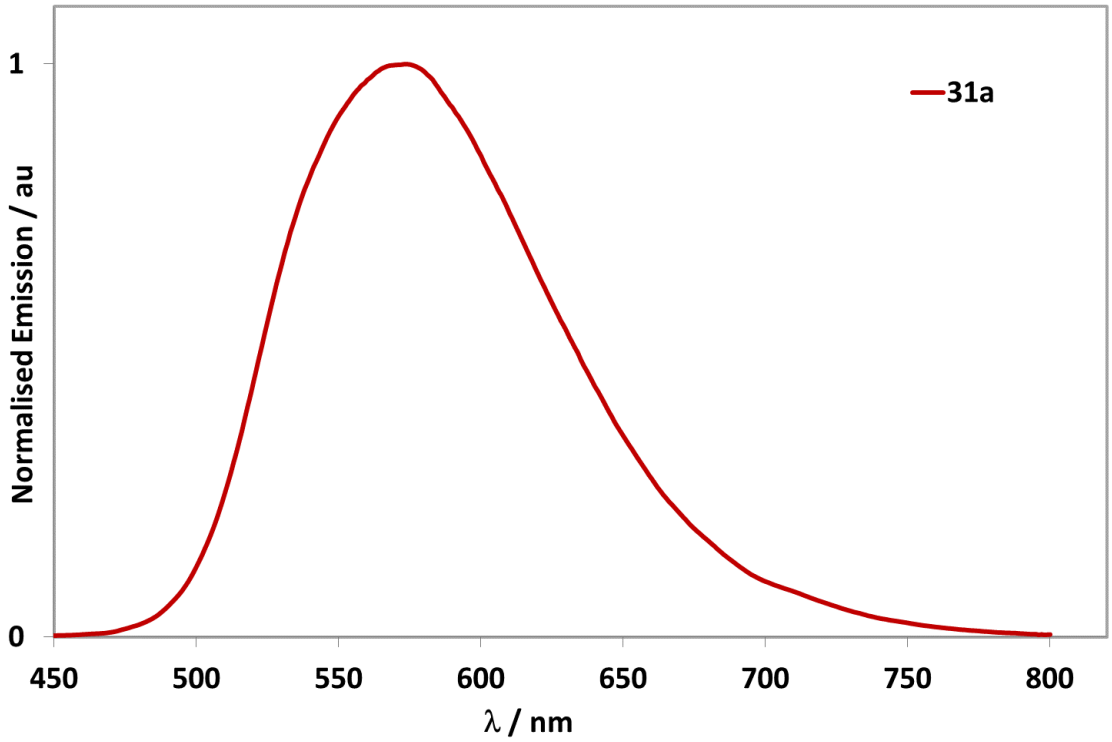

Figure **39**: Photoluminescence spectrum of complex **31a** in deaerated MeCN at 298 K.

Upon photoexcitation at 420 nm, complex **3a** exhibits a broad and featureless emission, indicative of an emission with mixed CT character, with a maximum at λ_{em} = 573 nm and a photoluminescence quantum yield (Φ_{PL}) of 7%. Compared to the unsubstituted analogue $[Ir(ppy)_2(dtBubpy)]PF_6$ (λ_{em} = 591 nm, Φ_{PL} = 29%) a blue-shift of 18 nm (532 cm^{-1}) and a notable lowering of the Φ_{PL} is observed.

Table **15**: Photophysical properties of complex **31a.**

	λ_{em}[a] / nm	Φ_{PL}[a,b] / %	τ_{PL}[c] / ns
31a	573	7	77 (28%) 671 (42%) 5107 (30%)

[b] Recorded at 298 K in deaerated MeCN solution (λ_{exc} = 420 nm); [c] $[Ru(bpy)_3](PF_6)_2$ in MeCN as the reference (Φ_{PL} = 1.8% in aerated MeCN at 298 K);[9] [c] λ_{exc} = 378 nm.

NLO studies

We used the EFISH method in order to study the second-order NLO response in solution of the complexes. This technique[166,167] provides direct information on the intrinsic molecular NLO properties, through

$$\gamma_{EFISH} = (\mu\beta_{EFISH}/5kT) + \gamma(-2\omega; \omega, \omega, 0)$$

where $\gamma_{EFISH}/5kT$ is the dipolar orientational contribution to the molecular nonlinearity, and $\gamma(-2\omega; \omega, \omega, 0)$, the second order polarizability, is a purely electronic cubic contribution to γ_{EFISH}, which can usually be neglected when studying the second-order NLO properties of dipolar molecules, dominated by the first hyperpolarizability. β_{EFISH} is the projection along the dipole moment axis of β_{vec}, the vectoral component of the tensor of the quadratic hyperpolarizability, working with an incident wavelength of a pulsed laser. To obtain the value of β_{EFISH}, it is therefore necessary to determine the ground state dipole moment μ of the molecule. To avoid overestimations of the β value due to resonance enhancements, it is essential to choose an incident wavelength whose second harmonic is remote from any absorption of the molecule investigated. It is worth noting that, although it has traditionally been used to study charge-neutral molecules, the EFISH technique can be applied to the determination of the

second-order NLO response of ionic species by working in a solvent of low dielectric constant like $CHCl_3$, which favours ion-pairing.[200,201]

We found that all the investigated complexes are characterised by a negative value of $\mu\beta_{EFISH}$ (Table **13**), in agreement with a negative value of $\Delta\mu$ (difference of the dipole moment in the excited and ground state) upon excitation,[202] as reported for other cyclometalated Ir(III) complexes.[34,55,57,194–198,203]

Complex **29a**, is characterised by a large second-order NLO response ($\mu\beta_{EFISH}$ = -1260 × 10^{-48} esu). A slightly higher absolute value of $\mu\beta_{EFISH}$ is observed for the related complex with the TPA substituent in position para to the Ir-$C_{C\wedge N}$ bond, **29a**. This enhancement is due to an increase of the dipole moment of the complex (Table **13**). A much higher NLO response is reached with **31a** ($\mu\beta_{EFISH}$ = -1880 × 10^{-48} esu), where TPA is para to the Ir-$N_{C\wedge N}$ bond, due to a much higher quadratic hyperpolarizability, β_{EFISH}, which prevails over the decrease of the dipole moment.

Complex **29a**, where TPA is *meta* to the Ir-$C_{C\wedge N}$ bond, is characterised by a large second-order NLO response ($\mu\beta_{EFISH}$ = -1260 × 10^{-48} esu). A slightly higher absolute value of $\mu\beta_{EFISH}$ is observed for the related complex with the TPA substituent in position *para* to the Ir-$C_{C\wedge N}$ bond, **30a**. This enhancement is due to an increase of the dipole moment of the complex (Table 1). A much higher NLO response is reached with **31a** ($\mu\beta_{EFISH}$ = -1880 × 10^{-48} esu), where TPA is *para* to the Ir-$N_{C\wedge N}$ bond, due to a much higher quadratic hyperpolarizability, β_{EFISH}, which prevails over the decrease of the dipole moment. This decrease is due to the more symmetric arrangement of the donating groups around the metallic centre that lead to vector contributions to the dipoles in opposite directions.

Complexes **29b-31b** possess a smaller dipole moment than their **29a-31a** analogues but they are characterised by a higher second-order NLO response due to an increase of the quadratic hyperpolarizability, as expected for the strong acceptor properties of 5-NO_2-1,10-

phenanthroline (Table **13**). Remarkably, their β_{EFISH} values are much higher than that previously reported for the related Ir(III) complex with 5-NO_2-1,10-phenanthroline but with two unsubstituted cyclometalated phenylpyridines (-79 x 10^{-30} esu).

Although the NLO responses of molecular systems are important to study, a further step is to obtain organised molecular materials showing a high second-order solid-state NLO response.[143,193] While some neutral organometallic compounds have been incorporated into polymeric films affording rather large second-harmonic generation (SHG) responses, [143,193,204,205] to the very best of our knowledge no NLO-active polymeric films based on ionic organometallic complexes has been reported. This observation prompted us to investigate the second-order NLO properties of **30b** incorporated in a polymeric film. This cationic complex was chosen because it is simultaneously characterised by one of the largest $\mu\beta_{EFISH}$ and a significant dipole moment (Table **13**) which should facilitate the orientation of the complex by poling.

Thus, we have prepared thin films of **30b** dispersed in a polymethylmethacrylate (PMMA) or polystyrene (PS) matrix, as reported in the experimental section. It turned out that the second-harmonic generation signal of films in PMMA rapidly faded due to the loss of orientation of the dyes. A much better behaviour was obtained by using polystyrene as matrix (Figure **40**).

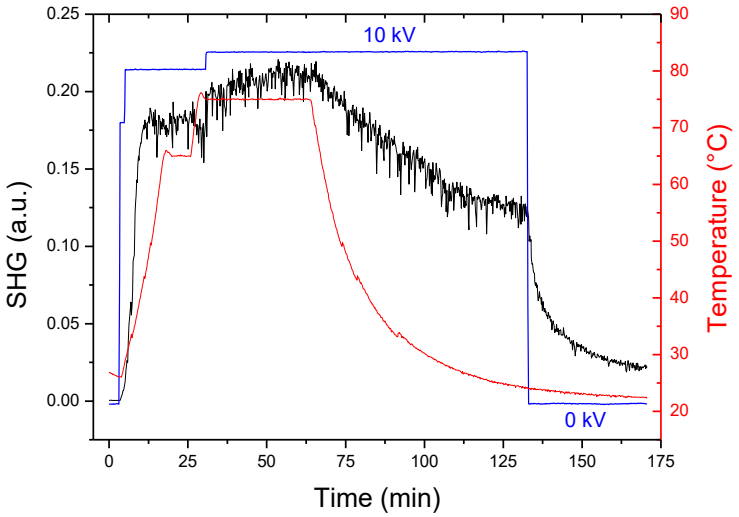

Figure **40**: Poling of the **30b**/polystyrene film. SHG (black line), temperature (red line) and electric field (blue line).

The SHG was negligible before applying the corona voltage and it quickly increased after application of the electric field. When the temperature was increased up to 70 – 80 °C, a large increase of the SHG occurred, due to the decrease of the viscosity of the polymeric matrix which allowed an easier orientation of the NLO-active complex. When a stable SHG was reached, the sample was cooled at room temperature and the electric field switched off. By fitting the Maker fringe measurements, the three nonzero coefficients of the second-order susceptibility tensor $\chi_{33}^{(2)}$, $\chi_{31}^{(2)}$ and $\chi_{15}^{(2)}$ for the poled film were found to be 1.7, 0.46 and 0.50 pm/V, respectively. Although this $\chi_{33}^{(2)}$ value is lower than that previously reached for a neutral cyclometalated Ir(III) complex (3.0 pm/V),[57] it remains an interesting result because it represents the first demonstration of SHG properties of a cationic organometallic complex embedded in a polymeric film.

Conclusions

In summary, this work has shown the good $\mu\beta_{EFISH}$ values of six new and well characterised cationic iridium(III) complexes bearing either 4,4'-di*tert*butyl-2,2'-bipyridine or 5-NO_2-1,10-phenanthroline along with three cyclometalated 2-phenylpyridines substituted with a triphenylamine in position meta or para to Ir-$C_{C\wedge N}$ bond or para to Ir-$N_{C\wedge N}$ bond. The best values are obtained with 5-NO_2-1,10-phenanthroline as ancillary ligand, due to the excellent acceptor properties of its π^* orbitals, and when the triphenylamine is in position para to the Ir-$N_{C\wedge N}$ bond.

Remarkably, polymeric film based on this kind of cationic iridium complexes can exhibit a good second-harmonic generation response which is particularly stable by using polystyrene as polymeric matrix. These results will stimulate further studies on polymeric films incorporating cationic complexes for NLO applications.

Chapter 4

Synthesis, Characterisation and Optoelectronic Properties of Iridium Complexes Bearing Nonconjugated Six-membered Chelating Ligands

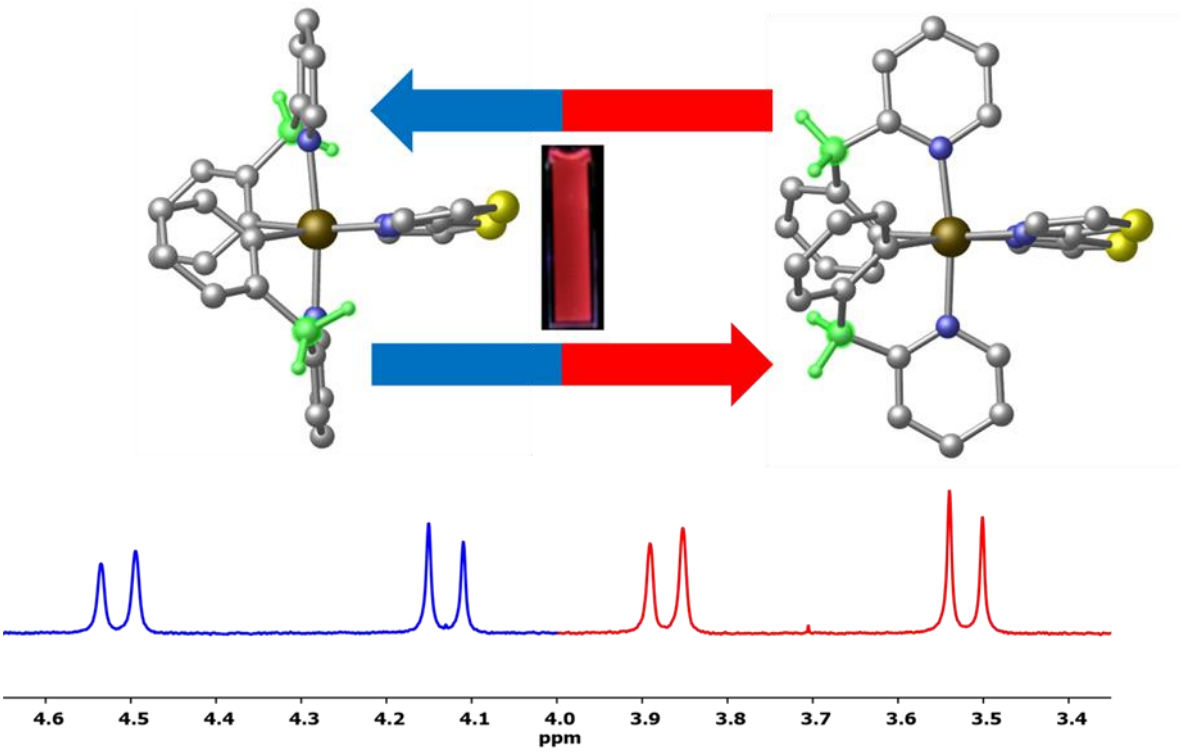

Cover picture: TOC graphic of publication arising from this chapter

Introduction

As mentioned in Chapter 1, one of the most widely studied class of iridium complexes are heteroleptic bis-cyclometalated complexes of the form $[Ir(C^N)_2(L^X)]^{n+}$, where C^N is the cyclometalating ligand and L^X is either a monoanionic ligand such as acetylacetonate (acac, n = 0), or a neutral diimine ligand such as 2,2'-bipyridine (bpy, n = 1).[5,31,206] The main strategies for tuning the emission energy of these complexes are the decoration of the ligands with either electron-withdrawing or electron-donating substituents, and the modification of the coordinating heterocycles.[5,33,207] The C^N ligands nearly always form five-membered chelates, typically based on 2-phenylpyridine (ppyH). Strategies involving interruption of the conjugation in these C^N ligands, such as going from a five-membered chelate to a six-membered chelate that incorporates a CH_2 spacer, are far less explored.

Indeed, photoactive iridium complexes bearing a six-membered cyclometalating chelate are very rare, and the few reported examples can be categorised into two families of complexes: those containing conjugated[92,94,208,209] or non-conjugated[95–97] bidentate cyclometalating ligands. For instance as mentioned in Chapter 1, Song *et al*.[96] reported in 2008 a phosphorescent Ir(III) complex $[Ir(dfbpz)_2(fptz)]$, **7** (where (dfbpz)H is 2,4-difluorobenzyl-*N*-pyrazole and fptz is 3-trifluoromethyl-5-(2-pyridyl) triazole) bearing a non-conjugated *N*-benzylpyrazole ligand forming a six-membered chelated framework (Figure **41**).

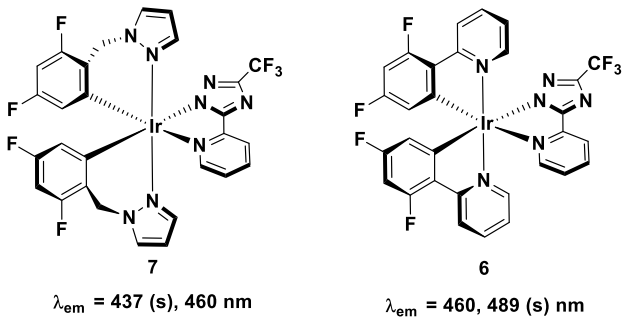

Figure **41**: Schematic representation of five-membered and six-membered chelated Ir(III) complexes.

This complex is a blue emitter in dichloromethane solution (λ_{em} = 437, 460 nm, Φ_{PL} = 10% and τ_{PL} = 0.10 μs). The CH_2 spacer of the cyclometalated ligand effectively disrupts the π-conjugation to produce a blue shift, compared to [Ir(dFppy)$_2$(fptz)], **6** [where (dFppy)H = 2-(2,4-difluorophenyl)pyridine and fptz = 3-trifluoromethyl-5-(2-pyridyl) triazole], containing a five-membered ring chelate C^N ligand and the same ancillary ligand (λ_{em} = 460, 489 nm in dichloromethane, Figure **41**. [99] By contrast, Zhu *et al*.[94] reported in 2005 the iridium(III) complex [Ir(bis[2-(*N*-carbazolyl)pyridinato-N,C3')picolinate], **32** ([Ir(cpy)$_2$(pic)], Figure **42**) containing a six-membered chelating framework where the ligand is fully conjugated leading to yellow luminescence in the recrystallised solid state with (λ_{em} = 538 nm, Φ_{PL} = 5%).

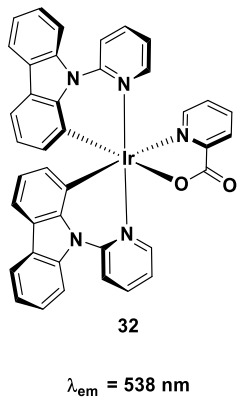

32

λ_{em} = 538 nm

Figure **42**: Schematic representation of an Ir(III) complexes containing a fully conjugated six-membered chelating framework.

To date, to the best of our knowledge, all iridium complexes employing nonconjugated six-membered chelate C^N ligands have included either a pyrazole[96,97] or benzyl-derived *N*-heterocyclic carbene[95] coordinating moiety as part of the ligand.

Surprisingly, the use of pyridine, such as with 2-benzylpyridinato (bnpy), has not yet been explored in the design of photoactive iridium complexes; this ligand has only been reported for iridium complexes used in catalysis.[210,211] The two C^N-coordination moieties in bnpy are separated by a CH_2 spacer, which fully disrupts the π-conjugation within the C^N ligands. This allows the decoration of the pyridine without influencing the electronic properties

of the phenyl ring and therefore the HOMO level of the complex; the HOMO being typically located on the phenyl rings of the C^N ligands and the iridium *d*-orbitals.[33]

This chapter deals about the study of a series of four new cationic Ir(III) complexes (Figure **43**) of the form $[Ir(bnpy)_2(N^N)](PF_6)$, where the N^N ligand is a neutral diimine chelate, with the goal to evaluate whether breaking the conjugation within the C^N ligands can aid in pushing the emission to the blue.

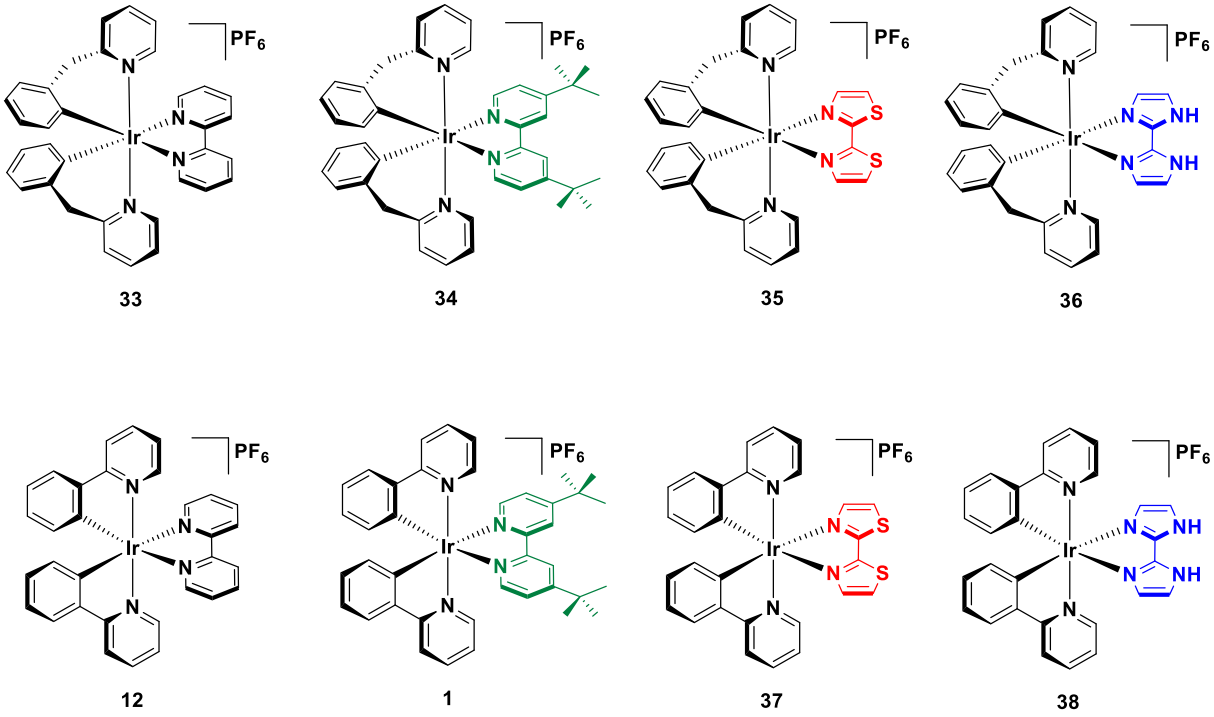

Figure **43**: Synthesised and characterised complexes (**33**, **34**, **35** and **36**) and the corresponding reference complexes (**12**, **1**, **37** and **38**) in this study.

Complexes **33** and **34** contain bipyridine-based ancillary ligands [**33**, N^N = bpy; **34** = 4,4'-di-*tert*-butyl-2,2'-bipyridine (d*t*Bubpy)] while complexes **35** and **36** each contain two 5-membered heterocycles in the electron deficient 2,2'-bithiazole (bthz) and the electron-rich 1*H*,1'*H*-2,2'-biimidazole (biim) ligands, respectively. The motivation for the choice of N^N ligands was to have a series of ligands that (1) spanned a wide electronic range and (2) whose bite angles varied in order to assess what impact, if any, this has in conjunction with the C^N ligands. The optoelectronic properties of these complexes are explored and compared with

benchmark complexes (**12**, **1**, **37** and **38**, Figure **43**) where the bnpy ligands have been replaced with ppy; **12**, **1** and **37** have been previously reported,[187,188] while **38** is new. The physical and photophysical properties of these complexes are corroborated by density functional theory (DFT) and time-dependent DFT (TD-DFT) investigations.

Results and Discussion

Synthesis

Complexes **33**, **34**, **35** and **36** were obtained as their hexafluorophosphate salts from the chloro-bridged dimer $[Ir(bnpy)_2Cl]_2$, upon reaction with the corresponding N^N ancillary ligand and subsequent anion exchange with NH_4PF_6 following standard reaction conditions (Figure **44**); complex **38** was obtained analogously using $[Ir(ppy)_2Cl]_2$.[64,65] In the first step, $[Ir(bnpy)_2Cl]_2$ was quantitatively obtained as a yellow solid by treatment of bnpyH with $IrCl_3.6H_2O$ in a 3:1 mixture of 2-ethoxyethanol/H_2O (125 °C, 24 h). This dimer was then cleaved with the appropriate N^N ligand in a 1:1 mixture of CH_2Cl_2/MeOH (40 °C, 18 h) to afford the cationic Ir(III) complexes as their chloride salts. After column chromatography on silica (eluent: 5% MeOH in CH_2Cl_2) followed by an ion exchange with aqueous NH_4PF_6, the complexes were isolated in excellent yield (78 – 91%) as their hexafluorophosphate salts. All complexes were characterised by ^1H, ^{13}C and ^{31}P NMR spectroscopy in $CDCl_3$, HR-ESI mass spectrometry, elemental analysis, and melting point determination. The ^1H-NMR spectra of **33** and **34** show the expected number of resonances. Characteristic signals for the CH_2 of the C^N ligand appear around 4.0 – 3.0 ppm. Complexes **35** and **36** show more resonances as expected. Characteristic signals are discussed below. With respect to the complexes in Chapter 2 these complexes behave in a comparable way in HR-ESI mass spectrometry and elemental analysis.

The structures of complexes **33**, **34**, **35** and the chloride salt of **38**, **38.Cl**, were determined by single crystal X-ray diffraction.

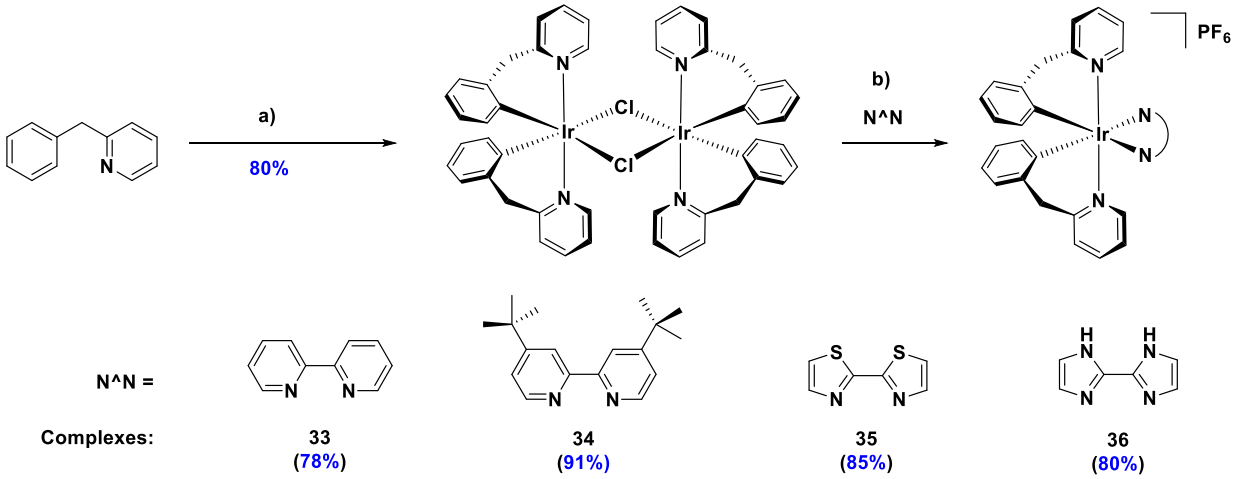

Figure **44**: Procedure for the synthesis of target complexes **33**, **34**, **35** and **36** in this study. a) $IrCl_3 \cdot 6H_2O$, 2-benzylpyridine (bnpyH), 2-ethoxyethanol/water (3:1), 125 °C, 24 h. b) 1. Corresponding N^N ligand, $MeOH/CH_2Cl_2$ (1:1), 40 °C, 18 h. 2. aq. NH_4PF_6.

Crystal Structures

Single crystals of sufficient quality of **33**, **34**, **35** and **38.Cl** were grown from vapor diffusion of a CH_2Cl_2 or acetone solution of the complex with diethyl ether acting as the anti-solvent. The structures of **33**, **34**, **35** and **38.Cl** were determined by single-crystal X-ray diffraction (Figure **45**, Table **16**). All three (**33**, **34**, **35**) complexes possess a distorted octahedral geometry, with the two bnpy ligands in complexes **33**, **34**, **35** coordinated to iridium to form a six-membered chelate ring. The pyridine rings of the C^N ligand are disposed in a mutually *trans* arrangement while the cyclometalating carbon atoms are *trans* to the nitrogen atoms of the N^N ligand, presenting an analogous binding mode to the majority of cationic Ir(III) complexes such as **12**, **1**, **37** and **38.Cl**. In **33**, **34**, **35** the Ir-C_{C^N} bonds are noticeably shorter [2.021(4) – 2.052(8) Å for **33**, **34**, **35**; 1.988(6) – 2.016(7) for **38.Cl**] than the Ir-N_{N^N} bonds, which range from 2.148(4) to 2.203(6) Å [2.153(5) – 2.184(5) Å for **38.Cl**]. These bond lengths are all similar to the analogous bond lengths in the reference complexes **12**, **1** and **37**.[187,188]

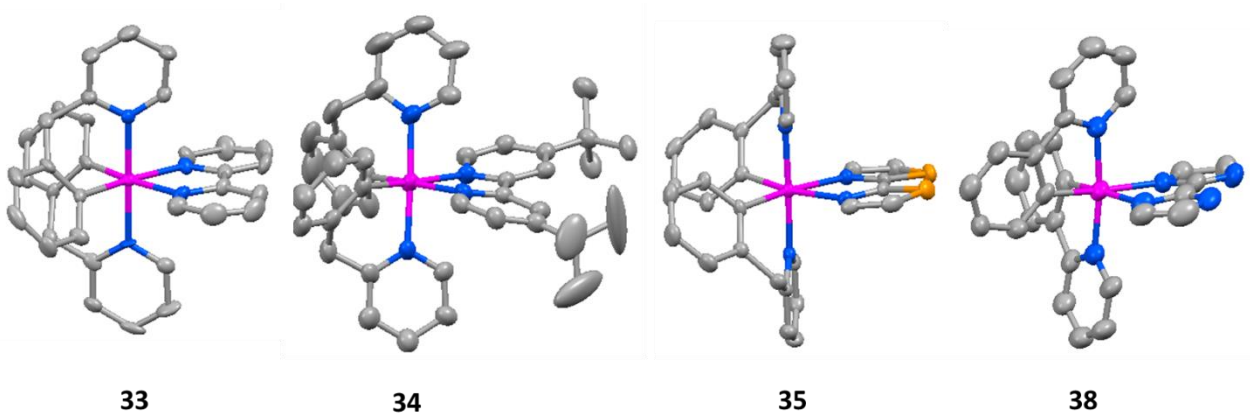

Figure **45**: Solid-state structures of complexes **33**, **34**, **35** and **38.Cl**. Hydrogen atoms, PF_6^- counterions and solvent molecules are omitted for clarity. Note the different orientations of the bnpy ligand in **33**, and **34** vs **35**. Colour codes for atoms are: C = light grey, N = blue, S = orange and Ir = magenta.

Table **16**: Selected crystallographic parameters for complexes **33**, **34** and **35**.

Complex	**Bond Length / Å**				**Bond Angle / °**
	Ir-C_{C^N}	Ir-N_{C^N}	Ir-N_{N^N}	N-Ir-N	C-Ir-N_{C^N}
33	2.052(8)	2.09(1)	2.153(8)	77.8(4)	88.1(3)
	2.04(2)	2.10(1)	2.16(1)		88.3(6)
34	2.032(6)	2.083(5)	2.148(4)	76.5(2)	88.8(2)
	2.041(7)	2.074(7)	2.154(5)		89.2(3)
35	2.021(4)	2.079(4)	2.199(3)	75.2(1)	87.97(13)
	2.032(6)	2.069(5)	2.203(6)		87.98(13)
38	1.988(6)		2.153(5)	76.1(2)	80.1(3)
	2.016(7)		2.184(5)		80.7(2)

The bite angles of the N^N ligands in **33**, **34** and **35** vary from 75.2(1) – 77.8(4)° [76.1(2)° for **38.Cl**], which are again similar to the reference complexes **12**, **1** and **37**.[187,188] The bite angles of the bnpy ligands vary between 87.97(13) and 87.98(13)° for **35**, 88.1(3) and 88.3(6)° for **33**, and 88.8(2) and 89.2(3)° for **34**; reflecting the increasing steric demand of the

different N^N ligands. These bite angles are in the same range as those observed in a related complex using a different nonconjugated C^N ligand with a CH_2 spacer, $[Ir(dFbpz)_2(pymbi)]PF_6$ [where dFbpzH is 1-(2,4-difluorobenzyl)-1*H*-pyrazole and pymbi 3-methyl-1-(2-pyridyl)-benzimidazolin-2-ylidene-*C*,C^2], the bite-angle across the dFbpz ligand being 88.80°.[97] As expected, the bite angles of the bnpy ligands are significantly larger than those seen in the reference complexes, which contain five-membered ring C^N chelates [**12**: 80.00°, **1**: 80.42°, **37**: 80.60° and **38.Cl**: 80.1(3) – 80.7(2)°].

In the X-ray structures, the conformation of the bnpy ligands in complexes **33** and **34** differs from that in **35**. Complexes **33** and **34** are found solely as one conformer where the pyridine rings of the C^N ligand are orientated towards the N^N ligand, whereas, in **35**, the other conformer, where the CH_2 groups point towards the N^N ligand, is observed, despite this being the minor conformer observed by ^{1}H NMR (see below). Given the small differences between the conformer free energies computed in solution for **35** (see below), it is not surprising that packing effects can affect the equilibrium and that the most favoured conformer differs in solution and in the solid-state. Complex **33** crystallises in the polar space group $P2_1$, so individual crystals could be enantiopure, resulting from conglomerate crystallisation; however, the Flack parameter [0.305(7)] indicates the likelihood of individually racemic crystals being present. Complexes **34** and **35** crystallise in centrosymmetric space groups ($P\bar{3}$ and $P\bar{1}$, respectively), so exist as racemates in the crystalline state.

Solution-State NMR studies

The room temperature ^{1}H NMR spectra in $CDCl_3$ of **33**, **34**, **35** and **36** are depicted in Figure **46**. Complexes **33** and **34** each show one set of two doublets in the region of δ = 4.80 – 3.30 ppm, corresponding to the diastereotopic CH_2 protons of the C^N ligand, the result of magnetic non-equivalence imparted by the proximal iridium stereocentre.

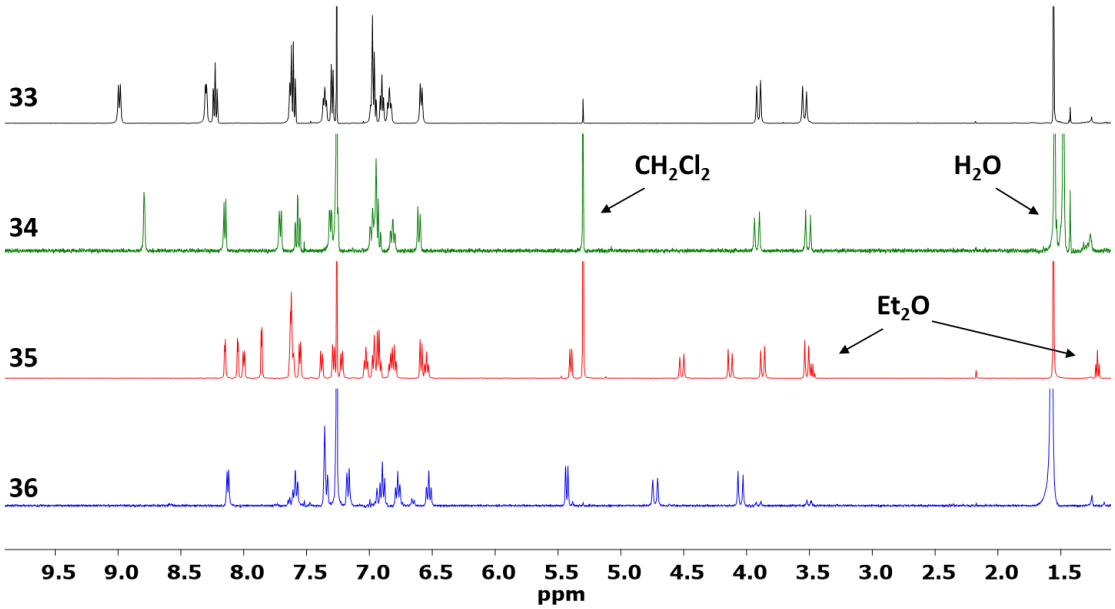

Figure **46**: ^{1}H-NMR spectra of complexes **33**, **34**, **35** and **36** in $CDCl_3$ at room-temperature.

By contrast, there are two sets of two doublets with an integration ratio of 1:1.2 in the same region of ^{1}H NMR spectrum of **35**. Furthermore, two sets of aromatic signals are also apparent, which implies the presence of two conformers (designed as a and b, see below) in solution. Two conformers, in a ratio of 1:0.2 for conformer a:conformer b, are also present in **36** as observed by ^{1}H NMR. This phenomenon was previously reported in related neutral Ir(III) complexes containing 1-(2,4-difluorobenzyl)-1*H*-pyrazole (dFbpzH) as the C^N ligands and was associated with restricted conformational flexibility of six-membered C^N chelates.[96]

This presence of two conformers prompted us to perform DFT calculations. For each of the complexes, we could optimise stable structures for both conformers, differing in orientation of the CH_2 bridge of the C^N ligand, as shown in Figure **47** for complex **35**. The conformer **35a** has the same orientation of the CH_2 bridge as found in the solid state by X-ray crystallography, whereas the geometry of **35b** is analogous to those found in the crystal structures of **33** and **34** (see above).

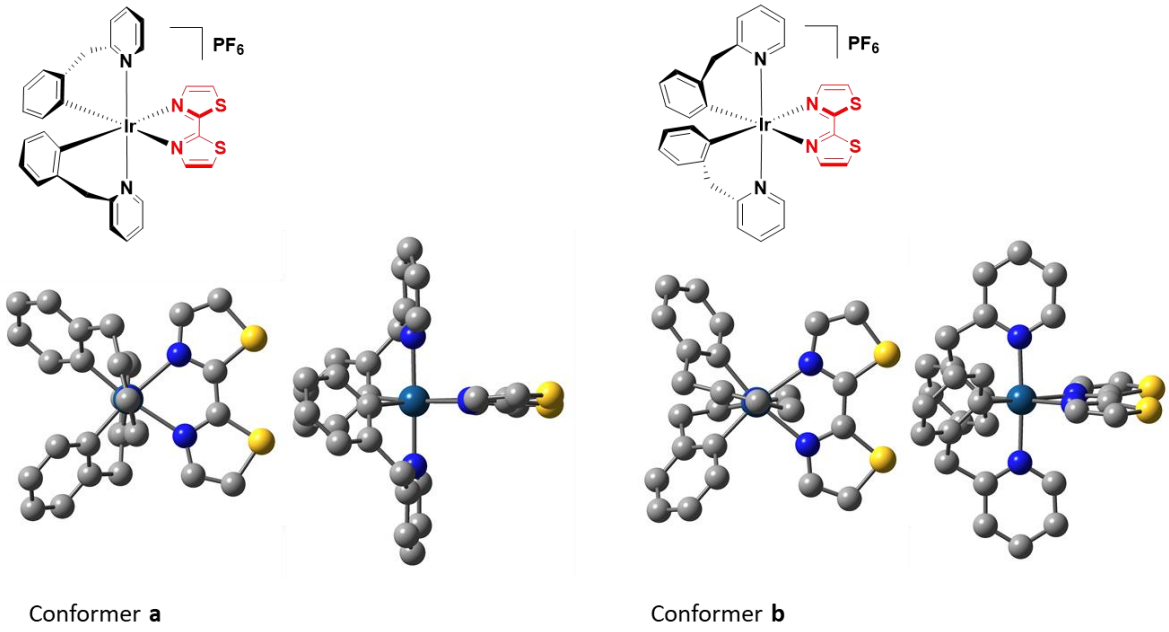

Figure **47**: DFT-optimised geometry of conformers **35a** (left) and **35b** (right). Hydrogen atoms are omitted for clarity.

For all complexes, both conformers belong to the C_2 point group. Given that DFT calculations have been performed in MeCN solution, the DFT-determined bond lengths reasonably match their experimental counterparts, e.g., the Ir-$C_{C\wedge N}$ bonds are 2.02 Å long by DFT and 2.022(5) – 2.052(7) Å for **33**, **34** and **35** in the X-ray, whereas the Ir-$N_{C\wedge N}$ distances are 2.10 Å according to the calculation and 2.069(4) – 2.098(11) Å for **33**, **34** and **35** in the solid-state structure. The chemical exchange cross-peaks (red highlighted) in the 2D ROESY NMR spectrum indicate the existence of a dynamic equilibrium between conformers **35a** and **35b** in solution (Figure **48**). Furthermore, the ROESY enables assignment of ^{1}H resonances to each of the conformers. The NOE cross-peak (blue highlighted) between doublets at 4.54 and 8.18 ppm is only possible for conformer **35a** that has one proton of the CH_2 bridge close (2.56 Å according to DFT) to the aromatic proton of the N^N ligand (Figure **47**).

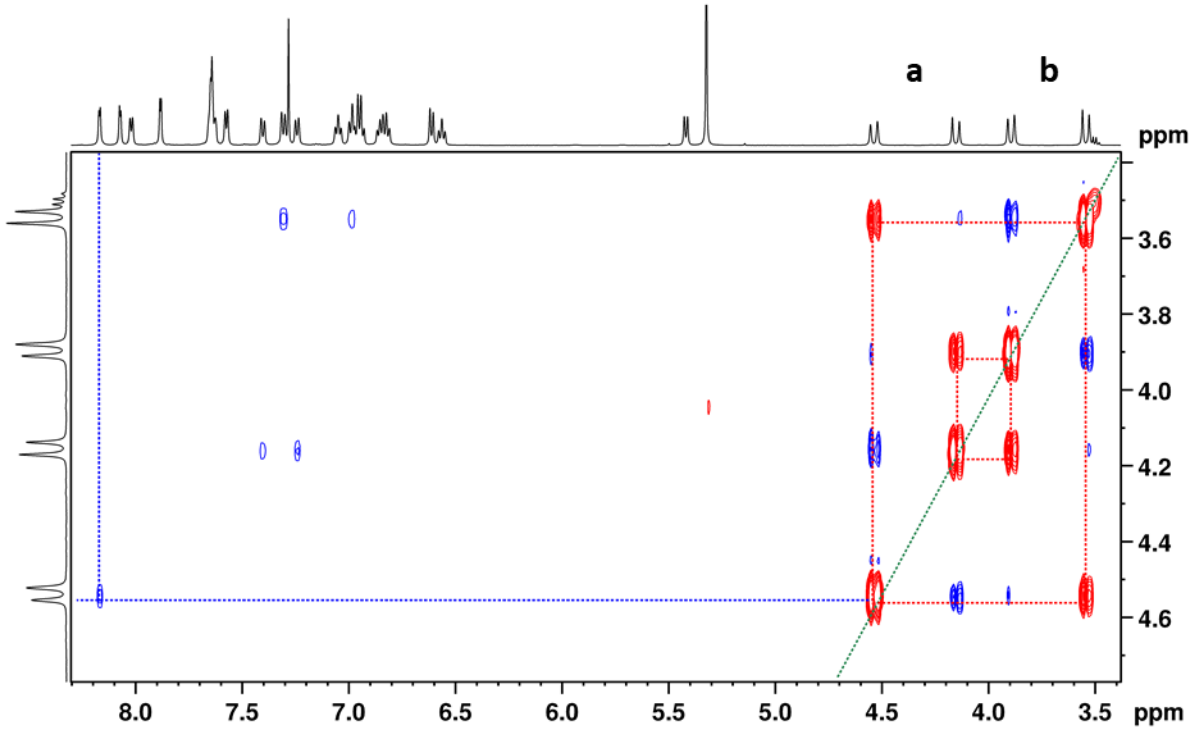

Figure **48**. 2D ROESY spectrum of **35** in $CDCl_3$ at room temperature. The blue and red cross-peaks indicate magnetisation transfer due to NOE and chemical exchange, respectively. The cross-peak between doublets at 4.54 and 8.18 ppm enables assignment of those resonances to conformer **35a**.

By contrast, this NOE enhancement is not observed for conformer **35b** due to a longer distance between the CH_2 bridge and the N^N ligand (5.12 Å according to DFT). DFT computed relative free energies and theoretical Boltzmann distribution can be found in Table **17**. As can be seen, there is a remarkable agreement between the ratio of the two conformers determined by theory and experimentally from the relative integral intensities of CH_2 group ^1H resonances (Table **17**). There seems to be a global trend that the steric stress, that decreases in the **33**~**34** > **35** > **36** series, makes conformer a more accessible in the latter compounds (**35a** and **36a**) than in the former (**33a** and **34a**).

Table **17**: Comparison of relative DFT Gibbs energies of the conformers b with respect to conformers a, respectively (ΔG^o), Boltzmann ratio, corresponding equilibrium constant, K, at 298 K and ratio of conformers derived from relative integral intensities of CH_2 group ^1H resonances.

	33	**34**	**35**	**36**
ΔG^o / kJ·mol^{-1}	-13.4	-9.6	-2.1	5.4
Boltzmann ratio (a:b)	0.004:1	0.02:1	0.43:1	1:0.11
K	223	48.2	2.33	0.113
Ratio of conformers a:b	0:1	0:1	0.83:1	1:0.17

The DFT determined distances between the (closest) hydrogen atoms of the methylene and N^N ligand are: 2.15, 2.14, 2.23 and 2.28 Å, in **33a**, **34a**, **35a** and **36a**, respectively. For **35**, we attempted to optimise by DFT a mixed conformer with one of the ligands in each conformation, but this induces a steric clash and the optimisation process led back to one of the two conformers. This clearly suggests that the transition from one conformation to the other should be a concerted process in which the two ligands simultaneously change their conformation. We therefore searched for the corresponding transition state, and we could locate it 66 kJ·mol^{-1} above the most stable **35b** structure on the free energy scale. This indicates that while thermal equilibration between the two conformers is attainable at room temperature, the interconversion will not be rapid, which is consistent with the fact that two separate sets of signals could be detected on the NMR timescale. The interconversion of conformers **35a** and **35b** was also studied by variable temperature NMR spectroscopy from 280 to 315 K in $CDCl_3$ and deuterated dimethyl sulfoxide. In DMSO, decomposition of the complex was observed upon heating over 305 K. The variable-temperature ^1H NMR studies in $CDCl_3$ showed considerable dependence of equilibrium constant, K, on the temperature (Figure **49**).

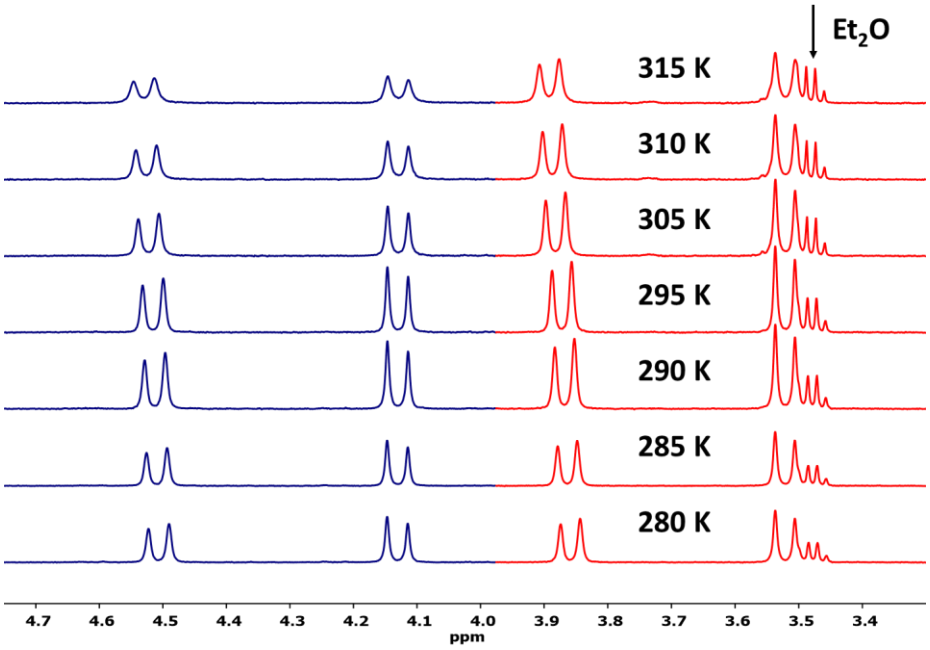

Figure **49**: Colour coded expansion for conformer **35a** (blue) and **35b** (red) in the temperature-dependent ^{1}H-NMR spectra of **35** in $CDCl_3$ between 280 to 314 K.

Analysis of the Van't Hoff plot yielded the following thermodynamic parameters ΔG^{o}_{298} = -0.63 ± 0.05 kJ·mol^{-1}, ΔH^{o} = 7.3 ± 0.4 kJ·mol^{-1} and ΔS^{o} = 26.6 ± 1.5 J·mol^{-1}·K^{-1}, indicating that at 298 K **35b** is moderately more stable than **35a**. The rate constants of interconversion between the two conformers were derived from the intensity of the exchange cross peaks in the ROESY spectra (Figure **50**).

The activation energy obtained experimentally for **35b** to **35a** (72.2 ± 3.2 kJ·mol^{-1}) is in very good agreement with the DFT calculation (66.6 kJ·mol^{-1}). Surprisingly both Eyring and Van't Hoff plot analysis suggest large positive entropy for the isomerisation of **35a** to **35b**. These significant entropic changes were not reproduced by DFT calculations, but we note that the entropic term is the most approximated thermodynamic term in the traditional DFT calculations of total and reaction (free) energies.

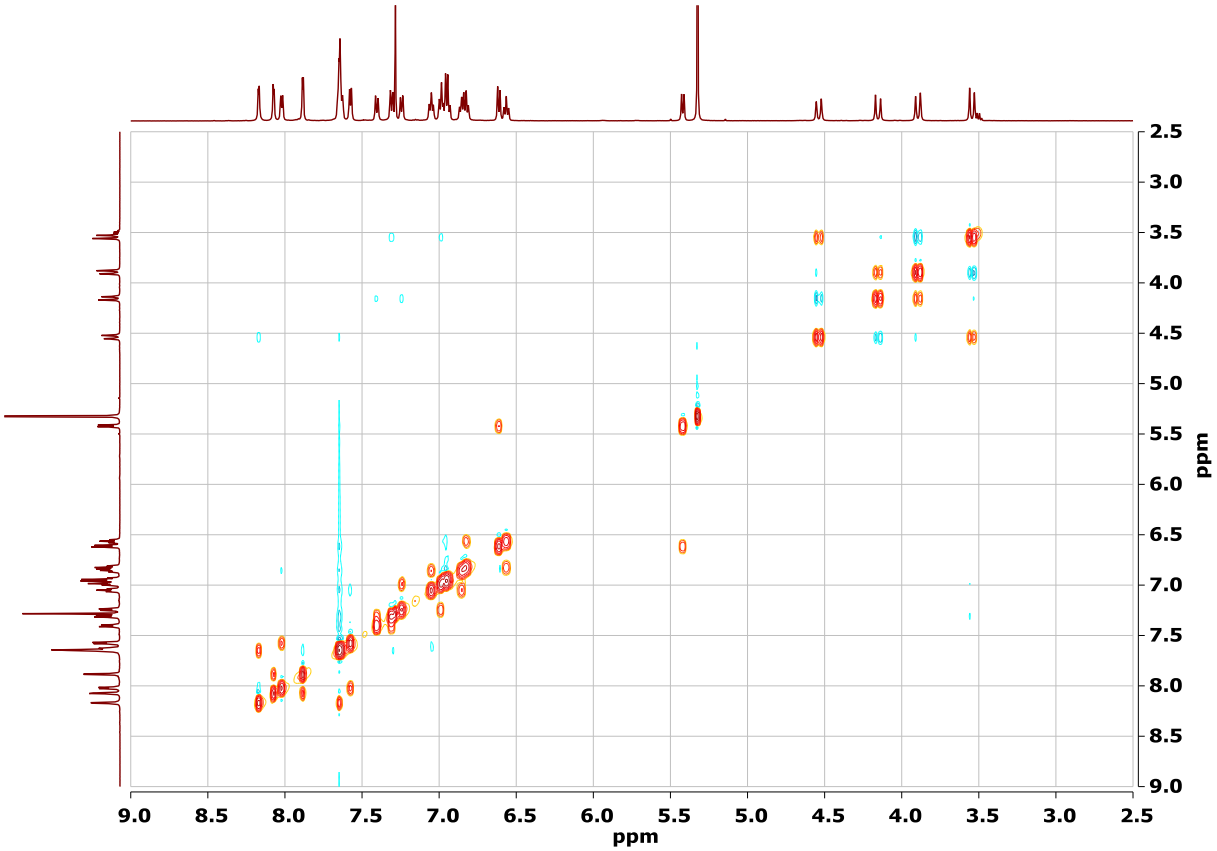

Figure **50**: ROESY-NMR spectrum of **35** in $CDCl_3$ at room temperature.

The corresponding activation parameters determined from an Eyring analysis are summarised in Table **18**.

Table **18**: Activation parameters for the interconversion for complex **35** between conformers **35a** and **35b** obtained by Eyring plot analysis of the rate constants for conformer interconversion at various temperatures.

Conformer	$\Delta G^{\ddagger}_{298\,K}$ / kJ·mol^{-1}	$\Delta H^{\ddagger}$ / kJ·mol^{-1}	$\Delta S^{\ddagger}$ / J·mol^{-1}·K^{-1}
a	70.6 ± 4.9	80.0 ± 2.4	31.6 ± 8.1
b	72.2 ± 3.2	71.9 ± 1.6	-0.8 ± 5.5

Electrochemical properties

The electrochemical behaviour for **33**, **34**, **35** and **36** and **38** was evaluated by cyclic voltammetry (CV) and differential pulse voltammetry (DPV) in deaerated MeCN solution containing *n*-Bu_4NPF_6 as the supporting electrolyte and ferrocene/ferrocenium (Fc/Fc^+) as the internal reference obtained at a scan rate of 100 mV s^{-1}. The potentials are referenced with respect to SCE (Fc/Fc^+ = 0.38 V in MeCN)[189] at 298 K. The voltammograms for **33**, **34**, **35** and **36** are shown in Figure **51** and the electrochemistry data can be found in Table **19**.

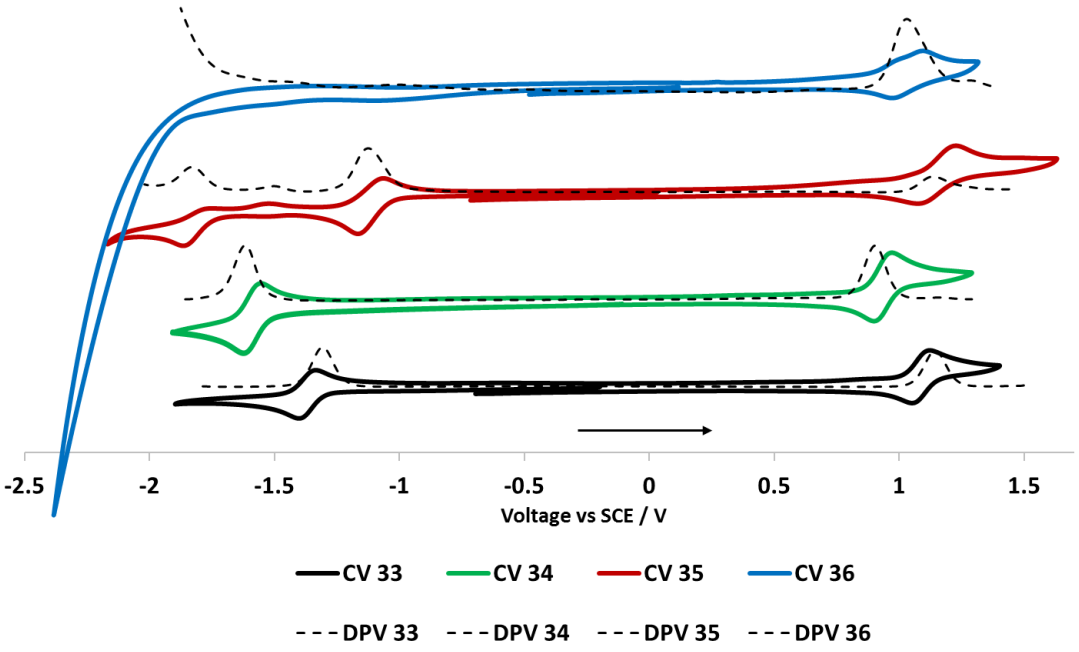

Figure **51**: Cyclic voltammograms (in solid lines) and differential pulse voltammetry (in dotted lines) for **33**, **34**, **35** and **36** carried out in degassed MeCN at a scan rate of 100 mV s^{-1}, with Fc/Fc^+ as the internal reference, referenced to SCE (0.38 V vs. SCE).[189]

All complexes show a quasi-reversible single electron oxidation peak, which is attributed to the Ir(III)/Ir(IV) redox couple with contributions from the phenyl rings of the bnpy. Throughout the series, complexes **33**, **34**, **35** and **36** are easier to oxidise than their corresponding reference complexes with cathodic shifts ranging from 0.09 to 0.40 V as the result of the interruption of the π-conjugation.

Table **19**: Electrochemical properties of **33**, **34**, **35** and **36** and **12**, **1**, **37** and **38**.

	Electrochemistry[a]						
	$E_{1/2}^{ox}$ / V	ΔE_p / mV	$E_{1/2}^{red}$ / V	ΔE_p / mV	ΔE_{redox}[b] / V	E_{HOMO}[c] / eV	E_{LUMO}[c] / eV
33	1.12	78	-1.38	74	2.50	-5.54	-3.04
34	0.91	75	-1.58	77	2.49	-5.33	-2.84
35	1.15	140	-1.11, -1.81[d]	80	2.26	-5.57	-3.31
36	1.05	75	n.d.[e]	-	-	-5.47	-
12[f]	1.27	56	-1.38	55	2.65	-6.07	-3.42
1[f]	1.31	106	-1.40	87	2.71	-6.11	-3.40
37[g]	1.24	-	-1.15	-	2.39	-5.85	-2.76
38	1.15	91	-1.95,[d] -2.29[d]	-	3.10	-5.57	-2.47

[a] in degassed MeCN at a scan rate of 100 mV s^{-1} with Fc/Fc^+ as internal reference, and referenced with respect to SCE (Fc/Fc^+ = 0.38 V in MeCN);[189] [b] ΔE_{redox} is the difference (V) between first oxidation and first reduction potentials; [c] $E_{HOMO/LUMO}$ = -[$E^{ox/red}$ vs Fc/Fc^+ + 4.8] eV;[191] [d] irreversible; [e] not detectable in MeCN; [f] from ref [187]; [g] from ref [188].

The absence of a conjugated coordinating pyridine results in a destabilised HOMO, compared to the analogous ppy reference complexes; for instance, according to DFT the HOMO is 0.24 eV lower in **12** than in **33** (Figure **52**).

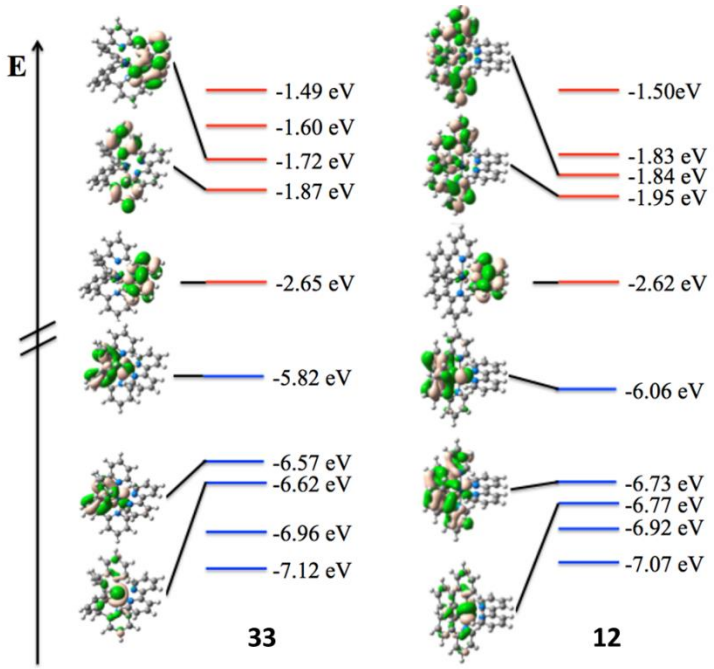

Figure **52**: Comparison between the MO diagrams of **33** and **12** (solvent: CH_2Cl_2).

For instance, the oxidation potential of **33** at 1.12 V is significantly shifted to less positive potential than that of **12** ($E_{1/2}^{ox}$ = 1.27 V).[15] A more dramatic cathodic shift of 400 mV is observed for **34** ($E_{1/2}^{ox}$ = 0.91 V) compared to **1** ($E_{1/2}^{ox}$ = 1.31 V).[16] The oxidation potential of **35** at 1.15 V is similar to **33** and, likewise is easier to oxidise than its reference complex **37** ($E_{1/2}^{ox}$ = 1.24 V).[24] The oxidation potential of **36** at 1.05 is modestly cathodically shifted by 7 mV compared to **33** and by 10 mV compared to **38** ($E_{1/2}^{ox}$ = 1.15 V). The cathodic shifting of the complexes **34** and **36** compared to that of **33** reflect the more electron-rich nature of the ancillary ligand, which serves to modulate the electronics of the iridium centre.

Complexes **33**, **34** and **35** show monoelectronic reversible first reduction waves, reflecting a reduction of the ancillary ligand in each case. No reduction wave was detected for **36**, a feature also found for related biim-containing cationic Ir(III) complexes such as [(dFppy)$_2$Ir(biim)](PF$_6$) (where dFppy = 2-(2,4-difluorophenyl)pyridinato).[20] The voltammograms for **38** however show two irreversible reduction waves at -1.95 V and -2.29 V. The reversible reduction potentials for **33**, **34** and **35** are in a similar range to those of **12**, **1**, **37**

and other related cationic Ir(III) complexes where N^N-based reduction is well-documented.[84] The reduction potential of **33** at -1.38 V is the same as that found for **12**.[187] Complex **34**, bearing the electron-rich d*t*Bubpy N^N ligand, is more difficult to reduce than **33**, with $E_{1/2}^{red}$ = -1.58 V. This reduction potential is significantly cathodically shifted however compared to **1** ($E_{1/2}^{red}$ = -1.40 V). In contrast the reduction potential for **35** is shifted anodically by 270 mV to -1.11 V compared to **34**, which is similar to that of **37** ($E_{1/2}^{red}$ = -1.15 V).[188] A second, irreversible reduction wave at -1.81 V is observed for **35**, also present in the voltammogram of **37**.

In acetonitrile, the DFT-computed HOMO levels in acetonitrile of the major conformer of complexes **33**, **34**, **35** and **36** are -5.67 eV (**33b**), -5.63 eV (**34b**), -5.69 eV (**35b**), -5.74 eV (**36a**), respectively. The HOMO levels inferred from the CV data are systematically slightly higher in energy compared to the DFT data at -5.54 eV (**33**), -5.33 eV (**34**), -5.57 eV (**35**) and -5.47 eV (**36**). A notable destabilisation of the experimentally determined HOMO of **33** and **34** is observed compared to their respective reference complexes **12** (-6.07 eV) and **1** (-6.11 eV); the same trend is found but is less pronounced when comparing the HOMO energies of **35** and **36** to **37** (-5.85 eV) and **38** (-5.57 eV). This destabilisation is consistent with the interruption of the electronic communication between the phenyl ring and the electron-withdrawing pyridine in the C^N ligands. The DFT computed LUMO energies in acetonitrile of **33**, **34**, **35** and **36** are -2.42 eV (**33b**), -2.23 eV (**34b**) and -2.82 eV (**35b**); the calculated LUMO energy for **36a** is -1.59 eV. The LUMO levels for **33**, **34** and **35** could be straightforwardly estimated from the CV data and the experimental results are in line with the computed trends. The experimentally inferred LUMO of **3** (E_{LUMO} = -2.84 eV) is destabilised compared to **33** (E_{LUMO} = -3.04 eV) as a result of the presence of the electron-donating *t*-butyl substituents on the N^N ligand. This effect is more pronounced than that observed between **12** and **1** (E_{LUMO} = -3.42 eV and -3.40 eV, respectively). The presence of the strongly π-accepting bithiazole N^N ligand in **35** leads to a significant stabilisation of the LUMO (E_{LUMO} = -3.31 eV) compared to those of **33** and **34**.

Complex **35**, however, exhibits a more stabilised LUMO level (E_{LUMO} = -3.31 eV) than **37** (E_{LUMO} = -2.76 eV). The HOMO-LUMO gap of complexes **33** and **34** (experiment: 2.50 and 2.49 eV, theory: 3.25 and 3.40 eV for **33** and **34**, respectively) are larger than that of **35** (experiment 2.26 eV, theory: 2.87 eV) but are all smaller compared to their reference complexes **12**, **1**, and **37** (experiment 2.65, 2.71 and 2.39 eV, respectively).

Photophysical properties

The UV-Visible absorption spectra of **33**, **34**, **35** and **36**, recorded in MeCN at 298 K, are shown in Figure **53** and the data are summarised in Table **20**.

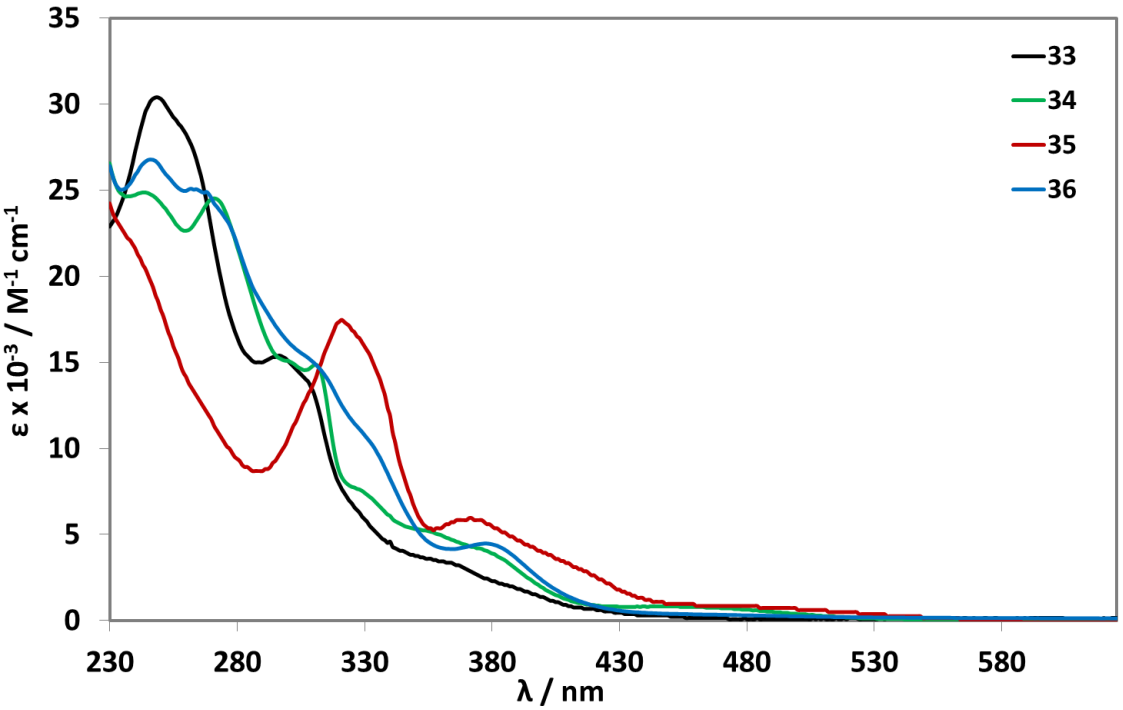

Figure **53**: UV−vis absorption spectra of complexes **33**, **34**, **35** and **36** in MeCN at 298 K.

All complexes show intense high-energy (ε on the order of 2.0 – 3.5 × 10^4 M^{-1} cm^{-1}) absorption bands below 280 nm that are attributed to $^1\pi$–π^* ligand-centred (^{1}LC) transitions localised on the ancillary ligand, analogous to the corresponding bands found for their reference complexes.[187,188]

Table **20**: Selected photophysical data for complexes **33**, **34**, **35**, **36** and **38**.

	λ_{abs} / nm [ε / $M^{-1}cm^{-1}$][a]
33	250 [30 295], 298 [15 137], 365 [3 290], 451 [230]
34	246 [24 756], 273 [24 373], 312 [14 619], 357 [5 230], 444 [1 070]
35	320 [17 353], 373 [5 824], 481 [832]
36	246 [26 791], 386 [4 367], 447 [419]
38	261 [39 180], 389 [4 223], 444 [1 559]

[a] recorded in aerated MeCN at 298 K.

The UV-vis spectrum of **35** is dominated by a moderately intense energy band at 322 nm (ε = 1.7 × 10^4 M^{-1} cm^{-1}) and a second less intense band at 374 nm (ε = 0.5 × 10^4 M^{-1} cm^{-1}). This absorption profile is similar to that for its reference complex **37**[188] and those observed in related systems containing thiazole-based ancillary ligands.[212,213] Complex **36** shows moderately intense bands at 386 nm (ε = 0.4 × 10^4 M^{-1} cm^{-1}), which are also present in **38**. Similar to the bands observed for the reference complexes, **33**, **34**, **35** and **36** show weak bands (ε on the order of 10^3 M^{-1} cm^{-1}) in the region of 440 – 490 nm and tailing to 550 nm. To probe the nature of the low-lying transitions in these complexes, we have used TD-DFT. For **33**, the TD-M06 calculations yield the four lowest singlet excited-states at 534 nm (*f*=0.003), 426 nm (*f*=0.002), 413 nm (*f*=0.010) and 399 nm (*f*=0.083). The former corresponds to a HOMO to LUMO transition (see Figure **54**) and can therefore be ascribed to a CT from the phenyl rings of the C^N ligand and the metal atom to the bipyridine. The second involves a HOMO-2 to LUMO transition and is clearly MLCT. The third is a HOMO-1 to LUMO+1 transition and can therefore be characterised as mainly an ILCT, the electronic density moving from the phenyl (and in part the metal) to the pyridyl rings of the C^N ligands.

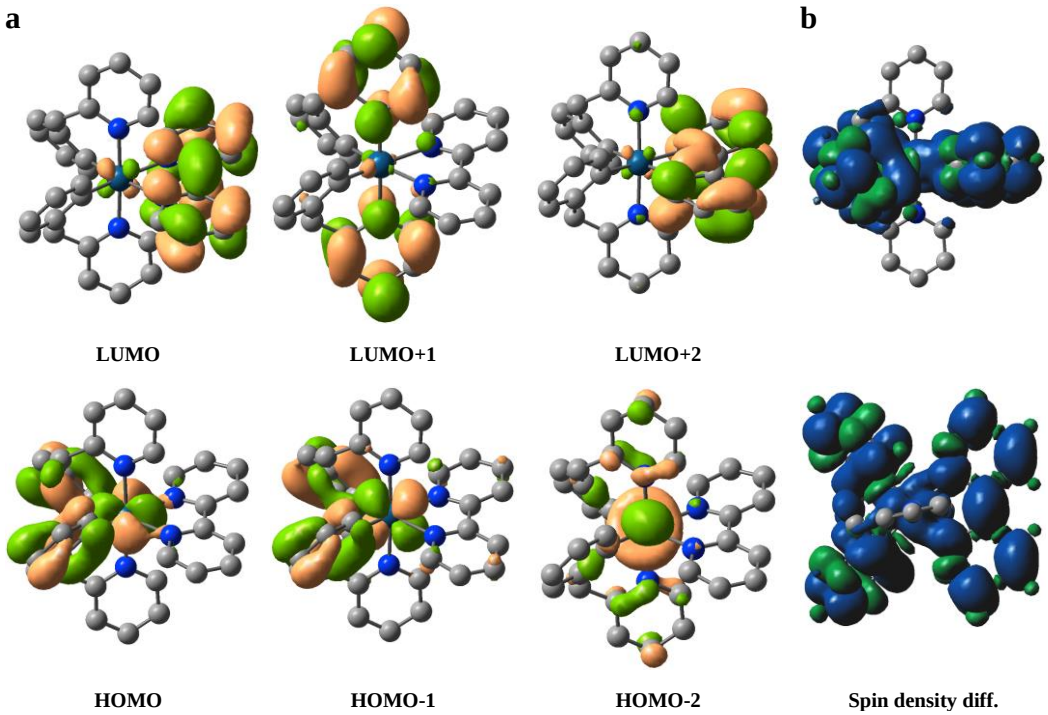

Figure **54**: a) Representation of the Kohn-Sham molecular orbitals for **33**. b) spin density difference of the lowest triplet state in its optimal geometry (two views).

The fourth transition is characterised by HOMO-1 to LUMO character and is also CT in nature, similar to the first band. For the **12** molecule, the two lowest TD-DFT singlets are located at 483 nm (*f*=0.0004) and 404 nm (*f*=0.064). In **12**, the HOMO and LUMO have the same electronic distribution as in **33**, but both HOMO-1 and LUMO+1 are more delocalised than in **33** (see Figure **54**), which is the consequence of breaking of the π-conjugation due to the methylene unit. For **34**, the four lowest singlet excited-states are calculated at 500 nm (*f*=0.003), 415 nm (*f*=0.008), 406 nm (*f*=0.007) and 385 nm (*f*=0.098). There is therefore a moderate hypsochromic displacement of the transitions between the ground state and the first, second and fourth singlet excited states as a consequence of the presence of the more electron-rich d*t*Bubpy N^N ligand in **34**, and a smaller shift for the third state, which is itself consistent with the fact that this transition does not involve the bipyridine in **33** nor in **34**.

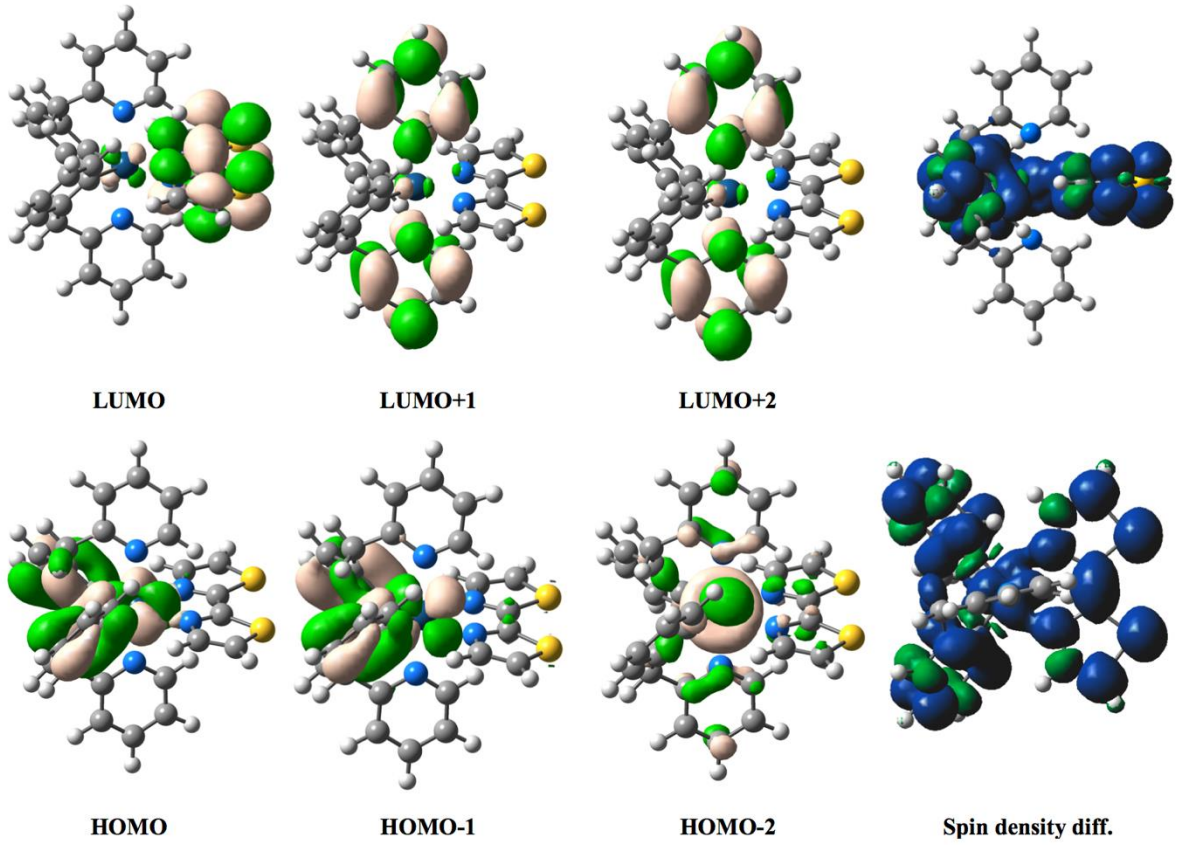

Figure **55**: Left: Representation of the Kohn-Sham molecular orbitals around the HOMO-LUMO gap for **35b**. Right: View of the spin density difference for the lowest triplet state at its optimal geometry.

Indeed, the nature of the states and the shapes of the orbitals in **34** are essentially unchanged compared to **33**. In **35**, the four lowest-lying singlet excited-states are at 638 nm (*f*=0.002), 486 nm (*f*=0.002), 443 nm (*f*=0.096) and 413 nm (*f*=0.014), and they mainly correspond to HOMO to LUMO, HOMO-2 to LUMO, HOMO-1 to LUMO and HOMO to LUMO+1 transitions, respectively. In **35**, the strongest low-lying transition is therefore significantly bathochromically shifted compared to **33**, which fits experimental trends (Figure **53**). The frontier MOs of **35b** are displayed in Figure **55** and the same nature as in **33** is found but for the LUMO+2 that is centred on the pyridyl of the C^N ligand in **35** rather than ancillary ligand in **33**.

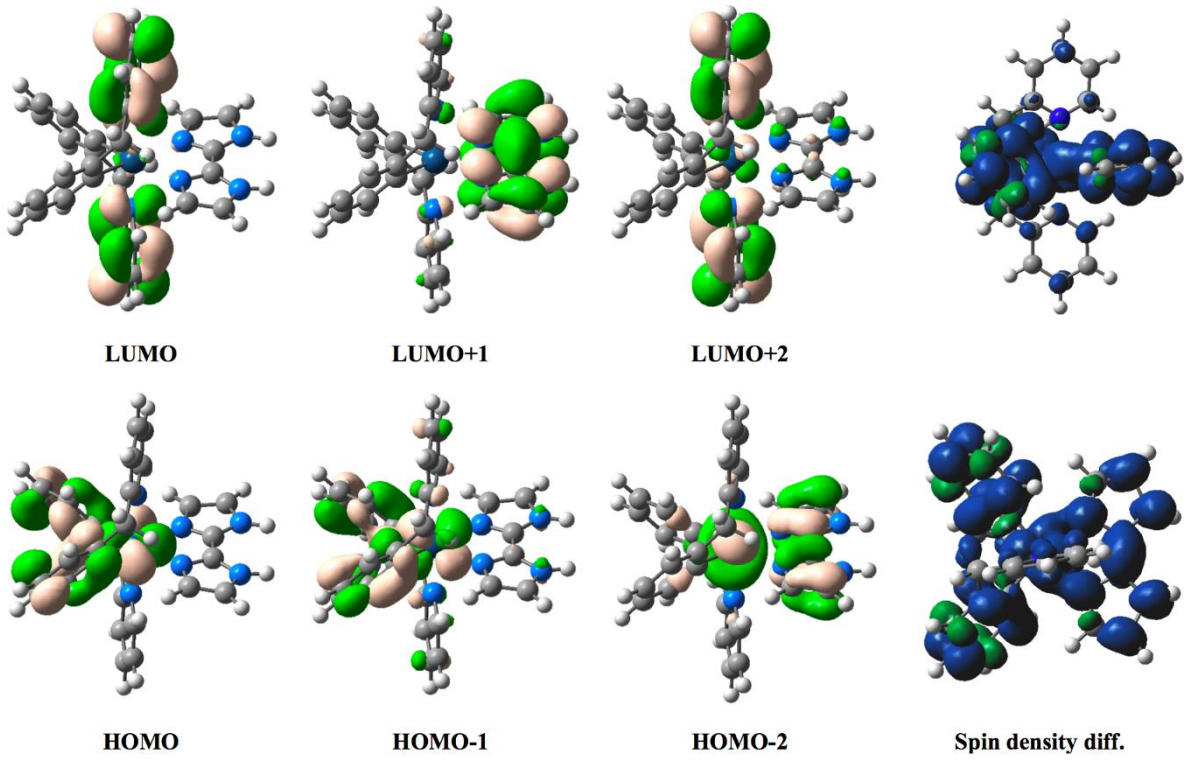

Figure **56**: Left: Representation of the Kohn-Sham molecular orbitals around the HOMO-LUMO gap for **36b**. Right two views of the spin density difference for the lowest triplet state at its optimal geometry.

In **36**, TD-DFT locates the lowest singlet states at higher energy than in **33**, **34** and **35**: 392 nm (*f*=0.001, HOMO-LUMO), 380 nm (*f*=0.001, HOMO-LUMO+1), 359 nm (*f*=0.007, HOMO-LUMO+2) and 353 nm (*f*=0.165, HOMO-1-LUMO+1). The topology of the MOs of **36b** are displayed in Figure **56** and it is notable that the LUMO and LUMO+1 are inverted compared to **35**, but the nature of the most intense low-lying intense CT band is conserved.

The photoluminescence properties of **33**, **34**, **35** and **36** were investigated at 298 K in degassed MeCN and in polymethyl methacrylate (PMMA) doped films (5wt% of complex in PMMA). The spectra are shown in Figure **57a**, whereas Figure **57b** shows the spectra in 2-methyltetrahydrofuran (2-MeTHF) glass at 77 K. The photophysical data of **33** – **36** and their reference complexes are summarised in Table **21**.

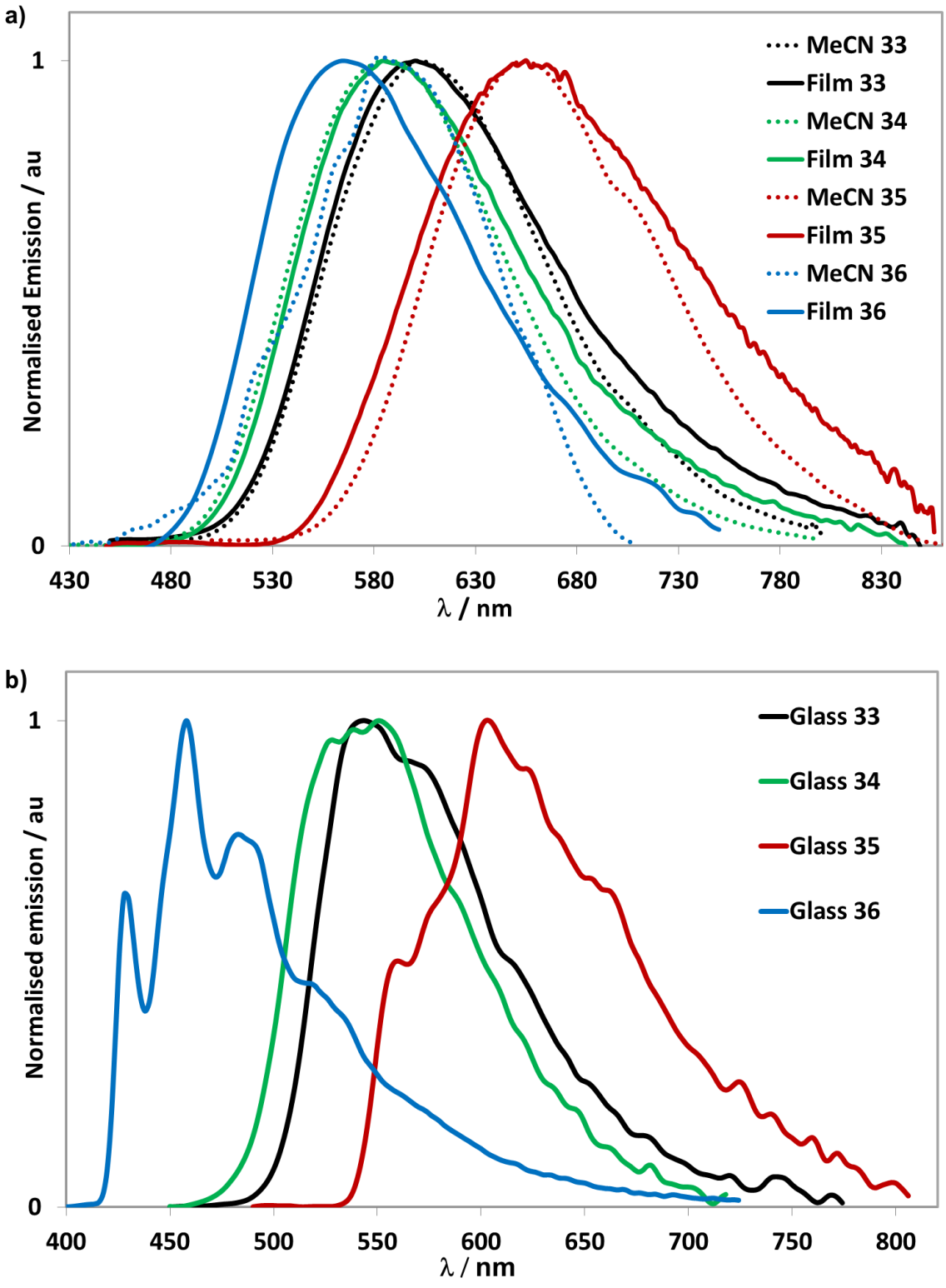

Figure **57**: Photoluminescence spectra of complexes **33** – **36**. a) recorded in MeCN (dotted lines) and PMMA doped films (5wt% of complex in PMMA) in solid lines (λ_{exc} = 420 nm for **33** – **35** and λ_{exc} = 400 nm for **36**). b) recorded in 2-MeTHF at 77 K. λ_{exc} = 420 nm for complexes **33** – **35** and λ_{exc} = 380 nm for **36**.

Table **21**: Photophysical properties of **33**, **34**, **35** and **36** and **12**, **1**, **37** and **38**.

	MeCN[a]			Film[b]			Glass[c]			
	λ_{em}[d] / nm	Φ_{PL}[e] / %	τ_{PL}[f] / ns	λ_{em}[d] / nm	Φ_{PL}[g] / %	τ_{PL}[f] / ns	λ_{em}[d] / nm	τ_{PL}[f] / ns	k_r[h] $\times 10^{-5}$ / s^{-1}	k_{nr}[i] $\times 10^{-5}$ / s^{-1}
33	602	3	26 (25%) 110 (60%) 346 (15%) Average: 124	600	15	124 (11%) 316 (56%) 646 (33%) Average: 404	544, 572 (sh)	2088	2.41	77.97
34	585	8	52 (29%) 215 (58%) 1038 (13%) Average: 275	584	21	99 (4%) 318 (43%) 695 (53%) Average: 509	528, 536, 552	2120	2.91	33.49
35	655	3	54 (79%) 95 (19%) 532 (2%) Average: 71	655	7	93 (16%) 254 (57%) 605 (27%) Average: 323	604	2363	4.20	135.95
36	580[j]	0.5	17 (3%) 131 (60%) 420 (37%) Average: 235	565[j]	1	49 (2%) 361 (23%) 1482 (75%) Average: 1196	428, 458, 484, 534 (sh)[k]	4423	0.21	42.43
12[l]	602	9	275			-	542	4770[m]	3.4	33
1[l]	591	27	386			-	473	4550[m]	7.0	19
37[n]	658	2	81			-	-	-	2.12	121.33
38	489, 512 (sh)	66	361 (27%) 720 (51%) 1761 (22%) Average: 852			-	-	-	7.75	3.99

[a] In deaerated MeCN at 298 K; [b] at 298 K, spin-coated from a 2-methoxyethanol solution of 5wt% of the complex in PMMA on a quartz substrate; [c] in 2-MeTHF at 77 K, if not specified differently; [d] λ_{exc} = 420 nm, if not specified differently; [e] $[Ru(bpy)_3](PF_6)_2$ in MeCN as reference (Φ_{PL} = 1.8% in aerated MeCN at 298 K);[9] [f] λ_{exc} = 378 nm, average weighted lifetimes were determined according to equation $\tau_{PL,avg} = \Sigma A_i \tau_i$ (A_i = pre-exponential factor of the ith lifetime τ_i); [g] Measured using an integrating sphere; [h] $k_r = \Phi_{PL,MeCN} / \tau_{PL}$; [i] $k_{nr} = [(1 - \Phi_{PL,\ MeCN})/ \tau_{PL}]$; [j] λ_{exc} = 400 nm; [k] λ_{exc} = 380 nm; [l] from ref [187]; [m] Measured in 1/1 MeOH/EtOH glass state at 77 K; [n] from ref [188].

Upon photoexcitation (λ_{exc} = 420 nm for **33** – **35** and 400 nm for **36**) each of the emission profiles observed at room temperature is broad and unstructured, which is consistent with an emission from a mixed MLCT/LLCT state (Figure **57a**), similar in character to that observed for their reference complexes. In solution, the emission maxima are ordered from 580, 585, 602 and 655 nm for **36**, **34**, **33** and **35**, respectively. The emission energy of **33** is the same as that for **12** (λ_{em} = 602 nm in MeCN).[187] Complexes **34** and **35** are very slightly shifted (6 nm, 174 cm^{-1}, and 3 nm, 70 cm^{-1}) compared to **1** and **37** (λ_{em} = 591 nm in MeCN[187] and λ_{em} = 658 nm in MeCN).[188] Comparing **36** to **38** (λ_{em} = 489 nm) a much larger shift of 91 nm (3208 cm^{-1}) is observed.

The photoluminescence quantum yields in MeCN ($\Phi_{PL,\ MeCN}$) for **33** – **36** are low (<10%) and each complex shows a Φ_{PL} that is reduced compared to the corresponding reference complexes, except complex **35**. For instance, the $\Phi_{PL,\ MeCN}$ for **33** and **34**, at 3% and 8%, are lower than that of **12** and **1**, at 9% and 27%, respectively.[187] The $\Phi_{PL,\ MeCN}$ for **35** is 3%, which is similar to that for **37** (2%).[188] Complex **36** is very weakly emissive with a $\Phi_{PL,\ MeCN}$ smaller than 1%, significantly lower than its **38** counterpart ($\Phi_{PL,\ MeCN}$ = 66%), showing the deleterious effect of the bnpy ligand in this case. Note that **36** is the only complex in the series for which conformer a is the most stable in the ground electronic state at room temperature, and this specific arrangement has an influence on the resulting photophysical properties as shown by DFT studies (see below). The increased conformational flexibility of the C^N ligands is the likely culprit for the reduced Φ_{PL} values in **33** – **36** compared to the reference complexes. To gain more insights, we performed DFT optimisations of the lowest triplet excited-states. We computed a 0-0 phosphorescence wavelength of 654 nm, 620 nm, 793 nm and 510 nm for **33**, **34**, **35** and **36**, respectively. Despite the obvious fact that the absolute DFT values do not perfectly match the experimental values (ca. 0.22 eV average error compared to the λ_{em} maxima in solution), we note that the theoretical **36** < **34** < **33** < **35** ranking does match the experimental

trend. More importantly, in the triplet state, DFT predicts that conformer b is always the most stable, even for **36**. This suggests that, after intersystem crossing, which is generally very efficient in Ir-complexes, **36** might change conformation before phosphorescence takes place, which would obviously be detrimental for the photoluminescence quantum yield. In turn, this might explain why **36** is the poorest emitter of the series.

Complexes **33**, **34**, **35** and **36** all exhibit a three-component decay in the sub-microsecond regime (Table **21**). The weighted average lifetimes, τ_{PL}, for **33** – **36** are 124, 275, 71 and 235 ns, respectively, and are shorter compared to their reference complexes (τ_{PL} = 275, 386, 81, 852 ns for **12**, **1**, **37** and **38**, respectively).[187,188] From these values, radiative and non-radiative rate constants in MeCN can be estimated. The radiative rate constants, k_r, for **33** (2.41×10^5 s^{-1}) and **34** (2.91×10^5 s^{-1}) are similar and much larger than that for **36** with $k_r = 0.21 \times 10^5$ s^{-1}. These complexes (**33**, **34** and **36**) all possess much smaller k_r than their reference complexes (**12**, **1** and **38**). Complex **35** shows the highest radiative rate constant with $k_r = 4.2 \times 10^5$ s^{-1}, which is also higher than **37** ($k_r = 2.12 \times 10^5$ s^{-1}). However, complex **35** also shows the highest non-radiative rate constant k_{nr} value (135.95×10^5 s^{-1}), and which is slightly higher than the value of **37** ($k_{nr} = 121.33 \times 10^5$ s^{-1}). Complex **33** ($k_{nr} = 77.97 \times 10^5$ s^{-1}) shows a higher k_{nr} than **34** (33.49×10^5 s^{-1}), which can be explained in part by the red-shifted emission of **33** compared to that of **34**. Compared to their reference complexes, both **33** and **34** shows much higher k_{nr} values ($k_{nr} = 33 \times 10^5$ s^{-1} for **12** and $k_{nr} = 19 \times 10^5$ s^{-1} for **1**). The poorly emissive complex **36** possesses a k_{nr} of 42.43×10^5 s^{-1}, which is much higher than the value for **38** (3.99×10^5 s^{-1}).

The emission energies in PMMA-doped films (5wt% of complex in PMMA) are not significantly changed compared from those in MeCN. The emission maxima in **33** – **35** remain essentially unchanged whereas complex **36** shows a modest blue shift of 15 nm (458 cm^{-1}) in the film. The photoluminescence quantum yields of the films ($\Phi_{PL,PMMA}$) are expectedly

significantly increased compared to the solution-state measurements and range from 1% (for **36**) to 7% (for **35**) to 15% (**33**) to 21% (**34**). The increase in Φ_{PL} in the doped films is attributed mainly to a reduction in k_{nr} due to the expected limitations of the conformational motion of the C^N ligands. Each of **33**, **34**, **35** and **36** in doped films exhibit a three-component emission decay in the sub-microsecond regime. The weighted average lifetimes for **33**, **34**, **35** and **36** are 404, 509, 323 and 1196 ns, respectively, which are on average longer than in those measured in solution-state.

The low-intensity emission spectra at 77 K in 2-MeTHF glasses of **33**, **34**, **35** and **36** are noisy. Figure **57b** shows the smoothed emission profiles. A significant hypsochromic shift is observed compared to the measurements at 298 K, both in MeCN and as doped films. For instance, the profile for complex **33** shows an emission maximum at 544 nm and a shoulder at 572 nm resulting in a blue shift of 58 nm (900 cm^{-1}) for the $E_{0,0}$ peak compared to the spectrum in MeCN at 298 K with almost no shift compared to the emission of **12** in the 2-MeTHF glass (λ_{em} = 542 nm). The blue shift is less pronounced for **34** (33 nm, 1022 cm^{-1}), with peaks at 528, 552 and 536 (λ_{em} = 552 nm). However, compared to **1** the highest intensity emission peak of complex **34** shows a significant red shift of 79 nm (3026 cm^{-1}). For complex **35** the normalised profile is centred at 604 nm (blue shift of 51 nm, 1289 cm^{-1} compared to the spectrum in MeCN). Complex **36** (λ_{exc} = 380 nm) is also very poorly emissive and the profile shows two moderately intense bands at 428 nm and 484 nm (and a shoulder at 534 nm) and the λ_{em} located at 458 nm shows significant blue shift compared to the spectrum in MeCN (122 nm, 4593 cm^{-1}). The monoexponential emission lifetimes at 77 K in the microsecond regime are significantly longer compared to both sets of room-temperature measurements and range from 2088 ns (**33**), to 2120 ns (**34**), to 2363 ns (**35**) and 4423 ns (**36**). Compared to the reported emission lifetimes at 77 K of **12** (4770 ns) and **1** (4550 ns),[187] **33** and **34** show significantly shorter lifetimes.

Conclusions

A new series of four cationic Ir(III) complexes bearing nonconjugated C^N ligands, using the bnpy ligand for the first time in luminescent Ir(III) complexes, have been synthesised and fully characterised. Comparative studies with the related series of ppy-based complexes show the impact of the methylene spacer present within the cyclometalated ligand on the electrochemical and photophysical properties. Analysis of the X-ray crystal structures for three of the complexes clearly illustrates the existence of two possible conformations. Depending on the nature of the ancillary ligand, phosphorescence ranging from yellow to deep red is observed in MeCN as well as in 5wt% PMMA doped films. Variable-temperature ^{1}H and 2D ROESY-NMR studies show the presence of two conformers for complex **35** as a result of the fluxional behaviour of the bridging methine group of the cyclometalated bnpy ligand, which is consistent with DFT calculations yielding a small free energy difference but a rather large barrier to interconversion between the two conformers. DFT calculations suggest that the transition from one conformation to the other is a concerted process in which the two ligands simultaneously change their conformation. A similar behaviour is observed **36**, but for this complex the major conformer is the opposite to the one observed for **35**. Under the same conditions, however, complexes **33** and **34** only show one conformer in the ^{1}H NMR at room temperature. All four complexes show quasi-reversible oxidation waves. Complexes **33 – 35** show quasi-reversible reduction waves while no reduction wave was detected within the solvent window for **36**. Compared to their reference complexes, **33 – 36** emit at similar energies but show much lower photoluminescence quantum yields and shorter emission lifetimes. DFT calculations predict that conformer b is the most stable in the triplet state for **33**, **34**, **35** and **36**. Breaking the conjugation of the C^N ligands did not change the triplet energy of the complexes despite reducing the electrochemical gap. This detailed joint theoretical and experimental study provides a better understanding of the role of the methine spacer in the 2-benzylpyridinato cyclometalating ligands within this new series of Ir(III) complexes.

Chapter 5

Neutral Ir(III) complexes bearing an unusual bis(six-membered) chelating tridentate tripod ligand of the form [Ir(C^N^C)(N^N)Cl]

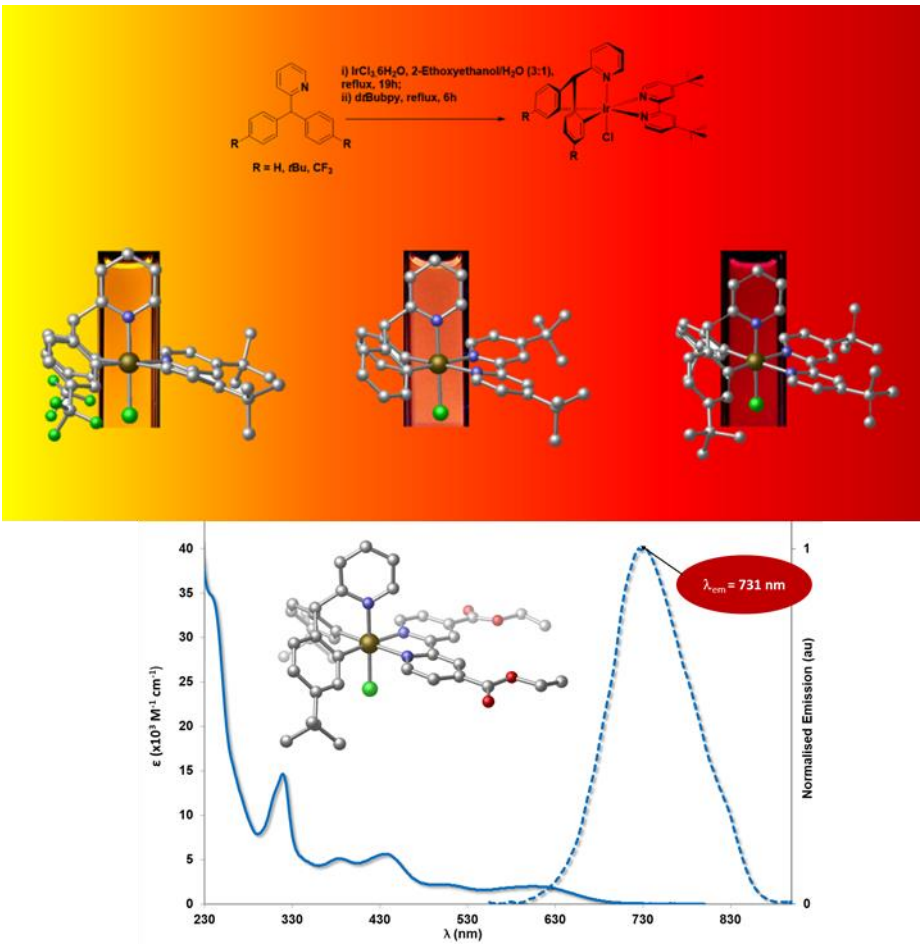

Cover picture: TOC graphics of publications arising from this chapter

Introduction

As mentioned in Chapters 1 and 4, nearly all of the photoactive iridium(III) complexes that are used as emitters in electroluminescent devices,[22,23,53,54,214] as dyes in solar cells,[59,215,216] in non-linear optics (NLO),[34,151,217] as photoredox catalysts,[61,62] as solar fuels[60] and in bioimaging[25,26] contain conjugated five-membered chelated ligands, such as the commonly used 2-phenylpyridine (ppyH), 2,2'-bipyridine (bpy), acetylacetonate (acac) and picolinate (pic). Photoactive iridium complexes bearing a six-membered cyclometalating chelate are very rare, and the few reported examples can be categorised into two families of complexes: those containing conjugated[92,94,208,209] or non-conjugated[95–97] bidentate cyclometalating ligands. As mentioned in Chapter 1 disrupting the conjugation of the C^N ligand may lead to a blue shift of the emission energy.

In an on-going effort in our group to develop charged blue-emitting phosphors for solution-processed light-emitting electrochemical cells (LEECs) and organic light emitting diodes (OLEDs), we investigated the coordination of 2-benzhydrylpyridine ($bhpyH_2$) derivatives with Ir(III) to access six-membered chelate complex **T1-T3** (Figure **58**).

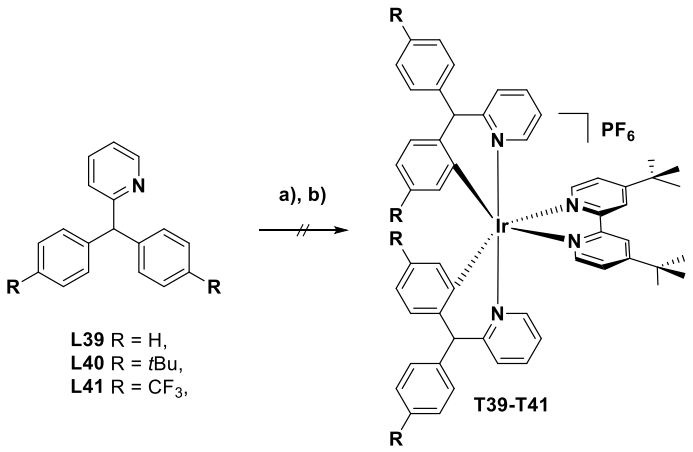

Figure **58**: Synthetic pathway for the synthesis of the initial target **T39-T41** . a) i) $IrCl_3.6H_2O$, 2-ethoxyethanol/H_2O (3:1), reflux, 19 h; ii) d*t*Bubpy, reflux, 6 h. b) aq. NH_4PF_6.

Surprisingly given the prior art, upon sequential treatment of $IrCl_3.6H_2O$ with $bhpyH_2$ and then 4,4'-di*tert*-butyl-2,2'-bipyridine (d*t*Bubpy) in a one-pot reaction,[187] **T39** was not obtained. Instead, neutral complex [Ir(bhpy)(d*t*Bubpy)Cl], **39**, was isolated (Figure **59**).

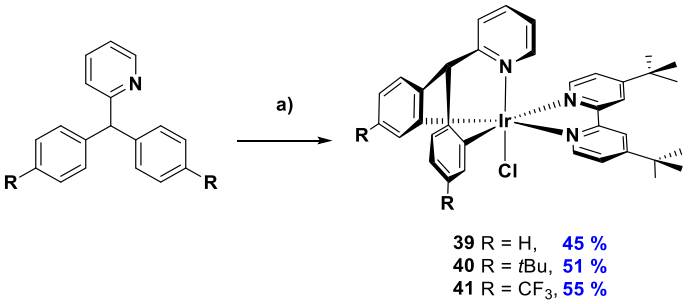

39 R = H, **45 %**
40 R = *t*Bu, **51 %**
41 R = CF_3, **55 %**

Figure **59**: Synthetic pathway for the synthesis of complexes **39-41** a) i) $IrCl_3.6H_2O$, 2-ethoxyethanol/H_2O (3:1), reflux, 19 h; ii) d*t*Bubpy, reflux, 6 h.

The formation of **39** arises from a highly unusual double C-H bond activation of the $bhpyH_2$ ligand, which binds to the iridium in a tripodal fashion. Following a similar synthetic protocol, analogues **40** and **41**, functionalised with either electron-donating *tert*-butyl or electron-withdrawing trifluoromethyl groups meta to the Ir-C bonds were obtained (Figure **59**). To the best of our knowledge, this is the first report of an iridium complex of the form [Ir(C^N^C)(N^N)Cl] and one in which the tridentate bis-cyclometalated C^N^C ligand is a tripod featuring two six-membered metallacycles.[218] Indeed, the complex with the closest binding motif is [Ir(bppy)(bpy)Cl],[219] **42** where bppy is 2-([1,1'-biphenyl]-3-yl)pyridine (Figure **60**).

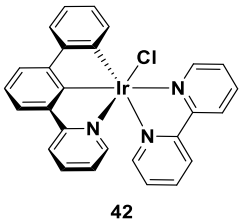

42

λ_{em} = 725 nm

Figure **60**: Ir(III) complex of the form [Ir(C^C^N)(N^N)Cl] with a planar C^C^N ligand

This previous complex possesses a related [Ir(C^C^N)(N^N)Cl] structure but the bppy ligand coordinates to the iridium in the more commonly observed planar five-membered chelate fashion; it is a very poorly luminescent near-IR emitter in CH_2Cl_2 (λ_{em} = 725 nm, Φ_{PL} = 0.084%).[219] Ir(III) complexes bearing monocyclometalating planar tridentate bis(five-membered) chelate ligands (e.g., N^N^C[219] or N^C^N[220–225]) and a cyclometalating bidentate ligand, C^N, have on the other hand been more widely explored while Kozhevnikov have reported dinuclear Ir(III) complexes with a bridging ligand featuring two N^C^N motifs.[226,227]

Modification of the cyclometalating ligand

Results and Discussion

Ligand Synthesis

Compounds **L39**, **L40** and **L41** (Figure **61**) were synthesised in two steps via a Grignard reaction[228] followed by a reduction step[228] and obtained as solids in good yields. In the first step elemental Mg was reacted with the corresponding bromo-arene followed by the addition of half of an equivalent of methyl picolinate to obtain the intermediate alcohols **A39-A41** (Figure **61**).

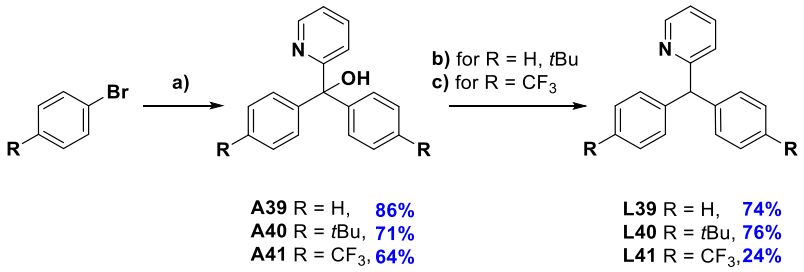

Figure **61**: Synthetic pathway for the synthesis of intermediates **A39-A41** and target ligands **L39-L41**. a) 1. Mg, 1,2-dibromoethane, THF, N_2, reflux, 4 h. 2. methyl picolinate, THF, 0 °C - r.t., 90 min; b) 1. HOAc, 57% HI, 100 °C, 4 h. 2. $NaOH_{aq}$., 0 °C - r.t.; c) 1. PBr_3, reflux, 2 h. 2. Zn, HOAc, 3. $NaOH_{aq}$., 0 °C - r.t.

Compounds **L39** and **L40** were obtained in good yields in HOAc and in the presence of HI (57%) according to a procedure for similar molecules.[228] However, the hydroxyl group in

intermediate **A41** could not be reduced under these conditions. The compound **L41** was obtained in moderate yields from **A41** by a bromination with PBr_3 followed by reduction with zinc in HOAc at room-temperature (Figure **61**).[229]

Complex Synthesis

Initially, the complexes were synthesised following Nonoyama's method,[65] in which a dimer complex is obtained from refluxing $IrCl_3.6H_2O$ in 2-ethoxyethanol mixture of the corresponding proligand followed by a dimer cleavage reaction in a CH_2Cl_2/MeOH mixture (1:1) with a slight excess of the ancillary ligand.[187] However, we found the intermediate species to be difficult to characterise through NMR spectroscopy and HR-ESI mass spectra due to very low solubility. For instance, the intermediate species to obtain complex **39** is green and is not soluble in organic solvents (e.g. CH_2Cl_2, $CHCl_3$, MeOH or MeCN) nor H_2O. Besides, this intermediate is characterised through low stability compared to classical Ir-dimer species. In DMSO solution this intermediate complex decomposed quickly (within 2 days). Adding the *tert*-butyl groups on the ligand increased the solubility in organic solvents (such as CH_2Cl_2 or $CHCl_3$) of the intermediate species significantly but did not increase stability in solution. Nevertheless, the isolated intermediate was used as such and the reaction was carried on following the cleavage reaction obtaining the desired complexes **39-41** in however unknown yields in this two-step synthesis. To address the issue of unknown yields, complexes **39-41** were prepared in a one-pot synthesis as follows: A mixture of the corresponding proligand and $IrCl_3.6H_2O$ in 2-ethoxyethanol/H_2O (3:1) was refluxed. After 19 h, the ancillary ligand 4,4′-di-*tert*-butyl-2,2′-bipyridine was added at once and heating was continued for 6 h to give the neutral complexes **39-41** as solids in 45%, 51% and 55% yield, respectively.

Complexes **39-41** were characterised by ^1H, ^{13}C and, for **41**, ^{19}F NMR spectroscopy in CD_2Cl_2, HR-ESI mass spectra, elemental analysis and melting point determination. A characteristic signal in the ^1H NMR is the C-H of the bridging carbon in the C^N^C ligand

appearing as a singlet around 5.5 – 5.0 ppm. Depending on the substitution, this bridging carbon gives rise to a signal at around 69.0 ppm in the ^{13}C NMR spectra. Two quartets are detectable in the ^{13}C NMR arsing from the CF_3 and the 5 position of the phenyl of the C^N^C ligand. In the ^{19}F NMR the CF_3 are detected as a singlet at – 61.58 ppm. The detected characterising ion in HR-ESI mass spectroscopy corresponds to the structure with a removed Cl^- ion. The detected species in elemental analysis includes the Cl^- monodentate ligand.

Crystal Structures

Single crystals of sufficient quality of **39-41** were grown from CH_2Cl_2/Et_2O at -18 °C. The structures of **39-41** were determined by single-crystal X-ray diffraction (Figure **62**, Table **22**).

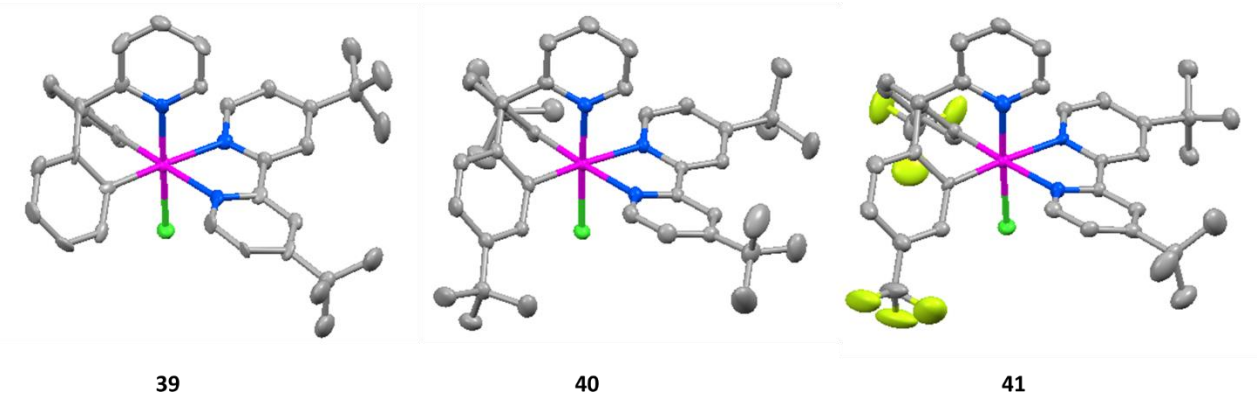

Figure **62**: X-ray crystal structure of **39-41**. Hydrogen atoms and solvent molecules have been removed for clarity. Colour codes for atoms are: C = light grey, N = blue, F = yellow, Cl = green and Ir = magenta.

All three complexes possess a distorted octahedral geometry with the tridentate tripod ligand coordinated to the iridium to form three six-membered chelated rings. Both cyclometalating carbon atoms are *trans* to the pyridine rings of the d*t*Bubpy and the pyridyl unit of the bhpy-type ligands is *trans* to the chloride. This contrasts with the configuration of the Ir-Cl bond in previously reported Ir(III) complexes,[219–221,226,227,230] where an Ir-C bond is *trans* to the chloride ligand.

Table **22**: Selected crystallographic parameters for complexes **39**-**41**.

Complex	**Bond Length / Å**				**Bond Angle / °**	
	Ir-$C_{C^N^C}$	Ir-$N_{C^N^C}$	Ir-N_{N^N}	Ir-Cl	N-Ir-N	C-Ir-C
39	2.048(13) 2.064(6)	2.055(11)	2.158(10) 2.159(11)	2.375(3)	75.60(4)	85.60(5)
40	2.028(4) 2.031(3)	2.044(3)	2.127(3) 2.140(3)	2.3612(8)	75.85(12)	85.65(15)
41	2.017(7) 2.027	2.032(7)	2.122(6) 2.133(5)	2.369(2)	76.1(2)	84.(3)

For **39**-**41** the Ir-Cl bond [2.375(3) Å for **39**, 2.3612(8) Å for **40** and 2.369(2) Å for **41**] is in the same range as that found for $[Ir(tpy)(dmbpy)Cl]^{2+}$ (2.357 Å, where tpy = 2,2':6',2''-terpyridine and dmbpy = 4,4'-dimethyl-2,2'-bipyridine)[231] but is significantly shorter (by ca. 0.1 Å) than the Ir-Cl bond in other cyclometalated tridentate Ir(III) complexes.[219–221,226,227,230] Given the short Ir-$C_{C^N^C}$ bonds [2.048(13) and 2.064(6) Å for **39**, 2.028(4) and 2.031(3) Å for **40** and 2.017(7) and 2.027 Å for **41**], this leads also to a correspondingly shorter Ir-$N_{C^N^C}$ bond [2.055(11) Å for **39**, 2.044(3) for **40** and 2.032(7) Å for **41**] compared to the Ir-N_{N^N} bonds [2.158(10) and 2.159(11) Å for **39**, 2.127(3) and 2.140(3) Å for **40** and 2.122(6) and 2.133(5) Å for **41**]. The bite angle of the N^N ligand is unremarkable at 75.60(4)° for **39**, 75.85(12)° for **40** and 76.1(2)° for **41** and in line with cationic Ir(III) complexes of the form $[Ir(C^N)_2(N^N)]^+$.[133,232,233] Owing to the presence of the six-membered chelates, the C-Ir-C bond angle is significantly larger [85.60(5)° for **39**, 85.65(15)° for **40** and 84.(3) for **41**] than the N_{N^N}-Ir-N_{N^N} bond angle.

Electrochemical properties

The electrochemical behaviour for **39-41** was evaluated by cyclic voltammetry (CV) and differential pulse voltammetry (DPV) in deaerated CH_2Cl_2 solution at 298 K at a scan rate of 50 mV s^{-1} using Fc/Fc^+ as the internal reference and referenced with respect to SCE (0.46 V vs. SCE).[234] The voltammograms are shown in Figure **63** and the electrochemistry data can be found in Table **23**.

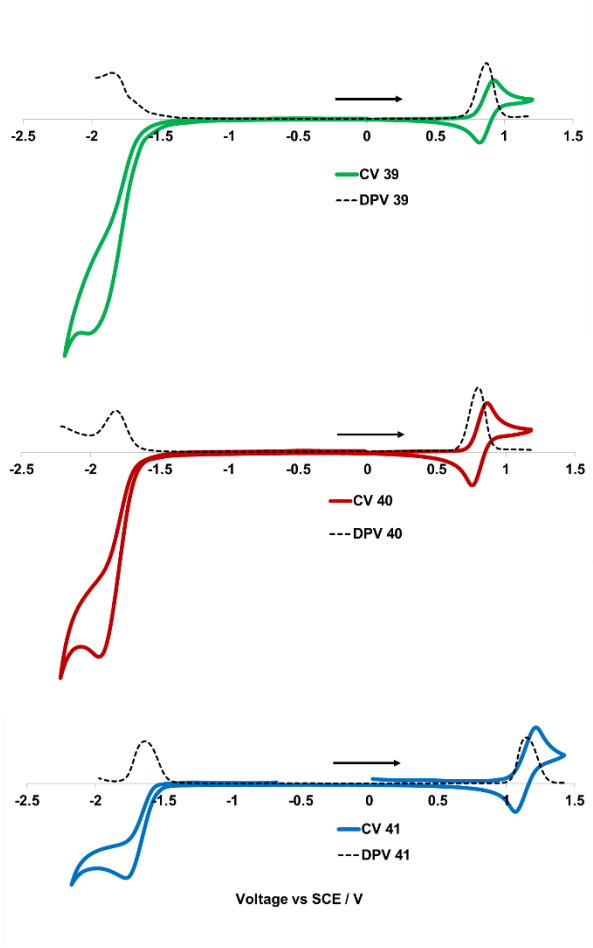

Figure **63**: Cyclic voltammograms (in solid lines) and differential pulse voltammetry (in dotted lines) for **39 – 41** carried out in degassed CH_2Cl_2 at a scan rate of 50 mV s^{-1}, with Fc/Fc^+ as the internal reference, referenced to SCE (0.46 V vs. SCE).[234]

All complexes exhibit a quasi-reversible single electron oxidation peak, which is assigned to the Ir(III)/Ir(IV) redox couple with contributions from the bhpy-type ligand. Complex **40** displays a lower oxidation potential (0.80 V) than **39** (0.87 V), both of which are notably lower

than [Ir(mesppy)$_2$(d*t*Bubpy)]PF$_6$, **21** ($E_{1/2;ox.}$ = 1.17 V in deaerated CH_2Cl_2, where mesppy is 2-phenyl-4-mesityl-pyridinato).[235] Conversely, **40** shows a significantly anodically shifted oxidation potential at 1.14 V.

Table **23**: Selected electrochemical data for complexes **39**-**41**.

	Electrochemistry[a]					
	$E_{1/2}^{ox}$ / V	ΔE_p / mV	$E_{1/2}^{red}$ / V	ΔE_{redox}[b] / V	E_{HOMO}[c] / eV	E_{LUMO}[c] / eV
39	0.87	99	-1.82[d]	2.69	-5.21	-2.52
40	0.80	101	-1.81[d]	2.61	-5.14	-2.53
41	1.14	143	-1.62[d]	2.76	-5.84	-2.72

[a] in degassed CH_2Cl_2 at a scan rate of 50 mV s^{-1} with Fc/Fc^+ as internal reference, and referenced with respect to SCE (0.46 V vs. SCE);[234] [b] ΔE_{redox} is the difference (V) between first oxidation and first reduction potentials; [c] $E_{HOMO/LUMO}$ = -[$E^{ox/red}$ vs Fc/Fc^+ + 4.8] eV;[191] [d] irreversible.

The CVs of **39**-**41** show irreversible reduction waves that are monoelectronic as inferred from the respective DPVs. DFT calculations (Figure **64a**) indicate that both the HOMO and HOMO-1, which are close in energy (Figure **65**) involve the iridium and chloride atoms and the two phenyl rings of the bhpy ligand. The LUMO is almost exclusively localised on the d*t*Bubpy ligand while the LUMO+1 is primarily on the pyridyl ring of the bhpy ligand. Therefore, we conclude that the reduction is based on the ancillary ligand. The reduction potentials of **39** and **40** are each found at -1.82 V while the reduction wave of **41** at -1.62 V is anodically shifted by 200 mV compared to **39** and **40**. All three complexes are significantly more difficult to reduce than [Ir(mesppy)$_2$(d*t*Bubpy)]PF$_6$ ($E_{1/2;red.}$ -1.15 V), which also shows an irreversible reduction in CH_2Cl_2.[235]

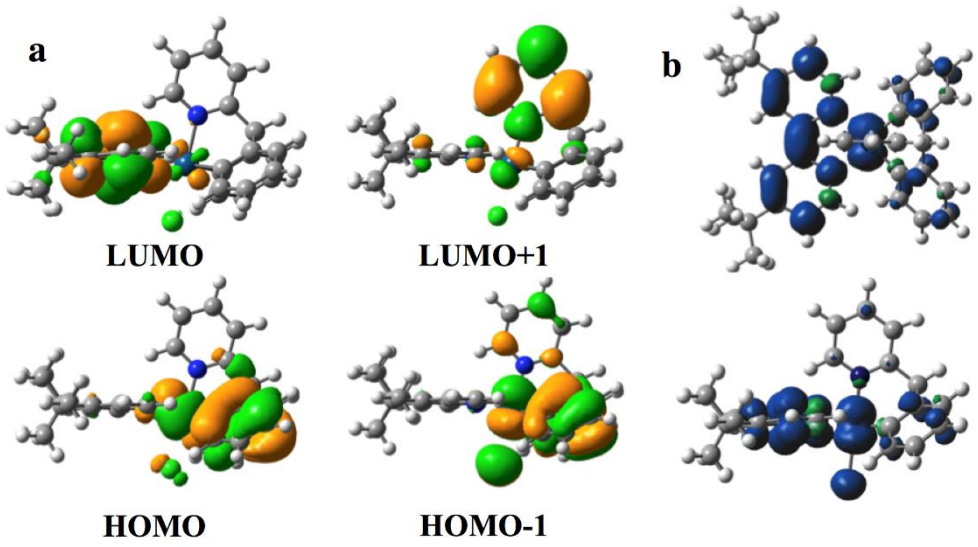

Figure **64**: Computed representations of **39** of a) the four frontier MOs. b) side and top views of the spin density distribution for the lowest triplet state (T_1).

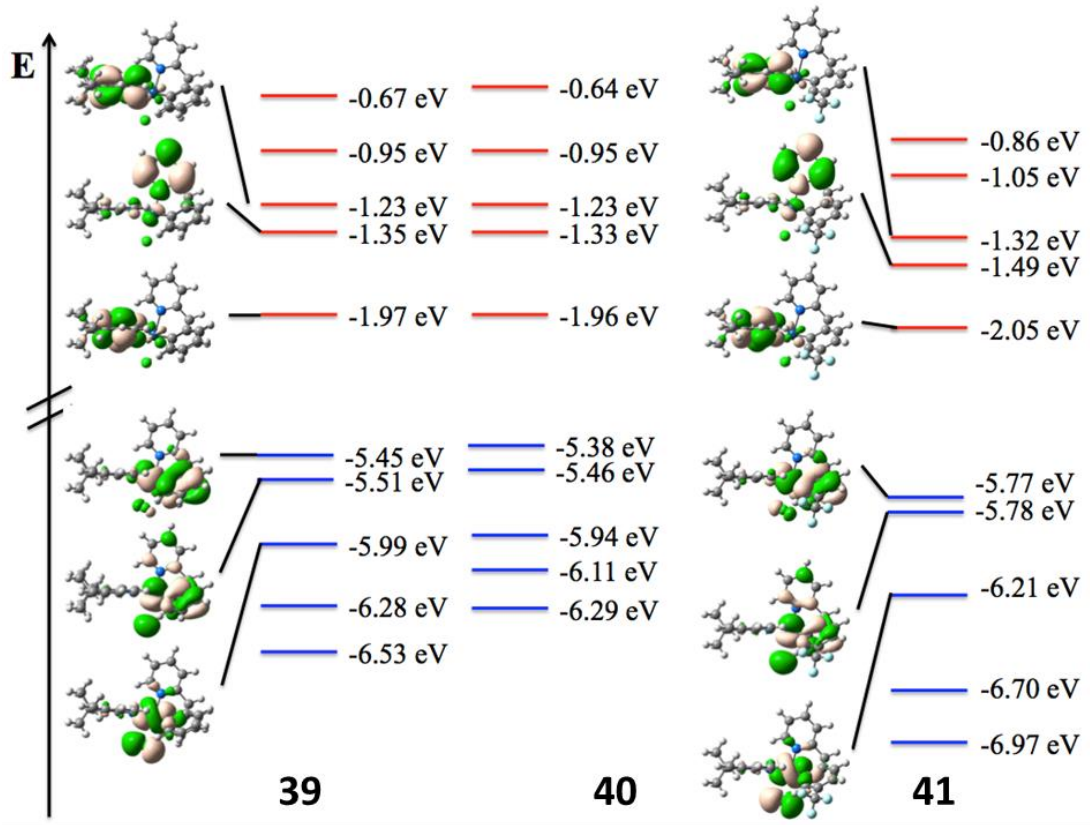

Figure **65**: Energy orbital diagram for **39**, **40** and **41** with representation of the key MOs for **39** and **41**. The blue and red bars represent occupied and unoccupied levels, respectively.

Photophysical properties

The UV-Vis absorption spectra of **39-41** recorded in CH_2Cl_2 at 298 K are depicted in Figure **66** and the data summarised in Table **24**.

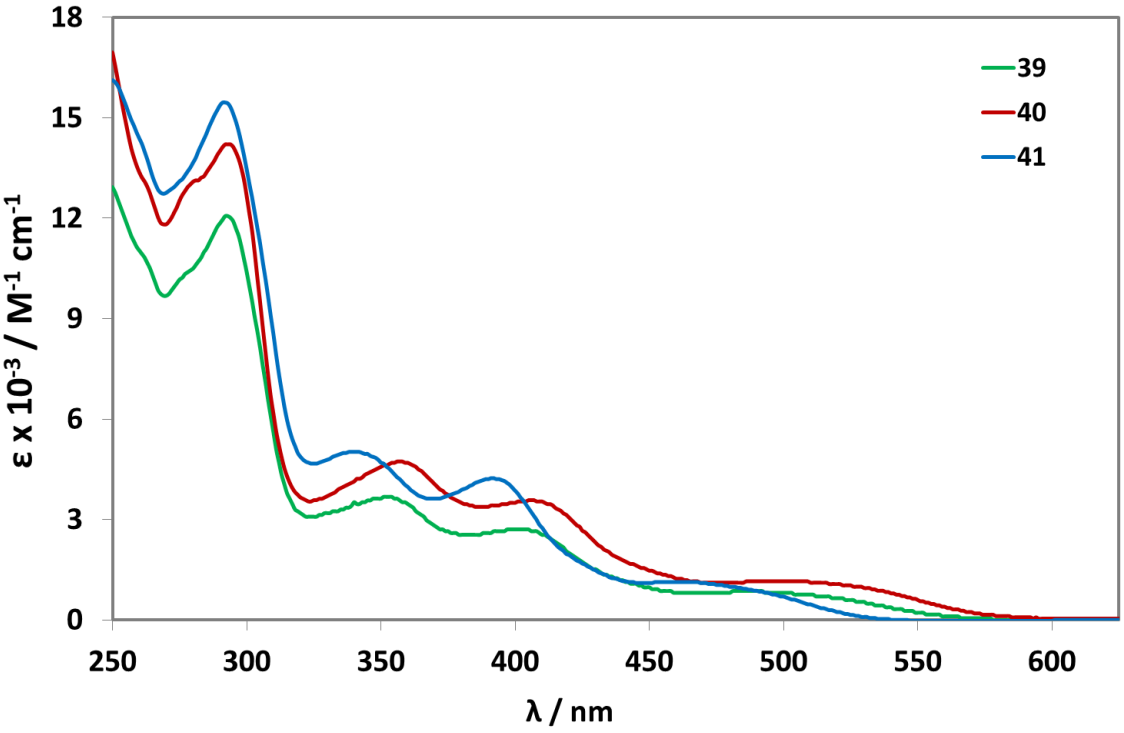

Figure **66**: The UV-Vis absorption spectra of **39-41** in CH_2Cl_2 at 298 K.

All complexes show similar absorption profiles. The invariance of the intense high-energy (ε on the order of 1 – 1.5 × 10^4 M^{-1} cm^{-1}) absorption bands below 300 nm are ascribed to $^1\pi$–π^* ligand-centred (^{1}LC) transitions localised on the d*t*Bubpy ligand. Two moderately intense bands (ε on the order of 3 – 5 x 10^3 M^{-1} cm^{-1}) in the region of 340-360 nm and 390-405 nm are assigned to mixed charge-transfer transitions with the former consisting of more metal-to-ligand/ligand-to-ligand charge-transfer (^{1}MLCT/^{1}LLCT) character while the latter, according to TD-DFT calculations, implicate an intraligand CT (^{1}ILCT) from the phenyl rings to the pyridyl heterocycle of the bhpy-type ligand (Figure **65**).

Table **24**: Photophysical properties of complexes **39-41**.

	λ_{abs}[a] / nm, [ε / $M^{-1}cm^{-1}$]	λ_{em}[b] / nm	Φ_{PL}[b,c] / %	τ_{PL}[d] / ns	k_r[e] × 10^{-5} / s^{-1}	k_{nr}[f] × 10^{-5} / s^{-1}
39	294 [12 008], 355 [3 624], 404 [2 704], 500 [696]	619	8	318	2.52	28.93
40	295 [14 123], 359 [4 697], 405 [3 336], 510 [1 114]	630	6	239	2.51	39.33
41	293 [15 433], 343 [4 989], 393 [4 206], 468 [1 131]	581	26	718	3.62	10.31

[a] in CH_2Cl_2; [b] λ_{exc} = 420 nm, recorded at 298 K in deaerated CH_2Cl_2; [c] $[Ru(bpy)_3](PF_6)_2$ in MeCN as reference (Φ_{PL} = 1.8% in aerated MeCN at 298 K);[9] [d] λ_{exc} = 378 nm; [e] $k_r = \Phi_{PL} / \tau_e$; [f] $k_{nr} = [(1 - \Phi_{PL})/ \tau_e]$.

Weak bands (ε on the order of 10^3 M^{-1} cm^{-1}) with onsets between 470-510 nm and tailing to 580 nm are attributed to a mixture of (^{1}MLCT/^{1}LLCT) and spin-forbidden (^{3}MLCT/^{3}LLCT) transitions involving the d*t*Bubpy ligand. Introduction of the *tert*-butyl groups in **41** results in only a small red-shift of the CT bands below 340 nm whereas the trifluoromethyl groups in **41** produce a significant blue-shift of these bands, trends that are corroborated by TD-DFT calculations (Figure **67**).

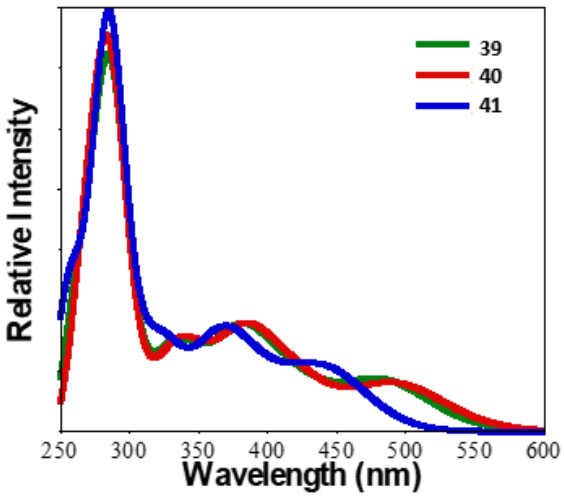

Figure **67**: Theoretical absorption spectra for **39 – 41** computed in the vertical approximation and convoluted with a Gaussian of FWHM of 0.2 eV.

The normalised photoluminescence (PL) spectra of **39-41** in degassed CH_2Cl_2 are shown in Figure **68** and the data are summarised in Table **24**. Upon photoexcitation at 420 nm, all complexes show a broad and unstructured profile, indicative of an emission with mixed CT character. In line with the trends observed in the absorption spectra and the oxidation potentials in the CVs, the emission maxima are 581, 619 and 630 nm for **41**, **39** and **40**, respectively.

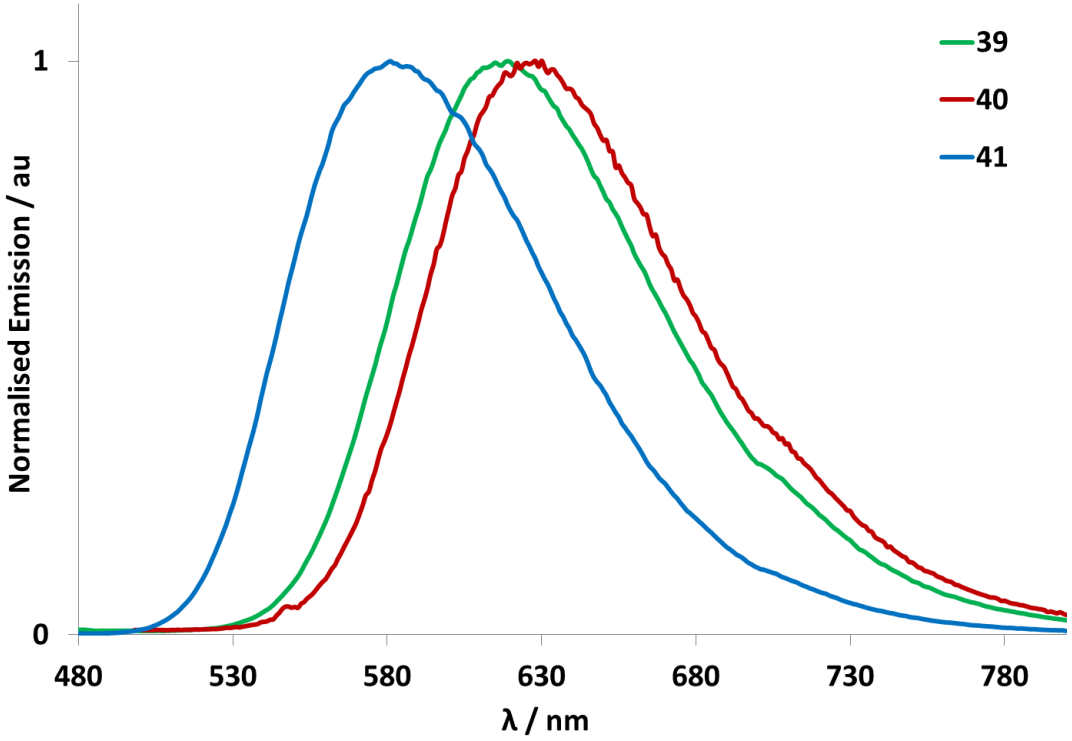

Figure **68**: Normalised emission spectra of complexes **39-41** in deaerated CH_2Cl_2 at 298 K.

These emission maxima match very closely to the vertical phosphorescence energies calculated by spin-unrestricted DFT, which predicts emissions at 573, 613 and 622 nm, respectively. The calculations reveal that the emissive triplet state is localised on the iridium, chlorine and d*t*Bubpy but does not include significant contributions from the bhpy ligand (Figure **64b** and Figure **69**).

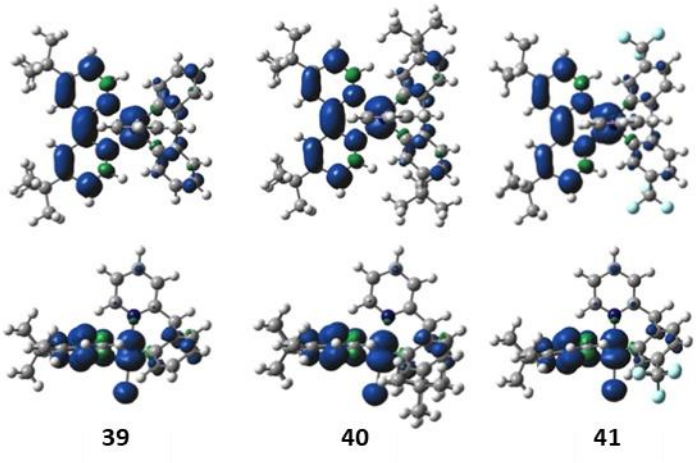

Figure **69**: Density difference plots for **39 – 41** obtained for the lowest triplet state. We show both the top (top) and side (bottom) views. A contour threshold of 0.002 au has been used for all complexes.

The photoluminescence quantum yield (Φ_{PL}) of **39** is 8%, which is lower than that of the yellow-emitting $[Ir(ppy)_2(dtBubpy)]PF_6$ (Φ_{PL} = 64% in CH_2Cl_2, λ_{em} = 570 nm, where ppyH is 2-phenylpyridine).[236] The Φ_{PL} of **40** is 6% while that of **41** is 26%. All three complexes show emission lifetimes, τ_e, in the sub-microsecond regime. The radiative rate constants, k_r, for **39** and **40** are similar (2.52 *vs.* 2.51 × 10^5 s^{-1}, respectively). However, **40** exhibits a significantly larger nonradiative rate constant, k_{nr}, (39.33 × 10^5 s^{-1}) compared to **39** (28.93 × 10^5 s^{-1}). Complex **41** possesses both the largest k_r (3.62 × 10^5 s^{-1}) and the smallest k_{nr} values (10.31 × 10^5 s^{-1}) in accordance with the energy gap law.

Summary

In summary, a new family of luminescent iridium(III) complexes bearing an unprecedented tripodal bis(six-membered) chelate tridentate ligand has been prepared through a highly unusual double cyclometalation reaction. The electrochemical and spectroscopic properties can easily be tuned through substitution on the cyclometalating aryl rings. Through the electron withdrawing groups in **41** a blue shift in the emission energy is observed and oxidation is shifted to higher potentials. The opposite effect is observed when introducing

electron donating groups in **40**. DFT calculations support a mixed charge-transfer emission. Efforts are focused on further modulating the electronics through a combination of modifications of the ancillary diimine and the monodentate chloride ligands.

This unprecedented tripodal ligand will open new perspectives for the design of tridentate Ir luminophores.

Substitution attempts of Ir-Cl bond

After the preparation and full characterisation of complexes **39-41**, efforts were focussed on further modulating the electronics through substitution of the monodentate chloride ligand. In 2006, Haga[220] and co-workers reported a complex of the form [Ir(Mebib)(ppy)X] [where Mebib is bis(*N*-methyl-2-benzimidazolyl)benzene and X = Cl for complex **42**, and X = CN for complex **43**, Figure **70**]. In CH_2Cl_2 solution, **42** exhibits a λ_{em} = 555 nm. Upon substitution of Cl^- by CN^- a significant blue-shift of 29 nm (993 cm^{-1}) was obtained (λ_{em} = 526 nm for complex **43**). Another recent example of substitution of a monodentate chloride ligand was demonstrated by Hanan *et al.* with ruthenium polypyridyl complexes of the form [Ru(pytpy)(bpy)X][237] (where pytpy is 4,4''-di-*tert*-butyl-4'-(pyridin-4-yl)-2,2':6',2''-terpyridine, Figure **70**). Through substitution of the Cl^- by neutral MeCN or pyridine the single positively charged complex **44** was converted into the twice positively charged **45**, which was used as a precursor for self-assembly to form squares, or **46**, which was used as a model complex.[237]

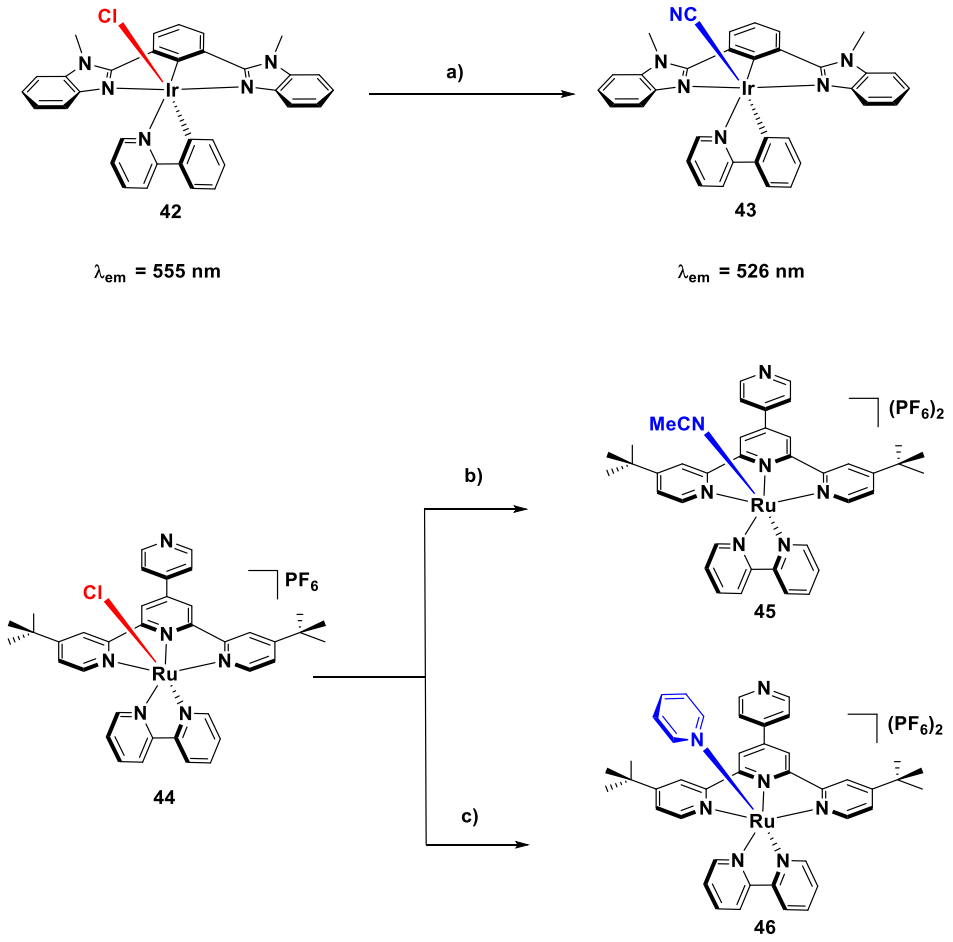

Figure **70**: Structural presentation of transition metal complexes bearing planar tridentate and bidentate ligands and a monodentate ligand. a) KCN, microwave irradiation (650 W), ethylene glycol, 5 min; b) 1. MeCN, AgOTf, Δ; 2. aq. KPF_6.; c) 1. Pyridine, AgOTf, 5 days, Δ. 2. aq. KPF_6.

Inspired by this work, we designed different targets. For complexes **T1-T4** we targeted to substitute the chloride with another negatively charged monodentate ligand and in case of **T5-T6** the monodentate ligand was neutrally charged to form a positively charged complex (Figure **71**).

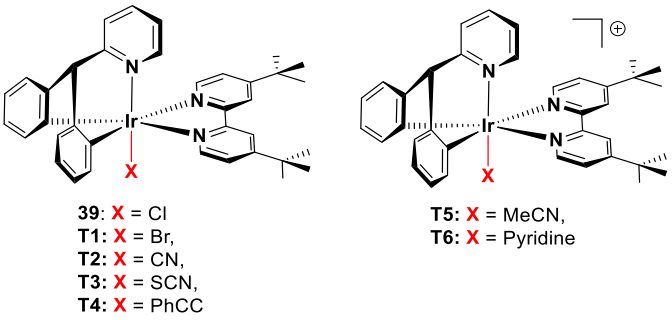

Figure **71**: Structural presentation of complex **39** and designed target complexes bearing different monodentate ligands.

Results and Discussion

Several attempts were carried out to obtain target complexes **T1-T4** using various conditions (Figure **72**, Table **25**)

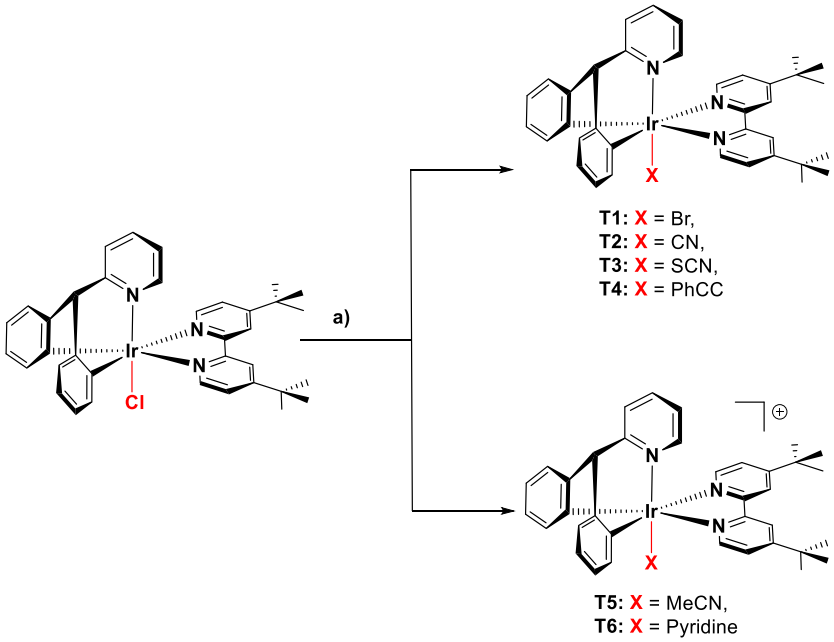

Figure **72**: Synthetic pathway for substitution Ir-Cl. a) reaction conditions see Table **25**.

Table **25**: Reaction conditions carried out for the synthesis of **T1-T4**.

Entry	Target Complex with X	Starting Material for Monodentate Ligand X	Solvent[b]	T / °C	Time / h	Silver salt
1	**T1 X = Br**	**NaBr**	CH_2Cl_2 / MeOH	40	2	$AgPF_6$
2	**T1 X = Br**	**NaBr**	CH_2Cl_2 / MeOH	40	18	$AgPF_6$
3	**T2 X = CN[a]**	**NaCN[a]**	CH_2Cl_2 / MeOH	40	0.5	$AgPF_6$
4	**T2 X = CN[a]**	**NaCN[a]**	CH_2Cl_2 / MeOH	40	2	$AgPF_6$
5	**T2 X = CN[a]**	**NaCN[a]**	CH_2Cl_2 / MeOH	r.t.	18	$AgPF_6$
6	**T3 X = SCN**	**NaSCN**	MeCN	40	96	AgOTf
7	**T3 X = SCN**	**NaSCN**	MeCN / CH_2Cl_2	40	96	AgOTf
8	**T5 X = PhC_2**	**Li-CCPh**	THF	50	18	-
9	**T5 X = MeCN**	**MeCN**	MeCN	40	96	AgOTf
10	**T6 X = pyridine**	**Pyridine**	pyridine	100	18	$AgPF_6$

[a] NaCN is highly toxic. Do not use in the presence of acids; [b] in case of solvent mixture (Entry **1-5** and **7**) the ratio is 1/1;

For targets **T1-T4**, a mixture of complex **39** and the corresponding inorganic salt was stirred in the mentioned solvent mixture (Figure **72**, Table **25**). The silver salt was added and a resulting colour to change from red to yellow was observed along with the appearance of a white precipitate. After the reaction time, the mixture was filtered, and the solvent was evaporated leaving a brown solid. These reactions were also performed without the addition of any silver salt. NMR spectroscopy and Mass spectrometry of the residue did not show the presence of the target complexes, but there was decomposition of the starting material. A stable product could not be isolated. Another strategy was to only reduce the volume of the solvent after filtration followed by the addition of hexane. Recrystallisations at -18 °C or at room temperature in the dark did not yield the target compounds. When heating **39** and NaSCN in

MeCN / CH_2Cl_2 in the presence of AgOTf (Entry **7**, Table **25**), the ^{1}H-NMR did not show decomposition of the starting material, but instead the formation of another product. However, after several careful attempts at purifications, decomposition of complex **39** was observed again, and the unknown product could not be isolated. A mixture of complex **39** and only $AgPF_6$ also led to the characteristic colour change from red to yellow. From this mixture, a stable compound could not be isolated either after the addition of the monodentate ligand.

Summary

The isolation of a stable product after substitution reaction was not successful. Two key steps are involved 1) removal of the Cl and 2) coordination of the target monodentate ligand. The successful removal of the chloride may be indicated by the presence of a colour change after the addition of the silver salt and the observation of a white precipitate (AgCl). However, it may be difficult to substitute the Ir-Cl due to the *trans*-influence of the weaker Ir-N bond *trans* to the Ir-Cl. In Ir-Complex **42**, the Ir-Cl is *trans* to the strong Ir-C bond leading to a weaker Ir-Cl bond. It was not possible to find out if the target complex was formed but lacked stability or if the formation of the target complex was not successful.

Modification of the diimine ancillary ligand

Miscellaneous ancillary ligands

Other possibilities to modify the ligand system is to change the nature of the ancillary ligand. Inspired by heteroleptic Ir(III) complexes bearing ancillary ligands based on 2,2′-bipyridine (bpy),[5,238] acetylacetonate (acac),[214,238,239] picolinate (pic)[238] and their derivatives, targets with different ancillary ligands were designed. For complexes **T7-T8** (Figure **73**), we targeted negatively charged ancillary ligands [picolinate (pic) and acetylacetonate (acac), respectively] to form a negatively charged complex, while in case of **T9-T10** the ancillary ligand was charge neutral [1,2-bis(diphenylphosphino)ethane (Dppe), 2,2'-bibenzo[*d*]thiazole

(bbthz), 1*H*,1'*H*-2,2'-biimidazole (biim)] to form neutrally charged complexes (Figure **73**). We also opted for 2,2'-(phenylmethylene)dipyridine (pmdp, Figure **73**) in the hope to access two new targets **T12** and **T13**. In **T12,** pmdp coordinates to iridium as a bidentate N^N ligand forming a six-membered ring chelate. In **T13** pmdp forms another tripod tridentate ligand chelating as a N^C^N ligand replacing the chloride monodentate ligand.

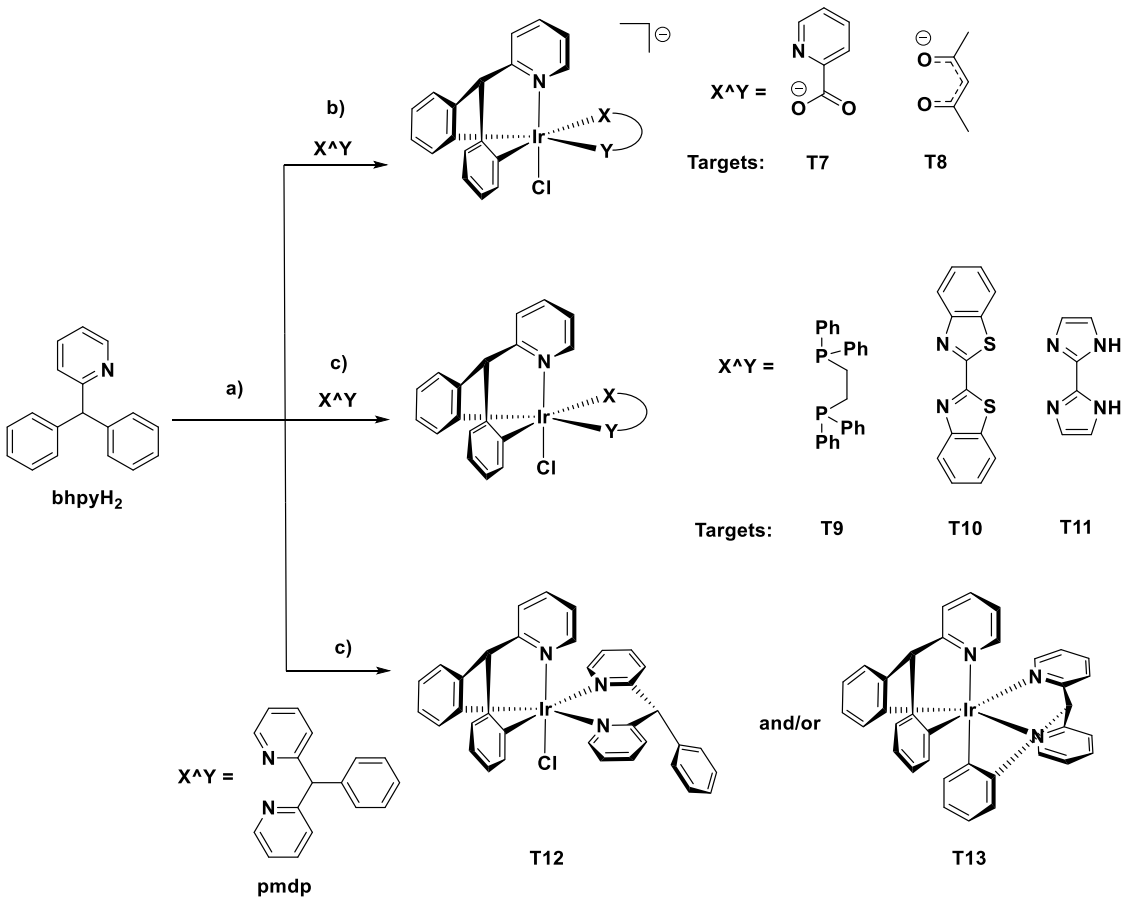

Figure **73**: Synthetic pathway for the synthesis of targets **T7-T13**. a) $IrCl_3.6H_2O$, 2-ethoxyethanol/H_2O (3:1), reflux, 19 h; b) corresponding X^Y ligand, Na_2CO_3 reflux, 6h. c) corresponding X^Y ligand, reflux, 6 h – 96 h.

Results and Discussion

Several attempts were carried out to obtain target complexes **T7-T13** using the two-step-one-pot protocol introduced above wherein a mixture of $bhpyH_2$ and $IrCl_3.6H_2O$ in 2-

ethoxyethanol/H_2O (3:1) was heated at reflux for 19 h and the formation of the intermediate was confirmed by NMR and by the the observation of the characteristic green product. The ancillary ligand was added followed by a further reaction time of 6 h, 24 h or 96 h. For targets **T7** and **T8**, Na_2CO_3 was added concomitant with the addition of the ancillary ligand. After the reaction time, the solvent was evaporated leaving a brown solid. NMR spectroscopy and mass spectrometry of this residue did not show the presence of the target complexes but did reveal decomposition of the ligand as well as the intermediate species.

Summary

It appears this C^N^C ligand system is highly selective to the nature of the ancillary ligand and so we targeted diimines based on 2,2-bipyridine (like in complexes **39-41**) to tune the electronics of this system.

2,2'-bypridine based ancillary ligand

As discussed in Chapters 1 and 4 addition of *tert*-butyl groups on the bpy ancillary ligand has been shown to lead to a blue shift of the emission, through destabilisation of the LUMO.[187] This effect can be studied when comparing the yellow-emitting complex **1**[187] with the orange-emitting complex **12**[187] (Figure **74**), where a blue-shift of 11 nm (309 cm^{-1}) is observed.

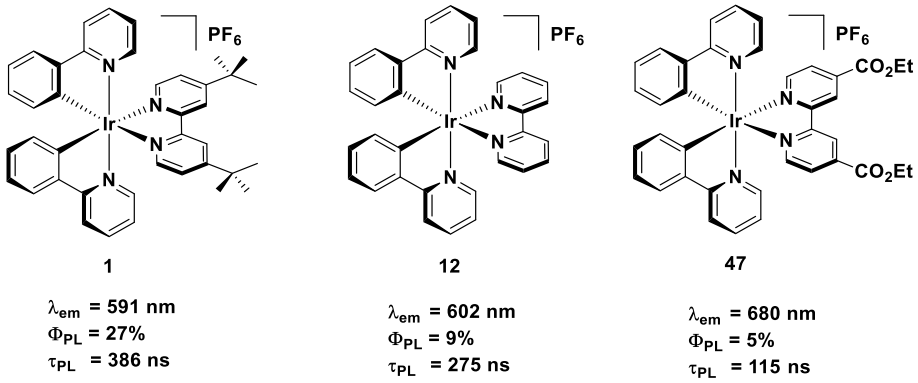

Figure **74**: Structural presentation of Ir(III) complexes bearing different substituents on the bpy ancillary ligand.

Comparing **12**[187] and $[Ir(ppy)_2(deeb)]PF_6$, **47**[240] (where deeb is diethyl [2,2'-bipyridine]-4,4'-dicarboxylate, Figure **74**) shows the impact of adding electron-withdrawing ethyl-ester groups onto the bpy ancillary ligand. A large red-shift of 78 nm (1906 cm^{-1}) is observed combined with a slight decrease in both the photoluminescence quantum yield and lifetime from 9% and 275 ns for **12** to 5% and 115 ns for **47**, which is a logical consequence of the energy gap law, which states that the nonradiative decay rate increases with decreasing emission energy.[89,241] The above study of complexes **39**-**41** demonstrated that through the addition of the *tert*-butyl groups on the C^N^C ligand (leading to the ligand 2-(bis(4-(*tert*-butyl)phenyl)methyl)pyridinato, d*t*Bubhpy), a red shift of 11 nm (282 cm^{-1}) is obtained, which is due to a destabilisation of the HOMO. With complex **40** red emission is achieved with an emission maximum of λ_{em} = 630 nm.

With the above findings, we designed complex **48** (see Figure **75**) bearing the C^N^C ligand of complex **40** (d*t*Bubhpy) and the ancillary ligand of complex **47**, both chosen to red shift the emission even further than **2** resulting in complex **48**, that is panchromatic and therefore a potential candidate for application in a dye-sensitized solar cell DSSC.[242]

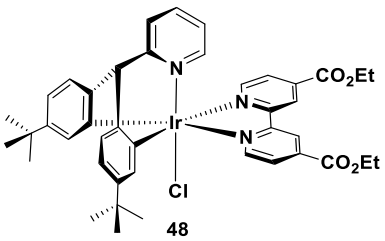

48

Figure **75**: Structural presentation of Ir(III) complex **48**.

Dye-sensitized solar cells (DSSCs)

Dye-sensitized solar cells (DSSCs) represent a promising solar cell technology.[12,59,215,216] The majority of champion DSSCs, those showing power conversion efficiencies (PCE) greater than 10%, are based on ruthenium(II) polypyridyl complexes. Iridium(III) complexes, dominant as emitters in electroluminescent devices,[21,152,218] have to

date fared poorly as dyes in DSSCs.[58,203,248,215,216,242–247] This is mainly because most iridium(III) complexes are not panchromatic, having absorption spectra that tail off by 550 nm. This induces low short circuit currents in the DSSC and consequently poor PCE; typically, less than 4%. Indeed, there are very few examples of iridium(III) complexes with significant absorption bands going up to the red or NIR parts of the visible spectrum.[59,197,249–252] Complex **48** shows panchromatic absorption, employing an electron-poor ancillary ligand (diethyl [2,2'-bipyridine]-4,4'-dicarboxylate, deeb), and its use as a DSSC dye is discussed.

Results and Discussion

Synthesis

The compound diethyl [2,2'-bipyridine]-4,4'-dicarboxylate (deeb) was prepared quantitatively according to literature methods[253] (Figure **76**).

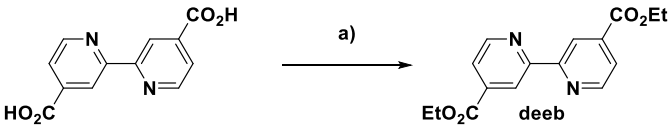

Figure **76**: Scheme for the synthesis of compound deeb. a) H_2SO_4, Ethanol, 70 °C, 4 days.

Complex **48** was obtained as a black solid in 52% yield using a two-step-one-pot protocol wherein a mixture of d*t*BubhpyH$_2$ and $IrCl_3.6H_2O$ in 2-ethoxyethanol/H_2O (3:1) was heated at reflux for 19h followed by the addition of deeb and a further reaction time of 6h (Figure **77**). Complex **48** was characterised by ^1H and ^{13}C NMR spectroscopy in CD_2Cl_2, HR-ESI mass spectrometry, elemental analysis and melting point determination. Complex **48** shows the expected number of resonances in the NMR with the characteristic singlet at 5.30 ppm in the ^1H NMR spectrum for the H on the bridge of the C^N^C ligand. With respect to the complexes **39 – 41** this complex behaves in a comparable way in HR-ESI mass spectrometry and elemental analysis.

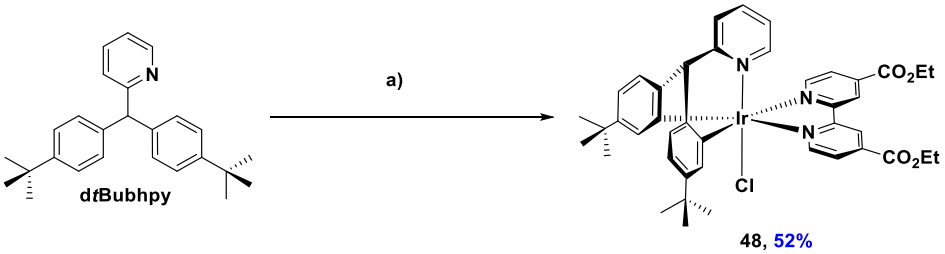

Figure **77**: Scheme for the one-pot synthesis of complex **48**. a) i) $IrCl_3.6H_2O$, 2-ethoxyethanol/H_2O (3:1), reflux, 19 h; ii) deeb, reflux, 6 h.

Crystal Structures

Single crystals of sufficient quality of **48** were grown from CH_2Cl_2/Et_2O at -18°C, and the structure of **48** was determined by single-crystal X-ray diffraction (Figure **78**, Table **26**).

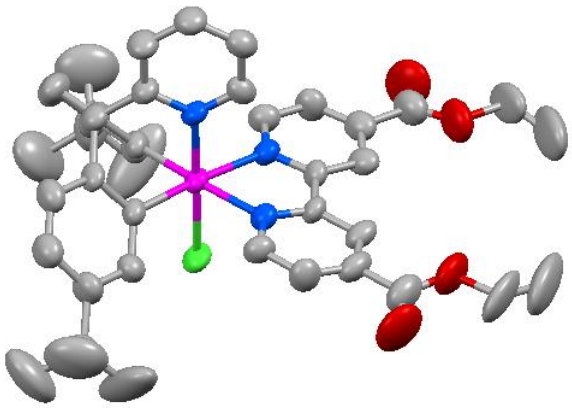

Figure **78**: Solid-state structure of complex **48**. Hydrogen atoms and solvent molecules are omitted for clarity. Colour code: C = light grey, N = blue, O = red, Cl = green and Ir = blue.

Table **26**: Selected crystallographic parameters for complexes **48**.

Complex	**Bond Length / Å**				**Bond Angle / °**	
	Ir-$C_{C^N^C}$	Ir-$N_{C^N^C}$	Ir-N_{N^N}	Ir-Cl	N-Ir-N	C-Ir-C
48	2.027(7)	2.038(8)	2.134(6)	2.346(3)	76.1(3)	85.2(4)
	2.026(7)		2.134(6)			

Complex **48**, [Ir(d*t*Bubhpy)(deeb)Cl], lies in a mirror plane; the pyridyl ring of d*t*Bubhpy, the iridium(III) and the chloride all lying directly in the plane. The tridentate C^N^C ligand d*t*Bubhpy shows a tripodal chelation motif. The remaining coordination sphere of **48** consists of the deeb N^N ligand and a chloride anion. Bond lengths and angles are in the same range as observed for complexes **39**-**41**.

Electrochemical properties

The electrochemical properties of **48** were evaluated by cyclic voltammetry (CV) and differential pulse voltammetry (DPV) in deaerated CH_2Cl_2 solution at 298 K at a scan rate of 100 mV s^{-1} using Fc/Fc^+ as the internal reference and referenced with respect to NHE (0.70 V vs. NHE).[191] The voltammograms are shown in Figure **79** and the electrochemical data are summarised in Table **27**.

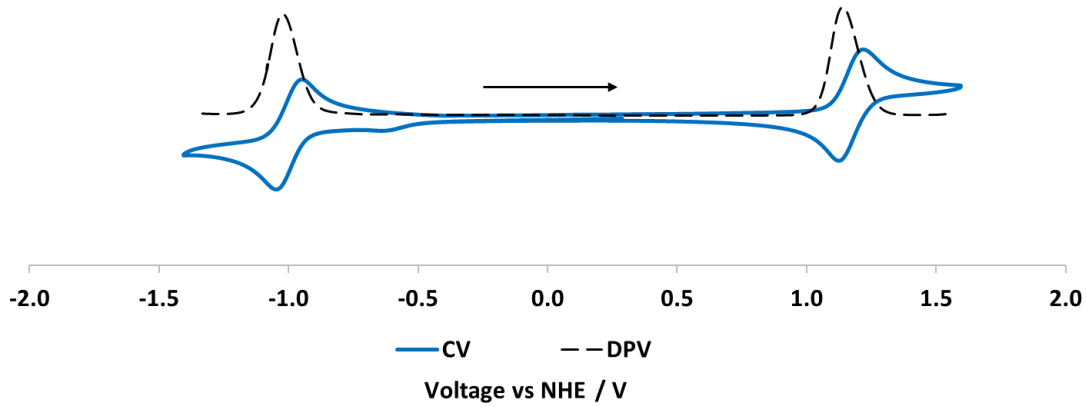

Figure **79**: Cyclic voltammograms (in blue solid lines) and differential pulse voltammetry (in dotted black lines) of complex **48** carried out in degassed CH_2Cl_2 at a scan rate of 100 mV s^{-1}, with Fc/Fc^+ as the internal reference, referenced to NHE (0.70 V vs. NHE).[191]

Table **27**: Selected electrochemical properties of complex **48**.

	Electrochemistry[a]						
	$E_{1/2}^{ox}$ / V	ΔE_p / mV	$E_{1/2}^{red}$ / V	ΔE_p / mV	ΔE_{redox}[b] / V	E_{HOMO}[c] / eV	E_{LUMO}[c] / eV
48	1.21	88	-0.97	99	2.18	-5.31	-3.13

[a] in degassed CH_2Cl_2 at a scan rate of 100 mV s^{-1} with Fc/Fc^+ as internal reference, and referenced with respect to NHE (Fc/Fc^+ = 0.70 V in CH_2Cl_2);[191] [b] ΔE_{redox} is the difference (V) between first oxidation and first reduction potentials; [c] $E_{HOMO/LUMO}$ = -[$E^{ox/red}$ vs Fc/Fc^+ + 4.8] eV.[191]

Complex **48** exhibits a quasi-reversible single electron oxidation wave at 1.21 V, which is assigned to the Ir(III)/Ir(IV) redox couple, with contributions from the two phenyl rings of d*t*Bubhpy and the chloro ligand. Compared to [Ir(d*t*Bubhpy)(d*t*Bubpy)Cl], **2**, the oxidation potential in **48** is significantly anodically shifted by 170 mV, reflecting the electron-withdrawing capacity of the ethyl ester groups of the N^N ligand, which modifies the electron density on iridium. However, the oxidation potential of **48** is less positive than that of $[Ir(ppy)_2(deeb)]PF_6$, **47**,[240] ($E_{1/2}^{ox.}$ = 1.57 V in deaerated MeCN vs NHE). Upon scanning to negative potential, **48** shows a single quasi-reversible reduction wave at -0.94 V, which is monoelectronic as inferred from the DPV. The electron-withdrawing effect of the ethyl ester groups of the N^N ligand results in a large anodic shift of 610 mV in the reduction wave of **48** compared to **40** ($E_{1/2}^{red.}$ -1.58 V vs NHE). Complex **47** showed two reversible reduction waves in MeCN. The first reduction located at -0.76 V is assigned to the reduction of the deeb ligand while the second one at -1.30 V is due to the reduction of the phenylpyridinato.[240] Thus, the reduction of the deeb ligand in **48** is shifted to more negative potentials compared to the same reduction in **47**. DFT calculations of **40** indicated that both the HOMO and HOMO-1 are close in energy and involve the iridium and chlorine atoms and the two phenyl rings of d*t*Bubhpy. As can be seen in Figure **80** the same electron density distribution is found in **11**. DFT calculations also show that the three lowest unoccupied orbitals are exclusively localised on the deeb ligand

in **11** (Figure **80**), while the LUMO+1 is primarily on the pyridyl of d*t*Bubhpy in **40**, illustrating the stronger accepting character of deeb. The $\Delta E_{\mathrm{redox}}$ for **48** (2.18 eV) is markedly smaller than that of **47** ($\Delta E_{\mathrm{redox}}$ = 2.33 V).[240]

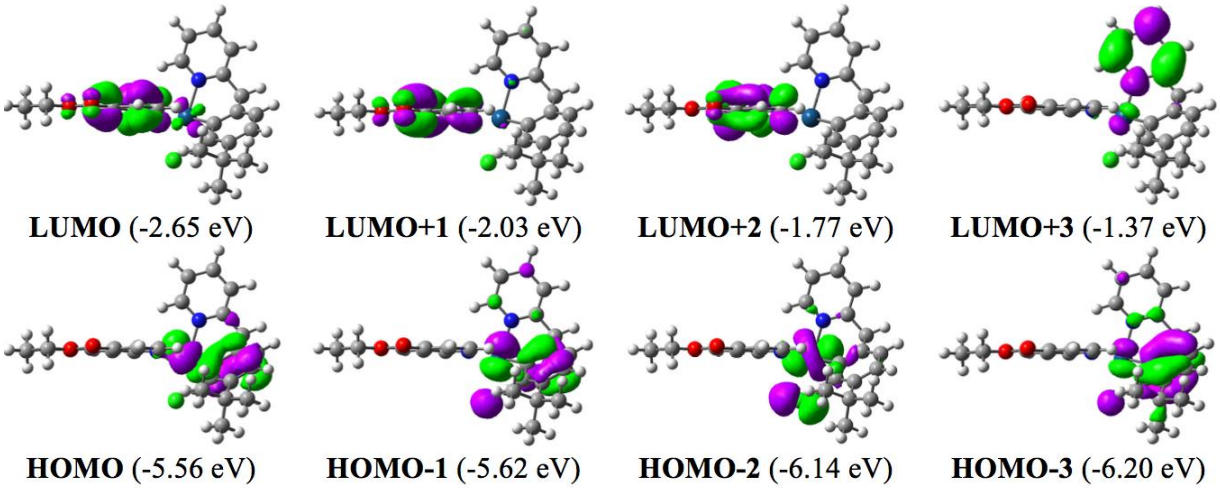

Figure **80**: Frontier molecular orbitals of **48** computed through DFT (M06 functional) and represented using a contour threshold of 0.03 au.

Photophysical properties

The photophysical data for **48** recorded in CH_2Cl_2 at 298 K are shown in Figure **81** and the data summarised in Table **28**. The absorption profile of **48** differs significantly from that of **40**. Complex **48** shows intense high-energy absorption bands (ε on the order of 3.5×10^4 M^{-1} cm^{-1}) below 250 nm, which are ascribed to $^1\pi$–π^* ligand-centred (^{1}LC) transitions localised on the deeb ligand. A moderately intense band (ε on the order of 1.5×10^4 M^{-1} cm^{-1}) at 319 nm is attributed to a ligand-centred (LC) transition on the deeb with a small CT character (see below). Weaker bands (ε on the order of $5 – 6 \times 10^3$ and 2×10^3 M^{-1} cm^{-1}) in the region of 380 – 440 nm and tailing to 500 – 600 nm are assigned to a mixture of (^{1}MLCT/^{1}LLCT) and spin-forbidden (^{3}MLCT/^{3}LLCT) transitions involving the deeb ligand. Iridium(III) complexes often do not show absorption onsets lower in energy than 550 nm;[188,212,254] though, there are known examples of neutral Ir(III) complexes showing absorption bands beyond 550 nm.[80,221,255,256]

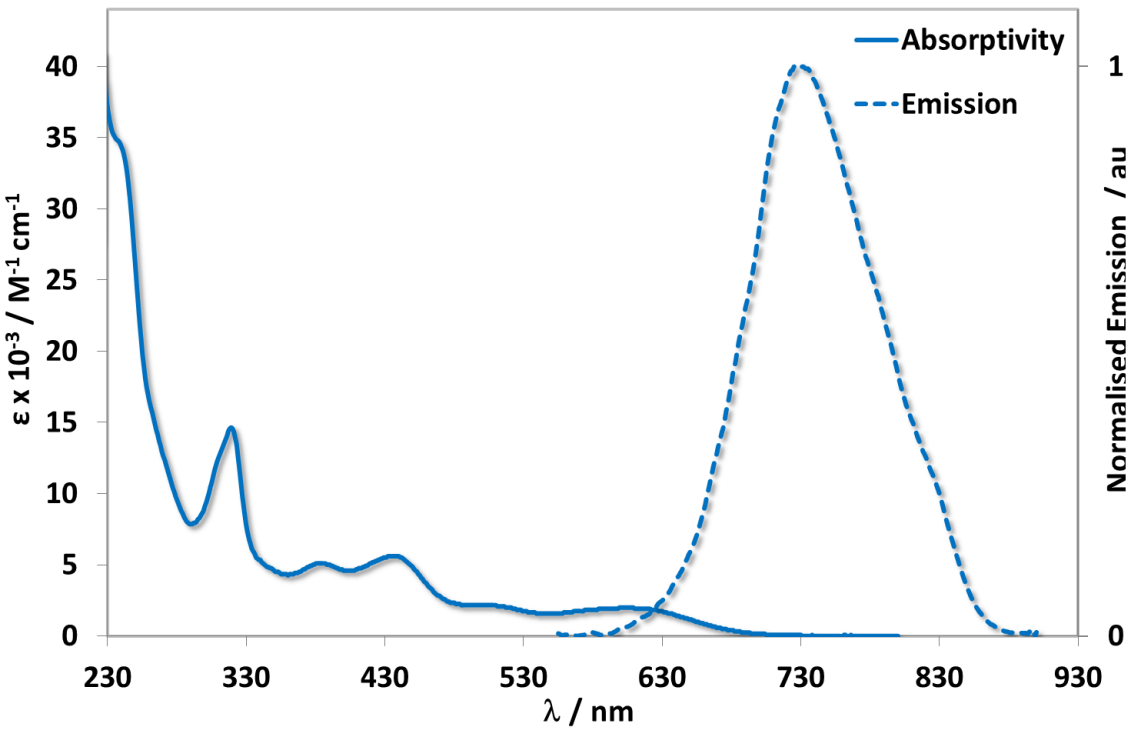

Figure **81**: The absorptivity and photoluminescence spectra of **48** in CH_2Cl_2 at 298 K.

Table **28**: Photophysical properties of complex **48**.

	λ_{abs} / nm, [ε / $M^{-1}cm^{-1}$][a]	λ_{em}[b] / nm	Φ_{PL}[b,c] / %	τ_{PL}[d] / ns
48	237 [34 819], 319 [14 647], 384 [5 105], 434 [5 607], 504 [2 176], 597 [1 925].	731	0.5	36 (73 %) 78 (19 %) 392 (8 %)

[a] Recorded in aerated CH_2Cl_2 at 298 K; [b] Recorded at 298 K in deaerated CH_2Cl_2 solution (λ_{exc} = 420 nm); [c] $[Ru(bpy)_3](PF_6)_2$ in MeCN as the reference (Φ_{PL} = 1.8% in aerated MeCN at 298 K);[9] [d] λ_{exc} = 378 nm.

The assignments for complex **48** were confirmed by TD-DFT calculations. The two lowest singlet states, computed at 623 and 611 nm, present relatively small intensities (oscillator strengths, *f*, of 0.010 and 0.056, respectively) and mainly correspond to HOMO-1 to LUMO and HOMO to LUMO transitions. This corresponds to a mixed CT process from the metal and the phenyl rings of the C^N^C ligand towards the deeb. The following significant vertical absorption are predicted by TD-DFT at 496 nm (*f*=0.071), 456 nm (*f*=0.027) and 443 nm (*f*=0.084) and these bands can be ascribed to HOMO-2 to LUMO, HOMO to LUMO+1 and

HOMO-1 to LUMO+1 transitions, respectively, and therefore all involve strong CT character towards the deeb moiety. The more intense and resolved band at 319 nm experimentally (see Table **28**) is computed at 315 nm by TD-DFT (*f*=0.162) and corresponds to a more LC excitation from a low-lying orbital centred on the deeb (and partly on chlorine atom) towards the LUMO centred on the deeb as well.

Upon photoexcitation at 420 nm, **48** exhibits a broad featureless profile, indicative of an emission with mixed CT character, with a maximum at λ_{em} = 731 nm, an emission that is significantly redshifted (99 nm, 2194 cm^{-1}) compared to **40** (λ_{em} = 630 nm). The red-shifted luminescence is due to the presence of the presence of the π-accepting deeb. The emission of **48** is likewise red-shifted (51 nm, 2194 cm^{-1}) compared to that of $[Ir(ppy)_2(deeb)]PF_6$, **47** (λ_{em} = 680 nm).[240] The DFT calculations returns an emission of the T_1 state at 762 nm, close to the experimental value, confirming emission from the lowest triplet excited state. The topology of this state, in terms of localisation of the excess α electrons, is displayed Figure **82**.

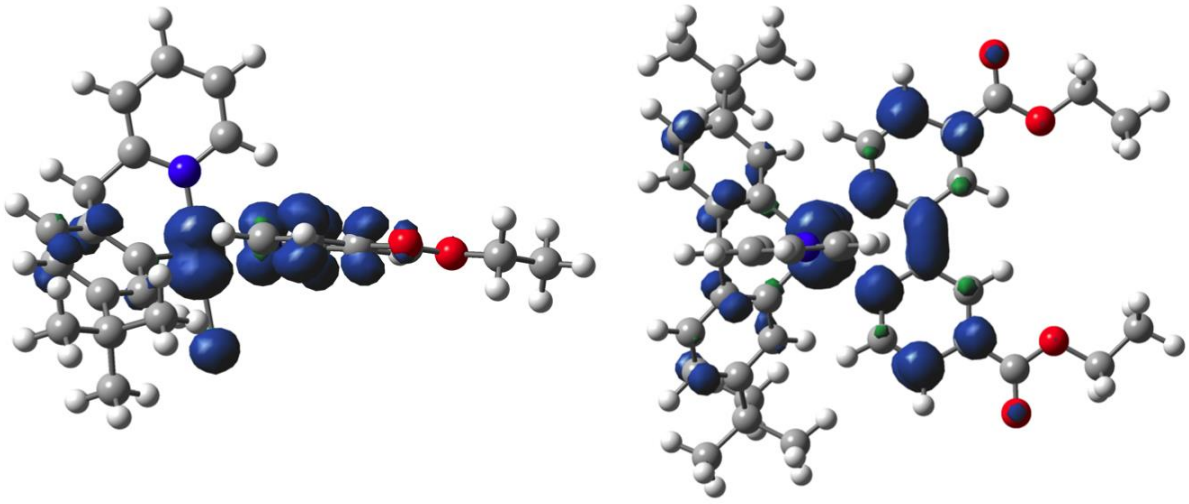

Figure **82**: DFT computed spin density difference plots for the lowest triplet state of **48**. Both side and top views are shown, and they have been drawn with a contour threshold of 3×10^{-3} au.

As can be seen, the spin density is mostly localised on the Ir and Cl atoms and on the ancillary ligand, the tridentate ligand playing only a minor role in this state. This localisation is consistent with the observed red-shift in emission compared to **40** and **47**. The measured photoluminescence quantum yield (Φ_{PL}) of **48** is 0.5%, lower than those of **40** (6%) and **47** (5%), a logical consequence of the energy gap law.[89,241] Among near-infrared emissive cationic Ir(III) emitters with λ_{em} beyond 700 nm bearing diimines as ancillary ligand, most examples exhibit Φ_{PL} values less than 4%.[188,255,257–259] However, NIR-emitting neutral Ir(III) complexes of the form [Ir(C^N)$_2$(O^O)] (where O^O a substituted β-diketonate ancillary ligand) employing highly conjugated C^N ligands have reached Φ_{PL} of up to 16%.[80,81,260] Complex **48** exhibits a multiexponential emission decay, a reflection of the large non-radiative decay rate constant.

Performance in Dye-sensitized solar cells (DSSCs)

Sandwich-type solar cells were assembled using **48**-sensitised nanocrystalline TiO_2 as the working electrodes, platinised conducting glass as the counter electrode and iodide/triiodide in acetonitrile as electrolyte. The photovoltaic performances of solar cells based **48** and **N719**, as benchmark sensitizer (Figure **83**), are summarised in Table **29**.

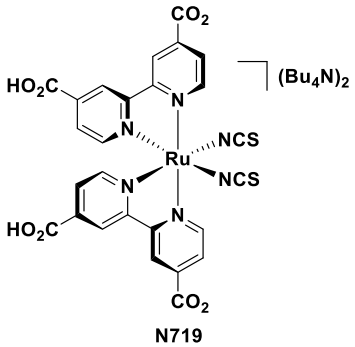

Figure **83**: Structure of the **N719** dye.

Table **29**. Photovoltaic performance of **48** and **N719**.

DYE	J_{SC}[a] / mA cm^{-2}	V_{OC} [a] / V	FF [a]	η [a] / %
48	0.995	0.67	0.74	0.49
N719	8.84	0.81	0.61	4.4

[a]J_{sc} is the short-circuit current density at the $V = 0$ intercept, V_{oc} is the open-circuit voltage at the $J = 0$ intercept, FF is the device fill factor, η is the power conversion efficiency.

Figure **84** shows the current–voltage characteristics of the dyes under AM 1.5 simulated sunlight (100 mW cm^{-2}) and in the dark. The photovoltaic efficiency (η = 0.26%) obtained with **48** is low, but comparable with results for iridium sensitizers reported elsewhere.[58,215,248,261] Both charge injection from the excited dye into TiO_2 and regeneration by the electrolyte are thermodynamically favourable. We therefore attribute the reason for the low efficiency for **48** compared to the benchmark Ru dye to be the weak absorption in the visible region, compared to ruthenium-based photosensitizers such as **N719**. The absorption spectrum of the TiO_2 electrode after immersion in the dye solution is provided in Figure **85** and the spectral response of the DSSC is given in Figure **86**.

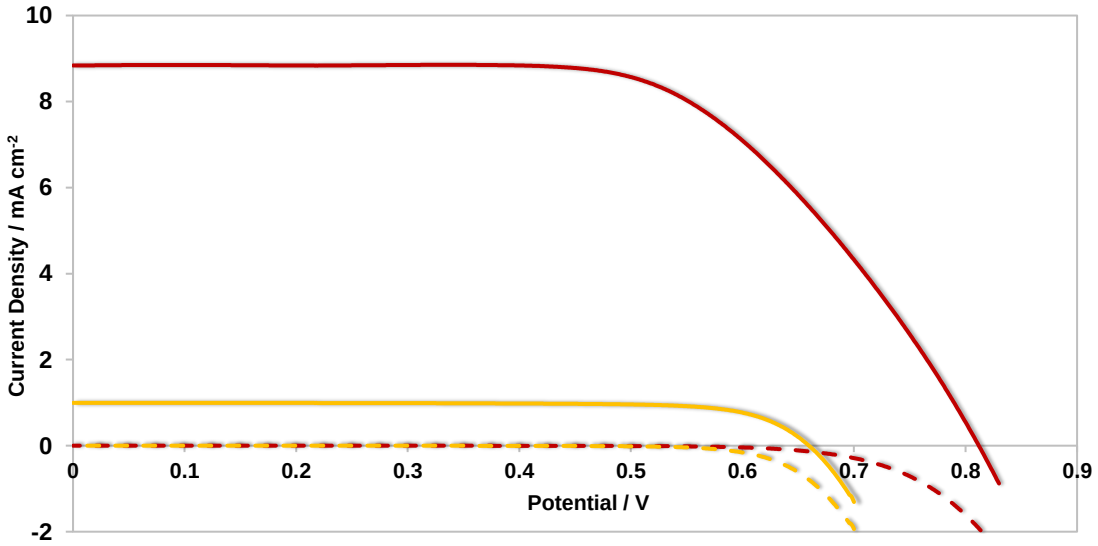

Figure **84**: Current-voltage curves for DSSCs constructed using **48** (yellow) and **N719** (red) in the dark (dashed line) and under simulated sunlight (solid line, AM1.5, 100 mW cm^{-2}).

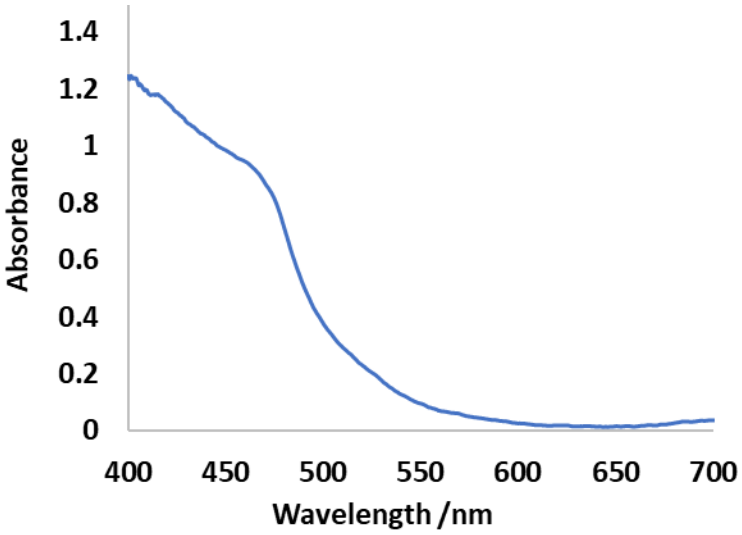

Figure **85**: Absorption spectrum of **48**-sensitized TiO

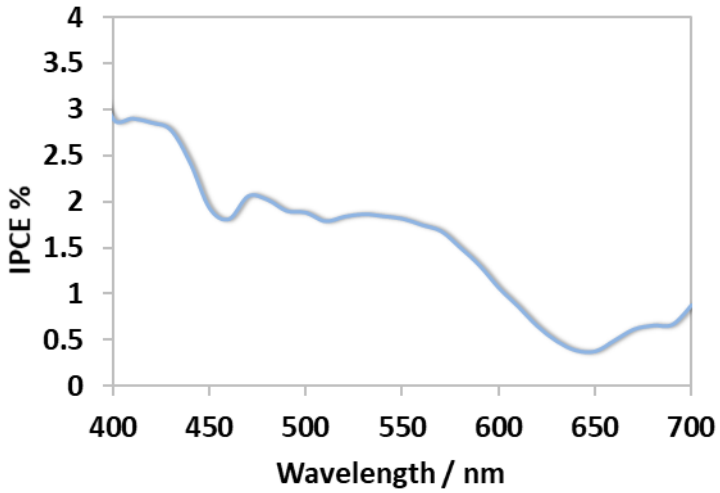

Figure **86**: IPCE spectra for DSSCs incorporating **48.**

The low incident photon-to current conversion efficiency (IPCE < 2%) is consistent with the poor light-harvesting at $\lambda > 500$ nm. While these dyes absorb broadly across the visible spectrum, the low ε (ε ~ 2 000 M^{-1} cm^{-1}) compared to ruthenium dyes (ε > 10 000 M^{-1} cm^{-1}) is a limitation to their solar cell performance.

Summary

In summary, a new panchromatically absorbing, NIR luminescent iridium(III) complexes bearing a tripodal tris(six-membered) chelate ligand has been obtained and comprehensively characterised, including by single crystal X-ray diffraction.

The absorption spectrum tails off at 700 nm, much further than most neutral iridium complexes while the emission is significantly shifted into the NIR, with a maximum of 731 nm. DSSCs using **48** as the dye achieved only modest efficiency of 0.49%, comparable to other Ir(III) dyes. This was attributed to the modest absorption coefficient, which leads to weak light harvesting in the visible region and low short-circuit current.

Conclusions

In conclusion, the development of tripodal C^N^C ligands, 2-benzhydrylpyridine ($bhpyH_2$) and its derivatives, which can coordinate to iridium, forming three six-membered chelate rings through a double C-H bond activation are reported. When combined with a bidentate diimine ligand such as 4,4'-di-*tert*-butyl-2,2'-bipyridine (d*t*Bubpy), a family of orange-to-red emitting neutral [Ir(C^N^C)(d*t*Bubpy)Cl] complexes was formed with absorption bands tailing off at 600 nm. X-ray crystal structures reveal an unstrained geometry thanks to the formation of three six-membered chelate rings. The substitution of the Ir-Cl was not successful, and a stable product could not be isolated. Replacing the bpy-based N^N ancillary ligand with other well-established ancillary ligands for Ir(III) complexes did not lead to the desired target complexes, with only starting material decomposition observed. An analogous complex, employing the electron-poor ancillary ligand diethyl [2,2'-bipyridine]-4,4'-dicarboxylate (deeb) shows panchromatic absorption and NIR emission. Its use as a dye in dye-sensitized solar cells (DSSC) reveals moderate performances comparable to other Ir(III) dyes. A full understanding why this system is sensitive and limited to bpy-type ancillary ligands and

why the replacement of the Ir-Cl is so delicate may help to design more targets for a successful synthesis. Identifying the intermediate species may provide further insight into this system.

This new unprecedented six-membered chelate tridentate tripod C^N^C ligand resulting from an unusual C-H bond activation of 2-benzhydrylpyridine (bhpyH_2) opens access to a new class of cyclometalated Ir(III) luminophores.

Chapter 6

Phosphorescent Cationic Iridium(III) Complexes Bearing a Nonconjugated Six-Membered Chelating Ancillary Ligand: A Strategy for Tuning the Emission Towards the Blue

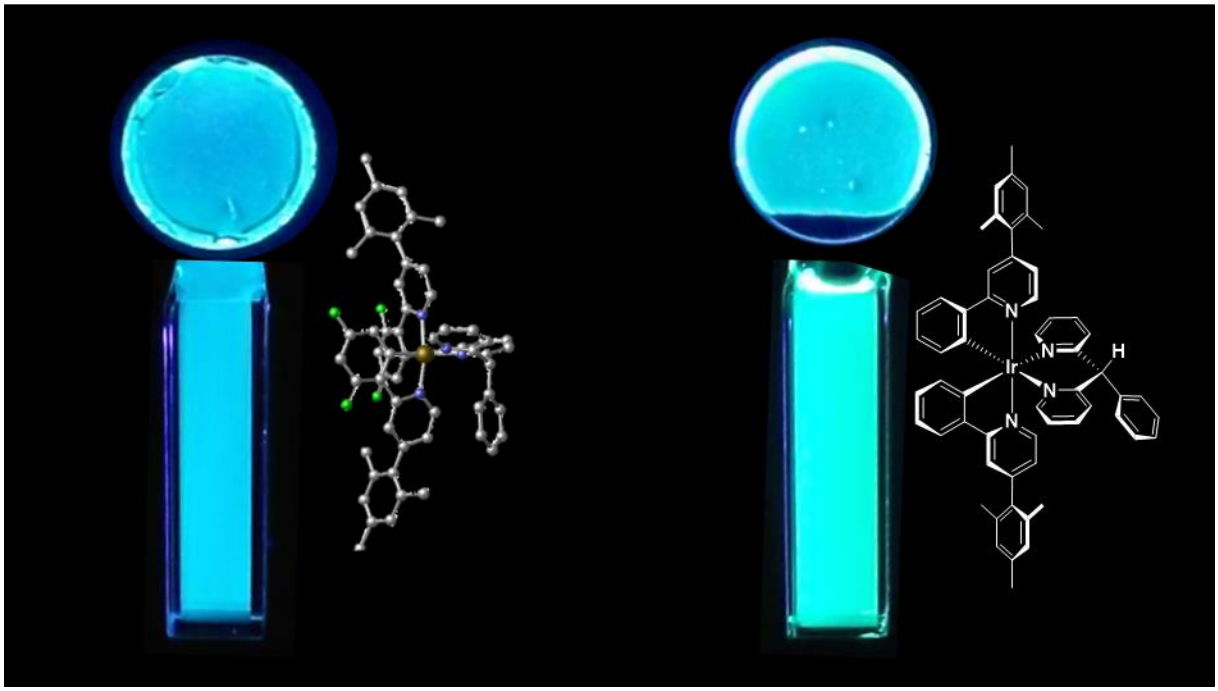

Cover picture: TOC graphic of publication arising from this chapter

Introduction

As outlined in the previous chapters, Iridium(III) complexes are attractive phosphors because of their excellent photophysical properties and the facile and wide emission colour tunability as a function of ligand identity.[5,207] In electroluminescent devices such as organic light emitting diodes (OLEDs)[170,262] and light-emitting electrochemical cells (LEECs),[21,23,172] blue emissive materials are critical components for full-colour displays and for the generation of white light in the context of solid-state lighting.[238] Charged complexes are particularly germane for LEECs. Typically, heteroleptic cationic Ir(III) complexes of the form $[Ir(C\hat{}N)_2(N\hat{}N)]^+$ consist of two cyclometalating C^N ligands typically based on a 2-phenylpyridinato (ppy) scaffold and one five-membered chelating diimine N^N ancillary ligand such as 2,2'-bipyridine (bpy), 1,10-phenanthroline (phen) or their derivatives.[238] The emission energy is normally tuned through substituent decoration about these ligand moieties, with electron-withdrawing groups attached to the C^N ligands and electron-donating groups incorporated onto the N^N ligand used in concert to increase the HOMO-LUMO gap, and by extension the energy of the emissive triplet state. As discussed in Chapters 1, 4 and 5, much less attention has been devoted to the effect of changing the chelate ring size on the emission energy, particularly in the context of the incorporation of a nonconjugating methylene space group between the coordinating rings.

The use of six-membered chelate ancillary ligands on cationic iridium(III) complexes is more common, though there are only a handful of reports here as well (Figure **87**). Examples include the use of a di(pyridin-2-yl)methane (dpm)[263] that incorporates a methylene spacer to interrupt the π-conjugation of the ligand such as $[Ir(ppy)_2(dpm)]PF_6$, **49**; no photophysics was reported.

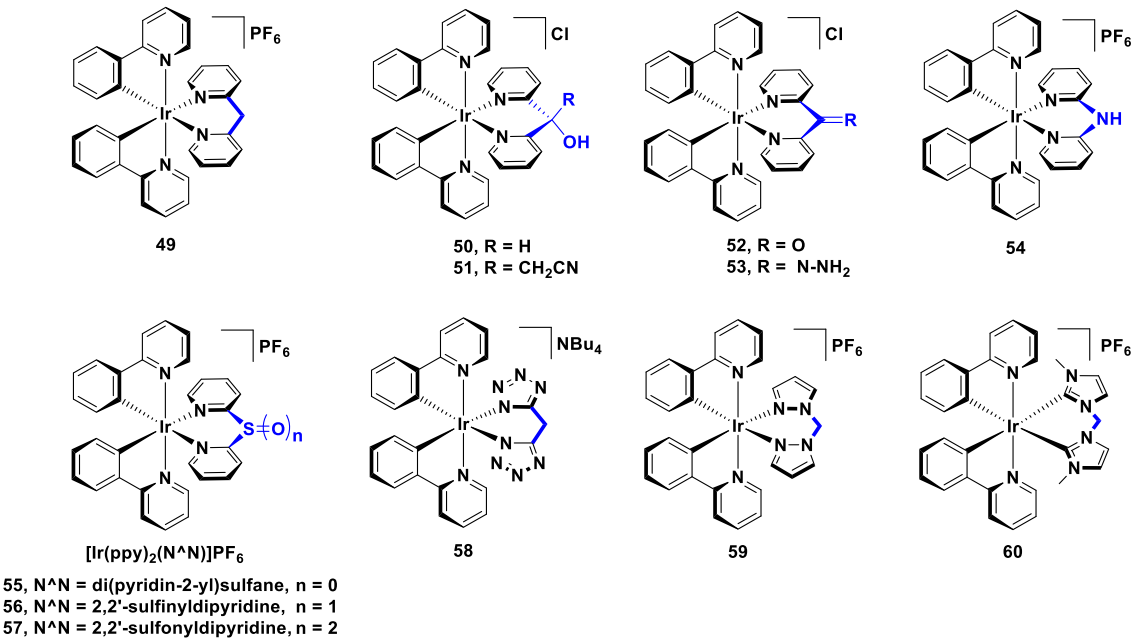

Figure **87**: Structural representation of iridium(III) complexes bearing conjugated and nonconjugated ancillary ligands reported in the literature.

Other studies have focused on the functionalisation of this methylene bridge. For instance, the complexes [Ir(ppy)$_2$(dpyOH-R)]Cl [with R = H, **50** and CH_2CN, **51** and dpyOH-R is di(pyridin-2-yl)methanol and 3-hydroxy-3,3-di(pyridine-2-yl)propanenitrile, respectively] have been investigated.[264] The effect of successfully interrupting the direct electronic crosstalk between the coordination moieties can be demonstrated by comparing the photophysical properties of **50** (with λ_{PL} = 477, 507 and 547 nm, Φ_{PL} = 10% in MeCN) and the reference complex **12**, [Ir(ppy)$_2$(bpy)]PF_6, (λ_{PL} = 602 nm, Φ_{PL} = 9% in MeCN),[187] where a large blue-shift of 125 nm (4353 cm^{-1}) is observed. The complex **51**[264] (with λ_{PL} = 535 nm, Φ_{PL} = 49% in MeCN) is a bright emitter exhibiting predominantly MLCT emission. The two complexes [Ir(ppy)$_2$(dpy-R)]Cl [with R = O, **52** and N-NH_2, **53** and dpy-R is di-2-pyridylketone and 2,2'-(hydrazonomethylene)dipyridine, respectively] are poorly emissive in acetonitrile, with Φ_{PL} < 0.5%. The former exhibits an unstructured emission centred at 678 nm, whereas the latter displays a blue-shifted, structured emission profile (λ_{PL} = 480, 510 nm).[264]

A more widely studied six-membered chelate N^N ligand is di(pyridin-2-yl)amine (dpa).[263,265–268] With $[Ir(ppy)_2(dpa)]PF_6$, **54** (λ_{PL} = 483, 514 (sh) nm, Φ_{PL} = 43% in CH_2Cl_2, Figure **87**) a significant blue-shift and increase in Φ_{PL} can be observed with respect to **12**, which in this case is due to the presence of the electron-releasing central amine.[265]

Through sulfur-bridged six-membered chelate N^N ligands (di(pyridine-2-yl)sulfane and its oxidised derivatives), the emission energy could be tuned as a function of the oxidation state of the central sulfur atom.[269] Ligand-centred (^{3}LC) emission was observed when the sulfur was in the +2 (**55**, with λ_{PL} = 478, 510, 548 (sh) nm, Φ_{PL} = 4% in CH_2Cl_2), and +4 oxidation states (**56**, with λ_{PL} = 478, 510, 548 (sh) nm, Φ_{PL} = 1% in CH_2Cl_2). Through oxidation of the sulfur atom to the +6 oxidation state (**57**, with λ_{PL} = 552 nm, Φ_{PL} = 3% in CH_2Cl_2) a red-shift and emission with ^{3}MLCT character was observed.

Examples of nonconjugated six-membered chelate ancillary rings employing coordinating heterocycles other than pyridine include those using bis(tetrazolate)[270,271] (*e.g.*, $NBu_4[Ir(ppy)_2(b\text{-}trz)]$, **58** where b-trz$H_2$ is di(1H-tetrazol-5-yl)methane, with λ_{PL} = 498, 520 (sh) nm, Φ_{PL} = 75% in MeCN), and bis(pyrazole)[272,273] (*e.g.*, $[Ir(ppy)_2(bpm)]PF_6$, **59** where bpm is bis(pyrazol-1-yl)methane, with λ_{PL} = 477 nm, Φ_{PL} = 21% in MeCN, Figure **87**) or bis-NHC[274–279] (*e.g.*, $[Ir(ppy)_2(dmdiim)]PF_6$, **60** where (dmdiimH_2)I_2 is 1,1'-dimethyl-3,3'-methylenediimidazolium diiodide, with λ_{PL} = 475, 503 nm, Φ_{PL} = 38% in MeCN) complexes. Recently, Chi and co-worker reported a nonplanar tetradentate N^N^N^N chelate bearing a pyrazole unit and a nonconjugated tripodal arranged terpyridine, which can coordinate to iridium forming a six-membered ring.[280] They obtained sky blue efficient OLEDs using this complex as the dopant emitter. In each of these literature examples the spacer disrupts the conjugation across the coordinating moieties, enabling a blue-shifted emission. The strongly donating character of the coordinating heterocycle contributed to the blue-to-sky-blue emission of these complexes.

The work presented in this chapter deals about the development of charged blue-emitting iridium(III) complexes for solution-processed OLEDs and LEECs. Here we investigate the coordination of the nonconjugated diimine 2,2'-(phenylmethylene)dipyridine (pmdp, Figure **88**) to iridium as the N^N ligand, in combination with either 2-(2,4-difluorophenyl)-4-mesitylpyridinato (dFmesppy) or 4-mesityl-2-phenylpyridine (mesppy) as C^N ligands to form complexes $[Ir(dFmesppy)_2(pmdp)]PF_6$, **61** and $[Ir(mesppy)_2(pmdp)]PF_6$, **62**, respectively (Figure **88**).

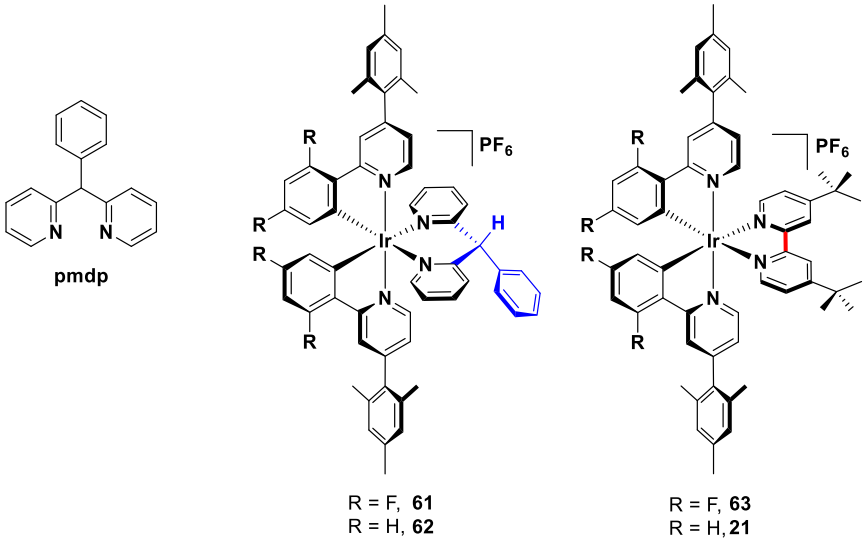

Figure **88**: Structural representations of 2,2'-(phenylmethylene)dipyridine (pmdp), and complexes **61** and **62** and their reference complexes **63** and **21** respectively.

The mesityl group was incorporated onto the C^N ligands to increase the solubility of the resultant complexes in organic solvents (e.g. MeCN and CH_2Cl_2), without affecting their emission energy due to the mutually orthogonal conformation between the mesityl substituent and the pyridine of the C^N ligands, thereby disrupting any formal conjugation.[174] The impact of the use of the pmdp ligand is studied through comparison with two reference complexes **63** and **21** bearing the same C^N ligands and a conjugated N^N ancillary ligand [4,4'-di-*tert*-butyl-2,2'-bipyridine (d*t*Bubpy)]. The photophysical properties of these complexes are corroborated by density functional theory (DFT) and time-dependent DFT (TD-DFT) investigations.

Results and Discussion

Synthesis

The ancillary ligand (pmdp) was obtained in 40% yield as a beige solid following a modified procedure[281] wherein 2-benzylpyridine was treated with *n*-BuLi at -78 °C and subsequently reacted with 2-fluoropyridine under S_NAr conditions (Figure **89**).

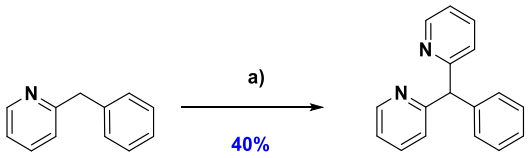

Figure **89**: Synthesis route for 2,2'-(phenylmethylene)dipyridine; (a) i) THF, *n*-BuLi, N_2, -78 °C, 1 h; ii) 2-fluoropyridine, THF, -78 °C to r.t., 18 h. (3) reflux, 3 h.

Complexes **61** and **62** were obtained as their hexafluorophosphate salts in a two-step synthesis following our previously reported protocol (Figure **90**).[174] In the first step, the bis(*μ*-Cl) dimer was obtained in high yields (91% and 94% for R = H and R = F, respectively) as a yellow solid by treatment of the corresponding C^N ligand with $IrCl_3.6H_2O$ in a 3:1 mixture of 2-ethoxyethanol/H_2O (125 °C, 24 h). This dimer was then cleaved with 2,2'-(phenylmethylene)dipyridine in a 1:1 mixture of CH_2Cl_2/MeOH (40 °C, 18 h) to afford the cationic Ir(III) complexes as their chloride salts. After column chromatography on silica (eluent: 8% MeOH in CH_2Cl_2) followed by an ion exchange with aqueous NH_4PF_6 and recrystallisation, complexes **61** and **62** were isolated as yellow solids in excellent yield (81% and 89%, respectively) as their hexafluorophosphate salts.

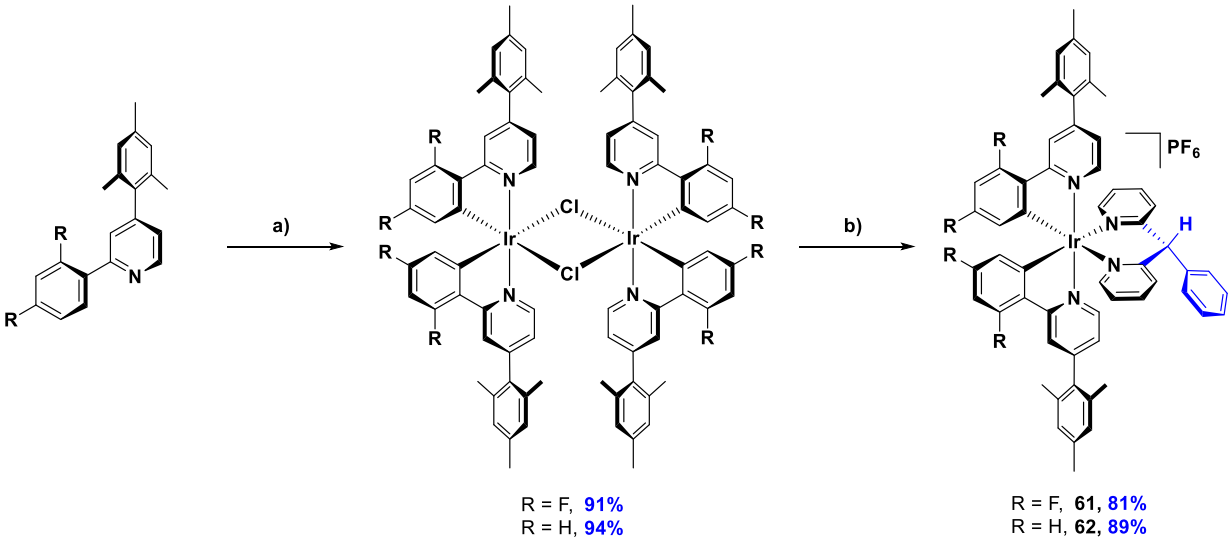

Figure **90**: Procedure for the synthesis of target complexes (**61** and **62**) in this study. a) $IrCl_3 \cdot 6H_2O$, corresponding C^N ligand, 2-ethoxyethanol/water (3:1), 125 °C, 24 h. b) 1. 2,2'-(phenylmethylene)dipyridine, $MeOH/CH_2Cl_2$ (1:1), 40 °C, 18h. 2. aq. NH_4PF_6.

Complexes **61** and **62** were characterised by ^{1}H, ^{13}C and ^{31}P NMR spectroscopy and, for **61**, ^{19}F NMR spectroscopy in $CDCl_3$; ESI-HR mass spectrometry, elemental analysis, and melting point determination. Due to the phenyl group on the N^N ligand, the two C^N ligands are no longer symmetrical as in the above examples of Chapter 2 – 4. This translates into the double amount of resonances for the C^N ligand. A characteristic signal in the ^{1}H NMR spectra is the singlet at around 5.90 – 5.30 ppm arising from the C-H on the bridge of the N^N ligand. As expected the ^{13}C NMR also shows a higher number of resonances compared to the examples from Chapter 2 – 4. For **61**, a splitting of resonances for the C-F carbons is detected leading to not well resolved doublets. With respect to the complexes in Chapter 2 these complexes behave in a comparable way in HR-ESI mass spectrometry and elemental analysis. The structure of complex **61** was determined by single crystal X-ray diffraction.

Crystal Structure

Single crystals of sufficient quality of **61** were grown from vapor diffusion of a CH_2Cl_2 solution of the complex with hexane acting as the anti-solvent. The structure of **61** was determined by single-crystal X-ray diffraction (Figure **91**, and Table **30**). Complex **1** shows a distorted octahedral coordination environment around the iridium with the two N atoms of the C^N ligands in the typical *trans* configuration. The Ir-C_{C^N} bond lengths of [2.005(4) and 2.005(5) Å] and the Ir-N_{C^N} bond lengths [2.049(3) and 2.057(4) Å] are expectedly in the same range as the respective average bond lengths in **63** [Ir-C_{C^N} = 2.000 Å and Ir-N_{C^N} = 2.035 Å]. The Ir-N_{N^N} bonds [2.200(4) and 2.197(4) Å], are notably longer than those of a related complex $[Ir(ppy)_2(dpa)]PF_6$ (average Ir-N_{N^N} = 2.171 Å).

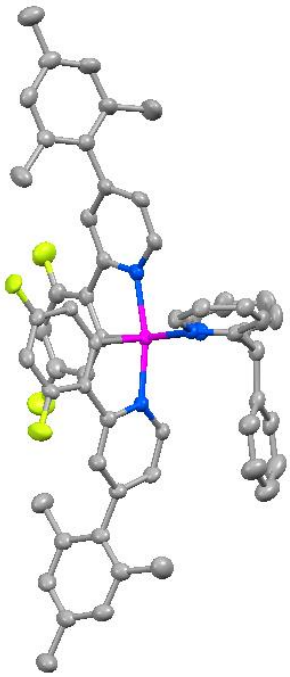

Figure **91**: Solid-state structures of complex **61**. Hydrogen atoms, PF_6^- counterions and solvent molecules are omitted for clarity. C = light grey, N = blue, F = yellow, Ir = magenta.

Table **30**: Selected crystallographic parameters for complexes **61**.

	Bond Length / Å			**Bond Angle / °**			**Plane Angle / °[a]**
	Ir-$C_{C\wedge N}$	Ir-$N_{C\wedge N}$	Ir-$N_{N\wedge N}$	C-Ir-$N_{C\wedge N}$	N-Ir-N	C-$C_{methylen}$-C[b]	
61	2.005(4)	2.049(3)	2.200(4)	80.3(2)	88.01	117.3(4)	71.4(2)
	2.005(5)	2.057(4)	2.197(4)	80.5(2)			78.8(2)

[a] Angles between the planes of mesityl ring and the pyridine of the C^N ligands; [b] Bond angle within ancillary ligand between the two pyridines occupying a mutually V-shape orientation.

Compared to the average bond lengths in **63** (2.125 Å), the Ir-$N_{N\wedge N}$ bonds in **61** are significantly longer.[176] The bite angles of the C^N ligands in **61** are 80.3(2)° and 80.5(2)°, which are in the same range as the corresponding bond angles in **63** (average $C_{C\wedge N}$-Ir-$N_{C\wedge N}$ = 80.8°). The bite angle of the ancillary ligand in **61** is 88.0(1)°, which is slightly increased compared to that in $[Ir(ppy)_2(dpa)]PF_6$ [86.0(2)°].[265] Expectedly, compared to the ancillary ligand bite angle found in **63** [76.2(4)°], a significant enlargement can be observed. The angles between the planes of mesityl ring and the pyridine of the C^N ligands in **61** are 71.4(2)° and 78.8(2)°, which are slightly smaller than analogous inter-planar angles in **63** [84.5° and 85.0°], while being larger than those found in the racemic form of **21** [57.3°], but falling between the angles found in the enantiopure forms of **21** [74.9° and 89.4°].[175,190]

A noticeable feature revealed by the crystal structure of **61** is the configuration of the spacer group, which orients the phenyl substituent in an axial position. The two N^N pyridines are not co-planary but occupy a mutually V-shape orientation with a bond angle of 117.3(4)°, which is significantly larger than that expected for bond angles on a pure tetrahedral carbon.

Electrochemical Properties

The electrochemical behaviour of **61** and **62** was evaluated by cyclic voltammetry (CV) and differential pulse voltammetry (DPV) in deaerated MeCN solution at 298 K at a scan rate of 100 mV s^{-1} using Fc/Fc^+ as the internal reference and referenced with respect to SCE (0.38

V vs. SCE).[189] The voltammograms are depicted in Figure **92** and the electrochemistry data are found in Table **31**. Both complexes exhibit a quasi-reversible single electron oxidation, which can be attributed to the Ir(III)/(IV) redox couple with contributions from the C^N ligands.[22] Complex **61**, bearing the dFmesppy C^N ligands, displays a notably more positive oxidation potential (1.79 V) than **62** (1.36 V) as a function of the presence of the electron-withdrawing fluorine atoms, a trend that can be also seen in the comparison of **63** (1.59 V) and **21** (1.17 V in CH_2Cl_2). Both **61** and **62** are more difficult to oxidise compared to their respective reference complexes **63** and **21**, demonstrating that the less-conjugated pmdp ligand influences less strongly the oxidation potential of the complex than the more π-accepting d*t*Bubpy ligand used in the reference complexes. Upon scanning to negative potential, surprisingly no reduction wave is observed for complex **61**. Complex **62** exhibits three reduction waves, with the first being irreversible (-1.90 V), while the second (-2.15 V) and third (-2.42 V) being quasi-reversible.

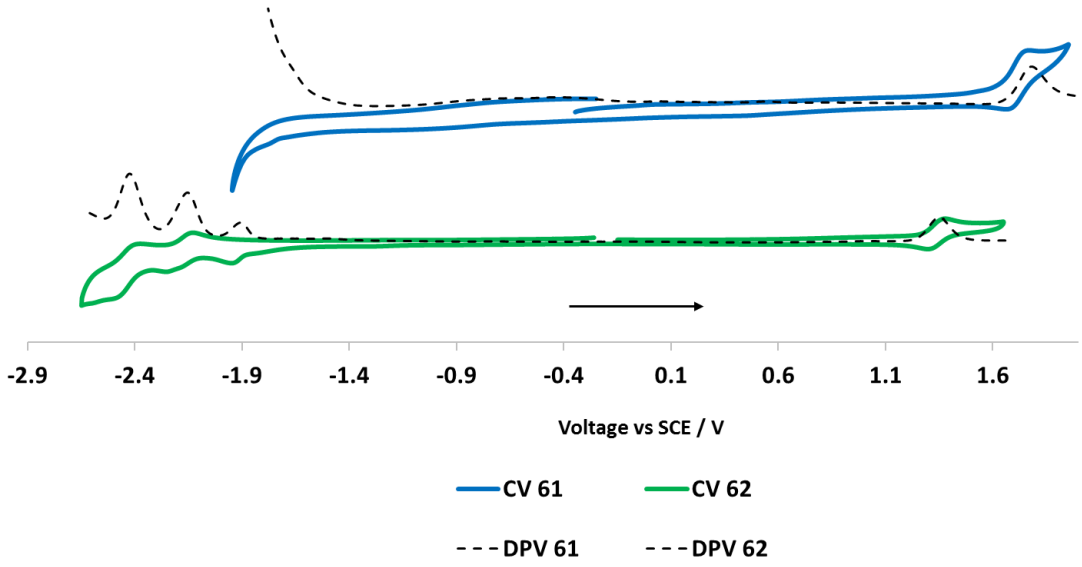

Figure **92**: Cyclic voltammetry (in solid line) and differential pulse voltammetry (in dotted line) of **61** and **62** carried out in degassed MeCN at a scan rate of 100 mV s^{-1}, referenced to SCE (Fc/Fc^+ = 0.38 V vs. SCE).[189]

Table **31**: Electrochemical properties of complex **61** and **62** and their reference complexes.

	Electrochemistry[a]						
	$E_{1/2}^{ox}$ / V	ΔE_p / mV	$E_{1/2}^{red}$ / V	ΔE_p / mV	ΔE_{redox}[b] / V	E_{HOMO}[c] / eV	E_{LUMO}[c] / eV
61	1.79	80	n.d.[d]	-	n.d. [d]	-6.21	-
62	1.36	78	-1.90[e], -2.15, -2.42,	-, 120, 98	3.26	-5.78	-2.52
63[f]	1.59	-	-1.36	-	2.95	-6.01	-3.06
21[g]	1.17	-	-1.15[e]	-	2.32	-	-

[a] in degassed MeCN at a scan rate of 100 mV s^{-1} with Fc/Fc^+ as internal reference, and referenced with respect to SCE (Fc/Fc^+ = 0.38 V in MeCN);[189] ΔE_{redox} is the difference (V) between first oxidation and first reduction potentials; [c] $E_{HOMO/LUMO}$ = -[$E^{ox/red}$ vs Fc/Fc^+ + 4.8] eV;[191] [d] not detectable; [e] irreversible; [f] from ref. [176]; [g] in CH_2Cl_2 from ref [175].

Compared to **21** (-1.15 V in CH_2Cl_2),[175] the first reduction wave of **62** is significantly shifted to more negative potential (by 0.75 V), reflecting the disruption of the conjugation of the N^N ligand, making a reduction more difficult. Based on a comparison with the electrochemistry reported by Thompson *et al.*[273] for the related complex $[Ir(topy)_2(pz_3CH)]CF_3SO_3$ [where topy is 2-*para*-tolylpyridinato and pz_3CH is η^2–tri(1*H*-pyrazol-3-yl)methane], the first two reduction waves are the result of successive reductions of the pyridyl rings of the two C^N ligands while the third reduction wave corresponds to the reduction of the ancillary ligand.

Photophysical Properties

UV-vis absorption spectra for **61** and **62** are shown in Figure **93** with the data summarised in Table **32**.

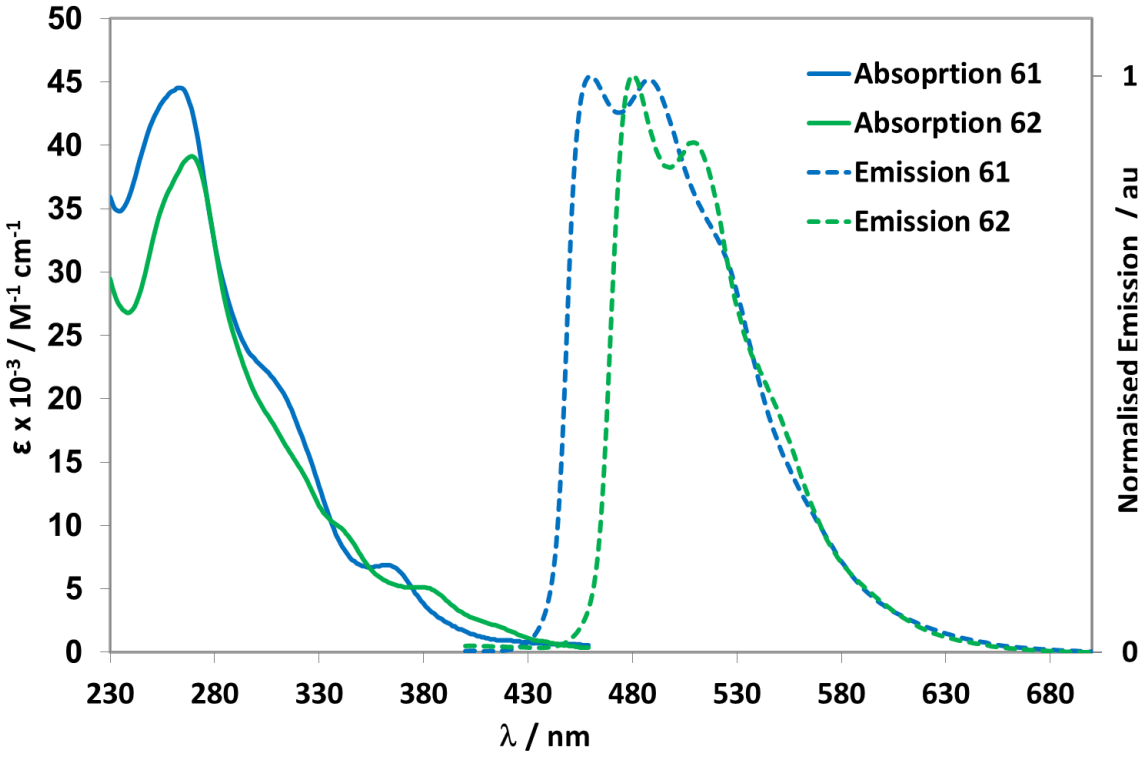

Figure **93**: UV-vis absorption and photoluminescence spectra of **61** and **62** in MeCN at 298 K.

Complexes **61** and **62** both exhibit similar absorption profiles to their respective reference complexes. High intensity bands below 270 nm (ε on the order of 39 – 45 × 10^3 $M^{-1}cm^{-1}$) are observed for **61** and **62** and are assigned as ligand-centred π–π* transitions, which is a typical feature for associated complexes of the form of $[Ir(C^N)_2(N^N)]^+$.[187] Complexes **61** and **62** both exhibit similar absorption profiles to their respective reference complexes. High intensity bands below 270 nm (ε on the order of 39 – 45 × 10^3 $M^{-1}cm^{-1}$) are observed for **61** and **62** and are assigned as ligand-centred π–π* transitions, which is a typical feature for associated complexes of the form of $[Ir(C^N)_2(N^N)]^+$.[187]

Table **32**: Photophysical properties of **61** and **62** and their reference complexes.

	MeCN[a]			PMMA Film[b]			Neat Film[c]			Glass[d]	
	λ_{PL}[e] / nm	Φ_{PL}[f] / %	τ_{PL}[g] / ns	λ_{PL}[e] / nm	Φ_{PL}[h] / %	τ_{PL}[g] / ns	λ_{PL}[e] / nm	Φ_{PL}[h] / %	τ_{PL}[g] / ns	λ_{PL}[e] / nm	τ_{PL}[g] / ns
61	460, 488 (sh)	30	186 (15 %) 445 (85 %)	459 (sh), 488	46	325 (5%) 1260 (35%) 3260 (60%)	464 (sh), 490, 527 (sh)	21	75 (12%) 263 (46%) 755 (42%)	455, 487 (sh) 516 (sh)	20 (1%) 2920 (99%)
62	481, 509 (sh)	11	95 (16 %) 206 (84 %)	478, 512 (sh)	26	162 (4%) 770 (31%) 2000 (65%)	485 (sh), 514, 581 (sh)	9	71 (33%) 210 (63%) 1195 (4%)	473, 508 (sh), 539 (sh),	200 (1%) 2800 (99%)
63[i]	515	80	1370	474 (sh), 502	97	16300	508	54	390 (68%) 1230 (34%)	-	-
21[j]	577	40	757	-	-	-	478, 516, 550	18	25 (6%) 211 (0.42) 672 (0.52)	-	-

[a] In deaerated MeCN at 298 K; [b] at 298 K, spin-coated from a 2-methoxyethanol solution of 5 wt% of the complex in PMMA on a pristine quartz substrate; [c] at 298 K, spin-coated from a 2-methoxyethanol solution; [d] in 2-MeTHF at 77 K; [e] λ_{exc} = 360 nm; [f] Quinine sulfate used as the reference (Φ_{PL} = 54.6% in 0.5 M H_2SO_4 at 298 K);[24] [g] λ_{exc} = 378 nm; [h] Measured using an integrating sphere; [i] from ref. [17a]; [j] in CH_2Cl_2 from ref [18].

Moderately intense bands (ε on the order of 9 – 20 × 10^3 $M^{-1}cm^{-1}$) in the region of 310 – 345 nm are assigned to a combination of spin-allowed singlet metal-to-ligand and ligand-to-ligand charger transfer (^{1}MLCT/^{1}LLCT) transitions, and appear as a shoulder and are blue-shifted by 31 nm (2879 cm^{-1}) for **61** compared to **62**, which is due to the electron-withdrawing fluorine atoms present in the former. At lower energies both complexes exhibit low intensity

bands (ε on the order of 0.5 – 6 × 10^{-3} $M^{-1}cm^{-1}$) in the region of 360 – 450 nm that are attributed to a combination of spin-forbidden ^{3}MLCT/^{3}LLCT transitions.

The photoluminescence properties of **61** and **62** were investigated at 298 K in degassed MeCN (Figure **93**), as polymethyl methacrylate (PMMA) doped films (5 wt% of complex in PMMA) and as spin-coated neat films (Figure **94a**). The spectra of **61** and **62** in a 2-methyltetrahydrofuran (2-MeTHF) glass at 77 K are depicted in Figure **94b**. The photophysical data of **61** and **62** and the reference complexes are summarised in Table **32**.

Upon photoexcitation at 360 nm in MeCN, **61** and **62** show structured emission profiles, indicative of a ligand-centred emission, with maxima at 460 and 480 nm for **61**, and 481 and 509 nm for **62**, the former being more intense in both cases. The emission maxima of **61** is blue-shifted by 55 nm (2322 cm^{-1}) compared to that of **63** (λ_{PL} = 515 nm),[176] which itself presents an unstructured mixed charge-transfer emission profile. The same trend is observed when comparing the emission of **62** to **21** (λ_{PL} = 577 nm in CH_2Cl_2).[175] Comparison of the photophysical properties of **62** with the archetype complex $[Ir(ppy)_2(bpy)]PF_6$, **12** (λ_{PL} = 602 nm, Φ_{PL} = 9%)[187] reveals an even more pronounced blue-shift (Δ = 121 nm, 4179 cm^{-1}). A comparison with the structurally related complex **50** (with λ_{PL} = 477, 507 (sh) nm, Φ_{PL} = 10% in MeCN) reveals an essentially similar photophysical profile.[264] The photoluminescence quantum yield ($\Phi_{PL,MeCN}$) of **61** is 30%, which is notably higher than that of **62** ($\Phi_{PL,MeCN}$ = 11%), a trend that is also observed in **63** and **21**.

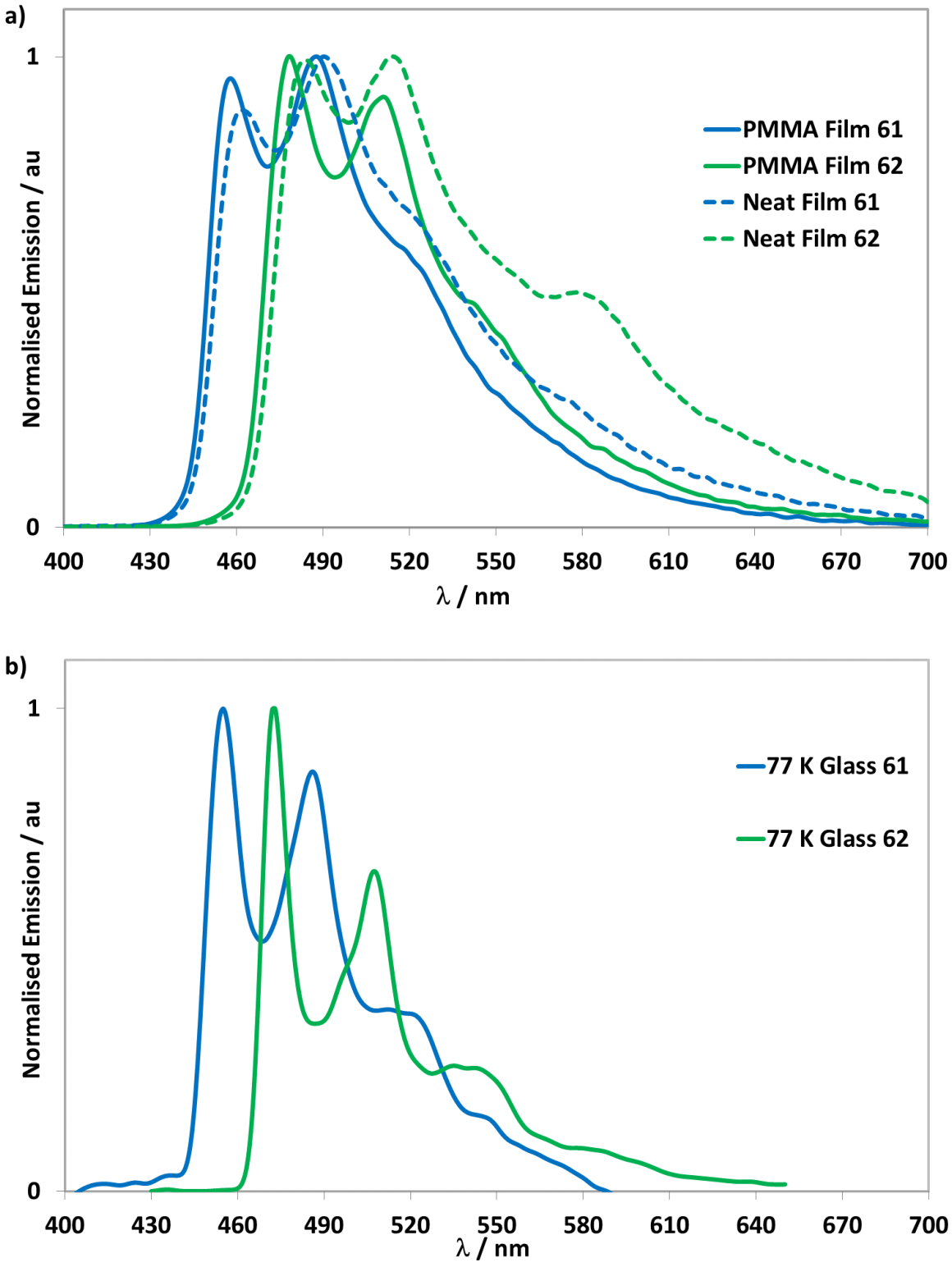

Figure **94**: Photoluminescence spectra of **61** and **62** a) recorded in PMMA doped films (5 wt% of complex in PMMA) in solid lines and in neat film (spin-coated from 2-methoxyethanol) in dotted lines (λ_{exc} = 360 nm); b) recorded in 2-MeTHF Glass at 77 K (λ_{exc} = 360 nm).

Compared to their reference complexes **63** (Φ_{PL} = 80%) and **21** (Φ_{PL} = 40%), **61** and **62** show much lower Φ_{PL} values, which can be rationalised by the flexibility of the N^N ancillary ligand leading to increased non-radiative decay. Both complexes exhibit bi-exponential emission lifetimes, τ_{PL}, in the sub-microsecond regime.

The emission energies and profiles of **61** and **62** in 5 wt% PMMA-doped films are not significantly changed compared to those in MeCN. The photoluminescence quantum yields of the PMMA-films are increased ($\Phi_{PL,\ PMMA}$ = 46 and 26% for **61** and **62**, respectively) compared to the solution-state measurements. This behaviour of an increase in Φ_{PL} in doped films is also observed in **63** and is attributed mainly to a reduction in k_{nr} due to the expected reduction of the conformational motions of both the mesityl groups, and in the case of **61**, the N^N ligand. Both complexes exhibit a three-component emission decay in the sub-microsecond regime in doped films, with the longest component significantly longer than the corresponding long component of τ_{PL} in MeCN.

In spin-coated neat films the structured emission profiles are likewise not significantly changed compared from those in MeCN; however, they exhibit a more pronounced shoulder at 527 and 581 nm, respectively. Compared to the neat films, the PMMA-doped films show a slight blue-shift ($\lambda_{PL,\ PMMA}$ = 459 (sh), 488 nm and $\lambda_{PL,\ PMMA}$ = 478, 512 (sh) nm for **61** and **62**, respectively). The photoluminescence quantum yields of the neat films ($\Phi_{PL,\ Neat}$) are lower ($\Phi_{PL,\ Neat}$ = 21 and 9% for **61** and **62**, respectively) compared to the solution-state measurements. The decrease in Φ_{PL} in neat films was also observed in **63** and **21** and can be explained by π-stacking intermolecular interactions between mesityl rings on adjacent complexes, providing an avenue for aggregation-caused quenching.

Both complexes exhibit a three-component emission decay in the sub-microsecond regime in neat films, which are significantly shorter compared to the measurements in PMMA films. There is no significant shifting in the emission energy at low temperature compared to

measurements at 298 K, a reflection that the emission under both sets of conditions remains ligand-centred. The emission decay profiles for both **61** and **62** are biexponential in the glass, with an expected much longer emission lifetime compared to those in MeCN.

Theoretical calculations

To gain more insights into the nature of the excited-states in both **61** and **62**, we have performed DFT and TD-DFT calculations in acetonitrile. First, for **61** the DFT optimized geometry present Ir-C_{C^N}, Ir-N_{C^N} and Ir-N_{N^N} bond lengths of 2.003 and 2.003 Å, 2.058 and 2.065 Å, and 2.223 and 2.242 Å, respectively. These values are close to the ones obtained from the crystal structure (*vide supra*) with a mean absolute deviation of 0.018 Å. The bite angles are 80.2° and 80.5° for the C^N ligands, and 86.9° for the ancillary ligand, are likewise close to their experimental counterparts. This indicates that the selected theoretical protocol is physically sound for the considered complexes. The DFT calculations indicate that when going from **61** to **62**, the energy of the HOMO increases by 0.34 eV, which is rather consistent with the electrochemical value (0.43 eV, see Table **31**), whereas the energy of the LUMO is shifted to higher energy by 0.11 eV, resulting in a HOMO-LUMO gap that is smaller by 0.23 eV in the fluorine-free complex. As can be seen in Figure **95**, the HOMO is mainly centred on the metal and the cyclometalating aryl rings of the C^N ligands, whereas the LUMO is principally localized on the pyridyl rings of the C^N ligand that is the furthest away from the ancillary phenyl ring. This holds for both compounds, so that the observed electrochemical differences are mainly due to the inductive effects of the fluorine atoms and not to a change in shape of the frontier orbitals. These MO topologies are also consistent with the fact that the energy of the HOMO significantly varies from **61** to **62**, whereas the LUMO energy is less affected.

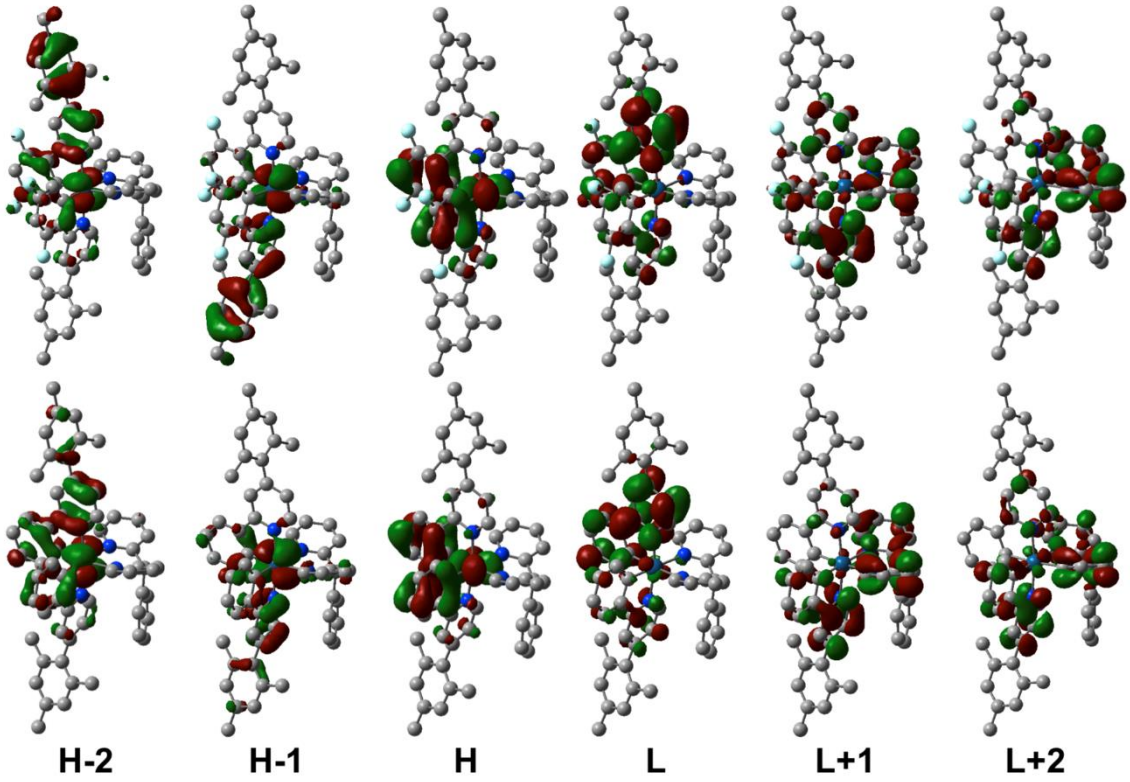

Figure **95**: Representation of the six frontier orbitals of **61** (top) and **62** (bottom). A contour threshold of 0.03 au is used, and the hydrogen atoms have been omitted for clarity.

TD-DFT calculations return several low-lying triplet states, the lowest being located at 442 nm in **61** and 463 nm in **62**. The lowest dipole-allowed singlet excited states are computed at 373 nm (f=0.054) in **61** and 399 nm (f=0.063) in **62**, corresponding to a blue-shift of 26 nm between the two complexes, in line of the experimental value (31 nm, *vide supra*) though the computed wavelengths are slightly longer than their experimental counterparts. These singlet transitions are mainly ascribable to a HOMO-LUMO electronic promotion, and therefore present a mixed ^{1}MLCT/^{1}LLCT character, L being the C^N ligand(s), with the N^N ligand not being involved in these transitions. In **61**, the next singlet transitions presenting significant oscillator strengths are located at 340 nm (f=0.012), 337 nm (f=0.025) and 329 nm (f=0.202). These three absorptions mainly correspond to HOMO-1 to LUMO+1, HOMO-2 to LUMO and HOMO-2 to LUMO+1 electronic transitions, indicating that the first and the third present a significant CT character towards the N^N ligand.

In **61**, the DFT computed 0-0 phosphorescence wavelength is 476 nm, a value that takes into account the zero-point vibrational effects. In **62**, the computed value is 501 nm, at lower energy in agreement with experimental data. In both **61** and **62**, the spin density plot of the lowest triplet excited-state shows contributions from the metal and C^N ligand residing the closest to the phenyl ring of the ancillary ligand, confirming the mixed nature of the emitting state (Figure **96**). We would therefore make the hypothesis that the interaction with the phenyl ring of the ancillary ligand tends to stabilize the spin density on the closest C^N ligand. Indeed, for **62**, we have been able to locate a triplet state presenting a more uniform delocalization of its density on both C^N ligands, but it is higher in energy than the one represented in Figure **96**.

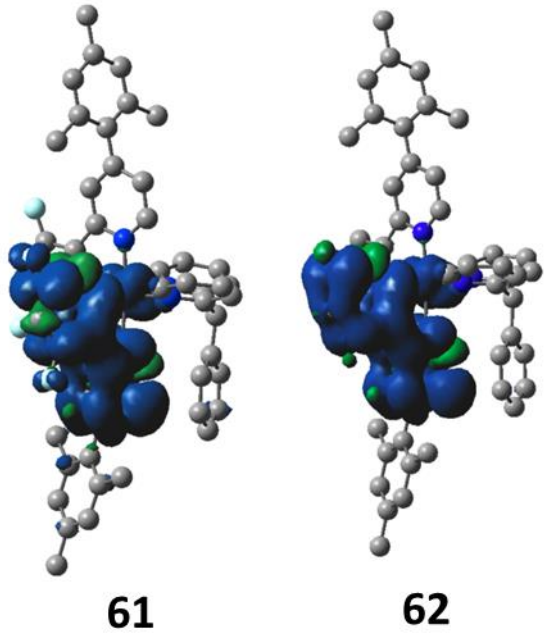

Figure **96**: Representation of the spin density difference plot for **1** (left) and **2** (right). Contour threshold: 0.0008 au.

Conclusions

Two new cationic blue and blue-green-emitting iridium complexes of the $[Ir(C^N)_2(N^N)]PF_6$ form bearing mesitylated C^N ligands and a six-membered chelate methine bridged N^N are reported. The ancillary ligand pmdp (2,2'-(phenylmethylene)dipyridine) consists of two pyridyl rings, whose electronic crosstalk is disrupted by a phenyl substituted methylene group. For both complexes we performed the synthesis, characterization and optoelectronic properties. The crystal structure of **61** reveals that the phenyl substituent on the ancillary ligand adopts a pseudo-axial configuration. By using such an ancillary ligand, a significant blue-shift in the emission is observed for **61** and **62** compared to their reference complexes. Adding the non-conjugated spacer in the ancillary ligand results in a switching of the nature of the emissive state from ^{3}MLCT/^{3}LLCT to ^{3}MLCT/^{3}ILCT when compared to bpy-based reference complexes. The photoluminescence quantum yields were lower compared to the reference complexes as a consequence of the increased fluxional motion of the ancillary ligand. Photoluminescence studies were also performed in neat films and the PMMA-doped films showing similar structured emission profiles.

It has been demonstrated that employing the nonconjugated N^N ligand 2,2'-(phenylmethylene)dipyridine, is a successful strategy to blue-shift the emission of Ir(III) complexes.

Chapter 7

Concluding Remarks

Phosphorescent Ir(III) complexes have attracted tremendous interest for their application in lighting and visual displays thanks to their excellent photophysical properties, which depend strongly on the ligand design. This work described the design, synthesis and characterisation as well as the optoelectronic properties of Ir(III) complexes for application in nonlinear optical and electroluminescent devices. Physical and photophysical properties of these complexes are corroborated by theoretical studies employing density functional theory (DFT) and time-dependent DFT (TD-DFT) calculations.

The structure of the complexes varies from the $[Ir(C\hat{}N)_2(N\hat{}N)]^+$-type (where C^N and N^N are five- or six-membered ring chelates) to the more unusual structure of [Ir(C^N^C)(N^N)Cl] [where C^N^C is a bis(six-membered)chelate tridentate tripodal ligand].

Two challenges for electroluminescent devices are the efficiency and stability, both of which can be improved by decorating the ligands with bulky substituents. Cationic complexes of the form $[Ir(C\hat{}N)_2(d\textit{t}Bubpy)]PF_6$ with hydrophobic bulky substituents were designed. The emission energy was essentially unchanged upon incorporation of various substituted aryl groups on the 4-position of the pyridine of the C^N ligand, due to the orthogonal orientation of the two aromatic substituents, a feature demonstrated by crystallographic studies. Selected complexes were tested in light-emitting electrochemical cells, resulting in bright yellow-emitting devices. For devices fabricated with complexes bearing bulky substituents, the devices were moderately efficient and with rather short lifetimes. The most stable devices were obtained for the complex without any substituents on the C^N ligands. The device with the complex substituted with a *tert*-butyl group at the 4 position of the pyridine of the C^N ligands showed the highest efficiency. Paradoxically, given what was previously reported in the literature the

concept of using bulky aromatic substituents was not successful since complexes with aromatic substituents generally showed very poor device performances.

Ir(III) complexes of the form $[Ir(C\hat{}N)_2(N\hat{}N)]^+$ can also show excellent NLO activity. In order to improve further their NLO activity triphenylamine (TPA) substituents were introduced at various positions onto the C^N ligands, which introduced intra-ligand charge transfer (ILCT) transitions. Cationic complexes bearing either 4,4'-di*tert*-butyl-2,2'-bipyridine or 5-NO_2-1,10-phenanthroline along with cyclometalated 2-phenylpyridines substituted with TPA *meta* or *para* to the Ir-$C_{C\hat{}N}$ bond or *para* to Ir-$N_{C\hat{}N}$ bond exhibited very good $\mu\beta_{EFISH}$ values. These results are amongst the best for cationic Ir(III) complexes. One of the prepared iridium compounds was incorporated into a polystyrene film, affording the first example of a second-order NLO active polymeric film based on a cationic organometallic complex exhibiting satisfactory results. Future studies may envisage using two TPA units on the C^N ligands coupled with other ancillary ligands bearing other acceptor groups designed to enhance LLCT. Molecular structures with second-order nonlinear optical (NLO) properties are useful as materials acting as building blocks for application in optical communications, optical data processing and storage, or optoelectronic devices.

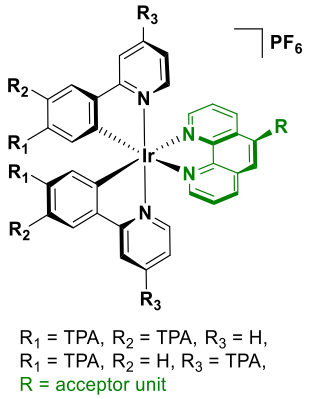

Figure **97**: Envisaged future study for NLO

We were also interested in investigating new ligand designs. Typically, cationic Ir(III) complexes consist of ligands (C^N and N^N ligands) that form a five-membered ring around

the metal centre. Expanding the ring size from a five- to six-membered chelate is rare. Using the nonconjugated benzylpyridinato as cyclometalating ligand resulted in a new series of cationic iridium(III) complexes containing six-membered chelate rings. The methylene spacer in the C^N ligands provided conformational flexibility leading to the formation of two conformers. The fluxional behaviour was investigated through NMR and detailed density functional theory (DFT) studies. Depending on the nature of the N^N ligand, phosphorescence ranging from yellow to red and marked variations of the ratio of the conformers was observed. Future studies may focus on trying to hinder conformational flexibility by incorporating bulky substituent on the CH_2 bridge forcing the system to stay in one conformation (Figure **98**).

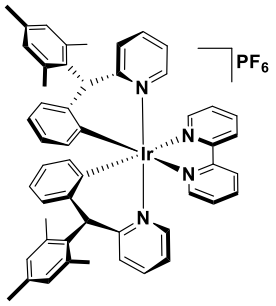

Figure **98**: Envisaged future study for bidentate six-membered ring chelates

An unusual double C−H bond activation of 2-benzhydrylpyridine ($bnpyH_2$) by complexation to iridium gave rise to an unprecedented tridentate tripod C^N^C ligand. The X-ray crystal structure reveals an unstrained geometry thanks to the formation of three six-membered chelate rings. Yellow to red phosphorescence could be obtained through changing the nature of the substituent on the C^N^C ligand. Many examples of tridentate ligands were successfully used in Ir chemistry, but the use of tripodal ligand in the field of luminescence is quite rare giving rise to a new class of Ir(III) complexes. Modification of the ancillary ligand and the monodentate ligand posed problems. Prospective studies may focus on overcoming the synthetic hurdles to substitute the monodentate ligand with other inorganic (e.g. bromide, iodide and isocyanate) or organic (phenylacetylide) monodentate ligands and altering the ancillary

ligand by other substituted diimines bearing electron-donating or electron-withdrawing groups to obtain new complexes of this class.

Substitution of the N^N with electron-withdrawing ester substituents resulted in a panchromatic NIR dye, suitable for DSSC applications. Only modest efficiency of 0.49% could be achieved, which is however comparable to other Ir(III) dyes. This can be attributed to the modest absorption coefficient, which lead to weak light harvesting in the visible region and low short-circuit current. Through a further investigation of this ligand system a better understanding of the relation between the structure and properties may be possible to explore further the field of Ir dyes for DSSC application. Future work may involve using other ligand systems to redshift the emission (Figure **99**).

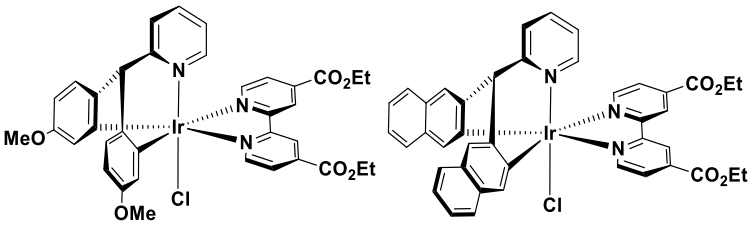

Figure **99**: Envisaged future study with a modified tripod ligand

In the last decade blue-emitting iridium(III) complexes have been successfully employed for solution-processed OLEDs and LEECs. However, it is still an ongoing challenge to develop blue-colour purity, high efficiency and good stability. One strategy to blue-shift the emission is to decorate the C^N ligand with electron-withdrawing groups or the N^N with electron-donating. Another successful approach to tune the emission towards the blue is to employ a nonconjugated ancillary ligand and some examples have been previously reported. We employed the nonconjugated diimine 2,2'-(phenylmethine)dipyridine, whose pyridine rings are separated by a phenyl-substituted methine bridge can form a six-membered ring when coordinated to iridium. The chelating motif was confirmed by single-crystal X-ray diffraction.

With C^N ligands based on 4-mesityl-2-phenylpyridinato blue-green and sky-blue emission can be obtained. A current challenge while developing blue emitters is to do without the use of fluorine substituents which have shown to lead to degradation during device operation. Our approach using this ligand is a strategy to successfully tune the emission to the blue. This study also shows the impact of the substituent on the methine spacer, on the photophysical characteristics, compared to reported related examples. Future studies may involve disubstituting the methine bridge to rigidify the system and reduce motional flexibility of the ancillary ligand (Figure **100**).

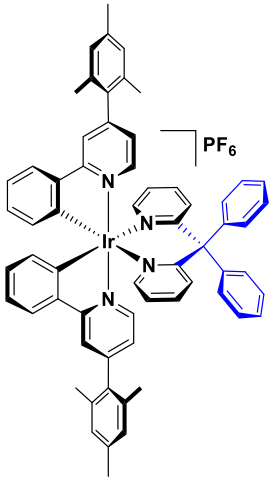

Figure **100**: Envisaged future study to rigidify the methine bridge

Chapter 8

Experimental

General Synthetic Procedures

Commercial chemicals were used as supplied. All reactions were performed using standard Schlenk techniques under inert (N_2 or Ar) atmosphere with reagent-grade solvents. Flash column chromatography was performed using silica gel (Silia-P from Silicycle, 60 Å, 40-63 μm). Analytical thin layer chromatography (TLC) was performed with silica plates with aluminium backings (250 μm with indicator F-254). Compounds were visualised under UV light. ^{1}H, ^{13}C, ^{19}F and ^{31}P solution-phase NMR spectra were recorded on a Bruker Avance spectrometer operating at 11.7 T (Larmor frequencies of 400, 500; 100, 101, 126; 376 and 162 MHz, respectively). The following abbreviations have been used for multiplicity assignments: "s" for singlet, "d" for doublet, "t" for triplet and "m" for multiplet. ^{1}H and ^{13}C NMR spectra were referenced to the solvent peak. Melting points (Mps) were recorded using open-ended capillaries on an electrothermal melting point apparatus and are uncorrected. High-resolution mass spectra were recorded at the EPSRC UK National Mass Spectrometry Facility at Swansea University on a quadrupole time-of-flight (ESI-Q-TOF), model ABSciex 5600 Triple TOF in positive electrospray ionisation mode and spectra were recorded using sodium formate solution as the calibrant. Elemental analyses were performed by Mr. Stephen Boyer, London Metropolitan University.

Syntheses of Ligands and organic Intermediates

Borylation Reactions

General Procedure

A solution of Bromo-aryl (1.00 equiv.) in dry THF was cooled to -80 °C in an EtOH/$N_{2,liq}$ bath and *n*-BuLi (1.80 equiv.) was added dropwise at -80 °C. The reaction mixture was kept at this temperature under stirring. After 45 min triisopropyl borate (3.00 equiv.) was added dropwise to the solution at -80 °C. The mixture was allowed to warm to room temperature. After 14 h of stirring without cooling the reaction mixture was poured onto ice water (50 mL), acidified with HCl until pH 2 and extracted with Et_2O (40 mL). The combined organic layers were washed with an aqueous $NaHCO_3$ solution till pH 6, washed with brine (10 mL), dried over $MgSO_4$, and concentrated in vacuum giving a crude residue which was used as such.

(3,5-di-*tert*-butylphenyl)boronic acid

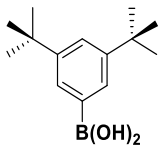

The synthesis of this compound was carried out using 1-bromo-3,5-di-*tert*-butylbenzene.

(4-(diphenylamino)phenyl)boronic acid

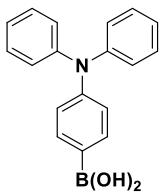

The synthesis of this compound was carried out using 4-bromo-*N*,*N*-diphenylaniline.

Suzuki-Miyaura Cross-Coupling Reactions

General Procedure

A mixture of the aryl halide (1.00 equiv.), aryl boronic acid (1.50 equiv.) in the presence of a base (5.00 equiv.) and 1,4-dioxane/water (4/1) was degassed via three purging cycles of N_2 and vacuum. $Pd(PPh_3)_4$ (0.05 equiv.) was added, and the reaction mixture was heated to 95 °C and kept at reflux. After the specific time, the reaction mixture was allowed to cool to room temperature and the solvent was removed leaving a residue which was dissolved in organic solvent and washed with water and brine. After layer separation, the combined organic layers were dried over $MgSO_4$. The solvent was evaporated leaving a residue, which was purified by column chromatography on silica.

2-chloro-4-mesitylpyridine

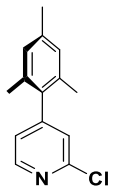

Cl21

The synthesis of this compound was carried out using 2-chloro-4-iodopyridine (1.00 equiv.), 2,4,6-trimethylphenylboronic acid (1.50 equiv.) and K_2CO_3 (5.00 equiv.). The reaction mixture was kept at reflux for 3 days. The crude was dissolved in toluene. The compound was purified by column chromatography (20% of EtOAc in petroleum ether on silica) yielding a colourless oil (0.685 g). **Yield:** 94%. **R_f:** 0.42 (10% EtOAc in petroleum ether on silica). **^{1}H NMR (400 MHz, $CDCl_3$) δ (ppm):** 8.37 (d, 1H), 7.10 (s, 1H), 6.97 (dd, 1H), 6.92 (s, 2H), 2.29 (s, 3H), 1.97 (s, 6H). **^{13}C{^{1}H} NMR (101 MHz, $CDCl_3$) δ (ppm):** 159.2, 152.7, 151.8, 149.7, 136.6, 130.3, 125.5, 124.0, 113.0, 55.2, 20.9. **HR-MS** ($FTMS^+$)**: $[M-H]^+$ Calculated:** ($C_{14}H_{14}ClNH$): 232.0888 **Found:** 232.0882. The characterisation matches that reported.[76]

2-chloro-4-(4-methoxy-2,6-dimethylphenyl)pyridine

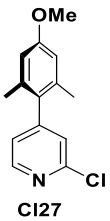

Cl27

The synthesis of this compound was carried out using 2-chloro-4-iodopyridine (1.00 equiv.), (4-methoxy-2,6-dimethylphenyl)boronic acid (1.50 equiv.) and K_2CO_3 (5.00 equiv.). The reaction mixture was kept at reflux for 3 days. The crude was dissolved in toluene. The compound was purified by column chromatography (15% of EtOAc in petroleum ether on silica) yielding a colourless oil (0.995 g). **Yield:** 94%. **R_f:** 0.32 (10% EtOAc in petroleum ether on silica). **^{1}H NMR (400 MHz, $CDCl_3$) δ (ppm):** 8.44 (d, *J*=5.0, 1H), 7.15 (m, 1H), 7.04 (d, *J*=5.0, 1H), 6.95 (s, 2H), 2.33 (s, 3H), 2.00 (s, 6H). **^{13}C{^{1}H} NMR (126 MHz, $CDCl_3$) δ (ppm):** 159.2, 152.7, 151.8, 149.7, 136.6, 130.4, 125.5, 124.0, 113.1, 55.2, 20.9. **HR-MS** ($FTMS^+$)**: [M-H]$^+$ Calculated:** ($C_{14}H_{15}ClNOH$): 248.0837 **Found:** 248.0837. **CHN**: **Calcd.** for $C_{14}H_{14}ClNO$: C, 67.88; H, 5.70; N, 5.65. **Found:** C, 67.76; H, 5.59; N, 5.57.

2-chloro-4-(3,5-di-*tert*-butylphenyl)pyridine

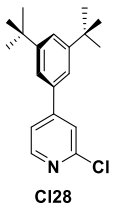

Cl28

The synthesis of this compound was carried out using 2-chloro-4-iodopyridine (1.00 equiv.), (3,5-di-*tert*-butylphenyl)boronic acid (1.50 equiv.) and K_2CO_3 (5.00 equiv.). The reaction mixture was kept at reflux for 3 days. The crude was dissolved in toluene. The compound was purified by column chromatography (15% of EtOAc in petroleum ether on silica) yielding a red solid (1.613 g). **Yield:** 96%. **R_f:** 0.40 (10 vol.% EtOAc in petroleum ether on silica). **Mp:** 68 °C. **^{1}H NMR (400 MHz, $CDCl_3$) δ (ppm):** 8.42 (d, 1H), 7.54 (d, 2H), 7.41 (m, 3H), 1.38 (s,

18H). **$^{13}C\{^{1}H\}$ NMR (101 MHz, $CDCl_3$) δ (ppm):** 152.8, 152.0, 151.9, 149.8, 136.4, 123.8, 122.3, 121.4, 120.8, 35.0, 31.4. **HR-MS** ($FTMS^+$)**: $[M-H]^+$ Calculated:** ($C_{19}H_{25}ClNH$): 302.1670 **Found:** 302.1668. **CHN**: **Calcd.** for $C_{19}H_{24}ClN$: C, 75.60; H, 8.01; N, 4.64. **Found:** C, 75.41; H, 7.93; N, 4.61.

2-(4-bromophenyl)pyridine

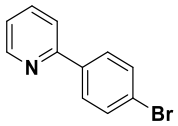

29Br

The synthesis of this compound was carried out using 2-bromo-pyridine (1.00 equiv.), (4-bromophenyl)boronic acid (1.50 equiv.) and K_2CO_3 (5.00 equiv.). The reaction mixture was kept at reflux for 3 days. The crude was dissolved in toluene. The compound was purified by column chromatography (10% of EtOAc in petroleum ether on silica) yielding a colourless liquid (1.915 g). **Yield:** 72%. **R_f:** 0.29 (10% of EtOAc in petroleum ether on silica). **Mp:** 60 – 63 °C. **Lit:** 60 – 65 °C.[282] **^{1}H NMR (400 MHz, $CDCl_3$) δ (ppm):** 8.69 (d, J = 4.3 Hz, 1H), 7.88 (d, J = 8.6 Hz, 2H), 7.80 – 7.68 (m, 2H), 7.60 (d, J = 8.6 Hz, 2H), 7.28 – 7.23 (m, 1H). **$^{13}C\{^{1}H\}$ NMR (126 MHz, $CDCl_3$) δ (ppm):** 156.4, 149.9, 138.3, 132.0, 128.6, 123.6, 122.6, 120.5, 117.5. **HR-MS** ($FTMS^+$)**: $[M]^+$ Calculated:** ($C_{11}H_8BrNH$): 233.9913; **Found:** 233.9915. The characterisation matches that reported.[282]

2-(3-bromophenyl)pyridine

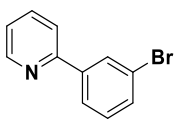

30Br

The synthesis of this compound was carried out using 2-bromo-pyridine (1.00 equiv.), (3-bromophenyl)boronic acid (1.50 equiv.) and K_2CO_3 (5.00 equiv.). The reaction mixture was kept at reflux for 3 days. The crude was dissolved in toluene. The compound was purified by

column chromatography (10% of EtOAc in petroleum ether on silica) yielding a colourless liquid (0.560 g). **Yield:** 48%. **R_f:** 0.52 (10% of EtOAc in petroleum ether on silica). **^{1}H NMR (400 MHz, $CDCl_3$) δ (ppm):** 8.69 (d, J = 4.5 Hz, 1H), 8.17 (s, 1H), 7.90 (d, J = 7.8 Hz, 1H), 7.78 – 7.66 (m, 2H), 7.53 (d, J = 7.9 Hz, 1H), 7.33 (t, J = 7.9 Hz, 1H). **^{13}C{^{1}H} NMR (126 MHz, $CDCl_3$) δ (ppm):** 155.8, 149.8, 141.4, 136.9, 131.9, 130.3, 130.0, 125.4, 123.1, 122.7, 120.6. **HR-MS** ($FTMS^+$)**: $[M]^+$ Calculated:** ($C_{11}H_8BrNH$): 233.9913; **Found:** 233.9910. The characterisation matches that reported.[185]

4-bromo-2-phenylpyridine

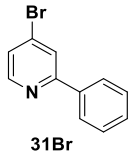

The synthesis of this compound was carried out using 2,4-dibromopyridine (1.00 equiv.), phenylboronic acid (1.50 equiv.) and KOH (5.00 equiv.). The reaction mixture was kept at reflux for 2 days. The crude was dissolved in toluene. The compound was purified by column chromatography (10% of EtOAc in petroleum ether on silica) yielding a colourless liquid (0.475 g). **Yield:** 32%. **R_f:** 0.30 (10% of EtOAc in petroleum ether on silica). **^{1}H NMR (400 MHz, $CDCl_3$) δ (ppm):** 8.50 (d, J = 5.3 Hz, 1H), 7.96 (dd, J = 8.1, 1.4 Hz, 2H), 7.90 (d, J = 1.6 Hz, 1H), 7.52 – 7.41 (m, 3H), 7.39 (d, J = 5.3 Hz, 1H). **^{13}C{^{1}H} NMR (126 MHz, $CDCl_3$) δ (ppm):** 156.2, 150.1, 141.8, 137.3, 132.2, 130.6, 130.4, 125.8, 123.4, 123.1, 121.0. **HR-MS** ($FTMS^+$)**: $[M]^+$ Calculated:** ($C_{11}H_8BrNH$): 233.9913; **Found:** 233.9915. The characterisation matches that reported.[199]

4-mesityl-2-phenylpyridine

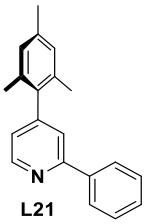

L21

The synthesis of this compound was carried out using 2-chloro-4-mesitylpyridine (1.00 equiv.), phenylboronic acid (1.50 equiv.) and Na_2CO_3 (5.00 equiv.). The reaction mixture was kept at reflux for 24 h. The crude was dissolved in CH_2Cl_2. The compound was purified by column chromatography (5% of EtOAc in petroleum ether on silica) yielding yellow oil (0.331 g). **Yield:** 90%. **R_f:** 0.39 (10 vol.% EtOAc in petroleum ether on silica). **^{1}H NMR (400 MHz, $CDCl_3$) δ (ppm):** 8.71 (d, *J* = 4.8 Hz, 1H), 8.02 – 7.97 (m, 2H), 7.56 (s, 1H), 7.50 – 7.37 (m, 3H), 7.07 (dd, *J* = 4.8 Hz, 1H), 6.99 (s, 2H), 2.48 (s, 3H), 2.19 (s, 6H). **^{13}C{^{1}H} NMR (101 MHz, $CDCl_3$) δ (ppm):** 157.7, 150.4, 150.0, 139.4, 137.7, 136.6, 135.3, 129.1, 128.9, 128.5, 127.0, 123.3, 121.6, 21.2, 20.7. **HR-MS** ($FTMS^+$)**: [M-H]$^+$ Calculated:** ($C_{20}H_{19}NH$): 247.1590. **Found:** 247.1590. The characterisation matches that reported.[76]

4-(4-methoxy-2,6-dimethylphenyl)-2-phenylpyridine

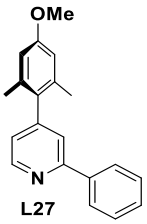

L27

The synthesis of this compound was carried out using 2-chloro-4-(4-methoxy-2,6-dimethylphenyl)pyridine (1.00 equiv.), phenylboronic acid (1.50 equiv.) and Na_2CO_3 (5.00 equiv.). The reaction mixture was kept at reflux for 24 h. The crude was dissolved in CH_2Cl_2. The compound was purified by column chromatography (5% of EtOAc in petroleum ether on silica) yielding colourless oil. **Yield:** 89%. **R_f:** 0.25 (10 vol.% EtOAc in petroleum ether on

silica). **^{1}H NMR (400 MHz, $CDCl_3$) δ (ppm):** 8.70 (dd, *J*=4.9, 1H), 8.00 (m, 2H), 7.55 (s, 1H), 7.46 (m, 3H), 7.06 (dd, *J*=4.9, 1H), 6.72 (s, 2H), 3.93 (s, 3H), 2.21 (s, 6H). **^{13}C{^{1}H} NMR (101 MHz, $CDCl_3$) δ (ppm):** 158.9, 157.6, 150.2, 149.8, 139.3, 136.8, 131.9, 129.0, 128.7, 126.9, 123.6, 121.9, 113.0, 55.2, 21.0. **HR-MS** ($FTMS^+$)**: [M-H]$^+$ Calculated:** ($C_{20}H_{19}NOH$): 290.1539 **Found:** 290.1538. **CHN**: **Calcd.** for $C_{20}H_{19}NO$: C, 83.01; H, 6.62; N, 4.84. **Found:** C, 82.89; H, 6.56; N, 4.73.

4-(3,5-di-*tert*-butylphenyl)-2-phenylpyridine

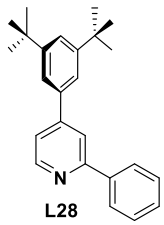

L28

The synthesis of this compound was carried out using 2-chloro-4-(3,5-di-*tert*-butylphenyl)pyridine (1.00 equiv.), phenylboronic acid (1.50 equiv.) and Na_2CO_3 (5.00 equiv.). The reaction mixture was kept at reflux for 24 h. The crude was dissolved in CH_2Cl_2. The compound was purified by column chromatography (5% of EtOAc in petroleum ether on silica) yielding a colourless solid. **Yield:** 85%. **R_f:** 0.22 (5 vol.% EtOAc in petroleum ether on silica). **^{1}H NMR (400 MHz, $CDCl_3$) δ (ppm):** 8.73 (d, 1H), 8.05 (d, 2H), 7.90 (s, 1H), 7.52 (m, 5H), 7.45 (d, 2H), 1.40 (s, 18H). **^{13}C{^{1}H} NMR (101 MHz, $CDCl_3$) δ (ppm):** 158.0, 151.7, 150.7, 149.9, 139.6, 138.2, 129.0, 128.8, 127.1, 123.2, 121.5, 120.8, 119.2, 35.0, 31.5. **HR-MS** ($FTMS^+$)**: [M-H]$^+$ Calculated:** ($C_{25}H_{29}NH$): 344.2371 **Found:** 344.2373. **CHN**: **Calcd.** for $C_{25}H_{29}N$: C, 87.41; H, 8.51; N, 4.08. **Found:** C, 87.31; H, 8.43; N, 4.14.

***N*,*N*-diphenyl-4'-(pyridin-2-yl)-[1,1'-biphenyl]-4-amine**

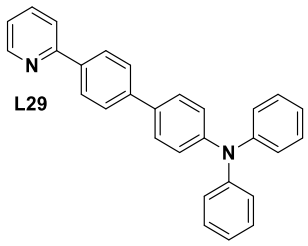

L29

The synthesis of this compound was carried out using 2-(4-bromophenyl)pyridine (1.00 equiv.), (4-(diphenylamino)phenyl)boronic acid (1.50 equiv.) and K_2CO_3 (5.00 equiv.). The reaction mixture was kept at reflux for 18 h. The crude was dissolved in toluene. The compound was purified by column chromatography (10% of EtOAc in petroleum ether on silica) yielding a grey solid (0.613 g). **Yield:** 73%. **R_f:** 0.34 (10% of EtOAc in petroleum ether on silica). **Mp:** 171 – 175 °C. **^{1}H NMR (400 MHz, $CDCl_3$) δ (ppm):** 8.71 (d, J = 4.8 Hz, 1H), 8.06 (d, J = 8.4 Hz, 2H), 7.77 (s, 2H), 7.69 (d, J = 8.4 Hz, 2H), 7.54 (d, J = 8.6 Hz, 2H), 7.29 (d, J = 8.3 Hz, 3H), 7.23 (dt, J = 6.1, 2.5 Hz, 1H), 7.16 (d, J = 2.3 Hz, 5H), 7.04 (t, J = 7.3 Hz, 2H). **^{13}C{^{1}H} NMR (126 MHz, $CDCl_3$) δ (ppm):** 157.2, 149.8, 147.7, 147.5, 141.2, 137.8, 136.8, 134.4, 129.4, 127.8, 127.4, 127.0, 124.6, 123.9, 123.1, 122.1, 120.5. **HR-MS** ($FTMS^+$)**: $[M]^+$ Calculated:** ($C_{29}H_{22}N_2H$): 399.1856; **Found:** 399.1851. The characterisation matches that reported.[283]

***N*,*N*-diphenyl-3'-(pyridin-2-yl)-[1,1'-biphenyl]-4-amine**

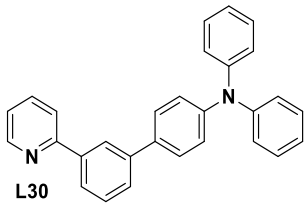

L30

The synthesis of this compound was carried out using 2-(3-bromophenyl)pyridine (1.00 equiv.), (4-(diphenylamino)phenyl)boronic acid (1.50 equiv.) and K_2CO_3 (5.00 equiv.). The reaction mixture kept at reflux for 18 h. The crude was dissolved in toluene. The compound

was purified by column chromatography (10% of EtOAc in petroleum ether on silica) yielding a brown solid (0.798 g). **Yield:** 94%. **R_f:** 0.28 (10% of EtOAc in petroleum ether on silica). **Mp:** 93 – 96 °C. **^{1}H NMR (400 MHz, $CDCl_3$) δ (ppm):** 8.75 (dt, J = 4.8, 1.5 Hz, 1H), 8.25 (t, J = 1.9 Hz, 1H), 7.96 (dt, J = 7.7, 1.5 Hz, 1H), 7.86 – 7.74 (m, 2H), 7.69 – 7.52 (m, 4H), 7.33 – 7.26 (m, 5H), 7.19 (td, J = 6.9, 3.4 Hz, 6H), 7.11 – 7.03 (m, 2H). **^{13}C{^{1}H} NMR (101 MHz, $CDCl_3$) δ (ppm):** 157.6, 149.8, 147.8, 147.4, 141.4, 139.9, 136.9, 135.1, 129.4, 129.3, 128.4, 127.4, 125.6, 125.5, 124.5, 124.1, 123.1, 122.3, 120.9. **HR-MS** ($FTMS^+$)**: $[M]^+$ Calculated:** ($C_{29}H_{22}N_2H$): 399.1856; **Found:** 399.1846. **CHN**: **Calcd.** for $C_{29}H_{22}N_2x1/5CH_2Cl_2$: C, 84.41; H, 5.43; N, 6.74. **Found:** C, 84.28; H, 5.79; N, 6.55.

***N*,*N*-diphenyl-4-(2-phenylpyridin-4-yl)aniline**

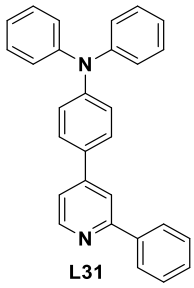

L31

The synthesis of this compound was carried out using 4-bromo-2-phenylpyridine (1.00 equiv.), (4-(diphenylamino)phenyl)boronic acid (1.50 equiv.) and K_2CO_3 (5.00 equiv.). The reaction mixture was kept at reflux for 18 h. The crude was dissolved in toluene. The compound was purified by column chromatography (10% of EtOAc in petroleum ether on silica) yielding a brown oil (0.513 g). **Yield:** 95%. **R_f:** 0.63 (20% of EtOAc in petroleum ether on silica). **^{1}H NMR (400 MHz, $CDCl_3$) δ (ppm):** 8.70 (d, J = 5.2 Hz, 1H), 8.07 – 8.00 (m, 2H), 7.90 (d, J = 1.6 Hz, 1H), 7.61 – 7.55 (m, 2H), 7.53 – 7.46 (m, 2H), 7.46 – 7.38 (m, 2H), 7.35 – 7.27 (m, 5H), 7.21 – 7.11 (m, 6H), 7.12 – 7.03 (m, 2H). **^{13}C{^{1}H} NMR (126 MHz, $CDCl_3$) δ (ppm):** 158.0, 150.0, 148.9, 148.6, 147.2, 139.6, 131.4, 129.4, 128.9, 128.7, 127.7, 127.0, 124.9, 123.5, 122.9, 119.5, 118.1. **HR-MS** ($FTMS^+$)**: $[M]^+$ Calculated:** ($C_{29}H_{22}N_2H$): 399.1856; **Found:** 399.1844.

Direct C-H Arylation with Arylboronic Acids

General Procedure

The synthesis is similar to a previously reported method.[184] A solution of *tert*-butylpyridine (1.00 equiv.) in CH_2Cl_2 was stirred at room temperature. Trifluoroacetic acid (1.00 equiv.) was added followed by arylboronic acid (1.50 equiv.), water (12 mL), a solution of silver(I) nitrate (0.20 equiv.) in 8 mL of water and potassium persulfate (3.00 equiv.). The solution was stirred vigorously for 6 h. The reaction was quenched with water (10 mL), extracted with CH_2Cl_2 (50 mL) and washed with conc. aqueous $NaHCO_3$ (10 mL). After layer separation, the organic layer was dried over $MgSO_4$ and the solvent was evaporated under vacuum leaving a residue which was purified on silica (10% of EtOAc in petroleum ether). The desired fractions were combined and reduced until dryness yielding the desired compound.

4-(*tert*-butyl)-2-phenylpyridine

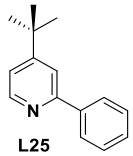

L25

The synthesis of this compound was carried out using phenylboronic acid (1.50 equiv.) to give colourless oil (0.351 g). **Yield:** 45%. **R_f:** 0.32 (10% of EtOAc in petroleum ether on silica). **^{1}H NMR (400 MHz, $CDCl_3$) δ (ppm):** 8.62 (d, 1H), 8.02 – 7.93 (m, 2H), 7.74 – 7.69 (m, 1H), 7.48 (q, *J* = 7.4 Hz, 2H), 7.41 (q, *J* = 7.4 Hz, 1H), 7.25 – 7.22 (m, 1H), 1.36 (s, 9H). **^{13}C{^{1}H} NMR (101 MHz, $CDCl_3$) δ (ppm):** 160.8, 157.6, 149.6, 140.1, 128.8, 128.7, 127.1, 119.4, 117.9, 35.0, 30.7. **HR-MS** ($FTMS^+$)**: [M-H]$^+$ Calculated:** ($C_{15}H_{17}NH$): 212.1434 **Found:** 212.1428. The characterisation matches that reported.[184]

4-(*tert*-butyl)-2-(4-(*tert*-butyl)phenyl)pyridine

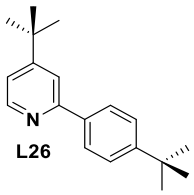

L26

The synthesis of this compound was carried out using (4-(*tert*-butyl)phenyl)boronic acid (1.50 equiv.) to give colourless oil (1.000 g). **Yield:** 46%, **R_f:** 0.36 (10% EtOAc in petroleum ether on silica). **^{1}H NMR (400 MHz, $CDCl_3$) δ (ppm):** 8.55 (d, 1H), 7.89 (d, *J* = 8.3 Hz, 2H), 7.68 (s, 1H), 7.49 (d, *J* = 8.3 Hz, 2H), 7.22 – 7.20 (m, 1H), 1.52 (s, 18H). The characterisation matches that reported.[284]

General Procedure for Grignard Reaction

The synthesis is similar to a previously reported method.[285] An oven-dried flask was charged under a nitrogen atmosphere with magnesium turnings (5.00 equiv.) and dry THF (80 mL) followed by 2 mL of 1,2-dibromoethane and was gently heated to 30 °C. After the observation of gas evolution, a solution of the arylbromide (3.00 equiv.) in dry THF (40 mL) was added dropwise. The reaction mixture was heated under stirring and kept at reflux for 4 h. The reaction mixture was then cooled in an ice bath and a solution of methyl picolinate (1.00 equiv.) in dry THF (40 mL) was added carefully. The solution was allowed to warm to room temperature and was stirred for 2 h. The reaction mixture was quenched with aqueous NH_4Cl (5 mL) and extracted with Et_2O (50 mL). The combined organic layers were dried over $MgSO_4$ and the solvent was evaporated leaving a residue, which was purified over silica (10% EtOAc in petroleum ether). The desired fractions were combined and reduced until dryness yielding the desired compound.

Diphenyl(pyridin-2-yl)methanol

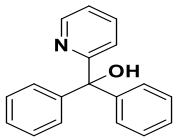

A39

The synthesis of this compound was carried out using bromobenze (3.00 equiv.) to give a colourless solid (1.686 g). **Yield:** 86%. **R_f:** 0.51 (10% EtOAc in petroleum ether on silica). **Mp:** 101 – 104 °C. **Lit:** 102 – 103 °C.[285] **^{1}H NMR (400 MHz, $CDCl_3$) δ (ppm):** 8.60 (d, *J* = 4.7 Hz, 1H), 7.64 (td, *J* = 7.8, 1.8 Hz, 1H), 7.40 – 7.21 (m, 11H), 7.12 (d, *J* = 7.9 Hz, 1H), 6.28 (s, 1H). **^{13}C{^{1}H} NMR (101 MHz, $CDCl_3$) δ (ppm):** 163.2, 147.7, 146.1, 136.4, 128.1, 127.9, 127.3, 122.9, 122.3, 80.8. **HR-MS** ($FTMS^+$)**: [M-H]$^+$ Calculated:** ($C_{18}H_{15}NOH$): 262.1226 **Found:** 262.1226. **CHN**: **Calcd.** for $C_{18}H_{15}NO$: C, 82.73; H, 5.79; N, 5.36. **Found:** C, 82.68; H, 5.73; N, 5.41. The characterisation matches that reported.[285]

Bis(4-(*tert*-butyl)phenyl)(pyridin-2-yl)methanol

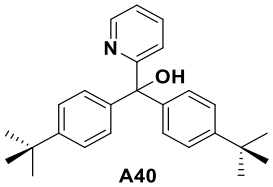

A40

The synthesis of this compound was carried out using 1-bromo-4-(*tert*-butyl)benzene (3.00 equiv.) to give a colorless solid (1.994 g). **Yield:** 71%. **R_f:** 0.39 (10% EtOAc in petroleum ether on silica). **Mp:** 156 °C. **Lit:** 156 °C.[286] **^{1}H NMR (400 MHz, $CDCl_3$) δ (ppm):** 8.58 (d, *J* = 3.2 Hz, 1H), 7.67 – 7.60 (m, 1H), 7.33 – 7.28 (m, 4H), 7.24 – 7.12 (m, 6H), 6.19 (s, 1H), 1.30 (s, 18H). **^{13}C{^{1}H} NMR (101 MHz, $CDCl_3$) δ (ppm):** 163.8, 150.1, 147.7, 143.3, 136.4, 127.9, 124.9, 123.1, 122.3, 80.6, 34.6, 31.5. **HR-MS** ($FTMS^+$)**: [M-H]$^+$ Calculated:** ($C_{26}H_{31}NOH$): 374.2478 **Found:** 374.2476. **CHN**: **Calcd.** for $C_{26}H_{31}NO$: C, 83.60; H, 8.37; N, 3.75. **Found:** C, 83.45; H, 8.51; N, 3.88. The characterisation matches that reported.[286]

Pyridin-2-ylbis(4-(trifluoromethyl)phenyl)methanol

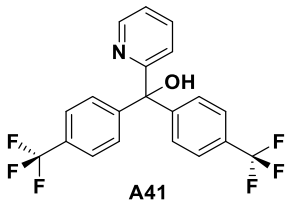

A41

The synthesis of this compound was carried out using 1-bromo-4-(trifluoromethyl)benzene (3.00 equiv.) to give a colorless solid (1.994 g). **Yield:** 64%. **R_f:** 0.26 (10% EtOAc in petroleum ether on silica). **Mp:** 164 °C. **^{1}H {^{19}F} NMR (400 MHz, $CDCl_3$) δ (ppm):** 8.64 (d, *J* = 7.4 Hz, 1H), 7.75 – 7.69 (m, 1H), 7.60 (s, 4H), 7.44 (s, 4H), 7.31 (d, *J* = 8.5 Hz, 1H), 7.13 (d, *J* = 9.7 Hz, 1H), 6.50 (s, 1H). **^{13}C{^{1}H} NMR (101 MHz, $CDCl_3$) δ (ppm):** 161.5, 149.4, 148.2, 136.9, 129.9 (q, *J* = 32.3 Hz), 128.5, 125.5, 125.1 (q, *J* = 4.0 Hz), 123.1, 122.7, 80.4. **^{19}F {^{1}H} NMR (376 MHz, $CDCl_3$) δ (ppm):** -62.59 (s, 6F). **HR-MS** ($FTMS^+$)**: [M-H]$^+$ Calculated:** ($C_{20}H_{13}F_6NOH$): 398.0974 **Found:** 398.0965. **CHN**: **Calcd.** for $C_{20}H_{13}F_6NO$: C, 60.46; H, 3.30; N, 3.53. **Found:** C, 60.51; H, 3.36; N, 3.59.

Reduction of Hydroxyl Group

Procedure for 2-benzhydrylpyridine & 2-(bis(4-(tert-butyl)phenyl)methyl)pyridine

The synthesis is similar to a previously reported method.[285] A mixture of the substituted methanol (1.00 equiv), aqueous 57% HI (2.5 mL), and HOAc (13 mL) was heated to 100 °C for 4 h. The resulting mixture was then cooled to 0 °C and basified to pH 9 with an aqueous NaOH solution (2 M). Ethyl acetate (100 mL) was added and the mixture was washed successively with an aqueous $NaHSO_3$ solution and brine. The combined organic layers were dried over $MgSO_4$ and the solvent was evaporated leaving a residue, which was purified over silica (10% EtOAc in petroleum ether). The desired fractions were combined and reduced until dryness yielding the desired compound.

2-benzhydrylpyridine

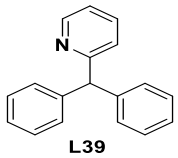

L39

The synthesis of this compound was carried out using diphenyl(pyridin-2-yl)methanol (1.00 equiv.) to give a beige solid (0.788 g). **Yield:** 74%. **R_f:** 0.30 (10% EtOAc in petroleum ether on silica). **Mp:** 95 °C. **^{1}H NMR (400 MHz, $CDCl_3$) δ (ppm):** 8.64 (d, *J* = 4.1 Hz, 1H), 7.66 – 7.59 (m, 1H), 7.33 (t, *J* = 7.3 Hz, 4H), 7.24 (dd, *J* = 21.8, 7.2 Hz, 6H), 7.18 – 7.10 (m, 2H), 5.76 (s, 1H). **^{13}C{^{1}H} NMR (101 MHz, $CDCl_3$) δ (ppm):** 163.2, 149.5, 142.7, 136.4, 129.4, 128.4, 126.5, 123.8, 121.4, 59.4. **HR-MS** ($FTMS^+$)**: $[M-H]^+$ Calculated:** ($C_{18}H_{15}NH$): 246.1277 **Found:** 246.1277. The characterisation matches that reported.[287]

2-(bis(4-(*tert*-butyl)phenyl)methyl)pyridine

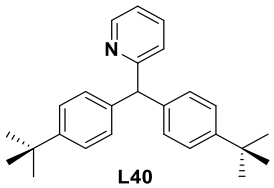

L40

The synthesis of this compound was carried out using bis(4-(*tert*-butyl)phenyl)(pyridin-2-yl)methanol (1.00 equiv.) to give a beige solid (0.788 g). **Yield:** 76%. **R_f:** 0.33 (10% EtOAc in petroleum ether on silica). **^{1}H NMR (400 MHz, $CDCl_3$) δ (ppm):** 8.62 – 8.56 (m, 1H), 7.62 – 7.56 (m, 1H), 7.31 (s, 4H), 7.10 (s, 6H), 5.62 (s, 1H), 1.29 (s, 18H). **^{13}C{^{1}H} NMR (126 MHz, $CDCl_3$) δ (ppm):** 163.8, 149.6, 149.2, 139.9, 136.5, 129.0, 125.4, 123.9, 121.4, 58.7, 34.5, 31.5. **HR-MS** ($ASAP^+$)**: $[M-H]^+$ Calculated:** ($C_{26}H_{32}NH$): 358.2535 **Found:** 358.2534.

2-(bis(4-(trifluoromethyl)phenyl)methyl)pyridine

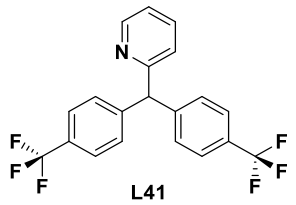

L41

The synthesis is similar to a previously reported method.[229] A mixture of pyridin-2-ylbis(4-(trifluoromethyl)phenyl)methanol (0.500 g, 1.26 mmol, 1.00 equiv.) and PBr_3 (25 mL) was vigorously stirred and heated and kept at 110 °C for 2 h. The mixture was then cooled to r.t. and was carefully poured onto ice and aqueous NaOH (2 M) was added till pH neutral. The organic layer was dried over $MgSO_4$ and the solvent was evaporated leaving a residue which was dissolved in acetic acid (50 mL) and zinc dust (0.799 g, 12.60 mmol, 10.00 equiv.) was added. The mixture was stirred at r.t. After 1 h, 20 mL of water was carefully added and aqueous NaOH (2 M) was added till pH neutral. The organic layer was dried over $MgSO_4$ and the solvent was evaporated leaving a residue which was purified over silica (10% EtOAc in petroleum ether as the solvent). The desired fractions were combined, and the solvent was evaporated leaving colourless oil (0.117 g). **Yield:** 24% **R_f:** 0.55 (20% EtOAc in petroleum ether on silica). **^{1}H {^{19}F} NMR (400 MHz, $CDCl_3$) δ (ppm):** 8.63 (ddd, *J* = 4.9, 1.9, 0.9 Hz, 1H), 7.66 (td, *J* = 7.7, 1.9 Hz, 1H), 7.57 (d, *J* = 8.2 Hz, 4H), 7.30 (d, *J* = 8.1 Hz, 4H), 7.20 (ddd, *J* = 7.6, 4.8, 1.1 Hz, 1H), 7.10 (dt, *J* = 7.9, 1.1 Hz, 1H), 5.75 (s, 1H). **^{13}C{^{1}H} NMR (126 MHz, $CDCl_3$) δ (ppm):** 161.4, 150.1, 146.0, 137.0, 129.8, 129.3 (q, *J* = 32.8 Hz), 125.7 (q, *J* = 3.8 Hz), 125.3, 124.0, 122.2, 58.9. **^{19}F {^{1}H} NMR (376 MHz, $CDCl_3$) δ (ppm):** -62.50 (s, 6F). **HR-MS** ($FTMS^+$)**: [M-H]$^+$ Calculated:** ($C_{20}H_{14}F_6NH$): 382.1030 **Found:** 382.1023.

Diethyl [2,2'-bipyridine]-4,4'-dicarboxylate

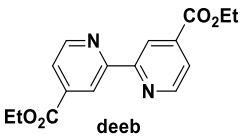

deeb

The synthesis is similar to a previously reported method.[253] A mixture of 2,2'-bipyridine-4,4'-dicarboxylic acid (500 mg, 2.00 mmol, 1.00 equiv.) in ethanol (40 mL) was stirred and concentrated sulfuric acid (95%) (0.5 mL) was added. The mixture was heated and kept at reflux. After 4 days the solution was cooled to room temperature. Distilled water was added (40 mL). A sodium hydroxide solution (5%) was added to reach pH 7. A precipitate was formed with was filtered and washed with distilled water, leaving a white solid (0.660 g). **Yield:** 91%. **Mp:** 159 – 162 °C **Lit:** 159 – 160.5 °C.[288] **^{1}H NMR (400 MHz, $CDCl_3$) δ (ppm):** 8.95 (dd, J = 1.6, 0.9 Hz, 2H), 8.87 (dd, J = 5.0, 0.9 Hz, 2H), 7.91 (dd, J = 5.0, 1.6 Hz, 2H), 4.46 (q, J = 7.1 Hz, 4H), 1.44 (t, J = 7.1 Hz, 6H). **^{13}C{^{1}H} NMR (126 MHz, $CDCl_3$) δ (ppm):** 165.3, 156.6, 150.2, 139.13, 123.4, 120.7, 62.0, 14.4. **HR-MS** ($FTMS^+$)**: $[M+H]^+$ Calculated:** ($C_{16}H_{16}N_2O_4H$): 301.1183 **Found:** 301.1185. The characterisation matches that reported.[253]

2,2'-(phenylmethylene)dipyridine

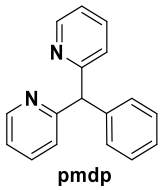

pmdp

The synthesis is similar to a previously reported method. A solution of dry THF (80 mL) and 2-benzylpyridine (1.00 equiv.) was cooled down in an Acetone/dry ice bath to -78 °C. *n*-BuLi (1.20 equiv.) was added carefully resulting in the colour to change immediately to red. The solution was stirred at that temperature for 1 h. 2-fluoropyridine (1.50 equiv.) was then added carefully. After 1 h the cooling bath was removed and stirring was continued. After 18 h the reaction mixture was heated and kept at 60 °C. After 3 h, the mixture was allowed to cool

to room temperature and was quenched carefully with water (20 mL) followed by the addition of 1 M HCl until pH neutral. The mixture was extracted with Et_2O (40 mL) and the organic layer was washed with brine (5 mL) and dried over $MgSO_4$. The solvent was evaporated leaving a residue which was purified over silica (10-100% EtOAc in hexanes). The desired fractions were combined, and the solvent evaporated leaving a beige solid (1.038 g). **Yield:** 40%. **R_f:** 0.45 (100% EtOAc on silica). **Mp:** 94 – 98 °C. **Lit**: 95 – 97 °C.[289] **^{1}H NMR (400 MHz, $CDCl_3$) δ (ppm):** 8.58 (s, 2H), 7.61 (s, 2H), 7.29 (s, 4H), 7.24 (s, 3H), 7.14 (s, 2H), 5.82 (s, 1H). **$^{13}C\{^1H\}$ NMR (126 MHz, $CDCl_3$) δ (ppm):** 162.2, 149.4, 141.7, 136.6, 129.4, 128.6, 126.8, 124.1, 121.6, 61.7. **HR-MS** ($FTMS^+$)**: $[M]^+$ Calculated:** ($C_{17}H_{14}N_2H$): 247.1230; **Found:** 247.1230. The characterisation matches that reported.[289]

Complex Synthesis

General procedure for the Synthesis of bis(μ-Cl) Ir(III) dimer

The synthetic protocol is a modified version of that originally reported.[65] The $IrCl_3.6H_2O$ (1.00 equiv.) and the corresponding C^N ligand (2.50 equiv.) were suspended in a mixture of 2-ethoxyethanol/water (75/25). The mixture was heated and kept at 125 °C under stirring. After 24 h, it was allowed to cool to r.t. and distilled water (5 mL) was added. A precipitate was observed. It was washed with Et_2O, H_2O and then dried under vacuum to give the intermediate $[Ir(C^N)_2Cl]_2$ dimer complex, which was used as such.

Tetrakis[4-(*tert*-butyl)-2-phenylpyridinato-N,C$^{2'}$]-bis(*μ*-chloro)diiridium(III)

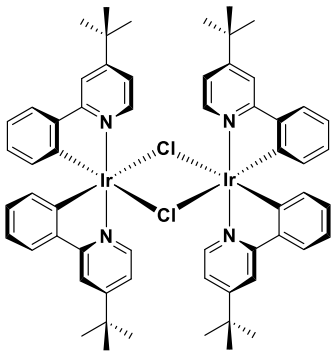

This compound was prepared following the general procedure for bis(*μ*-Cl) Ir(III) dimer. Yellow solid. **Yield:** 92%. **^{1}H NMR (400 MHz, $CDCl_3$) δ (ppm):** 9.09 (d, J = 5.9 Hz, 1H), 7.85 (d, J = 1.8 Hz, 1H), 7.48 (d, J = 6.8 Hz, 1H), 7.26 (s, 2H), 6.82 (dd, J = 5.9, 2.1 Hz, 1H), 6.73 (t, J = 6.9 Hz, 1H), 6.56 (t, J = 6.7 Hz, 1H), 5.86 (d, J = 7.2 Hz, 1H), 3.58 (q, J = 6.8 Hz, 4H), 1.68 (d, J = 9.2 Hz, 12H), 1.37 (t, J = 6.8 Hz, 6H).

Tetrakis[4-(*tert*-butyl)-2-(4-(*tert*-butyl)phenyl)-pyridinato-N,C$^{2'}$]-bis(*μ*-chloro)diiridium(III)

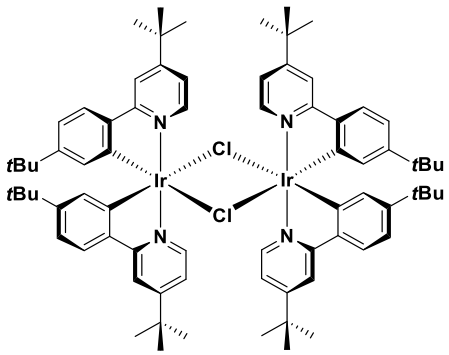

This compound was prepared following the general procedure for bis(*μ*-Cl) Ir(III) dimer. Yellow solid. **Yield:** 92%. **^{1}H NMR (400 MHz, $CDCl_3$) δ (ppm):** 9.23 (d, *J* = 5.9 Hz, 4H), 7.77 (d, *J* = 1.9 Hz, 4H), 7.37 (d, *J* = 8.0 Hz, 4H), 6.81 (dd, *J* = 6.0, 2.1 Hz, 4H), 6.75 (dd, *J* = 8.0, 1.7 Hz, 4H), 5.89 (d, *J* = 1.8 Hz, 4H), 1.62 (s, 36H), 1.06 (m, 36H).

Tetrakis[2-(phenyl)-4-(2,4,6-trimethylphenyl)pyridinato-N,C$^{2'}$]-bis(μ-chloro)diiridium(III)

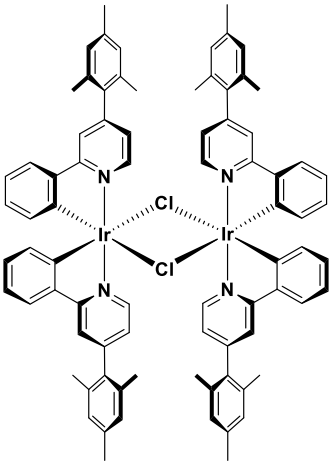

This compound was prepared following the general procedure for bis(μ-Cl) Ir(III) dimer. Yellow solid. **Yield:** 94%. **^{1}H NMR (400 MHz, $CDCl_3$) δ (ppm):** 9.64 (d, J=5.9, 4H), 7.65 (d, J=1.8, 4H), 7.41 (m, 4H), 7.01 (d, J=11.5, 8H), 6.79 (dd, J=5.9, 1.8, 4H), 6.73 (m, 4H), 6.59 (td, J=7.5, 1.4, 4H), 5.93 (m, 4H), 2.41 (s, 12H), 2.13 (d, J=11.4, 24H).

Tetrakis[4-(4-methoxy-2,6-dimethylphenyl)-2-phenylpyridinato-N,C$^{2'}$]-bis(*μ*-chloro)diiridium(III)

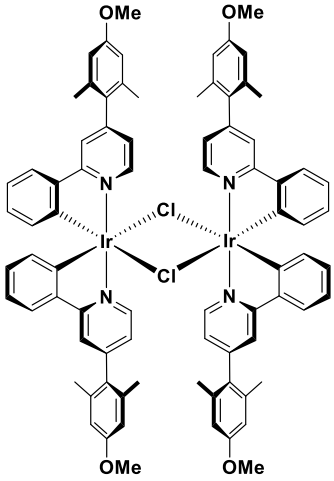

This compound was prepared following the general procedure for bis(*μ*-Cl) Ir(III) dimer. Yellow solid. **Yield:** 91%. **^{1}H NMR (400 MHz, $CDCl_3$) δ (ppm):** 9.62 (m, 4H), 7.65 (m, 4H), 7.41 (s, 4H), 6.74 (m, 16H), 6.60 (m, 4H), 5.94 (m, 4H), 3.88 (s, 12H), 2.14 (m, 24H).

Tetrakis[4-(3,5-di-*tert*-butylphenyl)-2-phenylpyridinato-N,C$^{2'}$]-bis(*μ*-chloro)diiridium(III)

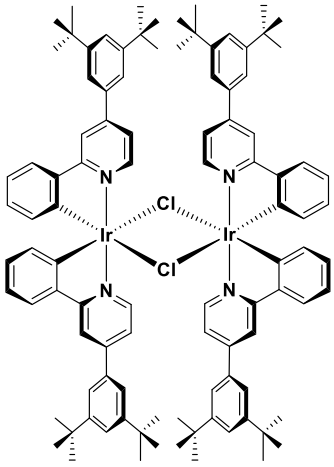

This compound was prepared following the general procedure for bis(*μ*-Cl) Ir(III) dimer. Yellow solid. **Yield:** 88%. **^{1}H NMR (400 MHz, $CDCl_3$) δ (ppm):** 9.37 (d, 4H), 8.07 (s, 4H), 7.59 (d, 5H), 7.52 (s, 13H), 7.02 (m, 4H), 6.78 (t, 4H), 6.60 (t, 4H), 6.04 (d, 4H), 1.34 (s, 72H).

Tetrakis[*N*,*N*-diphenyl-4'-(pyridin-2-yl)-[1,1'-biphenyl]-4-amine-N,C$^{2'}$]-bis(*μ*-chloro)diiridium(III)

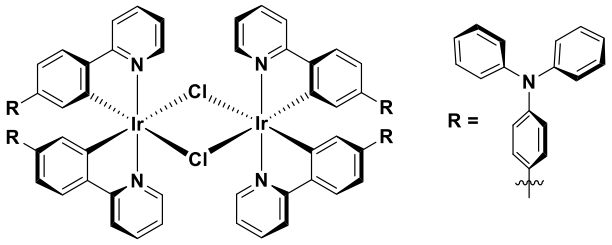

This compound was prepared following the general procedure for bis(*μ*-Cl) Ir(III) dimer. Yellow brown solid. **Yield:** 86%. **^{1}H NMR (400 MHz, $CDCl_3$) δ (ppm):** 9.32 (d, J = 6.1 Hz, 4H), 8.06 (d, J = 8.1 Hz, 4H), 7.88 (d, J = 2.7 Hz, 5H), 7.52 (s, 9H), 7.31 – 7.27 (m, 9H), 7.21 (dd, J = 8.5, 7.3 Hz, 24H), 7.16 – 7.12 (m, 13H), 7.03 (s, 36H), 7.02 – 6.96 (m, 19H), 6.91 (d, J = 8.7 Hz, 10H), 6.78 (s, 5H), 6.20 (s, 5H).

Tetrakis[*N*,*N*-diphenyl-3'-(pyridin-2-yl)-[1,1'-biphenyl]-4-amine-N,C$^{2'}$]-bis(μ-chloro)diiridium(III)

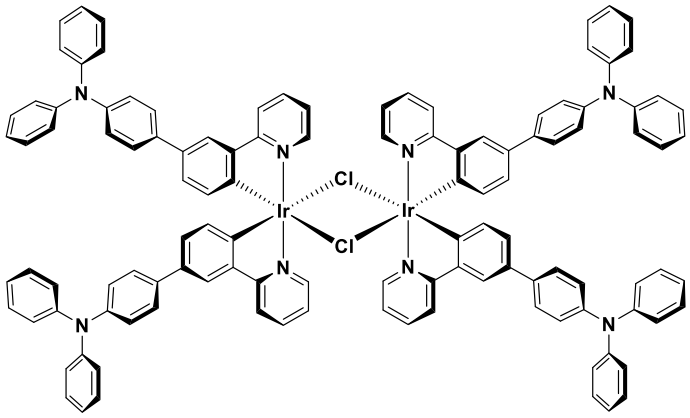

This compound was prepared following the general procedure for bis(*μ*-Cl) Ir(III) dimer. Yellow brown solid. **Yield:** 92%. **^{1}H NMR (400 MHz, $CDCl_3$) δ (ppm):** 9.31 (d, J = 5.7 Hz, 4H), 7.98 (d, J = 8.2 Hz, 4H), 7.80 – 7.77 (m, 4H), 7.69 (d, J = 2.0 Hz, 4H), 7.31 (d, J = 8.5 Hz, 8H), 7.22 (d, J = 7.7 Hz, 16H), 7.09 (d, J = 8.0 Hz, 16H), 7.03 (s, 8H), 6.98 (d, J = 7.3 Hz, 8H), 6.86 – 6.80 (m, 8H), 6.05 (d, J = 8.1 Hz, 4H).

Tetrakis[*N*,*N*-diphenyl-4-(2-phenylpyridin-4-yl)aniline-N,$C^{2'}$]-bis(*μ*-chloro)diiridium(III)

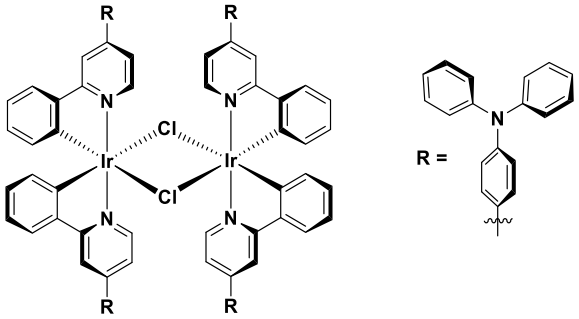

This compound was prepared following the general procedure for bis(*μ*-Cl) Ir(III) dimer. Yellow brown solid. **Yield:** 92%. **^{1}H NMR (400 MHz, $CDCl_3$) δ (ppm):** 9.27 (d, *J* = 6.1 Hz, 4H), 8.07 (d, *J* = 2.1 Hz, 4H), 7.60 (d, *J* = 9.4 Hz, 12H), 7.32 (d, *J* = 7.7 Hz, 12H), 7.17 – 7.11 (m, 37H), 6.94 (dd, *J* = 6.1, 2.0 Hz, 4H), 6.79 (d, *J* = 7.4 Hz, 4H), 6.61 (t, *J* = 7.5 Hz, 4H), 6.13 (d, *J* = 7.8 Hz, 4H).

Tetrakis[2-benzylpyrdinato-N,$C^{2'}$]-bis(*μ*-chloro)diiridium(III)

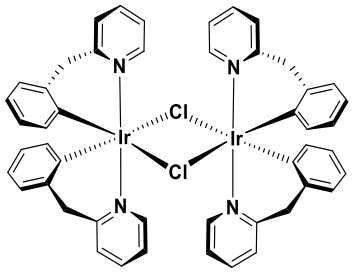

This compound was prepared following the general procedure for bis(*μ*-Cl) Ir(III) dimer. Yellow solid. **Yield:** 96%. **^{1}H NMR (400 MHz, $CDCl_3$) δ (ppm):** 8.65 (dd, J = 6.1, 1.5 Hz, 4H), 7.37 (td, J = 7.5, 1.6 Hz, 4H), 7.17 – 7.13 (m, 4H), 6.96 – 6.92 (m, 4H), 6.69 (td, J = 7.3, 1.3 Hz, 4H), 6.61 – 6.53 (m, 5H), 6.26 (td, J = 7.3, 1.4 Hz, 5H), 5.81 (d, J = 15.4 Hz, 4H), 5.03 (dd, J = 7.8, 1.3 Hz, 4H), 3.84 (d, J = 15.7 Hz, 4H).

General procedure A: for the Synthesis of cationic Ir(III) complexes

A suspension of the corresponding bis(μ-Cl) Ir(III) dimer (1.0 equiv.) and the corresponding ancillary ligand (2.2 equiv.) in a mixture of CH_2Cl_2/methanol (1:1) was degassed for 15 min and then heated and kept at reflux for 18 h under stirring. The solvent was then evaporated leaving a residue, which was purified over silica with dichloromethane and increasing percentages of methanol (0% - 10%). The desired fractions were collected and reduced till dryness, giving a solid that was then dissolved in methanol. An aqueous NH_4PF_6 solution (0.6 M) was added dropwise resulting in a precipitate. The suspension was stirred vigorously for 2 h and subsequently filtered. The solid was dissolved in CH_2Cl_2 and washed with water. The layers were separated, and the organic layer was reduced till dryness leaving a solid, which was recrystallised (CH_2Cl_2/hexane, 1/4) at -18 °C as precipitant. After filtration, the target complexes were obtained as solids. The spectroscopic data for complex **1** will be discussed and signals will be assigned. Selected NMR spectra are shown for complex **1**.

Bis[2-phenylpyridinato-N,C$^{2'}$]-N,N'-(4,4'-di-*tert*-butyl-2,2'-bipyridine)iridium(III) hexafluorophosphate

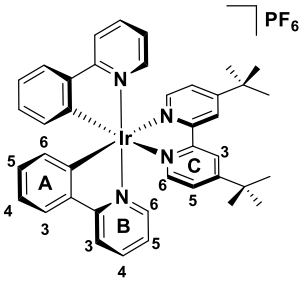

1

This complex was synthesised using the general method A. Yellow solid (0.102 g). **Yield:** 89%. **Mp:** 216 – 220 °C. **Lit**: 219 °C.[187] **^{1}H NMR (400 MHz, $CDCl_3$) δ (ppm):** 8.38 (s, 2H, H^{C3}), 7.88 (d, *J* = 8.0, 2H, H^{C6}), 7.82 (d, *J* = 5.8, 2H, H^{B3}), 7.74 (t, *J* = 8.0, 2H, H^{C5}), 7.66 (d, *J* = 7.4, 2H, H^{A6}), 7.61 (d, *J* = 5.8, 2H, H^{B4}), 7.37 (d, *J* = 5.8, 2H, H^{B5}), 7.08 (m, 2H, H^{B6}), 7.01 (t, *J* = 7.4, 2H, H^{A5}), 6.89 (t, *J* = 7.4, 2H, H^{A4}), 6.29 (d, *J* = 7.4, 2H, H^{A3}), 1.43 (s, 18H, H^{tBu}).

$^{13}C\{^{1}H\}$ NMR (126 MHz, $CDCl_3$) δ (ppm): 167.5, 163.8, 155.7, 150.8, 149.6, 149.1, 143.6, 137.9, 131.7, 130.6, 125.2, 124.5, 123.5, 122.3, 121.7, 119.3, 35.7, 30.2. **^{31}P NMR (162 MHz, $CDCl_3$) δ (ppm):** -144.4 (hept, *J* = 711.4 Hz). **HR-MS** ($FTMS^+$)**: $[M]^+$ Calculated:** ($C_{40}H_{40}IrN_4$): 767.2853 **Found:** 767.2836. **CHN**: Calcd. for $C_{40}H_{40}F_6IrN_4Px1/4CH_2Cl_2$: C, 51.69; H, 4.37, N, 5.99. Found: C, 52.04; H, 4.26; N, 5.83. The characterisation matches that reported.[187]

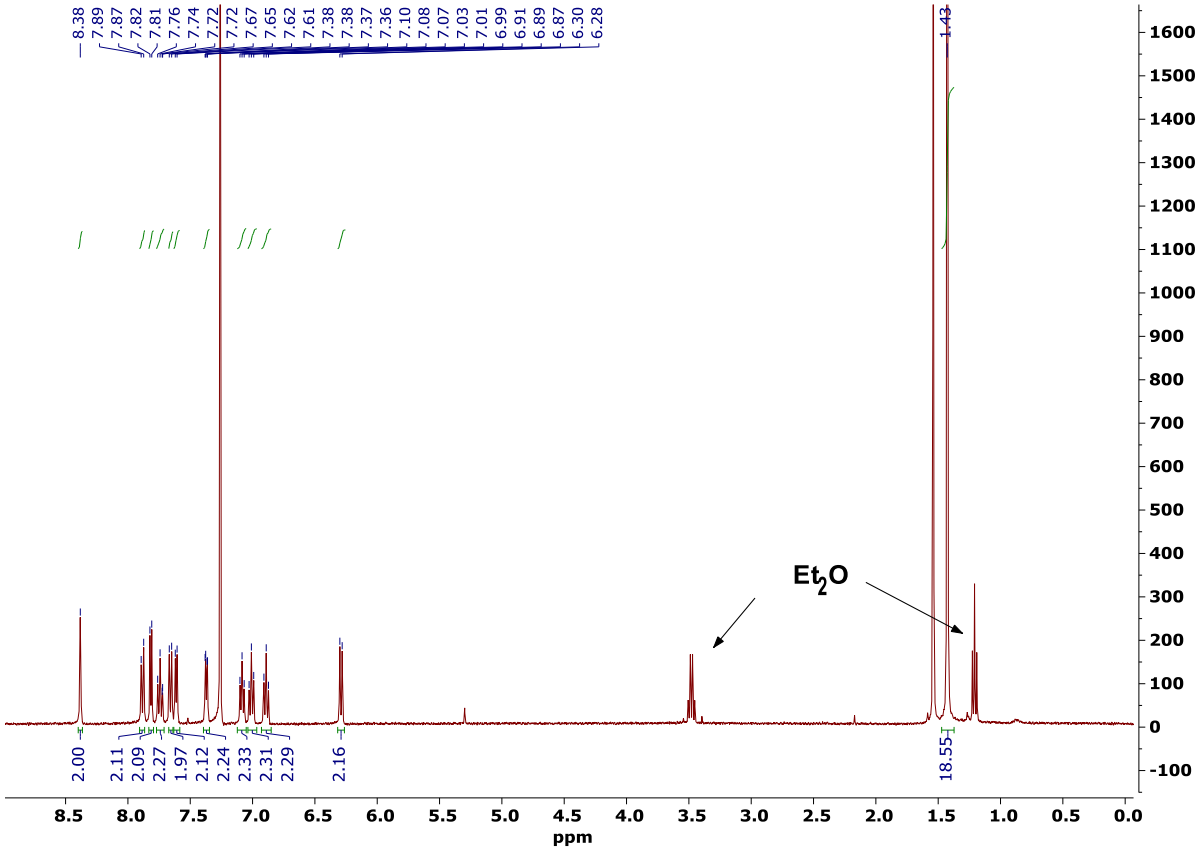

Figure **101**: ^{1}H NMR spectrum in $CDCl_3$ of complex **1**

Bis[4-(*tert*-butyl)-2-phenylpyridinato-N,C$^{2'}$]-N,N'-(4,4'-di-*tert*-butyl-2,2'-bipyridine)iridium(III) hexafluorophosphate

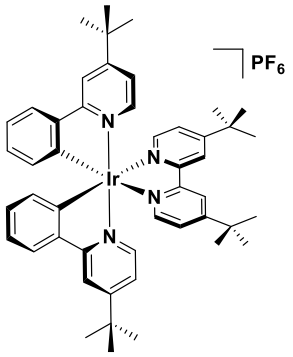

25

This complex was synthesised using the general method A. Yellow solid (0.094 g). **Yield:** 82%. **Mp:** 340 °C (decomp.). **^{1}H NMR (400 MHz, $CDCl_3$) δ (ppm):** 8.39 (d, *J* = 1.9, 2H), 7.90 – 7.81 (m, 4H), 7.67 (dd, *J* = 7.5, 1.3 Hz, 2H), 7.47 – 7.35 (m, 4H), 7.09 (dd, *J* = 6.2, 2.2 Hz, 2H), 7.00 (td, *J* = 7.5, 1.3 Hz, 2H), 6.90 (td, *J* = 7.5, 1.3 Hz, 2H), 6.28 (dd, *J* = 7.5, 1.3 Hz, 2H), 1.43 (s, 18H), 1.36 (s, 18H). **^{13}C{^{1}H} NMR (126 MHz, $CDCl_3$) δ (ppm):** 167.0, 163.8, 162.3, 155.8, 151.0, 149.8, 148.3, 144.0, 131.8, 130.4, 125.1, 124.2, 122.1, 121.7, 121.2, 116.1, 35.7, 35.2, 30.4, 30.3. **^{31}P NMR (162 MHz, $CDCl_3$) δ (ppm):** -144.8 (hept, *J* = 712.8 Hz). **HR-MS** ($FTMS^+$)**: $[M]^+$ Calculated:** ($C_{48}H_{56}IrN_4$): 879.4105 **Found:** 879.4093. **CHN**: Calcd. for $C_{48}H_{56}F_6IrN_4P$: C, 56.18; H, 5.50, N, 5.46. Found: C, 56.09; H, 5.36; N, 5.44.

Bis[4-(*tert*-butyl)-2-(4-(*tert*-butyl)phenyl)-pyridinato-N,C$^{2'}$]-N,N'-(4,4'-di-*tert*-butyl-2,2'-bipyridine)iridium(III) hexafluorophosphate

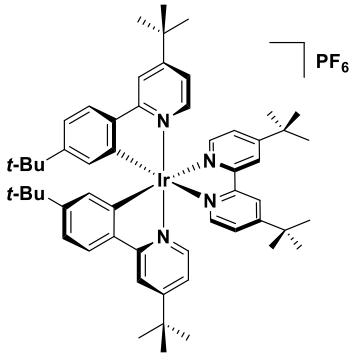

26

7.49 (d, J = 6.1 Hz, 2H), 7.38 (s, 2H), 7.10 (d, J = 6.9 Hz, 2H), 7.01 (d, J = 7.9 Hz, 2H), 6.22 (s, 2H), 1.60 (s, 19H), 1.51 (s, 19H), 1.23 (s, 18H).

This complex was synthesised using the general method A. Yellow solid (0.109 g). **Yield:** 85%. **Mp:** 345 °C (decomp.). **^{1}H NMR (400 MHz, $CDCl_3$) δ (ppm):** 8.35 (s, 2H), 7.79 (s, 4H), 7.54 (s, 2H), 7.49 (d, *J* = 6.1 Hz, 2H), 7.38 (s, 2H), 7.10 (d, *J* = 6.9 Hz, 2H), 7.01 (d, *J* = 7.9 Hz, 2H), 6.22 (s, 2H), 1.60 (s, 18H), 1.51 (s, 18H), 1.23 (s, 18H). **^{13}C{^{1}H} NMR (126 MHz, $CDCl_3$) δ (ppm):** 167.6, 163.6, 162.3, 156.0, 153.3, 149.1, 148.6, 141.6, 127.8, 127.7, 125.2, 123.8, 121.6, 120.5, 119.5, 115.7, 35.8, 35.2, 34.6, 31.2, 30.5, 30.4. **^{31}P NMR (162 MHz, $CDCl_3$) δ (ppm):** -144.5 (hept, *J* = 712.8 Hz). **HR-MS** ($FTMS^+$)**: $[M]^+$ Calculated:** ($C_{56}H_{72}IrN_4$): 991.5357 **Found:** 991.5339. **CHN**: **Calcd.** for $C_{48}H_{56}F_6IrN_4Px3/4CH_2Cl_2$: C, 53.72; H, 5.32, N, 5.14. **Found:** C, 53.44; H, 5.26; N, 5.14. The characterisation matches that reported.[183]

Bis[4-mesityl-2-phenylpyridinato-N,C$^{2'}$]-N,N'-(4,4'-di-*tert*-butyl-2,2'-bipyridine)iridium(III) hexafluorophosphate

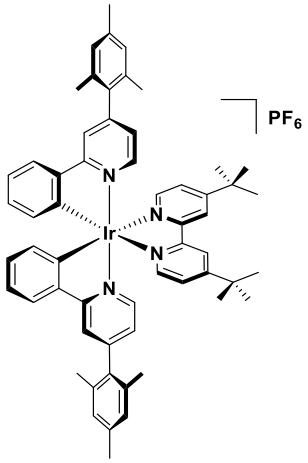

21

This complex was synthesised using the general method A. Yellow solid (0.125 g). **Yield:** 79%. **Mp:** 263 – 267 °C. **Lit:** 264 – 268 °C.[175] **^{1}H NMR (400 MHz, $CDCl_3$) δ (ppm):** 8.56 (d, *J* = 1.9 Hz, 2H), 7.96 (d, *J* = 5.8 Hz, 2H), 7.73 – 7.67 (m, 4H), 7.63 (d, *J* = 7.8 Hz, 2H), 7.45 (dd, *J* = 5.8, 1.9 Hz, 2H), 7.11 – 6.90 (m, 11H), 6.44 – 6.37 (m, 2H), 2.36 (s, 6H), 2.14 (s, 6H), 1.96 (s, 6H), 1.47 (s, 18H). **^{13}C{^{1}H} NMR (126 MHz, $CDCl_3$) δ (ppm):** 167.6, 164.1, 155.9, 151.8, 151.0, 149.7, 149.0, 143.8, 138.2, 135.0, 131.6, 130.7, 128.5, 128.5, 125.1, 12f4.8, 124.5, 122.3, 122.2, 120.4, 35.8, 30.2, 29.7, 21.0, 20.5, 20.4. **^{31}P NMR (121 MHz, $CDCl_3$) δ (ppm):** -144.6 (hept, *J* = 710.3 Hz). **HR-MS** ($FTMS^+$)**: [M]$^+$ Calculated:** ($C_{58}H_{60}IrN_4$): 1003.4418 **Found:** 1003.4411. **CHN**: **Calcd.** for $C_{58}H_{60}F_6IrN_4P$: C, 60.56; H, 5.26, N, 4.87. **Found:** C, 60.49; H, 5.13; N, 5.04. The characterisation matches that reported.[175]

Bis[4-(4-methoxy-2,6-dimethylphenyl)-2-phenylpyridinato-N,C$^{2'}$]-N,N'-(4,4'-di-*tert*-butyl-2,2'-bipyridine)iridium(III) hexafluorophosphate

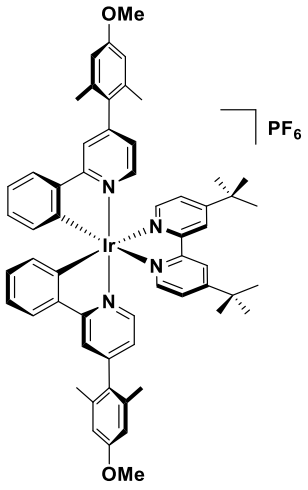

27

This complex was synthesised using the general method A. Yellow solid (0.185 g). **Yield:** 75%. **Mp:** 330 °C (decomp.). **^{1}H NMR (400 MHz, $CDCl_3$) δ (ppm):** 8.49 (s, 2H), 7.96 (d, *J* = 5.9 Hz, 2H), 7.71 – 7.62 (m, 6H), 7.45 (dd, *J* = 5.9, 1.9 Hz, 2H), 7.04 (t, *J* = 7.4 Hz, 2H), 6.97 – 6.90 (m, 4H), 6.71 (d, *J* = 14.4 Hz, 4H), 6.41 (d, *J* = 7.4 Hz, 2H), 3.85 (s, 6H), 2.17 (s, 6H), 1.99 (s, 6H), 1.47 (s, 18H). **^{13}C{^{1}H} NMR (126 MHz, $CDCl_3$) δ (ppm):** 167.5, 159.3, 155.9, 151.6, 149.7, 149.0, 131.7, 130.6, 130.5, 125.2, 124.5, 122.3, 122.0, 120.8, 113.1, 77.2, 55.2, 35.7, 30.2, 20.8. **^{31}P NMR (162 MHz, $CDCl_3$) δ (ppm):** -144.5 (hept, *J* = 712.8 Hz). **HR-MS** ($FTMS^{+}$)**: $[M]^{+}$ Calculated:** ($C_{58}H_{60}IrN_4O_2$): 1035.4317 **Found:** 1035.4294. **CHN**: Calcd. For $C_{58}H_{60}F_6IrN_4P$: C, 58.92; H, 5.12, N, 4.74. **Found**: C, 59.00; H, 5.22; N, 4.67.

Bis[4-(3,5-di-*tert*-butylphenyl)-2-phenylpyridinato-N,C$^{2'}$]-N,N'-(4,4'-di-*tert*-butyl-2,2'-bipyridine)iridium(III) hexafluorophosphate

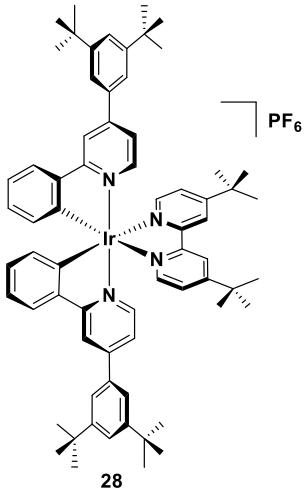

28

This complex was synthesised using the general method A. Yellow solid (0.163 g). **Yield:** 89%. **Mp:** 365 °C (decomp.). **^{1}H NMR (400 MHz, $CDCl_3$) δ (ppm):** 8.48 (d, *J* = 1.6, 2H), 8.09 (d, *J* = 1.6, 2H), 7.92 (d, *J* = 6.0, 2H), 7.80 (d, *J* = 6.9, 2H), 7.64 (d, *J* = 6.0, 2H), 7.55 (m, 6H), 7.43 (dd, *J* = 6.0, 1.9, 2H), 7.35 (d, *J* = 1.9, 2H), 7.08 (m, 2H), 6.97 (t, *J* = 6.8, 2H), 6.47 (d, *J* = 6.8, 2H), 1.47 (s, 18H), 1.41 (s, 36H). **^{13}C{^{1}H} NMR (126 MHz, $CDCl_3$) δ (ppm):** 167.4, 163.9, 155.8, 151.9, 151.2, 151.1, 149.7, 148.9, 143.8, 136.2, 131.9, 130.5, 125.2, 124.4, 124.2, 122.2, 121.8, 121.4, 121.4, 117.0, 35.7, 35.1, 31.4, 30.2. **^{31}P NMR (121 MHz, $CDCl_3$) δ (ppm):** -144.5 (hept, J = 710.3 Hz). **HR-MS** ($FTMS^{+}$)**: $[M]^{+}$ Calculated:** ($C_{68}H_{80}IrN_4$): 1143.5954 **Found:** 1143.5983. **CHN**: **Calcd.** for $C_{68}H_{80}F_6IrN_4P$: C, 63.28; H, 6.25, N, 4.34. **Found:** C, 63.23; H, 6.15, N, 4.40

Bis[*N*,*N*-diphenyl-4'-(pyridin-2-yl)-[1,1'-biphenyl]-4-amine-N,C$^{2'}$]-N,N'-(4,4'-di-*tert*-butyl-2,2'-bipyridine)iridium(III) hexafluorophosphate

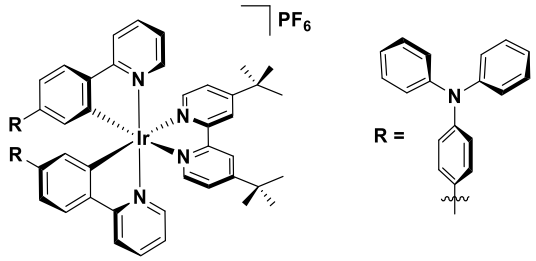

29a

This complex was synthesised using the general method A. Yellow brown solid (0.178 g). **Yield:** 92%. **Mp:** 248 – 253 °C. **^{1}H NMR (400 MHz, CDCl$_3$) δ (ppm):** 8.43 – 8.38 (m, 2H), 7.89 (t, *J* = 7.4 Hz, 4H), 7.77 – 7.67 (m, 4H), 7.63 (d, *J* = 5.9 Hz, 2H), 7.37 (dd, *J* = 5.9, 1.8 Hz, 2H), 7.26 – 7.21 (m, 14H), 7.11 – 7.05 (m, 10H), 7.04 – 6.98 (m, 8H), 6.55 (d, *J* = 1.6 Hz, 2H), 1.43 (s, 18H). **^{13}C{^{1}H} NMR (126 MHz, CDCl$_3$) δ (ppm):** 167.5, 164.0, 155.9, 151.3, 149.9, 149.2, 147.7, 147.5, 142.6, 142.1, 138.1, 134.5, 129.4, 129.2, 127.6, 125.5, 125.1, 124.7, 123.6, 123.4, 123.2, 121.8, 121.1, 119.5, 35.8, 30.4. **^{31}P NMR (162 MHz, CDCl$_3$) δ (ppm):** -144.6 (hept, *J* = 714.4 Hz). **HR-MS** (FTMS$^+$)**: [M]$^+$ Calculated:** ($C_{76}H_{66}IrN_6$): 1255.4980; **Found:** 1255.4974. **CHN**: **Calcd.** for $C_{76}H_{66}F_6IrN_6PxCH_2Cl_2$: C, 62.26; H, 4.61; N, 5.66. **Found:** C, 61.88; H, 4.35; N, 5.89.

Bis[*N*,*N*-diphenyl-3'-(pyridin-2-yl)-[1,1'-biphenyl]-4-amine-N,C$^{2'}$]-N,N'-(4,4'-di-*tert*-butyl-2,2'-bipyridine)iridium(III) hexafluorophosphate

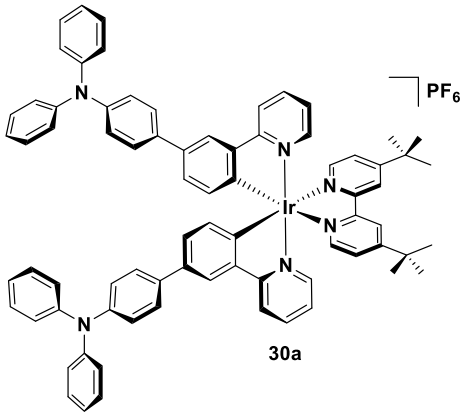

30a

This complex was synthesised using the general method A. Yellow brown solid (0.152 g). **Yield:** 86%. **Mp:** 185 – 190 °C. **^{1}H NMR (400 MHz, $CDCl_3$) δ (ppm):** 8.40 (d, *J* = 2.0 Hz, 2H), 7.99 (d, *J* = 8.0 Hz, 2H), 7.92 – 7.82 (m, 4H), 7.78 (td, *J* = 7.8, 1.4 Hz, 2H), 7.66 (dd, *J* = 5.7, 1.4 Hz, 2H), 7.49 – 7.42 (m, 4H), 7.39 (dd, *J* = 5.8, 1.9 Hz, 2H), 7.25 (d, *J* = 8.4 Hz, 10H), 7.17 – 7.08 (m, 14H), 7.01 (d, *J* = 8.9 Hz, 4H), 6.39 (d, *J* = 8.0 Hz, 2H), 1.43 (s, 18H). **^{13}C{^{1}H} NMR (126 MHz, $CDCl_3$) δ (ppm):** 167.6, 164.1, 155.9, 149.8, 149.7, 149.5, 147.8, 146.9, 144.4, 138.1, 135.5, 135.1, 132.3, 129.4, 129.3, 127.3, 125.5, 124.4, 124.3, 123.9, 123.0, 122.9, 122.0, 119.6, 35.9, 30.4. **^{31}P NMR (162 MHz, $CDCl_3$) δ (ppm):** -144.56 (hept, *J* = 714.4 Hz). **HR-MS** ($FTMS^+$)**: $[M]^+$ Calculated:** ($C_{76}H_{66}IrN_6$): 1255.4980; **Found:** 1255.4969. **CHN**: **Calcd.** for $C_{76}H_{66}F_6IrN_6P$: C, 65.18; H, 4.75; N, 6.00. **Found:** C, 64.97; H, 4.59; N, 6.17.

Bis[*N*,*N*-diphenyl-4-(2-phenylpyridin-4-yl)aniline-N,C$^{2'}$]-N,N'-(4,4'-di-*tert*-butyl-2,2'-bipyridine)iridium(III) hexafluorophosphate

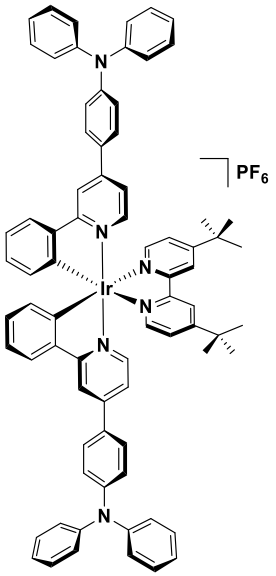

31a

This complex was synthesised using the general method A. Yellow brown solid (0.082 g). **Yield:** 82%. **Mp:** 250 °C (decomp.). **^{1}H NMR (400 MHz, $CDCl_3$) δ (ppm):** 8.45 – 8.42 (m, 2H), 8.07 – 8.04 (m, 2H), 7.89 (d, *J* = 5.9 Hz, 2H), 7.79 – 7.74 (m, 2H), 7.60 (t, *J* = 7.5 Hz, 6H), 7.42 – 7.39 (m, 2H), 7.35 – 7.32 (m, 6H), 7.18 – 7.10 (m, 20H), 7.06 – 7.02 (m, 2H), 6.96 – 6.90 (m, 2H), 6.44 (d, *J* = 7.5 Hz, 2H), 1.46 (s, 18H). **^{13}C{^{1}H} NMR (126 MHz, $CDCl_3$) δ (ppm):** 167.6, 164.1, 155.9, 151.3, 149.9, 149.9, 149.2, 149.0, 147.0, 143.9, 132.0, 130.6, 129.6, 128.9, 128.0, 125.4, 125.3, 124.5, 124.1, 122.4, 122.3, 122.1, 120.5, 115.9, 35.9, 30.4. **^{31}P NMR (162 MHz, $CDCl_3$) δ (ppm):** -144.55 (hept, J = 714.4 Hz). **HR-MS** ($FTMS^+$)**: [M]$^+$ Calculated:** ($C_{76}H_{66}IrN_6$): 1255.4980; **Found:** 1255.4976. **CHN**: **Calcd.** for $C_{76}H_{66}F_6IrN_6P$: C, 65.18; H, 4.75; N, 6.00 **Found:** C, 64.90; H, 4.68; N, 5.91.

Bis[2-benzylpyridinato-N,C$^{2'}$]-N,N'-(2,2'-bipyridine)iridium(III) hexafluorophosphate

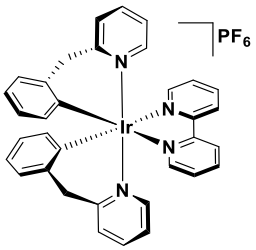

33

This complex was synthesised using the general method. Red solid (0.124 g). **Yield:** 78%. **Mp:** 244 – 248 °C. **^{1}H NMR (500 MHz, $CDCl_3$) δ (ppm):** 9.01 (d, *J* = 8.2 Hz, 2H), 8.32 (d, *J* = 5.4 Hz, 2H), 8.25 (td, *J* = 7.9, 1.6 Hz, 2H), 7.64 (s, 4H), 7.38 (t, *J* = 6.6 Hz, 2H), 7.32 (s, 2H), 7.00 (s, 4H), 6.92 (t, *J* = 6.5 Hz, 2H), 6.87 (t, *J* = 6.6 Hz, 2H), 6.61 (d, *J* = 7.6 Hz, 2H), 3.93 (d, *J* = 15.6 Hz, 2H), 3.56 (d, *J* = 15.7 Hz, 2H). **^{13}C{^{1}H} NMR (126 MHz, $CDCl_3$) δ (ppm):** 163.3, 155.9, 150.8, 150.6, 139.7, 139.2, 138.3, 136.4, 135.8, 127.3, 127.1, 127.0, 126.9, 126.1, 123.8, 123.3, 49.1. **^{31}P NMR (162 MHz, $CDCl_3$) δ (ppm):** -144.34 (hept, J = 712.8 Hz). **HR-MS** ($FTMS^+$)**: $[M]^+$ Calculated:** ($C_{34}H_{28}IrN_4$): 685.1939; **Found:** 685.1936. **CHN: Calcd** for ($C_{34}H_{28}F_6IrN_4P$): C, 49.21; H, 3.40; N, 6.75 **Found:** C, 49.06; H, 3.28; N, 6.68.

Bis[2-benzylpyridinato-N,C$^{2'}$]-N,N'-(4,4'-di-*tert*-butyl-2,2'-bipyridine)iridium(III) hexafluorophosphate

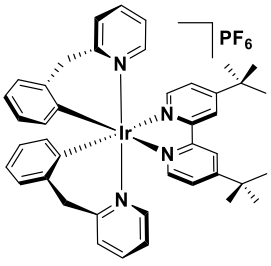

34

This complex was synthesised using the general method. Yellow solid (0.186 g). **Yield:** 91%. **Mp:** 252 – 257 °C. **^{1}H NMR (500 MHz, $CDCl_3$) δ (ppm):** 8.84 – 8.75 (m, 2H), 8.15 (d, *J* = 5.9 Hz, 2H), 7.71 (d, *J* = 7.0 Hz, 2H), 7.57 (td, *J* = 7.6, 1.4 Hz, 2H), 7.31 (dd, *J* = 5.9, 1.7

Hz, 2H), 7.25 (m, 2H), 7.03 – 6.89 (m, 6H), 6.82 (td, *J* = 7.6, 2.9 Hz, 2H), 6.61 (d, *J* = 7.3 Hz, 2H), 3.92 (d, *J* = 15.5 Hz, 2H), 3.51 (d, *J* = 15.5 Hz, 2H), 1.48 (s, 18H). **$^{13}C\{^{1}H\}$ NMR (126 MHz, $CDCl_3$) δ (ppm):** 163.9, 163.1, 156.0, 151.2, 150.0, 139.4, 138.0, 137.4, 136.0, 126.8, 126.5, 125.8, 124.7, 123.9, 123.6, 122.9, 49.2, 35.8, 30.3. **^{31}P NMR (162 MHz, $CDCl_3$) δ (ppm):** -142.42 (hept, J = 714.4 Hz). **HR-MS** ($FTMS^+$)**: $[M]^+$ Calculated:** ($C_{42}H_{44}IrN_4$): 797.3192; **Found:** 797.3188. **CHN**: **Calcd.** for $C_{42}H_{44}F_6IrN_4Px1/2CH_2Cl_2$: C, 51.85; H, 4.61; N, 5.96. **Found:** C, 51.89; H 4.28; N 5.51.

Bis[2-benzylpyridinato-N,$C^{2'}$]-N,N'-(2,2'-bithiazole)iridium(III) hexafluorophosphate

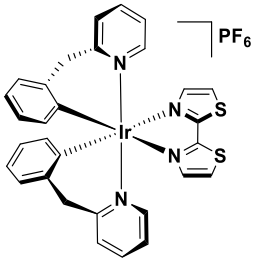

35

This complex was synthesised using the general method. Deep red solid (0.103 g). **Yield:** 85%. **Mp:** 235 °C (decomp.). **^{1}H NMR (500 MHz, $CDCl_3$) δ (ppm):** 8.14 (d, *J* = 3.3 Hz, 2H), 8.05 (d, *J* = 3.3 Hz, 2H), 7.99 (d, *J* = 5.4 Hz, 2H), 7.86 (d, *J* = 3.3 Hz, 2H), 7.65 – 7.57 (m, 6H), 7.55 (d, *J* = 6.0 Hz, 2H), 7.38 (d, *J* = 7.3 Hz, 2H), 7.28 (d, *J* = 7.4 Hz, 2H), 7.22 (d, *J* = 7.4 Hz, 2H), 7.02 (t, *J* = 6.2 Hz, 2H), 6.99 – 6.88 (m, 6H), 6.81 (dt, *J* = 14.1, 7.2 Hz, 4H), 6.59 (d, *J* = 7.4 Hz, 2H), 6.53 (t, *J* = 7.1 Hz, 2H), 5.39 (d, *J* = 7.7 Hz, 2H), 4.51 (d, *J* = 16.2 Hz, 2H), 4.13 (d, *J* = 16.3 Hz, 2H), 3.87 (d, *J* = 15.4 Hz, 2H), 3.52 (d, *J* = 15.5 Hz, 2H). **$^{13}C\{^{1}H\}$ NMR (126 MHz, $CDCl_3$) δ (ppm):** 163.5, 163.4, 162.5, 161.3, 155.4, 150.4, 143.2, 142.6, 140.3, 139.1, 138.6, 138.3, 136.8, 136.6, 135.4, 132.6, 126.8, 126.1, 126.5, 126.4, 126.2, 126.0, 125.9, 125.0, 123.9, 123.4, 123.4, 53.5, 49.1, 48.4.**^{31}P NMR (202 MHz, $CDCl_3$) δ (ppm):** -144.41 (hept, *J* = 711.0 Hz). **HR-MS** ($FTMS^+$)**: $[M]^+$ Calculated:** ($C_{30}H_{24}IrN_4S_2$): 697.1067;

Found: 697.1049. **CHN**: **Calcd.** for $C_{30}H_{24}F_6IrN_4PS_2$: C, 42.80; H, 2.87; N, 6.66. **Found:** C, 42.43; H 2.82; N 6.55. The NMR data correspond to the mixture of two conformers at 298 K.

Bis[2-benzylpyridinato-N,C$^{2'}$]-N,N-(1*H*,1'*H*-2,2'-biimidazole)iridium(III) hexafluorophosphate

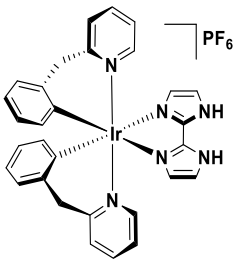

36

This complex was synthesised using the general method. Beige solid (0.081 g). **Yield:** 80%. **Mp:** 259 °C (decomp.). **^{1}H NMR (400 MHz, CDCl$_3$) δ (ppm):** 8.13 (d, *J* = 6.9 Hz, 2H), 7.59 (td, *J* = 7.6, 1.5 Hz, 2H), 7.36 – 7.32 (m, 3H), 7.24 (s, 2H), 7.17 (d, *J* = 7.7 Hz, 2H), 6.95 – 6.84 (m, 3H), 6.80 – 6.74 (m, 2H), 6.53 (t, *J* = 7.4 Hz, 2H), 5.43 (d, *J* = 8.7 Hz, 2H), 4.73 (d, *J* = 16.3 Hz, 2H), 4.04 (d, *J* = 16.0 Hz, 2H). **^{13}C{^{1}H} NMR (126 MHz, CDCl$_3$) δ (ppm):** 162.82, 156.23, 141.86, 140.51, 138.47, 137.85, 137.74, 128.59, 126.13, 125.84, 124.40, 122.88, 122.50, 120.15, 48.54. **^{31}P NMR (202 MHz, CDCl$_3$) δ (ppm):** -143.81 (hept, *J* = 713.1 Hz). **HR-MS** (FTMS$^+$)**: [M]$^+$ Calculated:** ($C_{30}H_{26}IrN_6$) 663.1844; **Found:** 663.1834. The NMR data correspond only to the major conformer at 298 K.

Bis[2-(4',6'-difluorophenyl)-4-(2,4,6-trimethylphenyl)pyridinato-N,C$^{2'}$]-N,N'-(2,2'-phenylmethylene)-dipyridine)iridium(III)hexafluorophosphate

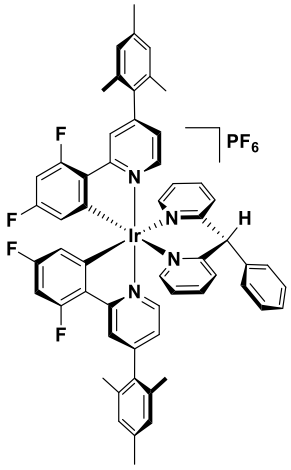

61

This complex was synthesised using the general method. Yellow solid (0.142 g). **Yield:** 81%. **Mp:** 282 °C (decomp.). **^{1}H {^{19}F} NMR (400 MHz, $CDCl_3$) δ (ppm):** 8.40 (d, *J* = 5.8 Hz, 1H), 8.16 (d, *J* = 8.7 Hz, 2H), 8.07 – 7.95 (m, 5H), 7.35 (dt, *J* = 18.3, 5.5 Hz, 3H), 7.19 – 7.13 (m, 4H), 7.02 – 6.95 (m, 5H), 6.68 (d, *J* = 7.1 Hz, 2H), 6.51 (dd, *J* = 16.8, 9.2 Hz, 2H), 6.36 – 6.30 (m, 2H), 5.64 (dd, *J* = 8.6, 2.3 Hz, 1H), 5.23 (dd, *J* = 8.8, 2.3 Hz, 1H), 2.35 (s, 6H), 2.13 (d, *J* = 3.2 Hz, 6H), 2.01 (s, 3H), 1.96 (s, 3H). **^{13}C{^{1}H} NMR (126 MHz, $CDCl_3$) δ (ppm):** 164.1 (d, *J* = 6.3 Hz), 163.8 (d, *J* = 6.3 Hz), 163.7, 162.4, 162.3, 158.2, 157.9, 153.5, 152.7, 152.5, 152.4, 152.3, 151.7 (d, *J* = 6.3 Hz), 151.4 (d, *J* = 6.3 Hz), 150.4, 149.1, 140.3, 139.9, 139.6, 138.5, 138.4, 134.9 (d, *J* = 6.3 Hz), 134.7 (*broad*-s), 134.5, 130.4, 130.3, 129.3, 128.7, 128.1, 125.8, 125.3, 125.2, 125.1, 124.5, 124.3, 123.9, 114.1 (d, *J* = 17.6 Hz), 113.1 (d, *J* = 17.6 Hz), 99.5, 59.8, 21.0, 20.7, 20.6, 20.5, 20.3. **^{19}F {^{1}H} NMR (126 MHz, $CDCl_3$) δ (ppm):** -72.20, -73.71, -105.23 (dd, *J* = 33.5, 28.6 Hz), -107.28 (d, *J* = 23.3 Hz), -107.98 (d, *J* = 23.4 Hz). **^{31}P NMR (162 MHz, $CDCl_3$) δ (ppm):** -144.55 (hept, *J* = 713.1 Hz). **HR-MS** ($FTMS^+$)**: [M]$^+$ Calculated:** ($C_{57}H_{46}F_6IrN_4$): 1055.3287; **Found:** 1055.3272. **CHN**: **Calcd.** for $C_{57}H_{46}F_{10}IrN_4P$: C, 57.04; H, 3.86; N, 4.67. **Found:** C, 57.12; H, 4.04; N, 4.58.

Bis[2-(phenyl)-4-(2,4,6-trimethylphenyl)pyridinato-N,C$^{2'}$]-N,N'-(2,2'-phenylmethylene)-dipyridine)iridium(III) hexafluorophosphate

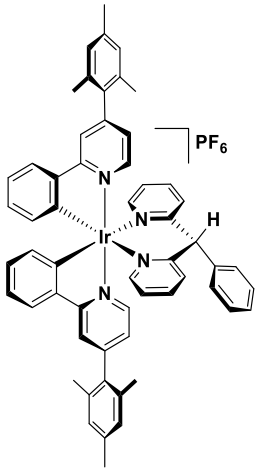

62

This complex was synthesised using the general method. Yellow solid (0.084 g). **Yield:** 89%. **Mp:** 260 °C (decomp.). **^{1}H NMR (400 MHz, CDCl$_3$) δ (ppm):** 8.50 (d, *J* = 6.2 Hz, 1H), 8.16 – 8.10 (m, 2H), 8.08 – 7.96 (m, 3H), 7.74 (d, *J* = 1.8 Hz, 1H), 7.62 (d, *J* = 1.9 Hz, 1H), 7.58 (td, *J* = 8.0, 1.3 Hz, 2H), 7.38 (t, *J* = 6.2 Hz, 2H), 7.28 – 7.24 (m, 1H), 7.19 (q, *J* = 7.2, 6.2 Hz, 3H), 7.10 (ddd, *J* = 7.3, 5.9, 1.3 Hz, 1H), 7.05 – 6.99 (m, 5H), 6.99 – 6.94 (m, 2H), 6.94 – 6.90 (m, 1H), 6.84 (td, *J* = 7.7, 1.1 Hz, 1H), 6.73 (d, *J* = 7.1 Hz, 2H), 6.35 – 6.29 (m, 2H), 6.29 – 6.25 (m, 1H), 5.91 (d, *J* = 7.6 Hz, 1H), 2.38 (s, 6H), 2.16 (d, *J* = 11.3 Hz, 6H), 2.06 (s, 3H), 1.98 (s, 3H). **^{13}C{^{1}H} NMR (126 MHz, CDCl$_3$) δ (ppm):** 167.8, 167.3, 167.2, 158.5, 158.2, 153.3, 152.8, 152.4, 151.2, 150.4, 149.0, 148.2, 147.7, 144.2, 144.0, 139.9, 139.5, 138.6, 138.4, 135.1, 135.0, 134.9, 134.8, 134.7, 131.9, 130.9, 130.8, 130.7, 129.9, 129.8, 129.3, 128.8, 128.7, 128.4, 128.1, 125.6, 125.5, 125.1, 124.9, 124.8, 124.5, 123.7, 122.9, 122.8, 121.1, 120.7, 60.1, 21.2, 20.8, 20.7, 20.5. **^{31}P NMR (162 MHz, CDCl$_3$) δ (ppm):** -144.46 (hept, *J* = 714.4 Hz). **HR-MS** (FTMS$^+$)**: [M]$^+$ Calculated:** ($C_{57}H_{50}IrN_4$): 983.3664; **Found:** 983.3656. **CHN**: **Calcd.** for $C_{57}H_{50}F_6IrN_4Px5/2CH_2Cl_2$: C, 53.31; H, 4.14; N, 4.18. **Found:** C, 53.08; H, 4.27; N, 4.45.

General procedure for the one-pot Synthesis of neutral Ir(III) complexes

A mixture of the corresponding C^N^C ligand (1.2 equiv.) and $IrCl_3.6H_2O$ (1 equiv.) in 2-ethoxyethanol (15 mL) and H_2O (5 mL) was heated under stirring to 125 °C. After 19 h, the corresponding N^N ancillary ligand (1.5 equiv.) was added and heating was continued. After 6 h, the solvent was evaporated leaving a solid, which was purified over silica (0 - 8% MeOH in CH_2Cl_2). The desired fractions were combined, and the solvent was evaporated leaving a solid which was washed with diethyl ether. After filtration, the desired complex was obtained as a solid. The ^{1}H NMR spectrum for **39** is shown.

(2-benzhydrylpyridinato-C$^{2''}$,N,C$^{2'}$)-N,N'-(4,4'-di-*tert*-butyl-2,2'-bipyridine)iridium(III) chloride

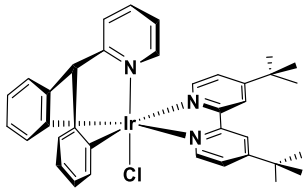

39

This complex was synthesised using the one-pot synthesis procedure. Red solid (0.127 g). **Yield:** 45%. **Mp:** 320 °C (decomp.). **^{1}H NMR (400 MHz, CD_2Cl_2) δ (ppm):** 8.75 (d, *J* = 5.8 Hz, 2H), 8.42 (d, *J* = 1.7 Hz, 2H), 7.70 (dd, *J* = 7.2, 1.5 Hz, 2H), 7.53 (d, *J* = 7.5 Hz, 1H), 7.49 (dd, *J* = 5.9, 1.9 Hz, 3H), 7.24 (dd, *J* = 7.2, 1.5 Hz, 2H), 7.19 (d, *J* = 5.9 Hz, 1H), 6.90 (dtd, *J* = 26.4, 7.3, 1.5 Hz, 4H), 6.45 – 6.39 (m, 1H), 5.28 (s, 1H), 1.50 (s, 18H). **^{13}C{^{1}H} NMR (126 MHz, CD_2Cl_2) δ (ppm):** 165.4, 162.6, 157.4, 151.8, 151.3, 143.9, 141.4, 138.7, 137.0, 125.8, 124.0, 123.8, 123.4, 122.7, 122.1, 120.8, 69.7, 35.9, 30.8. **HR-MS** ($ASAP^+$)**: [M-Cl]$^+$ Calculated:** ($C_{36}H_{37}IrN_3$): 704.2618 **Found:** 704.2618. **CHN: Calcd.** for $C_{36}H_{37}ClIrN_3$x3/2 H_2O: C, 56.42; H, 5.26; N, 5.48. **Found:** C, 56.45; H, 5.24; N, 5.28.

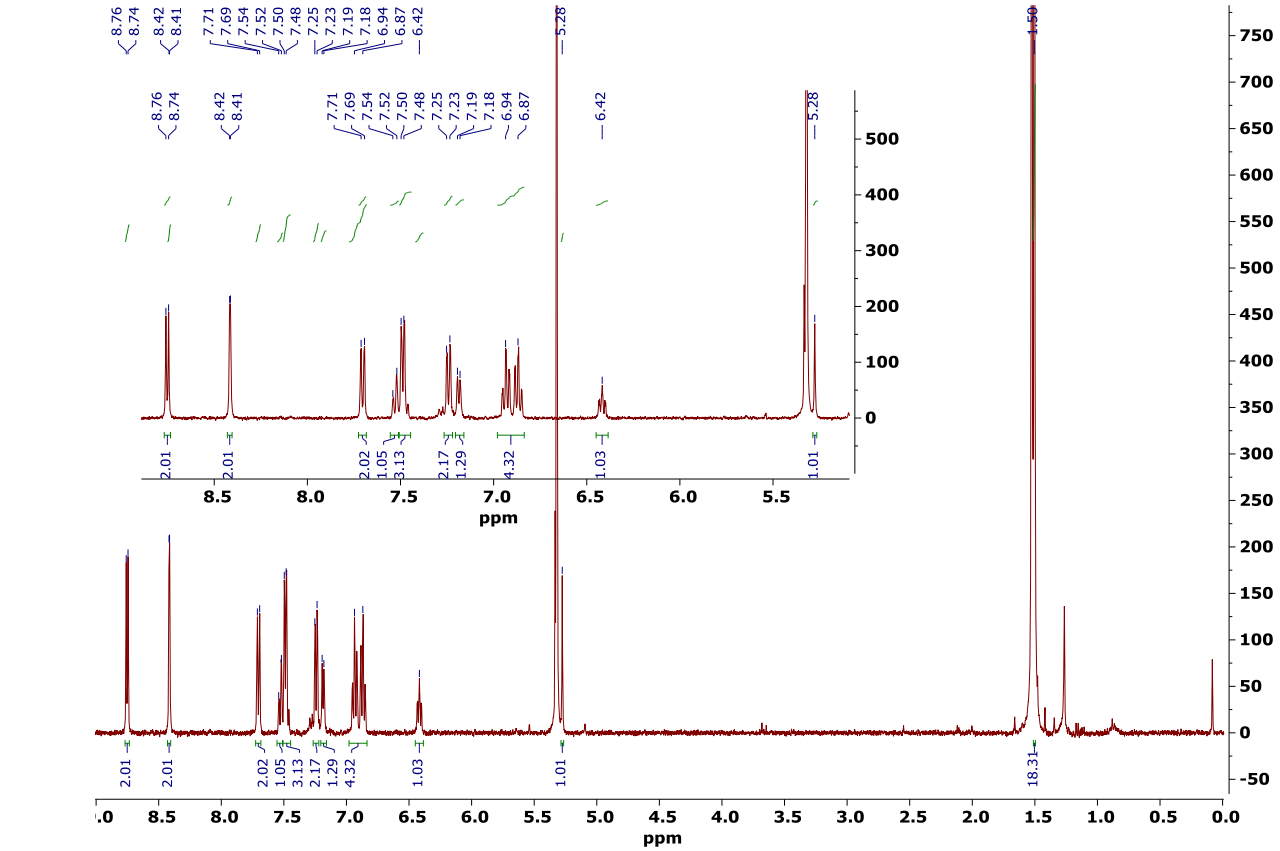

Figure **102**: ^{1}H-NMR spectrum in CD_2Cl_2 of complex **39**

[2-(bis(4-(*tert*-butyl)phenyl)methyl)pyridinato-C$^{2''}$,N,C$^{2'}$]-N,N'-(4,4'-di-*tert*-butyl-2,2'-bipyridine)iridium(III) chloride

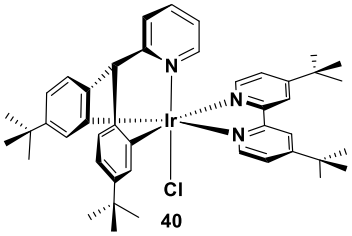

40

This complex was synthesised using the one-pot synthesis procedure. Red solid (0.129 g). **Yield:** 51%. **Mp:** 331 °C (decomp.). **^{1}H NMR (400 MHz, CD_2Cl_2) δ (ppm):** 8.79 (d, *J* = 5.9 Hz, 2H), 8.42 (d, *J* = 2.0 Hz, 2H), 7.80 (d, *J* = 2.1 Hz, 2H), 7.49 – 7.42 (m, 4H), 7.13 (d, *J* = 7.7 Hz, 3H), 6.89 (dd, *J* = 7.7, 2.1 Hz, 2H), 6.38 (ddd, *J* = 7.0, 5.9, 2.0 Hz, 1H), 5.22 (s, 1H), 1.51 (s, 18H), 1.32 (s, 18H). **^{13}C{^{1}H} NMR (126 MHz, CD_2Cl_2) δ (ppm):** 166.0, 162.6, 157.5, 151.7, 151.3, 147.8, 141.1, 140.4, 136.8, 135.9, 123.7, 123.6, 122.7, 122.4, 120.8, 118.8, 68.6,

35.9, 34.9, 32.1, 30.9. **[M-Cl]$^+$ Calculated:** ($C_{44}H_{53}IrN_3$): 816.3869 **Found:** 816.3867. **CHN**: **Calcd.** for $C_{44}H_{53}ClIrN_3$: C, 62.06; H, 6.27; N, 4.93. **Found:** C, 61.96; H, 6.31; N, 5.02.

[2-(bis(4-(trifluoromethyl)phenyl)methyl)pyridinato-C$^{2''}$,N,C$^{2'}$]-N,N'-(4,4'-di-*tert*-butyl-2,2'-bipyridine)iridium(III) chloride,

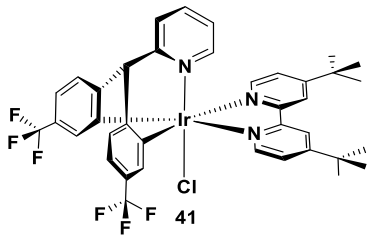

41

This complex was synthesised using the one-pot synthesis procedure. Yellow solid (0.096 g). **Yield:** 55%. **Mp:** 324 °C (decomp.). **^{1}H {^{19}F} NMR (400 MHz, CD_2Cl_2) δ (ppm):** 8.59 (d, *J* = 5.8 Hz, 2H), 8.44 (d, *J* = 2.0 Hz, 2H), 7.98 (d, *J* = 2.0 Hz, 2H), 7.62 – 7.48 (m, 4H), 7.37 (d, *J* = 7.7 Hz, 2H), 7.20 – 7.15 (m, 3H), 6.50 (ddd, *J* = 7.5, 5.9, 1.7 Hz, 1H), 5.46 (s, 1H), 1.51 (s, 18H). **^{13}C{^{1}H} NMR (126 MHz, CD_2Cl_2) δ (ppm):** 163.5, 163.3, 157.3, 151.9, 151.1, 147.4, 142.2, 137.6, 134.7, 127.6 (q, *J* = 30.2 Hz), 126.7, 124.5, 124.3, 123.5, 123.4, 121.2, 119.4 (q, *J* = 3.8 Hz), 69.2, 36.0, 30.8. **^{19}F {^{1}H} NMR (376 MHz, CD_2Cl_2) δ (ppm):** -61.58 (s, 6F). **[M-Cl]$^+$ Calculated:** ($C_{38}H_{35}F_6IrN_3$): 840.2364 **Found:** 840.2379. **CHN**: **Calcd.** for $C_{38}H_{35}F_6IrN_3$: C, 52.14; H, 4.03; N, 4.80. **Found:** C, 52.10; H, 4.16; N, 4.74.

[2-(bis(4-(*tert*-butyl)phenyl)methyl)pyridinato-$C^{2''}$,N,$C^{2'}$]-N,N'-(Diethyl[2,2'-bipyridine]-4,4'-dicarboxylate)iridium(III) chloride

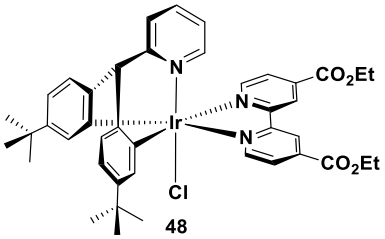

48

This complex was synthesised using the one-pot synthesis procedure. Dark green solid (0.031 g). **Yield:** 52%. **Mp:** 305 °C (decomp.). **^{1}H NMR (500 MHz, $CDCl_3$) δ (ppm):** 9.14 (d, J = 5.7 Hz, 2H), 9.07 (s, 2H), 7.99 – 7.92 (m, 2H), 7.83 (d, J = 1.9 Hz, 2H), 7.50 (d, J = 7.8 Hz, 1H), 7.39 (t, J = 7.6 Hz, 1H), 7.22 (s, 2H), 7.00 – 6.92 (m, 3H), 6.29 (t, J = 6.4 Hz, 1H), 5.30 (s, 1H), 4.57 (q, J = 7.1 Hz, 4H), 1.52 – 1.48 (m, 6H), 1.34 (s, 18H). **^{13}C{^{1}H} NMR (126 MHz, $CDCl_3$) δ (ppm):** 165.7, 164.3, 158.2, 152.5, 151.5, 148.1, 140.8, 139.7, 139.5, 137.5, 135.6, 126.0, 124.0, 123.8, 122.9, 122.7, 119.4, 68.3, 63.3, 34.9, 32.0, 14.6. **HR-MS** ($ASAP^+$)**: [M-Cl]$^+$ Calculated:** ($C_{36}H_{37}IrN_3$): 848.3042 **Found:** 848.3039. **CHN**: **Calcd.** for $C_{42}H_{45}ClIrN_3O_4$ x1/3CH_2Cl_2: C, 55.76; H, 5.05; N, 4.61. **Found:** 55.86; H, 5.29; N, 4.58.

Electrochemistry

Cyclic and differential pulse voltammetry measurements were performed on an Electrochemical Analyzer potentiostat model 600D from CH Instruments. Solutions for cyclic voltammetry were prepared in MeCN or CH_2Cl_2 and degassed with solvent-saturated nitrogen by bubbling for about 10 min prior to scanning. Tetra(*n*-butyl)ammoniumhexafluorophosphate ([TBA](PF_6); ca. 0.1 M in MeCN or CH_2Cl_2) was used as the supporting electrolyte. Two Ag/Ag^+ electrode (silver wire in a solution of 0.1 M KCl in H_2O) were used as the pseudoreference electrode and counter electrode, respectively; a platinum electrode was used for the working electrode. The redox potentials are reported relative to a saturated calomel electrode electrode (SCE) or a normal hydrogen electrode (NHE) with a ferrocene/ferrocenium (Fc/Fc^+) redox couple as an internal reference (0.38 V[189] vs. SCE and 0.70[191] vs. NHE).

Photophysical data

All samples were prepared in HPLC grade MeCN with varying concentrations in the order of micromolar. Absorption spectra were recorded at room temperature using a Shimadzu UV-1800 double beam spectrophotometer. Molar absorptivity determination was verified by linear least-squares fit of values obtained from at least four independent solutions at varying concentrations ranging from 10^{-4} to 10^{-6} M.

The sample solutions for the emission spectra for complexes (Chapter 3-6) were prepared in HPLC grade MeCN and degassed via three freeze−pump−thaw cycles using an in-house designed quartz cuvette. Steady-state and time-resolved emission spectra were recorded at room temperature using Gilden photonics Fluorimeter. For steady-state measurements at room temperature the complexes were excited at 360 – 400 nm. The excited-state lifetimes of the complexes were obtained by time correlated single photon counting (TCSPC) at an excitation wavelength of 378 nm using an Edinburgh Instruments FLS980 fluorimeter using a

pulsed diode laser, and PL emission was detected at the corresponding steady-state emission maximum for each complex. The room temperature PL decays were fitted with a mono, bi- or multi exponential decay function. The PL decays at 77 K were fitted with a single exponential decay function. Emission quantum yields were determined using the optically dilute method.[290] A stock solution with absorbance of ca. 0.2 was prepared, and then four dilutions were prepared with dilution factors between 2 and 20 to obtain solutions with absorbances of ca. 0.100, 0.075, 0.050, and 0.025, respectively. The Beer−Lambert law was found to be respected (linear dependency) at the concentrations of the solutions. The emission spectra were then measured. For each sample, linearity between absorption and emission intensity was verified through linear regression analysis, and additional measurements were acquired until the Pearson regression factor (R^2) for the linear fit of the data set surpassed 0.9. Individual relative quantum yield values were calculated for each solution, and the values reported represent the slope value. The $\Phi_s = \Phi_r(A_r/A_s)(I_s/I_r)(n_s/n_r)^2$ equation was used to calculate the relative quantum yield of each of the sample, where Φ_r is the absolute quantum yield of the reference, *n* is the refractive index of the solvent, *A* is the absorbance at the excitation wavelength, and *I* is the integrated area under the corrected emission curve. The subscripts *s* and *r* refer to the sample and reference, respectively. A solution of $[Ru(bpy)_3](PF_6)_2$ in aerated MeCN (Φ_{PL} = 1.8%)[9] or Quinine sulfate in 0.5 M H_2SO_4 (Φ_{PL} = 54.6%)[291] was used as a reference at 298 K.

The excitation source for emission lifetime measurements for complexes from Chapter 2 was the 400 nm output (third harmonic) of a Quanta-Ray Q-switched GCR-150-10 pulsed Nd-YAG laser. Luminescence quantum yields were measured by the optically dilute method[292] using an aerated aqueous solution of $[Ru(bpy)_3]Cl_2$ (Φ_{PL} = 4%)[293] as the reference. Luminescence decay signals from a Hamamatsu R928 photomultiplier tube were converted into potential changes by a 50 Ω load resistor and then recorded with a Tektronix Model TDS 620A digital oscilloscope.

EFISH measurements

EFISH measurements were carried out in $CHCl_3$ solutions at a concentration of 10^{-3} M, with a non-resonant incident wavelength of 1.907 μm, obtained by Raman-shifting the fundamental 1.064 μm wavelength produced by a Q-switched, mode-locked Nd^{3+}:YAG laser manufactured by Atalaser. The $\mu\beta_{EFISH}$ values reported are the mean values of 16 measurements performed on the same sample.

Preparation of composite films.

Thin films of complex **30b** (5% w/w relative to the polymer) dispersed in poly(methyl methacrylate) (PMMA) or polystyrene (PS) were prepared by spin-coating a few drops of a dichloromethane solution on ordinary non-pretreated glass substrates (thickness 1 mm), previously cleaned with water/acetone. The spinning parameters were set at the following values: RPM 1 = 800; ramp 1 = 1 s, time 1 = 5 s; RPM 2 = 2000; ramp 2 = 4 s, time 2 = 83 s.

Corona Poling Setup and SHG measurements.

The fundamental incident light was generated by a 1064 nm Q-switched Nd:YAG laser. The output pulse was attenuated to 0.5 mJ and was focused on the sample, placed over the hot stage. The fundamental beam was polarised in the incidence plane (p-polarised) with an incidence angle of 55° respect to the sample. A corona-wire voltage (up to 10 kV across a 10 mm gap) was applied. After rejection of the fundamental beam by an interference filter and a glass cutoff filter, the p-polarised SHG signal at 532 nm was detected with a UV-vis photomultiplier (PT). The output signal from the PT was set to a digital store oscilloscope and then processed by a computer. Then, in the Maker fringe experiment, the second harmonic (SH) intensity was detected as a function of the incidence angle of the fundamental beam and normalised with respect to that of a calibrated quartz crystal wafer (X-cut) 1 mm thick whose

d_{11} is 0.46 pm/V. The incidence angle was changed by rotating the poled film, while the polarisation of the fundamental and SH beam could be changed by a half-wave plate and a cube beam splitter, respectively. In order to determine the nonzero independent components of the susceptibility tensor for poled films Maker fringe measurements were conducted with polarisations p → p, s → p, and 45 → s (where p and s indicate the polarisation of the beam in the plane parallel and orthogonal to the incident one, respectively).[294,295]

DFT and TD-DFT calculations

To perform DFT and TD-DFT calculations, we have used the Gaussian09 program. Our calculations consisted in geometry optimization vibrational spectra determinations and TD-DFT calculations of the different structures. We have applied default procedures, integration grids, algorithms and parameters, except for improved energy (typically 10^{-10} *a.u.*) and internal forces (10^{-5} *a.u.*) convergence thresholds and the use of the *ultrafine* integration DFT grid. The ground-state geometrical parameters have been determined with the M06 functional.[296] The vibrational spectrum has been subsequently determined analytically at the same level of theory and it has been checked that all structures correspond to true minima of the potential energy surface. At least, the first forty low-lying excited-states have been determined within the vertical TD-DFT approximation using the same functional that is suited for optical spectra.[297,298] Phosphorescence wavelengths were obtained by first optimizing the lowest triplet excited-state with unrestricted DFT (M06 functional) and next computing the singlet ground-state energy on that structure. For all nuclei, we have used the LanL2DZ(5*d*,7*f*) basis set and pseudopotential augmented by additional *d* and *f* functions of contraction length one. During all steps, a modelling of bulk solvent effects (here CH_2Cl_2) through the Polarizable Continuum Model (PCM),[299] using the liner-response approach for the TD-DFT part of the calculation.

References

1 V. Balzani and A. Juris, *Coord. Chem. Rev.*, 2001, **211**, 97–115.

2 J. P. Paris and W. W. Brandt, *J. Am. Chem. Soc.*, 1959, **81**, 5001–5002.

3 F. Xue, Y. Lu, Z. Zhou, C. Zhang and S. Fang, *J. Coord. Chem.*, 2014, **67**, 1353–1360.

4 L. Favereau, A. Makhal, D. Provost, Y. Pellegrin, E. Blart, E. Göransson, L. Hammarström and F. Odobel, *Phys. Chem. Chem. Phys.*, 2017, **19**, 4778–4786.

5 A. F. Henwood and E. Zysman-Colman, *Chem. Commun.*, 2017, **53**, 807–826.

6 V. W. Yam, *Bull. Jpn. Soc. Coord. Chem.*, 2016, **67**, 21–28.

7 K. J. Kilpin, E. L. Gavey, C. J. McAdam, C. B. Anderson, S. J. Lind, C. C. Keep, K. C. Gordon and J. D. Crowley, *Inorg. Chem.*, 2011, **50**, 6334–6346.

8 J. A. Gareth Williams, S. Develay, D. L. Rochester and L. Murphy, *Coord. Chem. Rev.*, 2008, **252**, 2596–2611.

9 K. Suzuki, A. Kobayashi, S. Kaneko, K. Takehira, T. Yoshihara, H. Ishida, Y. Shiina, S. Oishi and S. Tobita, *Phys. Chem. Chem. Phys.*, 2009, **11**, 9850.

10 M. K. Nazeeruddin, a Kay, E. Miiller, P. Liska, N. Vlachopoulos, M. Gratzel, C.-Lausanne and R. April, *J. Am. Chem. Soc.*, 1993, **115**, 6382–6390.

11 K. Kalyanasundaram and M. Grätzel, *Coord. Chem. Rev.*, 1998, **177**, 347–414.

12 N. Robertson, *Angew. Chem. Int. Ed.*, 2006, **45**, 2338–2345.

13 M. Grätzel, *J. Photochem. Photobiol. C Photochem. Rev.*, 2003, **4**, 145–153.

14 Y. Cao, Y. Saygili, A. Ummadisingu, J. Teuscher, J. Luo, N. Pellet, F. Giordano, S. M. Zakeeruddin, J.-E. Moser, M. Freitag, A. Hagfeldt and M. Grätzel, *Nat. Commun.*, 2017, **8**, 15390.

15 J. Xuan and W. J. Xiao, *Angew. Chem. Int. Ed.*, 2012, **51**, 6828–6838.

16 R. L. House, N. Yukie, M. Iha, R. L. Coppo, L. Alibabaei, B. D. Sherman, P. Kang, M. K. Brennaman, P. G. Hoertz and T. J. Meyer, *J. Photochem. Photobiol. C Photochem. Rev.*, 2015, **25**, 32–45.

17 J. Otsuki, T. Akasaka and K. Araki, *Coord. Chem. Rev.*, 2008, **252**, 32–56.

18 E. C. Harvey, B. L. Feringa, J. G. Vos, W. R. Browne and M. T. Pryce, *Coord. Chem. Rev.*, 2015, **282**–**283**, 77–86.

19 F. Barigelletti and L. Flamigni, *Chem. Soc. Rev.*, 2000, **29**, 1–12.

20 C. Joachim, J. K. Gimzewski and A. Aviram, *Nature*, 2000, **408**, 1–8.

21 A. F. Henwood and E. Zysman-Colman, *Top. Curr. Chem.*, 2016, **374**, 36.

22 Y. Chi and P.-T. Chou, *Chem. Soc. Rev.*, 2010, **39**, 638–655.

23 R. D. Costa, E. Ortí, H. J. Bolink, F. Monti, G. Accorsi and N. Armaroli, *Angew. Chem. Int. Ed.*, 2012, **51**, 8178–8211.

24 O. Filevich, L. Zayat, L. M. Baraldo and R. Etchenique, *Luminescent and Photoactive Transition Metal Complexes as Biomolecular Probes and Cellular Reagents*, 2015, vol. 165.

25 K. K. W. Lo, *Acc. Chem. Res.*, 2015, **48**, 2985–2995.

26 K. K.-W. Lo and K. Y. Zhang, *RSC Adv.*, 2012, **2**, 12069–12083.

27 K. J. Suhr, L. D. Bastatas, Y. Shen, L. A. Mitchell, B. J. Holliday and J. D. Slinker, *ACS Appl. Mater. Interfaces*, 2016, **8**, 8888–8892.

28 H. Le Bozec and T. Renouard, *Eur. J. Inorg. Chem.*, 2000, 229–239.

29 O. Maury and H. Le Bozec, *Acc. Chem. Res.*, 2005, **38**, 691–704.

30 C. Dhenaut, I. Ledoux, I. D. W. Samuel, J. Zyss, M. Bourgault and H. Le Bozec, *Nature*, 1995, **374**, 339–342.

31 K. P. S. Zanoni, R. L. Coppo, R. C. Amaral and N. Y. Murakami Iha, *Dalton Trans.*, 2015, **44**, 14559–14573.

32 Z. Liu, W. Qi and G. Xu, *Chem. Soc. Rev.*, 2015, **44**, 3117–3142.

33 S. Ladouceur and E. Zysman-Colman, *Eur. J. Inorg. Chem.*, 2013, 2985–3007.

34 A. Valore, E. Cariati, C. Dragonetti, S. Righetto, D. Roberto, R. Ugo, F. De Angelis, S. Fantacci, A. Sgamellotti, A. Macchioni and D. Zuccaccia, *Chem. Eur. J.*, 2010, **16**, 4814–4825.

35 G. B. Porter, *J. Chem. Educ.*, 1983, **60**, 785.

36 L. J. Vandergriff, *Fundam. Photonics*, 2008, 1–38.

37 A. B. P. Lever, *J. Chem. Educ.*, 1974, **51**, 5.

38 A. Samoson, T. Tuherm, J. Past, A. Reinhold, T. Anupõld, I. Heinmaa, A. Meijere, K. N. Houk, H. Kessler, J. M. Lehn, S. V Ley, S. L. Schreiber, J. Thiem, B. M. Trost, F. Vögtle, H. Yamamoto and J. Klinowski, *Topics in Current Chemistry*, 2007, vol. 280.

39 V. W.-W. Yam and K. M.-C. Wong, *Chem. Commun.*, 2011, **47**, 11579.

40 M. G. Colombo and H. U. Guedel, *Inorg. Chem.*, 1993, **32**, 3081–3087.

41 A. Valore, E. Cariati, S. Righetto, D. Roberto, F. Tessore, R. Ugo, I. L. Fragalà, M. E. Fragalà, G. Malandrino, F. De Angelis, L. Belpassi, I. Ledoux-Rak, K. H. Thi and J. Zyss, *J. Am. Chem. Soc.*, 2010, **132**, 4966–4970.

42 J. D. Slinker, D. Bernards, P. L. Houston, H. D. Abruña, S. Bernhard and G. G. Malliaras, *Chem. Commun.*, 2003, 2392–2399.

43 B. Valeur and M. N. Berberan-Santos, *J. Chem. Educ.*, 2011, 731–738.

44 B. Y. M. Kasha, *Discuss. Faraday Soc.*, 1950, **9**, 14–19.

45 A. Jablonski, *Nature*, 1933, **131**, 839.

46 G. G. Stokes, *Philos. Trans. R. Soc. London*, 1853, **143**, 385–396.

47 Z. Liu, D. Nie, Z. Bian, F. Chen, B. Lou, J. Bian and C. Huang, *ChemPhysChem*, 2008, **9**, 634–640.

48 M. a. Baldo, S. Lamansky, P. E. Burrows, M. E. Thompson and S. R. Forrest, *Appl. Phys. Lett.*, 1999, **75**, 4–6.

49 M. Xu, W. Li, Z. An, Q. Zhou and G. Wang, *Appl. Organomet. Chem.*, 2005, **19**, 1225–1231.

50 T. Sajoto, P. I. Djurovich, A. B. Tamayo, J. Oxgaard, W. A. Goddard and M. E. Thompson, *J. Am. Chem. Soc.*, 2009, **131**, 9813–9822.

51 J. A. Weinstein, *Applied Photochemistry*, 2013.

52 A. Barbieri, G. Accorsi and N. Armaroli, *Chem. Commun.*, 2008, 2185.

53 G. Zhou, W. Y. Wong and X. Yang, *Chem. Asian J.*, 2011, **6**, 1706–1727.

54 I. Omae, *Coord. Chem. Rev.*, 2016, **310**, 154–169.

55 C. Dragonetti, S. Righetto, D. Roberto, R. Ugo, A. Valore, S. Fantacci, A. Sgamellotti and F. De Angelis, *Chem. Commun.*, 2007, **2**, 4116–8.

56 V. Aubert, L. Ordronneau, M. Escadeillas, J. A. G. Williams, A. Boucekkine, E. Coulaud, C. Dragonetti, S. Righetto, D. Roberto, R. Ugo, A. Valore, A. Singh, J. Zyss, I. Ledoux-Rak, H. Le Bozec and V. Guerchais, *Inorg. Chem.*, 2011, **50**, 5027–5038.

57 C. Dragonetti, A. Colombo, D. Marinotto, S. Righetto, D. Roberto, A. Valore, M. Escadeillas, V. Guerchais, H. Le Bozec, A. Boucekkine and C. Latouche, *J. Organomet. Chem.*, 2014, **751**, 568–572.

58 A. Sinopoli, C. J. Wood, E. A. Gibson and P. I. P. Elliott, *Inorg. Chim. Acta*, 2017, **457**, 81–89.

59 A. F. Henwood, Y. Hu, M. T. Sajjad, G. K. V. V. Thalluri, S. S. Ghosh, D. B. Cordes, A. M. Z. Slawin, I. D. W. Samuel, N. Robertson and E. Zysman-Colman, *Chem. Eur. J.*,

2015, **21**, 19128–19135.

60 N. D. McDaniel and S. Bernhard, *Dalton Trans.*, 2010, **39**, 10021.

61 K. Teegardin, J. I. Day, J. Chan and J. Weaver, *Org. Process Res. Dev.*, 2016, **20**, 1156–1163.

62 C. K. Prier, D. A. Rankic and D. W. C. MacMillan, *Chem. Rev.*, 2013, **113**, 5322.

63 W. C. H. Choy, W. K. Chan and Y. Yuan, *Adv. Mater.*, 2014, **26**, 5368–5399.

64 A. F. Henwood and E. Zysman-Colman, *Top. Curr. Chem.*, 2016, **374**, 1–41.

65 M. Nonoyama, *Bull. Chem. Soc. Jpn.*, 1974, **47**, 767.

66 K. P. S. Zanoni, R. L. Coppo, R. C. Amaral and N. Y. Murakami Iha, *Dalton Trans.*, 2015, **44**, 14559–14573.

67 C. Ulbricht, B. Beyer, C. Friebe, A. Winter and U. S. Schubert, *Adv. Mater.*, 2009, **21**, 4418–4441.

68 Z. Liu, Z. Bian and C. Huang, *Top. Organomet. Chem.*, 2010, **28**, 75.

69 J. Sun, W. Wu and J. Zhao, *Chem. Eur. J.*, 2012, **18**, 8100–8112.

70 A. B. Tamayo, B. D. Alleyne, P. I. Djurovich, I. Tsyba, N. N. Ho, R. Bau, M. E. Thompson, I. Tsyba, N. N. Ho, R. Bau and M. E. Thompson, *J. Am. Chem. Soc*, 2003, **125**, 7377–7387.

71 A. R. McDonald, M. Lutz, L. S. von Chrzanowski, G. P. M. van Klink, A. L. Spek and G. van Koten, *Inorg. Chem.*, 2008, **47**, 6681–6691.

72 J. W. Facendola, M. Seifrid, J. Siegel, P. I. Djurovich and M. E. Thompson, *Dalton Trans.*, 2015, **44**, 8456–8466.

73 D. Rota Martir, A. K. Bansal, V. Di Mascio, D. B. Cordes, A. F. Henwood, A. M. Z. Slawin, P. C. J. Kamer, L. Martínez-Sarti, A. Pertegás, H. J. Bolink, I. D. W. Samuel and E. Zysman-Colman, *Inorg. Chem. Front.*, 2016, **3**, 218–235.

74 S. Ladouceur, D. Fortin and E. Zysman-Colman, *Inorg. Chem.*, 2010, **49**, 5625–5641.

75 R. D. Costa, E. Ortí, H. J. Bolink, S. Graber, S. Schaffner, M. Neuburger, C. E. Housecroft and E. C. Constable, *Adv. Funct. Mater.*, 2009, **19**, 3456–3463.

76 V. N. Kozhevnikov, Y. Zheng, M. Clough, H. A. Al-Attar, G. C. Gri, K. Abdullah, S. Raisys, V. Jankus, M. R. Bryce and A. P. Monkman, *Chem. Mater.*, 2013, **25**, 2352–2358.

77 D. Schneidenbach, S. Ammermann, M. Debeaux, A. Freund, M. Zöllner, C. Daniliuc, P. G. Jones, W. Kowalsky and H. H. Johannes, *Inorg. Chem.*, 2010, **49**, 397–406.

78 K. S. Bejoymohandas, A. Kumar, S. Varughese, E. Varathan, V. Subramanian and M. L. P. Reddy, *J. Mater. Chem. C*, 2015, **3**, 7405–7420.

79 A. K. Pal, A. F. Henwood, D. B. Cordes, A. M. Z. Slawin, I. D. W. Samuel and E. Zysman-Colman, *Inorg. Chem.*, 2017, **56**, 7533–7544.

80 S. Kesarkar, W. Mróz, M. Penconi, M. Pasini, S. Destri, M. Cazzaniga, D. Ceresoli, P. R. Mussini, C. Baldoli, U. Giovanella and A. Bossi, *Angew. Chem. Int. Ed.*, 2016, **55**, 2714–2718.

81 X. Cao, J. Miao, M. Zhu, C. Zhong, C. Yang, H. Wu, J. Qin and Y. Cao, *Chem. Mater.*, 2014, **27**, 96–104.

82 M. Lepeltier, T. K. M. Lee, K. K. W. Lo, L. Toupet, H. Le Bozec and V. Guerchais, *Eur. J. Inorg. Chem.*, 2007, **2**, 2734–2747.

83 L. Sun, A. Galan, S. Ladouceur, J. D. Slinker and E. Zysman-Colman, *J. Mater. Chem.*, 2011, **21**, 18083.

84 J. D. Slinker, A. A. Gorodetsky, M. S. Lowry, J. Wang, S. Parker, R. Rohl, S. Bernhard and G. G. Malliaras, *J. Am. Chem. Soc.*, 2004, **126**, 2763–2767.

85 A. K. Pal, D. B. Cordes, A. M. Z. Slawin, C. Momblona, E. OrtÍ, I. D. W. Samuel, H. J. Bolink and E. Zysman-Colman, *Inorg. Chem.*, 2016, **55**, 10361–10376.

86 R. D. Costa, E. Ortí, H. J. Bolink, S. Graber, S. Schaffner, M. Neuburger, C. E. Housecroft and E. C. Constable, *Adv. Funct. Mater.*, 2009, **19**, 3456–3463.

87 X. Zeng, C. Rothe, C. J. Chiang, V. Jankus, K. Abdullah, R. Jitchati, A. S. Batsanov, M. R. Bryce and A. P. Monkman, *Adv. Funct. Mater.*, 2009, **19**, 2038–2044.

88 M. S. Lowry and S. Bernhard, *Chem. Eur. J.*, 2006, **12**, 7970–7977.

89 M. Bixon, J. Jortner, J. Cortes, H. Heitele and M. E. Michel-Beyerle, *J. Phys. Chem.*, 1994, **98**, 7289–7299.

90 A. B. Tamayo, S. Garon, T. Sajoto, P. I. Djurovich, I. M. Tsyba, R. Bau and M. E. Thompson, *Inorg. Chem.*, 2005, **44**, 8723–8732.

91 F. De Angelis, S. Fantacci, N. Evans, C. Klein, S. M. Zakeeruddin, J.-E. Moser, K. Kalyanasundaram, H. J. Bolink, M. Gratzel and M. K. Nazeeruddin, *Inorg. Chem.*, 2007, **46**, 5989–6001.

92 H. C. Li, P. T. Chou, Y. H. Hu, Y. M. Cheng and R. S. Liu, *Organometallics*, 2005, **24**, 1329–1335.

93 V. Thamilarasan, A. Jayamani, P. Manisankar, Y. Kim and N. Sengottuvelan, *Inorg. Chim. Acta*, 2013, **408**, 240–245.

94 R. Zhu, J. Lin, G.-A. Wen, S.-J. Liu, J.-H. Wan, J.-C. Feng, Q.-L. Fan, G.-Y. Zhong, W. Wei and W. Huang, *Chem. Lett.*, 2005, **34**, 1668–1669.

95 C. F. Chang, Y. M. Cheng, Y. Chi, Y. C. Chiu, C. C. Lin, G. H. Lee, P. T. Chou, C. C. Chen, C. H. Chang and C. C. Wu, *Angew. Chem. Int. Ed.*, 2008, **47**, 4542–4545.

96 Y. H. Song, Y. C. Chiu, Y. Chi, Y. M. Cheng, C. H. Lai, P. T. Chou, K. T. Wong, M. H. Tsai and C. C. Wu, *Chem. Eur. J.*, 2008, **14**, 5423–5434.

97 F. Zhang, D. Ma, L. Duan, J. Qiao, G. Dong, L. Wang and Y. Qiu, *Inorg. Chem.*, 2014, **53**, 6596–6606.

98 S. Lamansky, P. Djurovich, D. Murphy, F. Abdel-Razzaq, R. Kwong, I. Tsyba, M. Bortz, B. Mui, R. Bau and M. E. Thompson, *Inorg. Chem.*, 2001, **40**, 1704.

99 S.-J. Yeh, C.-T. Chen, Y.-H. Song, Y. Chi and C. H. Chen, *SID J. Soc Inf*, 2005, 857.

100 Eurpäische Kommission, *Dimens. Contemp. Ger. Arts Lett.*, 2010, 1–25.

101 J. H. Kamlage and P. Nanz, *Glob. Soc.*, 2017, **31**, 65–82.

102 S. Bouzarovski and S. Tirado Herrero, *Eur. Urban Reg. Stud.*, 2017, **24**, 69–86.

103 A. De Almeida, B. Santos, B. Paolo and M. Quicheron, *Renew. Sustain. Energy Rev.*, 2014, **34**, 30–48.

104 J. Y. Tsao, in *LEDs for General Illumination Update 2002 – Full Edition*, 2002.

105 R. Haitz and J. Y. Tsao, *Light. Technol.*, 2011, 26–30.

106 G. Zorpette, *IEEE Spectr.*, 2002, **39**, 70–74.

107 C. J. Humphreys, *MRS Bull.*, 2008, **33**, 459–470.

108 Z. Xia and Q. Liu, *Prog. Mater. Sci.*, 2016, **84**, 59–117.

109 J. Y. Tsao, *IEEE Circuit. Dev.*, 2004, **20**, 28.

110 B. Geffroy, P. le Roy and C. Prat, *Polym. Int.*, 2006, **55**, 572–582.

111 R. D. Costa, E. Ortí and H. J. Bolink, *Pure Appl. Chem.*, 2011, **83**, 2115–2128.

112 G. Kalyuzhny, M. Buda, J. Mcneill, P. Barbara and A. J. Bard, *J. Am. Chem. Soc*, 2003, **125**, 6272–6283.

113 M. A. Baldo, D. F. O'Brien, Y. You, A. Shoustikov, S. Sibley, M. E. Thompson, S. R. Forrest, M. A. Baldo, D. F. O'Brien, Y. You, A. Shoustikov, S. Sibley and M. E. Thompson, *Nature*, 1998, **395**, 151–154.

114 D. F. O'Brien, M. a. Baldo, M. E. Thompson and S. R. Forrest, *Appl. Phys. Lett.*, 1999, **74**, 442.

115 L. Zhang, H. Van Eersel, P. A. Bobbert and R. Coehoorn, *Chem. Phys. Lett.*, 2016, **652**, 142–147.

116 L. F. Gildea and J. A. G. Williams, *3 – Iridium and platinum complexes for OLEDs*, 2013.

117 C. Fan, L. Zhu, B. Jiang, C. Zhong, D. Ma, J. Qin and C. Yang, *Org. Electron. physics, Mater. Appl.*, 2013, **14**, 3163–3171.

118 C. Adachi, R. C. Kwong, P. Djurovich, V. Adamovich, M. A. Baldo, M. E. Thompson and S. R. Forrest, *Appl. Phys. Lett.*, 2001, **79**, 2082–2084.

119 Z. B. Wang, M. G. Helander, J. Qiu, D. P. Puzzo, M. T. Greiner, Z. M. Hudson, S. Wang, Z. W. Liu and Z. H. Lu, *Nat. Photonics*, 2011, **5**, 753–757.

120 S. Reineke, F. Lindner, G. Schwartz, N. Seidler, K. Walzer, B. Lüssem and K. Leo, *Nature*, 2009, **459**, 234–238.

121 U. Mitschke and P. Bäuerle, *J. Mater. Chem.*, 2000, **10**, 1471–1507.

122 Q. Pei, G. Yu, C. Zhang, Y. Yang and A. J. Heeger, *Science*, 1995, **269**, 1086.

123 Z. Zhang, K. Guo, Y. Li, X. Li, G. Guan, H. Li, Y. Luo, F. Zhao, Q. Zhang, B. Wei, Q. Pei and H. Peng, *Nat. Photonics*, 2015, **9**, 233–238.

124 L. He, L. Duan, J. Qiao, R. Wang, P. Wei, L. Wang and Y. Qiu, *Adv. Funct. Mater.*, 2008, **18**, 2123–2131.

125 H. C. Su, F. C. Fang, T. Y. Hwu, H. H. Hsieh, H. F. Chen, G. H. Lee, S. M. Peng, K. T. Wong and C. C. Wu, *Adv. Funct. Mater.*, 2007, **17**, 1019–1027.

126 J. D. Slinker, J. Rivnay, J. S. Moskowitz, J. B. Parker, S. Bernhard, H. D. Abruña and G. G. Malliaras, *J. Mater. Chem.*, 2007, **17**, 2976.

127 S. Bernhard, J. A. Barron, P. L. Houston, D. Abrun, J. L. Ruglovksy, X. Gao and G. G. Malliaras, *J. Am. Chem. Soc*, 2002, **124**, 13624–13628.

128 K. J. Suhr, L. D. Bastatas, Y. Shen, L. A. Mitchell, G. A. Frazier, D. W. Taylor, J. D. Slinker and B. J. Holliday, *Dalton Trans.*, 2016, **45**, 17807–17823.

129 H. J. Bolink, E. Coronado, D. Costa, N. Lardie and E. Ortí, *Inorg. Chem.*, 2008, **47**, 9149–9151.

130 L. He, L. Duan, J. Qiao, G. Dong, L. Wang and Y. Qiu, *Chem. Mater.*, 2010, **22**, 3535–3542.

131 H. J. Bolink, E. Coronado, R. D. Costa, E. Ortí, M. Sessolo, S. Graber, K. Doyle, M. Neuburger, C. E. Housecroft and E. C. Constable, *Adv. Mater.*, 2008, **20**, 3910–3913.

132 R. D. Costa, E. Ortí, H. J. Bolink, S. Graber, C. E. Housecroft and E. C. Constable, *J. Am. Chem. Soc.*, 2010, **132**, 5978–5980.

133 R. D. Costa, E. Ortí, H. J. Bolink, S. Graber, C. E. Housecroft, M. Neuburger, S. Schaffner and E. C. Constable, *Chem. Commun.*, 2009, 2029–2031.

134 S. B. Meier, D. Tordera, A. Pertegás, C. Roldán-Carmona, E. Ortí and H. J. Bolink, *Mater. Today*, 2014, **17**, 217–223.

135 N. Kaihovirta, C. Larsen and L. Edman, *ACS Appl. Mater. Interfaces*, 2014, **6**, 2940–2947.

136 T. Hu, L. He, L. Duan and Y. Qiu, *J. Mater. Chem.*, 2012, **22**, 4206.

137 H. J. Bolink, L. Cappelli, E. Coronado, M. Grätzel, E. Ortı, D. Costa, P. M. Viruela and K. Nazeeruddin, *J. Am. Chem. Soc*, 2006, **128**, 14786–14787.

138 J. D. Slinker, J. Rivnay, J. S. Moskowitz, J. B. Parker, S. Bernhard, H. D. Abruña and G. G. Malliaras, *J. Mater. Chem.*, 2007, **17**, 2976.

139 N. J. Long, *Angew. Chem. Int. Ed.*, 1995, **34**, 21–38.

140 S. Di Bella, C. Dragonetti, M. Pizzotti, D. Roberto, F. Tessore and R. Ugo, *Top. Organomet. Chem.*, 2010, **28**, 1–55.

141 W. Zinth and U. Zinth, *Optik*, 2009.

142 J. Zyss and I. Ledoux, *Chem. Rev.*, 1994, **94**, 77–105.

143 E. Cariati, M. Pizzotti, D. Roberto, F. Tessore and R. Ugo, *Coord. Chem. Rev.*, 2006, **250**, 1210–1233.

144 C. Wang, T. Zhang and W. Lin, *Chem. Rev.*, 2012, **112**, 1084–1104.

145 E. Cariati, E. Lucenti, C. Botta, U. Giovanella, D. Marinotto and S. Righetto, *Coord. Chem. Rev.*, 2016, **306**, 566–614.

146 B. M. Walsh, *Opt. Mater. (Amst).*, 2016, **65**, 6–11.

147 R. Dworczak and D. Kieslinger, *Phys. Chem. Chem. Phys.*, 2000, **2**, 5057–5064.

148 J. L. Oudar, *J. Chem. Phys.*, 1977, **67**, 446–457.

149 E. A. Guggenheim, *Trans. Faraday. Soc.*, 1949, **45**, 714.

150 Boyd, *J. Chem. Inf. Model.*, 2013, **53**, 1689–1699.

151 H. Zhao, P. V. Simpson, A. Barlow, G. J. Moxey, M. Morshedi, N. Roy, R. Philip, C. Zhang, M. P. Cifuentes and M. G. Humphrey, *Chem. Eur. J.*, 2015, **21**, 11843–11854.

152 S. Fantacci and F. De Angelis, *Coord. Chem. Rev.*, 2011, **255**, 2704–2726.

153 O. Maury, L. Viau, K. Sénéchal, B. Corre, J. P. Guégan, T. Renouard, I. Ledoux, J. Zyss and H. Le Bozec, *Chem. Eur. J.*, 2004, **10**, 4454–4466.

154 H. M. Kim and B. R. Cho, *J. Mater. Chem.*, 2009, **19**, 7402.

155 S. Di Di Bella, I. Fragalà, I. Ledoux and J. Zyss, *Chem. Eur. J.*, 2001, **7**, 3738–3743.

156 B. J. Coe, J. Fielden, S. P. Foxon, B. S. Brunschwig, I. Asselberghs, K. Clays, A. Samoc and M. Samoc, *J. Am. Chem. Soc.*, 2010, **132**, 3496–3513.

157 I. D. Morrison, R. G. Denning, W. M. Laidlaw and M. A. Stammers, *Rev. Sci. Instrum.*, 1996, **67**, 1445–1453.

158 C. Feuvrie, O. Maury, H. Le Bozec, I. Ledoux, J. P. Morrall, G. T. Dalton, M. Samoc and M. G. Humphrey, *J. Phys. Chem. A*, 2007, **111**, 8980–8985.

159 K. Sénéchal, O. Maury, H. Le Bozec, I. Ledoux and J. Zyss, *J. Am. Chem. Soc.*, 2002, **124**, 4560–4561.

160 M. Joffre, D. Yaron, D. Yaron, R. J. Silbey and J. Zyss, *J. Chem. Phys.*, 1992, **97**, 5607.

161 T. Renouard, L. Bozec, S. Brasselet, I. Ledoux and J. Zyss, *Chem. Commun.*, 1999, 871–872.

162 K. Sénéchal, L. Toupet, I. Ledoux, J. Zyss, H. Le Bozec and O. Maury, *Chem. Commun.*, 2004, **573**, 2180–2181.

163 A. Bourdolle, M. Allali, A. D'Aléo, P. L. Baldeck, K. Kamada, J. A. Gareth Williams, H. Le Bozec, C. Andraud and O. Maury, *ChemPhysChem*, 2013, **14**, 3361–3367.

164 A. Valore, A. Colombo, C. Dragonetti, S. Righetto, D. Roberto, R. Ugo, F. De Angelis and S. Fantacci, *Chem. Commun.*, 2010, **46**, 2414–2416.

165 C. Adachi, M. A. Baldo, M. E. Thompson and S. R. Forrest, *J. Appl. Phys.*, 2001, **90**, 5048–5051.

166 B. F. Levine and C. G. Bethea, *Appl. Phys. Lett.*, 1974, **24**, 445–447.

167 B. F. Levine and C. G. Bethea, *J. Chem. Phys.*, 1975, **62**, 2666.

168 R. C. Evans, P. Douglas and C. J. Winscom, *Coord. Chem. Rev.*, 2006, **250**, 2093–2126.

169 S. Ladouceur, K. N. Swanick, S. Gallagher-Duval, Z. Ding and E. Zysman-Colman, *Eur. J. Inorg. Chem.*, 2013, 2985–3007.

170 H. Xu, R. Chen, Q. Sun, W. Lai, Q. Su, W. Huang and X. Liu, *Chem. Soc. Rev.*, 2014, **43**, 3259–3302.

171 R. D. Costa, E. Ortí, H. J. Bolink, F. Monti, G. Accorsi and N. Armaroli, *Angew. Chemie - Int. Ed.*, 2012, **51**, 8178–8211.

172 S. B. Meier, D. Tordera, A. Pertegás, C. Roldán-Carmona, E. Ortí and H. J. Bolink, *Mater. Today*, 2014, **17**, 217–223.

173 C. E. Housecroft and E. C. Constable, *Coord. Chem. Rev.*, 2017, **350**, 155–177.

174 V. N. Kozhevnikov, Y. Zheng, M. Clough, H. A. Al-Attar, G. C. Griffiths, K. Abdullah, S. Raisys, V. Jankus, M. R. Bryce and A. P. Monkman, *Chem. Mater.*, 2013, **25**, 2352–2358.

175 D. Rota Martir, C. Momblona, A. Pertegás, D. B. Cordes, A. M. Z. Slawin, H. J. Bolink and E. Zysman-Colman, *ACS Appl. Mater. Interfaces*, 2016, **8**, 33907–33915.

176 A. F. Henwood, A. K. Bansal, D. B. Cordes, A. M. Z. Slawin, I. D. W. Samuel and E. Zysman-Colman, *J. Mater. Chem. C*, 2016, **4**, 3726–3737.

177 A. M. Bünzli, E. C. Constable, C. E. Housecroft, A. Prescimone, J. A. Zampese, G. Longo, L. Gil-Escrig, A. Pertegás, E. Ortí and H. J. Bolink, *Chem. Sci.*, 2015, **6**, 2843–2852.

178 H. J. Bolink, E. Coronado, R. D. Costa, N. Lardiés and E. Ortí, *Inorg. Chem.*, 2008, **47**, 9149–9151.

179 A. B. Tamayo, S. Garon, T. Sajoto, I. Peter, I. M. Tsyba, R. Bau, M. E. Thompson and P. I. Djurovich, *Inorg. Chem.*, 2005, **44**, 8723–8732.

180 J. D. Slinker, A. A. Gorodetsky, M. S. Lowry, J. Wang, S. Parker, R. Rohl, S. Bernhard and G. G. Malliaras, *J. Am. Chem. Soc.*, 2004, **126**, 2763–2767.

181 H. J. Bolink, E. Coronado, R. D. Costa, E. Ort??, M. Sessolo, S. Graber, K. Doyle, M. Neuburger, C. E. Housecroft and E. C. Constable, *Adv. Mater.*, 2008, **20**, 3910–3913.

182 R. D. Costa, E. Ortí, H. J. Bolink, S. Graber, C. E. Housecroft and E. C. Constable, *Adv. Funct. Mater.*, 2010, **20**, 1511–1520.

183 M. S. Lowry, W. R. Hudson, R. A. Pascal and S. Bernhard, *J. Am. Chem. Soc.*, 2004, **126**, 14129–14135.

184 I. B. Seiple, S. Su, R. a. Rodriguez, R. Gianatassio, Y. Fujiwara, A. L. Sobel and P. S. Baran, *J. Am. Chem. Soc.*, 2010, **132**, 13194–13196.

185 M. Vojtičková, J. Dobiaš, G. Hanquet, G. Addová, R. Cetin-Atalay, D. C. Yildirim and A. Boháč, *Eur. J. Med. Chem.*, 2015, **103**, 105–122.

186 X. Zeng, M. Tavasli, I. F. Perepichka, A. S. Batsanov, M. R. Bryce, C. J. Chiang, C. Rothe and A. P. Monkman, *Chem. - A Eur. J.*, 2008, **14**, 933–943.

187 S. Ladouceur, D. Fortin and E. Zysman-Colman, *Inorg. Chem.*, 2011, **50**, 11514–11526.

188 A. K. Pal, D. B. Cordes, A. M. Z. Slawin, C. Momblona, A. Pertegás, E. Ortí, H. J. Bolink and E. Zysman-Colman, *RSC Adv.*, 2017, **7**, 31833–31837.

189 V. V. Pavlishchuk and A. W. Addison, *Inorg. Chim. Acta*, 2000, **298**, 97–102.

190 D. Rota Martir, G. J. Hedley, D. B. Cordes, A. M. Z. Slawin, D. Escudero, D. Jacquemin, T. Kosikova, D. Philp, D. M. Dawson, S. E. Ashbrook, I. D. W. Samuel and E. Zysman-Colman, *Dalton Trans.*, 2016, **45**, 17195–17205.

191 C. M. Cardona, W. Li, A. E. Kaifer, D. Stockdale and G. C. Bazan, *Adv. Mater.*, 2011, **23**, 2367–2371.

192 K. Hasan, A. K. Bansal, I. D. W. Samuel, C. Roldán-Carmona, H. J. Bolink and E. Zysman-Colman, *Sci. Rep.*, 2015, **5**, 1–16.

193 V. Guerchais, L. Ordronneau and H. Le Bozec, *Coord. Chem. Rev.*, 2010, **254**, 2533–2545.

194 C. Dragonetti, S. Righetto, D. Roberto, R. Ugo, A. Valore, F. Demartin, F. De Angelis, A. Sgamellotti and S. Fantacci, *Inorg. Chim. Acta*, 2008, **361**, 4070–4076.

195 A. Colombo, E. Garoni, C. Dragonetti and S. Righetto, *Polyhedron*, 2018, **140**, 116–121.

196 C. Dragonetti, S. Righetto, D. Roberto, A. Valore, T. Benincori, F. Sannicolò, F. De Angelis and S. Fantacci, *J. Mater. Sci. Mater. Electron.*, 2009, **20**, 460–464.

197 V. Aubert, L. Ordronneau, M. Escadeillas, J. a G. Williams, A. Boucekkine, E. Coulaud, C. Dragonetti, S. Righetto, D. Roberto, R. Ugo, A. Valore, A. Singh, J. Zyss, I. Ledoux-Rak, H. Le Bozec and V. Guerchais, *Inorg. Chem.*, 2011, **50**, 5027–38.

198 M. Zaarour, A. Singh, C. Latouche, J. A. G. Williams, I. Ledoux-Rak, J. Zyss, A. Boucekkine, H. Le Bozec, V. Guerchais, C. Dragonetti, A. Colombo, D. Roberto and A. Valore, *Inorg. Chem.*, 2013, **52**, 7987–7994.

199 Q. Zhou, B. Zhang, L. Su, T. Jiang, R. Chen, T. Du, Y. Ye, J. Shen, G. Dai, D. Han and H. Jiang, *Tetrahedron*, 2013, **69**, 10996–11003.

200 V. Alain, M. Blanchard-Desce, I. Ledoux-Rak and J. Zyss, *Chem. Commun.*, 2000, 353–354.

201 F. Tessore, E. Cariati, F. Cariati, D. Roberto, R. Ugo, P. Mussini, C. Zuccaccia and A. Macchioni, *ChemPhysChem*, 2010, **11**, 495–507.

202 D. R. Kanis, P. G. Lacroix, M. A. Ratner and T. J. Marks, *J. Am. Chem. Soc.*, 1994, **116**, 10089–10102.

203 C. Dragonetti, A. Valore, A. Colombo, S. Righetto and V. Trifiletti, *Inorg. Chim. Acta*, 2012, **388**, 163–167.

204 C. Dragonetti, A. Colombo, M. Fontani, D. Marinotto, F. Nisic, S. Righetto, D. Roberto, F. Tintori and S. Fantacci, *Organometallics*, 2016, **35**, 1015–1021.

205 A. Colombo, C. Dragonetti, D. Marinotto, S. Righetto, G. Griffini, S. Turri, H. Akdas-Kilig, J.-L. Fillaut, A. Amar, A. Boucekkine and C. Katan, *Dalton Trans.*, 2016, **45**, 11052–11060.

206 C. Bizzarri, F. Hundemer, J. Busch and S. Bräse, *Polyhedron*, 2018, **140**, 51–66.

207 C. W. Lu, Y. Wang and Y. Chi, *Chem. Asian J.*, 2016, **22**, 17892–17908.

208 V. Thamilarasan, A. Jayamani, P. Manisankar, Y.-I. Kim and N. Sengottuvelan, *Inorg. Chim. Acta*, 2013, **408**, 240–245.

209 A. J. Hallett, N. White, W. Wu, X. Cui, P. N. Horton, S. J. Coles, J. Zhao and S. J. A. Pope, *Chem. Commun.*, 2012, **48**, 10838.

210 L. Li, W. W. Brennessel and W. D. Jones, *Organometallics*, 2009, **2**, 3492–3500.

211 Y. Boutadla, D. L. Davies, R. C. Jones and K. Singh, *Chem. - A Eur. J.*, 2011, **17**, 3438–3448.

212 C. D. Ertl, C. Momblona, A. Pertegás, J. M. Junquera-Hernández, M. G. La-Placa, A. Prescimone, E. Ortí, C. E. Housecroft, E. C. Constable and H. J. Bolink, *J. Am. Chem. Soc.*, 2017, **139**, 3237–3248.

213 F. Gärtner, D. Cozzula, S. Losse, A. Boddien, G. Anilkumar, H. Junge, T. Schulz, N. Marquet, A. Spannenberg, S. Gladiali and M. Beller, *Chem. Eur. J.*, 2011, **17**, 6998–7006.

214 C. Fan and C. Yang, *Chem. Soc. Rev.*, 2014, **43**, 6439–6469.

215 E. Baranoff, J. H. Yum, M. Graetzel and M. K. Nazeeruddin, *J. Organomet. Chem.*, 2009, **694**, 2661–2670.

216 E. I. Mayo, K. Kils?, T. Tirrell, P. I. Djurovich, A. Tamayo, M. E. Thompson, N. S. Lewis and H. B. Gray, *Photochem. Photobiol. Sci.*, 2006, **5**, 871.

217 J. Wang, W. Y. Wang, X. Y. Fang and Y. Q. Qiu, *J. Mol. Model.*, 2015, **21**, 2–10.

218 Y. Chi, T.-K. Chang, P. Ganesan and P. Rajakannu, *Coord. Chem. Rev.*, 2017, **346**, 91–100.

219 Y. Koga, M. Kamo, Y. Yamada, T. Matsumoto and K. Matsubara, *Eur. J. Inorg. Chem.*, 2011, 2869–2878.

220 S. Obara, M. Itabashi, F. Okuda, S. Tamaki, Y. Tanabe, Y. Ishii, K. Nozaki and M. A. Haga, *Inorg. Chem.*, 2006, **45**, 8907–8921.

221 P. Brulatti, R. J. Gildea, J. A. Howard, V. Fattori, M. Cocchi and J. A. G. Williams, *Inorg. Chem.*, 2012, **51**, 3813–3826.

222 L. F. Gildea, A. S. Batsanov and J. A. G. Williams, *Dalton Trans.*, 2013, **42**, 10388.

223 J. Kuwabara, T. Namekawa, M. Haga and T. Kanbara, *Dalton Trans.*, 2012, **41**, 44–46.

224 M. Ashizawa, L. Yang, K. Kobayashi, H. Sato, A. Yamagishi, F. Okuda, T. Harada, R. Kuroda and M.-A. Haga, *Dalton Trans.*, 2009, 1700–1702.

225 J. A. G. Williams, A. J. Wilkinson and V. L. Whittle, *Dalton Trans.*, 2008, 2081–2099.

226 R. E. Daniels, S. Culham, M. Hunter, M. C. Durrant, M. R. Probert, W. Clegg, J. A.

Gareth and V. N. Kozhevnikov, *Dalton Trans.*, 2016, **45**, 6949–6962.

227 P.-H. Lanoë, C. M. Tong, R. W. Harrington, M. R. Probert, W. Clegg, J. A. G. Williams and V. N. Kozhevnikov, *Chem. Commun.*, 2014, **50**, 6831–6834.

228 B. F. Shi, N. Maugel, Y. H. Zhang and J. Q. Yu, *Angew. Chem. Int. Ed.*, 2008, **47**, 4882–4886.

229 F. Marchetti, F. Marchetti, F. Masi, G. Pampaloni, V. Passarelli, A. Sommazzi and S. Spera, *J. Fluor. Chem.*, 2009, **130**, 341–347.

230 L. Yang, F. Okuda, K. Kobayashi, K. Nozaki, Y. Tanabe, Y. Ishii and M. A. Haga, *Inorg. Chem.*, 2008, **47**, 7154–7165.

231 N. Yoshikawa, J. Sakamoto, N. Kanehisa, Y. Kai, T. Matsumura-Inoue, H. Takashima and K. Tsukahara, *Acta Cryst. E*, 2003, **59**, m830–m832.

232 S. Ladouceur, D. Fortin and E. Zysman-Colman, *Inorg. Chem.*, 2010, **49**, 5625–5641.

233 S. J. Liu, Q. Zhao, Q. L. Fan and W. Huang, *Eur. J. Inorg. Chem.*, 2008, 2177–2185.

234 N. G. Connelly and W. E. Geiger, *Chem. Rev.*, 1996, **96**, 877–910.

235 D. Rota Martir, G. J. Hedley, D. B. Cordes, A. M. Z. Slawin, D. Escudero, D. Jacquemin, T. Kosikova, D. Philp, D. M. Dawson, S. E. Ashbrook, I. D. W. Samuel and E. Zysman-Colman, *Dalton Trans.*, 2016, **45**, 17195–17205.

236 Y. J. Yuan, Z. T. Yu, H. L. Gao, Z. G. Zou, C. Zheng and W. Huang, *Chem. Eur. J.*, 2013, **19**, 6340–6349.

237 B. Laramée-Milette, F. Nastasi, F. Puntoriero, S. Campagna and G. S. Hanan, *Chem. Eur. J.*, 2017, **23**, 16497–16504.

238 X. Yang, G. Zhou and W. Wong, *Chem. Soc. Rev.*, 2015, **44**, 8484–8575.

239 S. Lamansky, P. Djurovich, D. Murphy, F. Abdel-Razzaq, H.-E. Lee, C. Adachi, P. E. Burrows, S. R. Forrest and M. E. Thompson, *J. Am. Chem. Soc.*, 2001, **123**, 4304–4312.

240 D. N. Chirdon, C. E. McCusker, F. N. Castellano and S. Bernhard, *Inorg. Chem.*, 2013, **52**, 8795–8804.

241 J. V. Caspar and T. J. Meyer, *J. Phys. Chem.*, 1983, **87**, 952–957.

242 S. I. Bezzubov, Y. M. Kiselev, A. V. Churakov, S. A. Kozyukhin, A. A. Sadovnikov, V. A. Grinberg, V. V. Emets and V. D. Doljenko, *Eur. J. Inorg. Chem.*, 2016, **2016**, 347–354.

243 Y. J. Yuan, J. Y. Zhang, Z. T. Yu, J. Y. Feng, W. J. Luo, J. H. Ye and Z. G. Zou, *Inorg. Chem.*, 2012, **51**, 4123–4133.

244 D. D. Wang, Y. Wu, H. Dong, Z. X. Qin, D. Zhao, Y. Yu, G. J. Zhou, B. Jiao, Z. X. Wu,

M. Gao and G. Wang, *Org. Electron.*, 2013, **14**, 3297–3305.

245 M. Gennari, F. Légalité, L. Zhang, Y. Pellegrin, E. Blart, J. Fortage, A. M. Brown, A. Deronzier, M. N. Collomb, M. Boujtita, D. Jacquemin, L. Hammarström and F. Odobel, *J. Phys. Chem. Lett.*, 2014, **5**, 2254–2258.

246 Z. Ning, Q. Zhang, W. Wu and H. Tian, *J. Organomet. Chem.*, 2009, **694**, 2705–2711.

247 A. Zucca, S. Stoccoro, M. A. Cinellu, G. L. Petretto, D. Chimica, V. Vienna, R. V May, P. Ii, N. N. C, N. N. C. H. Pt and N. N. Ch, *Organometallics*, 2007, **26**, 5621–5626.

248 A. Sinopoli, C. J. Wood, E. A. Gibson and P. I. P. Elliott, *Eur. J. Inorg. Chem.*, 2016, **2016**, 2887–2890.

249 K. Hasan and E. Zysman-Colman, *Inorg. Chem.*, 2012, **51**, 12560–12564.

250 A. B. Tamayo, S. Garon, T. Sajoto, P. I. Djurovich, I. M. Tsyba, R. Bau and M. E. Thompson, *Inorg. Chem.*, 2005, **44**, 8723–8732.

251 A. L. Medina-Castillo, J. F. Fernández-Sánchez, C. Klein, M. K. Nazeeruddin, A. Segura-Carretero, A. Fernández-Gutiérrez, M. Graetzel and U. E. Spichiger-Keller, *Analyst*, 2007, **132**, 929–36.

252 Q. Zhao, S. Liu, M. Shi, C. Wang, M. Yu, L. Li, F. Li, T. Yi, C. Huang, Q. Zhao, S. Liu, M. Shi, C. Wang, M. Yu, L. Li, F. Li and T. Yi, *Inorg. Chem.*, 2006, **45**, 6152–6160.

253 W. Y. He, J. M. Fontmorin, P. Hapiot, I. Soutrel, D. Floner, F. Fourcade, A. Amrane and F. Geneste, *Electrochim. Acta*, 2016, **207**, 313–320.

254 Q. Zhao, M. Yu, L. Shi, S. Liu, C. Li, M. Shi, Z. Zhou, C. Huang and F. Li, *Organometallics*, 2010, **29**, 1085–1091.

255 L. Xin, J. Xue, G. Lei and J. Qiao, *RSC Adv.*, 2015, **5**, 42354–42361.

256 G. Zhang, H. Zhang, Y. Gao, R. Tao, L. Xin and J. Yi, *Organometallics*, 2014, **33**, 61–68.

257 R. Tao, J. Qiao, G. Zhang, L. Duan, L. Wang and Y. Qiu, *J. Phys. Chem. C*, 2012, **116**, 11658.

258 K. Hasan, A. K. Bansal, I. D. W. Samuel, C. Roldán-Carmona, H. J. Bolink and E. Zysman-Colman, *Sci. Rep.*, 2015, **5**, 1–16.

259 L. Wang, H. Yin, P. Cui, M. Hetu, C. Wang, S. Monro, R. D. Schaller, C. G. Cameron, B. Liu, S. Kilina, S. A. Mcfarland and W. Sun, *Dalton Trans.*, 2017, **46**, 8091–8103.

260 R. Tao, J. Qiao, G. Zhang, L. Duan, C. Chen, L. Wang and Y. Qiu, *J. Mater. Chem. C*, 2013, **1**, 6446.

261 E. Baranoff, J. H. Yum, I. Jung, R. Vulcano, M. Gratzel and M. K. Nazeeruddin, *Chem. Asian J.*, 2010, **5**, 496–499.

262 C. Bizzarri, F. Hundemer, J. Busch and S. Bräse, *Polyhedron*, 2018, **140**, 51–66.

263 E. Sauvageot, P. Lafite, E. Duverger, R. Marion, M. Hamel, S. Gaillard, J.-L. Renaud and R. Daniellou, *J. Organomet. Chem.*, 2016, **808**, 122–127.

264 G. Volpi, C. Garino, E. Breuza, R. Gobetto and C. Nervi, *Dalton Trans.*, 2012, **41**, 1065–1073.

265 M. C. Tseng, W. L. Su, Y. C. Yu, S. P. Wang and W. L. Huang, *Inorg. Chim. Acta*, 2006, **359**, 4144–4148.

266 W. T. Chen, Y. J. Chen, C. S. Wu, J. J. Lin, W. L. Su, S. H. Chen and S. P. Wang, *Inorg. Chim. Acta*, 2013, **408**, 225–229.

267 F. Sguerra, R. Marion, G. H. V. Bertrand, R. Coulon, É. Sauvageot, R. Daniellou, J.-L. Renaud, S. Gaillard and M. Hamel, *J. Mater. Chem. C*, 2014, **2**, 6125.

268 E. Sauvageot, R. Marion, F. Sguerra, A. Grimault, R. Daniellou, M. Hamel, S. Gaillard and J.-L. Renaud, *Org. Chem. Front.*, 2014, **1**, 639.

269 C. M. Brown, M. J. Kitt, Z. Xu, D. Hean, M. B. Ezhova and M. O. Wolf, *Inorg. Chem.*, 2017, **56**, 15110–15118.

270 E. Matteucci, A. Baschieri, A. Mazzanti, L. Sambri, J. Ávila, A. Pertegás, H. J. Bolink, F. Monti, E. Leoni and N. Armaroli, *Inorg. Chem.*, 2017, **56**, 10584–10595.

271 A. Baschieri, F. Monti, E. Matteucci, A. Mazzanti, A. Barbieri, N. Armaroli and L. Sambri, *Inorg. Chem.*, 2016, **55**, 7912–7919.

272 S. Meng, I. Jung, J. Feng, R. Scopelliti, D. Di Censo, M. Grätzel, M. K. Nazeeruddin and E. Baranoff, *Eur. J. Inorg. Chem.*, 2012, **2**, 3209–3215.

273 J. Li, P. I. Djurovich, B. D. Alleyne, M. Yousufuddin, N. N. Ho, J. C. Thomas, J. C. Peters, R. Bau and M. E. Thompson, *Inorg. Chem.*, 2005, **44**, 1713–1727.

274 C.-H. Yang, J. Beltran, V. Lemaur, J. Cornil, D. Hartmann, W. Sarfert, R. Fröhlich, C. Bizzarri and L. De Cola, *Inorg. Chem.*, 2010, **49**, 9891–9901.

275 S. B. Meier, W. Sarfert, J. M. Junquera-Hernández, M. Delgado, D. Tordera, E. Ortí, H. J. Bolink, F. Kessler, R. Scopelliti, M. Grätzel, M. K. Nazeeruddin and E. Baranoff, *J. Mater. Chem. C*, 2013, **1**, 58–68.

276 F. Monti, F. Kessler, M. Delgado, J. Frey, F. Bazzanini, G. Accorsi, N. Armaroli, H. J. Bolink, E. Ortí, R. Scopelliti, M. K. Nazeeruddin and E. Baranoff, *Inorg. Chem.*, 2013, **52**, 10292–10305.

277 L. He, Z. Wang, L. Duan, C. Yang, R. Tang, X. Song and C. Pan, *Dalton Trans.*, 2016, **45**, 5604–5613.

278 C. Yang, F. Mehmood, T. L. Lam, S. L.-F. Chan, Y. Wu, C.-S. Yeung, X. Guan, K. Li, C. Y.-S. Chung, C.-Y. Zhou, T. Zou and C.-M. Che, *Chem. Sci.*, 2016, **7**, 3123–3136.

279 J. Jin, H. W. Shin, J. H. Park, J. H. Park, E. Kim, T. K. Ahn, D. H. Ryu and S. U. Son, *Organometallics*, 2013, **32**, 3954–3959.

280 Y. S. Li, J. L. Liao, K. T. Lin, W. Y. Hung, S. H. Liu, G. H. Lee, P. T. Chou and Y. Chi, *Inorg. Chem.*, 2017, **56**, 10054–10060.

281 A. Santoro, C. Sambiagio, P. C. McGowan and M. A. Halcrow, *Dalton Trans.*, 2015, **44**, 1060–1069.

282 R. Sharma, N. Patel, R. A. Vishwakarma, P. V. Bharatam and S. B. Bharate, *Chem. Commun.*, 2016, **52**, 1009–1012.

283 W. Wu, C. Cheng, W. Wu, H. Guo, S. Ji, P. Song, K. Han, J. Zhao, X. Zhang, Y. Wu and G. Du, *Eur. J. Inorg. Chem.*, 2010, 4683–4696.

284 A. Deb, S. Manna, A. Maji, U. Dutta and D. Maiti, *Eur. J. Org. Chem.*, 2013, 5251–5256.

285 J. Yang and G. B. Dudley, *J. Org. Chem.*, 2009, **74**, 7998–8000.

286 I. Karthikeyan, D. Arunprasath and G. Sekar, *Chem. Commun.*, 2015, **51**, 1701–1704.

287 G. Song, Y. Su, X. Gong, K. Han and X. Li, *Org. Lett.*, 2011, **13**, 1968–1971.

288 G. Maerker and F. H. Case, *J. Am. Chem. Soc*, 1958, **80**, 2745.

289 T. Niwa, H. Yorimitsu and K. Oshima, *Org. Lett.*, 2007, **9**, 2373–2375.

290 J. N. Demas and G. A. Crosby, *J. Phys. Chem.*, 1971, **75**, 991.

291 W. H. Melhuish, *J. Phys. Chem.*, 1961, **65**, 229–235.

292 G. A. Crosby and J. N. Demas, *J. Phys. Chem.*, 1971, **75**, 991–1024.

293 H. Ishida, S. Tobita, Y. Hasegawa, R. Katoh and K. Nozaki, *Coord. Chem. Rev.*, 2010, **254**, 2449–2458.

294 W. N. Herman and L. M. Hayden, *J. Opt. Soc. Am. B*, 1995, **12**, 416.

295 D. Marinotto, R. Castagna, S. Righetto, C. Dragonetti, A. Colombo, C. Bertarelli, M. Garbugli and G. Lanzani, *J. Phys. Chem. C*, 2011, **115**, 20425.

296 Y. Zhao and D. G. Truhlar, *Theor. Chem. Acc.*, 2008, **120**, 215–241.

297 D. Jacquemin, E. A. Perpète, I. Ciofini, C. Adamo, R. Valero, Y. Zhao and D. G. Truhlar, *J. Chem. Theory Comput.*, 2010, **6**, 2071–2085.

298 D. Jacquemin, C. Adamo and B. Mennucci, *J. Chem. Theory Comput.*, 2012, **8**, 2359–2372.

299 J. Tomasi and B. Mennucci, *Chem. Rev.*, 2005, **105**, 2999–3093.